



N° d'ordre : 42418

THESE

pour obtenir le grade de

DOCTEUR DE L'UNIVERSITE DE LILLE 1

Discipline

ELECTRONIQUE, MICROELECTRONIQUE, NANOELECTRONIQUE
ET MICRO-ONDES

Présentée par :

Julie HERRBACH-EUVRARD

Organic semiconductor p-doping: Toward a better understanding of the doping mechanisms and integration of the p-doped layer in organic photodetectors

Thèse soutenue publiquement le 6 octobre 2017 devant le jury composé de :

Mr KOCH Norbert	Professeur à l'université de Humboldt à Berlin	Rapporteur
Mr HIRSCH Lionel	Directeur de recherche CNRS, Bordeaux	Rapporteur
Mr CLERC Raphaël	Professeur à l'université Jean Monnet à Saint-Etienne	Examinateur
Mr KAHN Antoine	Professeur à l'université de Princeton	Co-Encadrant
Mme REVAUX Amélie	Ingénieur-Chercheur au CEA Grenoble	Co-Encadrante
Mr VUILLAUME Dominique	Directeur de recherche CNRS, Lille	Directeur de thèse

Abstract/Résumé

English

Organic electronics is a promising route for the next generation of electronic devices. With large area scalability, compatibility with flexible and semitransparent substrates, and low temperature processability, printed electronics offers an interesting alternative to conventional silicon-based electronics. On its way to achieve better performances, hole and electron doping needs to be developed to improve the material conductivity as well as the polymer-metal electrode contact.

In this work, we have studied the electrical characteristics of the polymer PBDTTT-c upon addition of p-dopant $\text{Mo}(\text{tfd-COCF}_3)_3$. Complementary electrical (variable temperature current voltage, capacitance, admittance spectroscopy), optical (UV-visible absorption and photoluminescence spectroscopy) and material (NMR, SEM, TEM) characterization techniques have been used to analyze the impact of the doping concentration on the electrical properties of the polymer and improve our understanding of the doping mechanism involved. The doped layer was then successfully integrated in an organic photodetector using soft contact transfer lamination to replace the widely used PEDOT:PSS layer, known to be responsible for stability issues. Finally, both the lamination technique and the knowledge acquired on organic semiconductor doping were used to study the impact of unintentional oxygen doping on the organic photodetector performances.

Although further works are necessary to complete our understanding of organic semiconductor doping, enhance the lamination processes and introduce doped layers in various solution printed devices, present results are promising for the improvement of organic electronic devices.

Keywords: Organic electronics, Organic semiconductors, Semiconductor doping, Photodiodes, Molecular doping

Français

Contrairement à l'électronique conventionnelle à base de silicium, l'électronique organique offre de nouvelles possibilités telles que la production sur grande surface et à faible bilan thermique, ou encore l'utilisation de substrats flexibles et transparents. Afin d'améliorer la conductivité des semi-conducteurs ainsi que le contact polymère-électrode métallique, le dopage en électrons et en trous doit être développé dans les matériaux organiques.

Dans cette thèse, des techniques de caractérisation électrique (courant tension à température variable, capacité, spectroscopie d'admittance), optique (spectroscopie UV-visible et de photoluminescence) et matériau (RMN, MEB, MET) ont été utilisées pour analyser l'influence de la concentration en dopant $\text{Mo}(\text{tfd-COCF}_3)_3$ sur les propriétés électriques du polymère PBDTTT-c et améliorer notre compréhension du mécanisme mis en jeu dans le dopage. La couche dopée a été intégrée avec succès dans un photodétecteur organique en utilisant une technique de laminage afin de remplacer la couche habituellement utilisée de PEDOT:PSS, connue pour générer des problèmes de stabilité dans le dispositif. Enfin, la technique de laminage et le savoir acquis sur le dopage des semi-conducteurs organiques ont permis d'étudier l'impact du dopage non intentionnel par l'oxygène sur les performances des photodétecteurs organiques.

Bien qu'il soit encore nécessaire de renforcer notre compréhension sur le dopage des semi-conducteurs organiques, améliorer la technique de dépôt par laminage et introduire la couche dopée dans divers dispositifs imprimés, les résultats présentés dans cette thèse sont prometteurs pour le développement de l'électronique organique.

Mots-clés : Electronique organique, Semiconducteurs organiques, Semiconducteur-dopage, Photodiodes, Dopage moléculaire

Acknowledgements

The last three years of my life have been a wonderful journey. As with any adventure, I had intense and joyful moments but also had to face some hard time, especially when I began to question myself. Also, an adventure is not possible without the help of many people, both in terms of work and mental support. This section is dedicated to those people and, as I had the opportunity to work with Francophones and Anglophones, I will mix both languages.

To begin with, I would like to warmly thank the members of the jury, Norbert Koch, Lionel Hirsch and Raphaël Clerc, for agreeing to read my manuscript and come to Grenoble for my Thesis defense.

Now for French! Mes prochains remerciements sont consacrés à mes encadrants. Tout d'abord, je dois un très très grand merci à mon encadrante du quotidien, Amélie Revaux. Si j'ai pu vivre cette aventure c'est grâce à toi ! Merci pour ton implication, du montage du sujet jusqu'à la préparation de la soutenance en passant par les points thèse chaque semaine, les nombreuses discussions sur ce mystérieux mécanisme du dopage, ton soutien pour que je puisse partir en conférence, et bien sûr, pour la relecture du manuscrit. MERCI !

Je dois aussi un grand merci à Antoine Kahn. Merci de m'avoir accueilli 6 mois au sein de votre laboratoire à Princeton, mais aussi pour votre encadrement tout au long de cette thèse. Cette expérience dans ce cadre exceptionnel aura été très importante pour moi.

Enfin, je remercie chaleureusement mon directeur de thèse, Dominique Vuillaume. Malgré ces quelques centaines de km qui nous ont séparés, vous avez toujours répondu présent. J'ai beaucoup apprécié nos discussions scientifiques. Merci de m'avoir fait découvrir la spectroscopie d'admittance, et merci pour votre accueil à Lille, dont je garde un très bon souvenir.

Cette aventure je la dois aussi à toutes les personnes qui ont contribué aux résultats présentés dans ce manuscrit. Merci Sonia de Sousa Nobre de m'avoir formée sur la photoluminescence et de m'avoir apporté ton aide. Merci Michel Bardet et Pierre-Alain Bayle pour les mesures de RMN solide et liquide ainsi que pour nos passionnantes discussions. Merci Simon Charlot pour m'avoir formée sur bon nombre d'équipements, pour tous tes conseils en terme de process, pour les nombreuses commandes et pour les images MEB. Merci à Christelle Laugier. Nos évaporations d'aluminium étaient très lentes et capricieuses, mais elles m'auront donné l'occasion de discuter plus longuement de foot, chevaux et volley avec toi. Merci Stéphanie Jacob pour les simulations Silvaco et nos longues et passionnantes discussions. Mais je te remercie aussi pour ton amitié et notre passion commune pour les lapins. Merci Sébastien Noël pour ton aide sur l'adaptation du banc de vieillissement. Ton savoir-faire m'a été plus que nécessaire et je suis déçue de ne pas avoir eu plus le temps de mettre à profit ce banc. Je suis sûre que Tamara en fera bon usage. Merci Alexandra Cantarano pour notre superbe collaboration lors de ton stage de 2^e année. J'ai beaucoup apprécié ton sérieux, ta curiosité, ton humilité et ta gentillesse. Je te souhaite tout de bon pour cette thèse qui t'attend ! Merci à Joël Bleuse pour les mesures de photoluminescence résolues en temps et, surtout, pour avoir eu la patience de me réexpliquer les bases de l'optique. Merci Alexandre Pereira pour ton encadrement en début de thèse et pour nos nombreuses conversations qui auront suivies. Et merci beaucoup pour ton aide sur toute la partie optique de la thèse. Merci à Sylvie Lepilliet pour son aide sur le banc de spectroscopie d'admittance. Je n'oublierai pas ton énergie et ta gentillesse à l'image des Ch'ti. C'est aussi grâce à toi que je garde un très bon souvenir de mes déplacements à Lille. Merci Mohammed Benwadih pour ton aide sur plusieurs parties process de ma thèse mais aussi pour nos passionnantes discussions. Merci à Nathalie Pelissier pour les mesures TEM. Merci aussi à

Rachel Wilkenson qui a corrigé et nettement amélioré mon introduction. Merci à Yoann Roth pour son aide sur Latex lorsque ce logiciel jouait avec mes nerfs. To finish this paragraph, I need to switch back to English as I wish to thank a few people from Princeton. Thank you An Dai for teaching me the lamination process. Thank you Andrew Higgins for your patience when you taught me how to use the VTIV bench. I also warmly thank Andrew, James Endres, Xin Lin and Gabriel Man for having been present whenever I needed help in the lab.

Mais cette aventure n'aurait certainement pas été pareille sans le soutien de mes collègues et de mes proches. Je remercie donc tous les membres actuels ou passés du LCI / LCOI / LCEI / LFVC / (LEME??). Un grand merci à Laurent Tournon pour m'avoir accueillie dans son bureau pièce 247 et pour m'avoir supportée pendant trois ans. Partager ton bureau va vraiment me manquer ! Un autre grand merci aux thésards qui m'ont rejoint au cours de la thèse : Pierre Lheritier, Clara Haddad, Alexandre Gaïtis, Tamara Nunes-Domschke et enfin Smail Amari. J'ai énormément apprécié votre présence au quotidien. Je vous souhaite bon courage pour la fin de votre thèse ! Et une petite pensée toute particulière pour Tamara : je suis trop contente que tu reprennes la suite de ma thèse ! Amuse-toi bien. Je continue mes remerciements avec le fameux groupe de 13h, avec qui j'ai partagé mes repas: Simon Charlot, Jamal Tallal, Laurent Tournon, Stéphanie Jacob, Marine Galliari, Olivier Haon, Didier Gallaire et Jean-Marie Vérilhac. Cette pause de midi à vos côtés était une bouffée d'oxygène qui me permettait de repartir pleine d'énergie pour tout l'après-midi ! Et puis il y a les habitués du café le matin, avec qui je commençais ma journée. Tout d'abord Julia De Girolamo, je te remercie pour ta gentillesse, ta douceur et ta sensibilité. C'était un privilège de te rencontrer. Merci aussi à Julien Routin, Christelle Laugier, Stéphanie Lombard, Karine Lambert, Nadine Bagwaneza et Micaël Charbonneau. Et enfin, merci à tous les autres membres du labo que j'ai eu le plaisir de côtoyer.

I would also like to thank all my friends from Grenoble, Princeton and all over the world. Thank you Yao for your wonderful kindness and for being an amazing friend. Merci à mes parents, Catherine et Guy, pour leur soutien depuis toujours et pour le magnifique pot qu'ils m'ont préparé ! Merci à mon mari, Nicolas, qui aura été mon plus grand soutien, même lorsque nous étions séparés par plusieurs milliers de km. Pour finir, merci Gizmo !

To Nicolas,
I couldn't have done it without you.

Contents

Introduction	1
1 Organic semiconductors, doping and integration in electronic devices: the foundations for this work	7
1.1 Principles of organic electronics: from the semiconductor to the device	8
1.1.1 What is an organic semiconductor?	8
1.1.2 Transport properties in organic semiconductors	11
1.1.3 Toward the detection of photons	15
1.2 Doping in organic semiconductors: how does it work?	17
1.2.1 Principles of the doping mechanisms	18
1.2.2 Alternative model to explain organic semiconductor doping	21
1.2.3 What do we use as dopant?	24
1.3 Doping to push the boundaries of organic electronic devices	25
1.3.1 Enhancement of the transport properties	25
1.3.2 Ohmic contact for improved injection and collection	28
1.3.3 Doping in organic devices: from evaporated OLED to solution printed solar cells	29
2 Electrical characterization of molecular p-doping	31
2.1 Molecular p-doping by solution processing	32
2.2 Impact of doping concentration on hole conductivity and hopping transport activation energy	34
2.2.1 Device processing and experimental set-up	35
2.2.2 Hole conductivity with varying doping concentration	36
2.2.3 Impact of p-doping on hole hopping transport activation energy	39
2.2.4 Trap filling and saturation regimes	41
2.3 Evolution of hole concentration with p-doping	42
2.3.1 Mott-Schottky law and Schottky diodes processing	42
2.3.2 Ionized dopant concentration	44
2.3.3 p-doping activation energy	49
2.4 Possible origin of limited doping efficiency at high concentration	51
2.4.1 Formation of aggregates with increasing doping concentration	51
2.4.2 Composition of the aggregates	56
2.4.3 Impact of doped polymer morphology on electrical performances	60

Contents

2.5	Effective barrier lowering at the organic/metal interface	63
2.5.1	Experiment	63
2.5.2	Injection regimes in polymer p-doped with varying concentrations	64
2.5.3	Enhancement of the organic/metal interface	66
2.6	Summary and outlook	68
3	Analysis of the doping mechanism involved in Mo(tfd-COCF₃)₃ doped PBDTTT-c	71
3.1	Sub-bandgap absorption with p-doping	73
3.1.1	Experiment	73
3.1.2	Formation of sub-bandgap absorption peaks with doping concentration	74
3.1.3	Sub-bandgap peaks related to Charge Transfer Complex (CTC) formation	77
3.2	Doping induced fluorescence quenching	84
3.2.1	Experiment	86
3.2.2	Photoluminescence quenching	88
3.2.3	Static or Dynamic quenching?	91
3.3	Characterization of gap states related to organic semiconductor p-doping	97
3.3.1	Admittance spectroscopy	97
3.3.2	Samples and experimental set-up	101
3.3.3	Trap states formation with p-doping	102
3.3.4	Trap concentration and Density of States	106
3.3.5	From UV-visible absorption spectroscopy to admittance spectroscopy	109
3.4	How to explain the effective p-doping?	110
3.4.1	Density of States broadening	110
3.4.2	Light assisted p-doping	112
3.5	Summary and outlook	114
4	P-doped organic semiconductor as potential replacement for PEDOT:PSS in organic photodetectors	117
4.1	Experiment	119
4.2	p-doped polymer versus PEDOT:PSS as HTL in OPDs figures of merit	122
4.2.1	I(V) characteristics	122
4.2.2	External Quantum Efficiency	125
4.2.3	Similarities between both HTLs	125
4.3	Deeper analysis on the impact of p-doped polymer as HTL	127
4.3.1	Photocurrent dependency on light intensity	127
4.3.2	Active area localization induced by p-doped polymer	133
4.4	Preliminary ageing studies on OPDs with p-doped PBDTTT-c as HTL	135
4.4.1	Reduced humidity impact on series resistance	135
4.4.2	Thermal ageing with p-doped polymer as HTL	137
4.4.3	Establishment of a detailed experimental design for future works	139

4.5	Summary and outlook	140
5	Impact of unintentional oxygen doping on organic photodetectors	143
5.1	Experiment	145
5.2	Impact of oxygen plasma treatment on OPD performances	146
5.2.1	IV characteristics	146
5.2.2	External Quantum Efficiency (EQE)	147
5.2.3	Capacitance measurements	149
5.2.4	Summary and Hypothesis	153
5.3	p-doping impact on electronic structure of OPD active layer	154
5.3.1	Hole conductivity increase	154
5.3.2	Trap levels determination by admittance spectroscopy	156
5.3.3	Summary	160
5.4	Assumption verification with TCAD simulations	161
5.4.1	Simulation principles and parameters	161
5.4.2	Electrical characterization fitting	162
5.4.3	Band bending explanation	167
5.5	Summary and outlook	173
	Summary and future work	175
	Appendix A-Summary of the structures studied	181
	Appendix B-TLM on pure PBDTTT-c	183
	Appendix C-Supplier and reference information	185
	Appendix D-Experimental Protocol of solid-state NMR	187
	Bibliography	189

1. Context

Why organic electronics?

Let's imagine the potential innovations of the future.

Today, our planet is threatened by significant modifications, primarily driven by pollution induced global warming, which has exponentially increased our need to find alternative and sustainable energy solutions [1]. As a result, energy transition is one of the 21st century's major challenges. One potential answer to this problem is through the usage of transparent solar cell windows, which would provide significant energy yields with minimal inconvenience [2]. Additionally, producing lightweight rolls of plastic solar cells would be a solution, not only to urban areas, but would also provide remote villages with access to electricity much more easily [3].

The environment is not the only future concern. Enhancing our quality of life through major breakthroughs in medicine is an important additional consideration. The development of synthetic skin could have a variety of interesting applications such as the ability to reintroduce the sense of touch to amputees. Developing biocompatible devices interfacing directly with neurons, that would record the brain activity without causing internal harm, would give insight into our cerebral processes, by providing knowledge of the most mysterious part of the human body [4]. Further, we could potentially stimulate the brain to avoid seizures and help in the discovery of treatments for neurological disorders as epilepsy, Parkinson and Alzheimer diseases [5, 6].

Flexible and conformable electronic components with transparent display and smart packaging that will have the ability to be integrated into textiles and other objects that will become part of the future Internet of Things (IoT), are the technological developments that will comprise the innovations of tomorrow [7]. For example, in the near future, athletes will be able to monitor their health and performances during training or competition with medically embedded smart devices [8]. Health monitoring through physiological data acquisition is an attractive proposition for medical follow-ups specifically for at-home patients [9]. Fireman's clothing embedding temperature sensors or tents with integrated solar cells might be part of our future as well [10, 11].

In order to render these ideas a reality, we need an alternative to the usual, silicon

based electronic systems, which gained popularity during the second part of the 20th century. Inorganic electronics have achieved excellent performances and followed the path of miniaturization. However, this technology will never be useful for the applications mentioned above. Constrained by size, thickness, brittleness, absence of transparency and incompatibility with organic tissues, the devices fabricated on silicon wafers are not suitable for stretchable, conformable, transparent and biocompatible electronics.

In the late 1970s, A. J. Heeger, A. G. MacDiarmid and H. Shirakawa offered a new era in technology with the discovery of organic materials with semiconducting properties, for which they were awarded the 2000 Nobel Prize in Chemistry [12]. Scientists soon sensed the potential of this discovery. Using carbon based compounds as building blocks for electronic devices unlocks the possibilities for future technologies. Organic semiconductors can be processed using solution printing techniques in semi-transparent thin films using a low thermal budget [13]. Glass, plastic, paper, metal, almost any type of substrate can be considered. Developed in mass production, manufacturing costs can be reduced compared to inorganic devices. Finally, organic semiconductors, mainly composed of carbon and hydrogen atoms, are particularly interesting for bio-applications as they offer a softer transition from living tissues to electric information than inorganic devices [4]. Combined with thin, flexible and stretchable substrates they could be deposited directly onto the skin, the brain or muscles and used to record various signals.

The development of organic electronic devices

Organic Light Emitting Diode (OLED) displays are the major actor in the organic electronic industry as it was the first device of this type to be mass produced and commercialized by Samsung and LG [7]. OLED displays offer improved image quality as well as possibilities for flexible, lightweight and transparent applications. The use of OLED for large area lighting is one of the expected future applications for this product [14]. Conventional lamps will soon be replaced by wide light panels of this type embedded in the environment.

Solar energy is another area in which there has been significant research invested in terms of the use of organic materials [15]. Although it is unlikely that organic solar cells will compete with their silicon counterparts, this technology opens new opportunities for solar energy by taking advantage of their transparent and flexible properties. Thus, the world we imagined for tomorrow is closer than one might have thought.

Alternative photon-to-electron convertors, photodetectors, have also emerged in the organic electronics area. Photodectors can be used as light sensors or integrated in imagers [16, 17]. Plastic based medical imagers are particularly promising for mobile equipments compared to their fragile silicon-made counterpart. Moreover, printing techniques would enable the production of large area medical imagers at a lower cost.

Sensors are used to detect the world surrounding us, recording various types of information that can improve our quality of life. Organic printable sensors are the next generation of temperature, gas, humidity and force detectors [7]. Cheaper to produce and compatible with a varied range of substrates, they can be integrated into any object:

Introduction

in packaging, on touch screens displays or even on and in our body. Organic electronics might indeed be extremely valuable for future discoveries and treatments in medicine. The possibility to integrate electronic devices in textiles offers plenty of new applications as well [18]. Organic electronics is of great interest for wearable technologies.

All these applications would not be possible without the basic component of every electronic device, the transistor. Electric switch or current amplifier, transistors are used to create logic gates and display backplanes. Organic Thin Film Transistors (OTFTs) are therefore a key element of organic electronics research and development. p-type and n-type transistors have successfully been developed and associated to create inverters [19].

In 2010, the market value of printed electronic products was estimated at USD 5.6 billion. In 6 years, the market has been multiplied by 5 reaching a value of USD 26.9 billion. Forecasts expect a market value above USD 40 billion by 2020 for printed electronic devices [7]. Although organic devices might be able to compete with their poly-silicon counterparts for some applications, the main goal of this new market is to address technologies unattainable by classic inorganic electronics.

What are the major challenges for the years to come?

Organic electronics face many challenges including processing, reliability and efficiency issues. Research labs and industries work together to transfer lab-scale experiments into large-scale manufacturing. Deposition techniques need to be roll-to-roll or sheet-to-sheet compatible, easy to implement, reproducible and cost-effective. Taking into account worldwide awareness regarding environmental concerns, the industrialization of organic electronics also needs to consider eco-friendly materials and plan for the devices life-cycle [7].

The major obstacle to the industrialization of organic electronics is probably the devices reliability. Inherent to their composition, organic semiconductors are sensitive to their environment. This includes oxygen, humidity, UV radiations and temperature [20]. Additional research to further understand the degradation mechanisms involved and develop solutions needs to be undertaken. Efficient encapsulation materials and techniques are investigated as well [7]. Electronic devices are subject to bias-stress, which they need to tolerate throughout their lifetime. Mechanical stress also needs to be considered along with the development of flexible, conformable and stretchable applications [21].

Efficiency related challenges depend on the type of device considered, but all types of devices are concerned by the quality of contacts [22]. Every device requires a good interface between the semiconductor active layer and the electrodes in order to provide an efficient injection and collection of charges. This challenge has been completed in inorganic electronics with semiconductor doping [23]. The goal is therefore to implement the doping principle into organic electronics.

2. Aims of this study

The development of organic semiconductor doping is an interesting tool to push the boundaries of organic electronics. Interface layers are currently used to match semiconductors transport levels with electrodes work-function but the materials with appropriate energy levels and good stability are limited. The replacement of interface layers with doped semiconductor layers could provide a greater flexibility in choosing the electrode materials [24]. As interface semiconductor doping provides efficient contact properties which do not depend on the electrode work-function, the novel conducting inks compatible with solution processing techniques will be suitable for any semiconductor active layer. Doping can also be beneficial for the semiconductor transport properties, improving carriers conductivity and mobility.

This study draws on important works carried out in the field of organic semiconductor doping. The impact of molecular p-doping on the electronic properties of polymers has been thoroughly studied by An Dai [25, 26, 27]. She highlighted the Fermi level shift in the polymer bandgap upon dopant addition, as well as an enhancement of the carriers conductivity and mobility. After demonstrating the ability of organic semiconductor doping to decrease the effective injection barrier for holes, providing efficient ohmic contact, she introduced doped layers in organic solar cells as hole interface layer to replace PEDOT:PSS. To enable solution processing of the doped layer and avoid the use of orthogonal solvents, she developed a lamination technique called Soft Contact Transfer Lamination (SCTL).

The underlying mechanisms of organic semiconductor doping have been widely investigated by the group of Prof. Norbert Koch [28, 29, 30]. Most studies describe the doping process by a complete and direct transfer of an electron from the semiconductor HOMO toward the dopant LUMO for p-doping, called Integer Charge Transfer (ICT) [31, 32, 33]. The free hole created on the polymer gives rise to a polaron. However, this model fails to explain some observations made on certain semiconductor-dopant mixtures. The group of Prof. Norbert Koch introduced an alternative mechanism involving the formation of Charge Transfer Complex (CTC) between the molecular semiconductor and dopant. In this configuration, the charge transfer is partial since the electron needs to overcome an energy barrier of several hundreds of meV to reach the acceptor state for p-doping. According to Salzmann *et al.* [30], the mechanisms (ICT or CTC) involved in the doping process depends on the nature of the organic semiconductor. Nevertheless, there remain many issues to be resolved and processes to be understood in the doping of organic semiconductors.

As mentioned previously, doped organic semiconductor layers are of great interest to replace common interface layers and provide efficient ohmic contacts. Indeed, electron and hole interface layers as Zinc Oxide (ZnO), PEI or PEDOT:PSS are known to induce device stability issues [34, 35, 36]. In particular, the hole transport layer PEDOT:PSS is sensitive to humidity, oxygen and UV [37, 38, 39]. First attempts to remove PEDOT:PSS in organic solar cells have been carried out leading to improved device stability [40]. However, the lack of electron blocking layer can be detrimental for photodetectors, which

Introduction

require a low dark current density. Doped layers processable in solution using SCTL as deposition technique are a promising route for PEDOT:PSS replacement.

The purpose of this work is to deepen our understanding of the doping mechanisms in organic semiconductors and introduce this doped layer in a complete device as interface layer. In this thesis we have chosen to focus on p-doping. Doped layers have been barely used in solution printed devices due to processing issues. In this work we will use SCTL to deposit the interface layer processed in solution. The knowledge acquired during this work will also be useful to further understand non-intentional doping consequences due to oxygen in organic devices. The underlying questions of this work are illustrated in Figure 1.

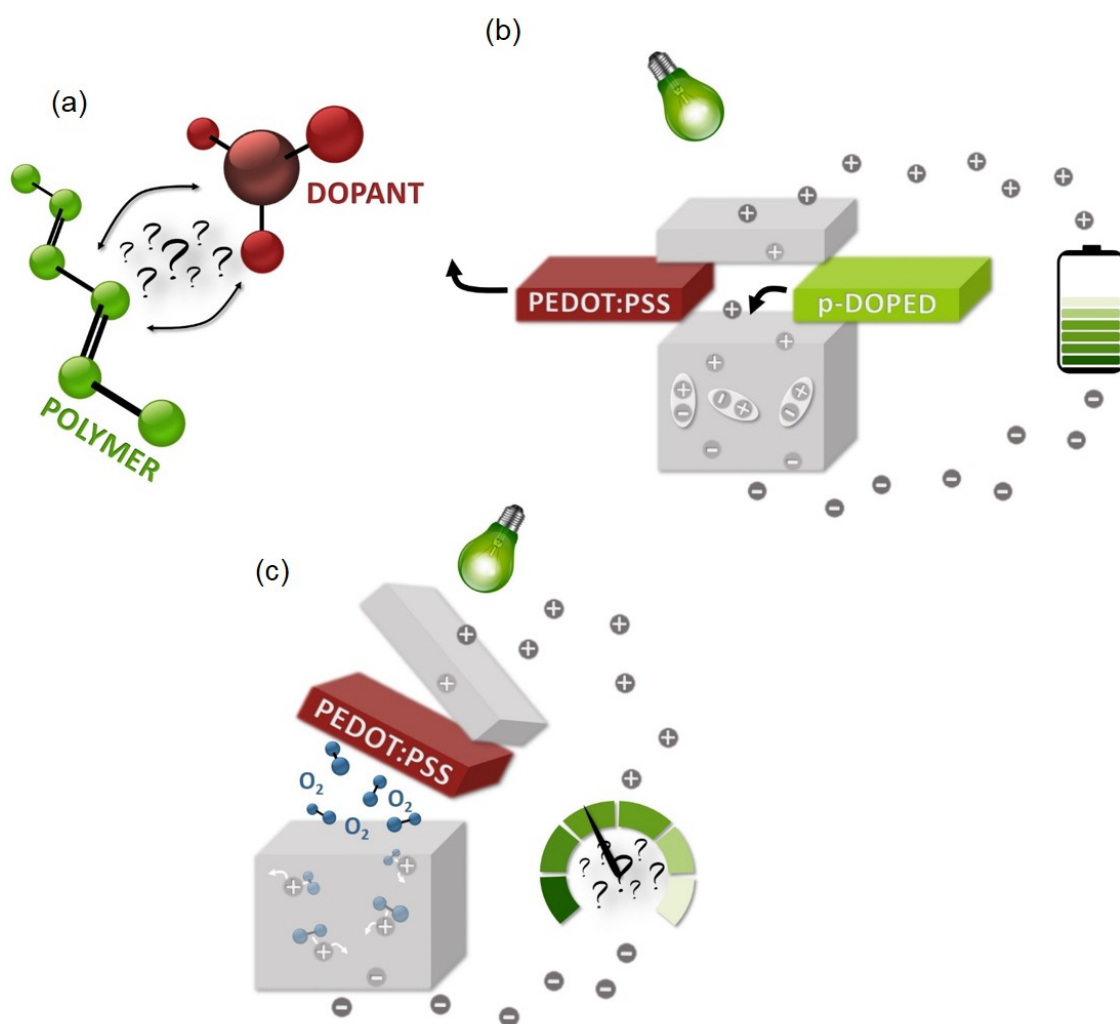


Figure 1: Illustration of the underlying questions studied in Chapter 2 and 3 (a), Chapter 4 (b) and Chapter 5 (c).

This dissertation starts with an overview of the the organic electronics principles and the basics about organic semiconductor doping in Chapter 1. We will also have a look at the different benefits of doping and its integration in organic electronic devices.

As a first step of the experimental work carried out throughout this thesis, we aimed at verifying the p-doping ability of the chosen molecular dopant, $\text{Mo}(\text{tfd-COCF}_3)_3$, on the semiconducting polymer PBDTTT-c, presented in Chapter 2. Through electrical characterization of thin films doped at various concentrations, we identified different regimes. The impact of the doping concentration has been further studied using material and chemical characterization techniques. The ability of doped polymer to form ohmic contacts is also verified with the view to using doped organic semiconductor layers in complete devices.

One of the key challenges of this work was the study of the polymer-dopant interaction. Chapter 3 deals with the potential doping mechanisms involved in our system. We used complementary optical and electrical characterization techniques to deepen our understanding of this doping process. This work raised some questions, which will require further work from the community.

As one of the major goal of organic semiconductor doping is to be integrated as interface layers in organic electronic devices, we introduced the doped PBDTTT-c layer in an organic photodetector (OPD). In Chapter 4, we compared the widely used PEDOT:PSS hole transport layer with our doped material, which has been deposited using lamination techniques. Through various electrical characterization techniques we identified the advantages and limits of this novel transport layer.

As a last step, we took advantage of the knowledge acquired throughout this work to study the impact of unintentional oxygen doping. We used lamination to evaluate the impact of a well-known surface treatment, oxygen plasma, on the OPD performances. This study illustrates the drawbacks of homogeneous doping and highlights the need for localized doped layers.

1

Organic semiconductors, doping and integration in electronic devices: the foundations for this work

Chapter contents

1.1 Principles of organic electronics: from the semiconductor to the device	8
1.1.1 What is an organic semiconductor?	8
1.1.2 Transport properties in organic semiconductors	11
1.1.3 Toward the detection of photons	15
1.2 Doping in organic semiconductors: how does it work?	17
1.2.1 Principles of the doping mechanisms	18
1.2.2 Alternative model to explain organic semiconductor doping	21
1.2.3 What do we use as dopant?	24
1.3 Doping to push the boundaries of organic electronic devices	25
1.3.1 Enhancement of the transport properties	25
1.3.2 Ohmic contact for improved injection and collection	28
1.3.3 Doping in organic devices: from evaporated OLED to solution printed solar cells	29

1.1 Principles of organic electronics: from the semiconductor to the device

How can we obtain semiconducting properties with a carbon-based polymer? How are electrons and holes transported along the molecule and between two molecules? Is it possible to detect photons using organic semiconductors? This first section is dedicated to these questions.

1.1.1 What is an organic semiconductor?

Before introducing organic semiconductors, we start by a short reminder on their inorganic counterparts. Inorganic semiconductors like Silicon (Si), Germanium (Ge) or Gallium-Arsenide (GaAs) are usually described as ordered crystals with defined atomic position as shown in Figure 1.1 (a). The electronic structure of such atomic pattern can be described by wave functions forming energy bands separated by bandgaps. In the case of semiconductors, the Fermi level, which is defined as a threshold energy where a state has a 50% probability of getting occupied, is situated within a bandgap of the order of an electron-volt. Therefore, all states in the energy band below, called valence band, are filled and all states in the energy band above, called conduction band, are empty. This configuration, between metals and insulators, led to the emergence of the microelectronics industry. Figure 1.1 (b) summarizes the position of the valence E_V and conduction band E_C as well as the Fermi level E_F . In this example, the Fermi level is situated in the middle of the bandgap, corresponding to an intrinsic semiconductor. All energies are given with respect to the vacuum level E_0 . The distance between the vacuum level and the conduction band, Fermi level and valence band are called electron affinity EA , work function W_f and ionization potential IP respectively. Finally, the energy required for an electron in the valence band to be excited toward the conduction band is defined by the semiconductor bandgap E_G .

To address flexible, semi-transparent and large area technologies, it could be interesting to replace inorganic semiconductors by organic compounds, which are compatible with solution printing processes. To understand the origin of semiconducting properties in organic materials, we need to take a closer look at atomic orbitals. When brought in contact with a neighboring atom, carbon can have three different hybridization configurations: sp , sp^2 and sp^3 [13]. Each configuration is related to the type of bond formed with the neighboring atom. If we consider a chain with carbon atoms in their sp^2 configuration, the in plane $2p_x$ and $2p_y$ orbitals combine to form σ bonds and the $2p_z$ orbital remains unchanged and perpendicular to the bonds as illustrated in Figure 1.2. The

1.1. Principles of organic electronics: from the semiconductor to the device

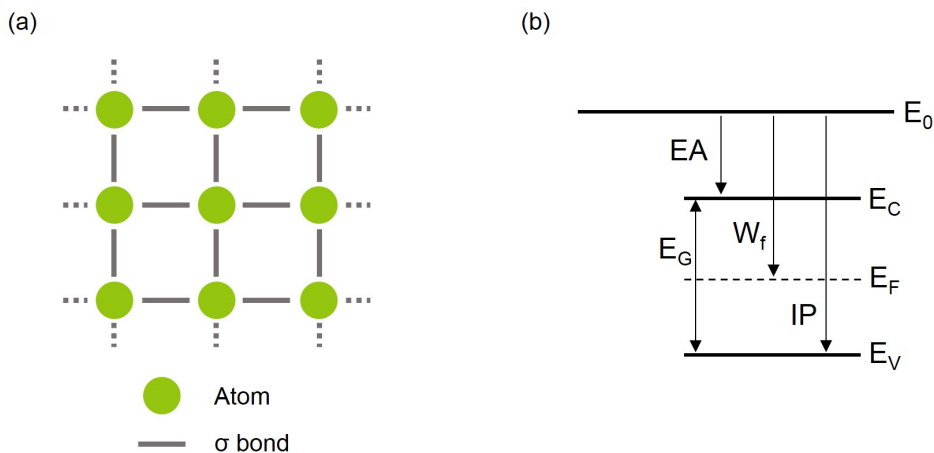


Figure 1.1: Schematic of an inorganic semiconductor crystal structure (a) and corresponding electronic energy levels (b).

overlap between the $2p_z$ orbitals of two neighboring atom leads to the formation of a π bond. The remaining sp orbital forms a σ bond with a hydrogen atom. We finally obtain a π -conjugated molecule as illustrated in Figure 1.3 (a).

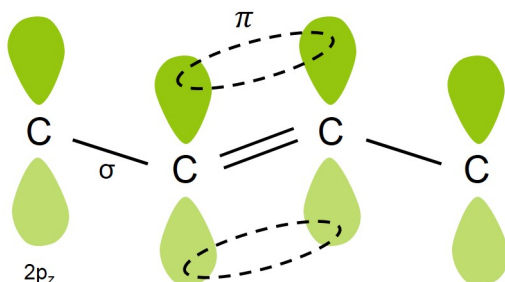


Figure 1.2: Schematic representation of a π bond formation through the overlap of two $2p_z$ orbitals.

Alternating $\sigma - \pi$ bonds in molecules, called π conjugation, can lead to the π bond delocalization. The molecule illustrated in Figure 1.3 (a) can be transformed as shown in Figure 1.3 (b). Such delocalization, as illustrated with a dotted line in Figure 1.3 (c), enables charge transport in the molecule.

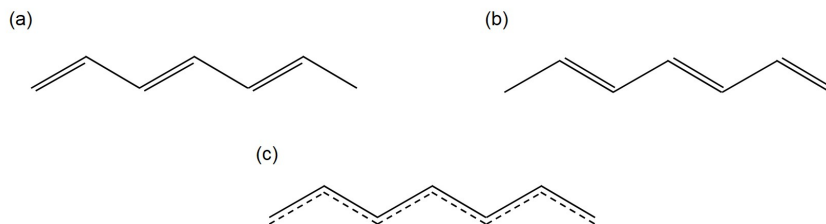


Figure 1.3: Schematic of a π conjugated molecule in its two possible forms (a),(b). The transition is driven by charge delocalization (c).

A bond between two carbon atoms in the sp^2 configuration will lead to π bonding and anti-bonding molecular orbitals as shown in Figure 1.4 (a). If we consider a row with several carbon atoms forming a molecule with alternating $\sigma - \pi$ bonds, the resulting number of bonding and anti-bonding levels will increase as illustrated in Figures 1.4 (b) and (c) [41]. All bonding levels are filled and all anti-bonding levels are empty in the ground state. The Highest Occupied Molecular Orbital (HOMO) and Lowest Unoccupied Molecular Orbital (LUMO) are separated by a gap. If the row is composed of an infinite number of atoms, the gap between each discrete orbitals gets very small and the bonding and anti-bonding orbitals can be considered as bands separated by a gap as shown in Figure 1.4 (d). In this configuration, the Fermi level is situated in the bandgap, between the HOMO and the LUMO. Therefore, π conjugated molecule chains exhibit equivalent semiconducting properties as their inorganic counterparts.

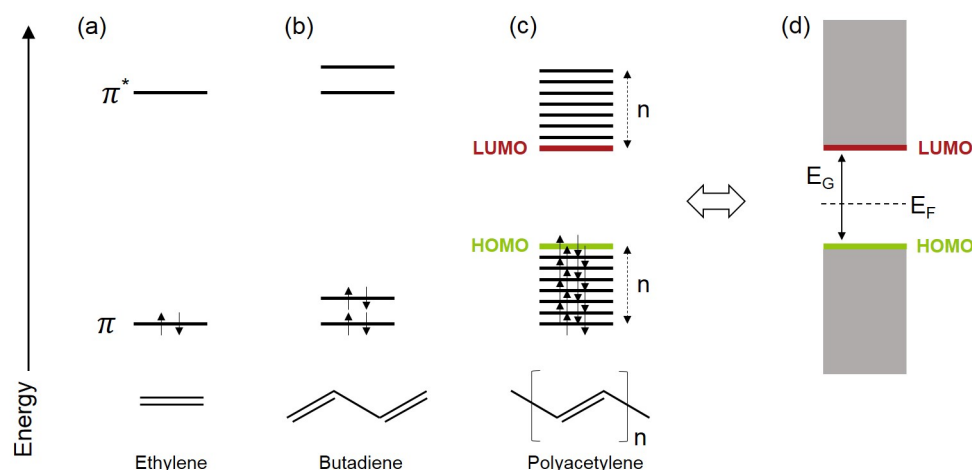


Figure 1.4: Schematic of the formation of bonding π and anti-bonding π^* molecular orbitals for Ethylene (a), Butadiene (b) and Polyacetylene (c). An alternative representation is given for Polyacetylene with the formation of energy bands separated by a bandgap E_G (d). The Fermi level lies in the bandgap, between the HOMO and the LUMO.

The idea of using organic compounds, and especially π conjugated polymers, was first proposed in 1960 [13] but the first organic polymer with good electrical conductivity was discovered in 1977. A. J. Heeger, A. G. MacDiarmid and H. Shirakawa discovered the possibility to dope trans-polyacetylene (Figure 1.5 (a)) upon oxidation and reduction, which led to a Nobel Prize in Chemistry in 2000 [12, 42]. During the 1980s and early 1990s, many studies have been carried out throughout the world to develop convenient and efficient semiconducting polymers. The first challenge was to obtain soluble semiconductors. This goal was achieved using alkyl side chains [41]. The race to innovation continued with the development of various building blocks for semiconducting polymers such as polythiophene (PT), polyparaphenylene (PPP) or polyphenylenevinylene (PPV) (Figures 1.5 (b) to (d)) [43]. By tuning the chemical structure of these compounds, improvement was made in their electrical properties, absorption spectra and electroluminescence performances. Among those polymers, poly(3-hexylthiophene) (P3HT) (Figure 1.5 (e)) has been the most widely studied organic semiconductor [44]. This polymer exhibits good solubility and mobility with its semi-crystalline structure [45]. However, it left room for

1.1. Principles of organic electronics: from the semiconductor to the device

open-circuit voltage (V_{OC}), absorption spectrum and stability improvement. More recently, new building blocks have been developed to address these issues. The family of PTB polymers developed by Liang *et al.* consists in alternating thieno[3,4-b]thiophene (TT) and benzodithiophene (BDT) units (Figures 1.5 (f) and (g)) [46]. In this work, we have chosen a polymer of the PTB family, PBDTTT-c, which will be further presented in Chapter 2. These polymers exhibit improved mobility, V_{OC} and absorption spectrum. Although the last decade was dedicated to the constant improvement of semiconducting polymer performances, one of the main challenges for the years to come is their stability regarding oxygen, UV, temperature, humidity and electrical stresses.

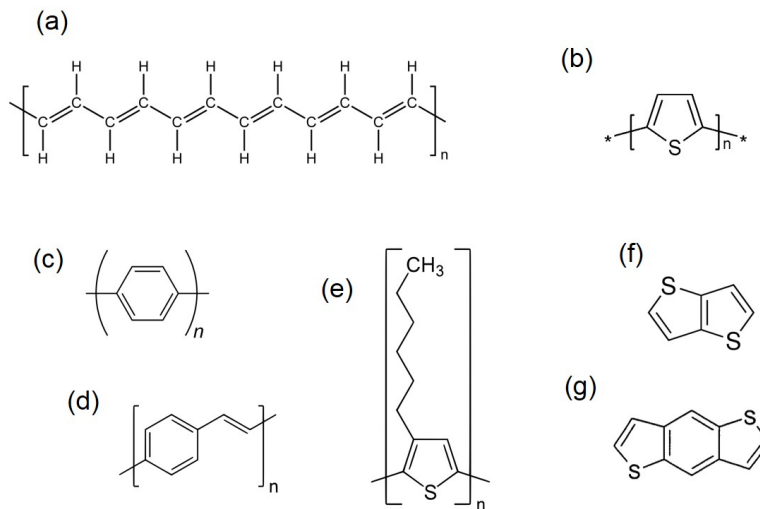


Figure 1.5: Molecular structures of trans-polyacetylene (a), polythiophene (b), polyparaphenylene (c), polyphenylenevinylene (d), poly(3-hexylthiophene) (e), thieno[3,4-b]thiophene (f) and benzodithiophene (g).

1.1.2 Transport properties in organic semiconductors

Inorganic semiconductors exhibit a crystalline structure with a 3D repetition of the exact similar pattern. Moreover, all atoms strongly interact with their neighboring atoms. The translation symmetry and strong interaction lead to the formation of energy bands with a long-range delocalization for charges [47]. As a result, in inorganic semiconductors like crystalline silicon or germanium, electrons and holes can reach mobilities of the order of $10^2 - 10^3 \text{ cm}^2/Vs$ [47]. In these materials, the mobility is usually limited by scattering effect. Band-like transport can be observed in highly pure and crystalline small organic molecules [48] but does not describe the transport properties of most organic semiconductors at room temperature and especially of π conjugated polymers.

The synthesis of π conjugated polymers leads to polymer chains of variable lengths. Moreover, when polymer chains organize themselves to form a solid thin film, the obtained structure is usually amorphous or semi-crystalline. Different polymer chains can also exhibit different spatial configurations within the film. Such disorder induces a broad and inhomogeneous distribution of density of states (DOS) $g(E)$ available for carriers

[13]. Charged impurities originating from the synthesis or due to the environment also participate to the DOS broadening. In 1993, Bässler suggested the approximation of DOS distributions with Gaussian functions as follows [49]:

$$g(E) = \frac{N}{\sigma\sqrt{2\pi}} \exp\left(-\frac{E}{2\sigma^2}\right) \quad (1.1)$$

where E is the energy of the sites, N the concentration of sites enabling the transport of charges and σ the Gaussian width. The broadening of the DOS distribution compared to inorganic materials leads to significant changes in the transport mechanisms.

Figures 1.6 (a) and (b) show a schematic representation of the DOS in energy with respect to the depth of the layer for two different Gaussian distributions. If the Gaussian distribution is narrow (Figure 1.6 (a)), a high density of sites is situated at the same energy and close to the center of the Gaussian function. Therefore, the charge carriers benefit from a highway of sites available for transport enabling an efficient charge transfer from site to site. In this configuration, the charge is considered delocalized as it can move freely from one molecule to the other and the resulting mobility is high [13]. However, band-like transport, as explained in this example, is rarely observed in organic semiconductors.

For a broader Gaussian DOS (Figure 1.6 (b)), the density of sites at a given energy is reduced. Therefore, the charges are localized on the molecules and need to hop from one site to the other. This mechanism is called hopping transport and is observed in most organic semiconductors, which exhibit a reduced mobility [13]. The hopping process in disordered organic materials has been described by a model proposed by Miller and Abrahams [50]. They highlighted the impact of the energetic disorder but also the electronic coupling between different polymer chains on the transport efficiency. Therefore, a wide range of mobilities has been extracted in organic semiconductors from $10^{-7} \text{ cm}^2/Vs$ for amorphous π conjugated polymers [51] to $1 - 10 \text{ cm}^2/Vs$ for organic materials with a relatively good crystallinity [52].

When hopping is involved in the transport of carriers, a trade-off takes place between the need for electrons to decrease their energy and their need for sufficient density of states. Therefore, due to the broad density of states, the average energy level at which the transport takes place is not the center of the LUMO (LUMO level) for electrons and the center of the HOMO (HOMO level) for holes but transport levels E_T situated slightly below the LUMO level or above the HOMO level for n and p-doping respectively. This transport level corresponds to the most efficient pathway for carrier transport [53]. If the number of carriers n or p is low, most of the charges are situated at the tail of the DOS Gaussian distribution as shown in Figure 1.7 (a) for electrons. An activation energy E_A is then required to bring the charges toward the transport level E_T and enable hopping transport. On the other hand, if the carrier density increases, the DOS is progressively filled with a threshold closer to the transport level E_T as illustrated in Figure 1.7 (b). As the threshold energy between filled and empty states is given by the Fermi level E_F , the determination of the activation energy E_A can give insight into the position of the Fermi level with respect to the transport level. This property will be used in Chapter 2 to follow the impact of doping.

Hopping transport can be strongly affected by energy levels situated in the polymer

1.1. Principles of organic electronics: from the semiconductor to the device

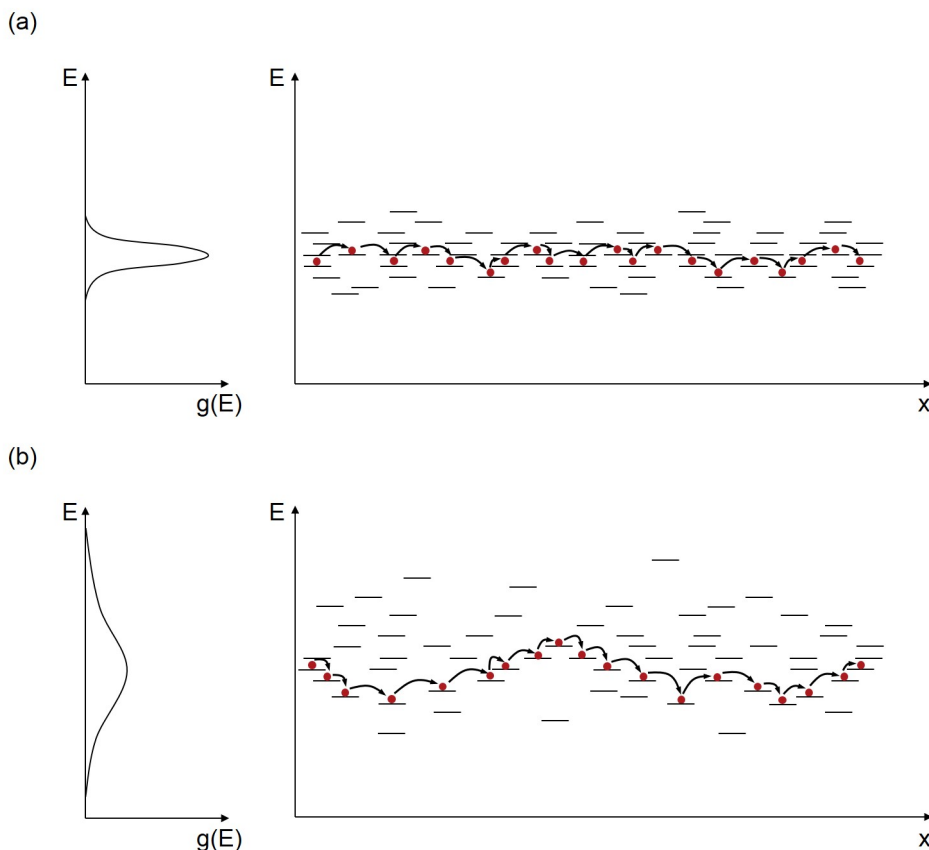


Figure 1.6: Schematic of electron band-like transport for a semiconductor with a narrow DOS distribution $g(E)$ (a). Schematic of electron hopping transport for a semiconductor with a broad DOS distribution (b).

bandgap. These trap states, caused by defects, impurity or disorder, capture and emit charges with a given probability. Figure 1.8 (a) illustrates the different capture and emission processes for electrons and holes for a trap state situated in the middle of the bandgap. There exist two families of trap states: donor and acceptor levels. An acceptor level can trap electrons from the LUMO level affecting the effective electron mobility. Similarly, a donor level can trap holes from the HOMO level altering the effective hole mobility. Acceptor states are negatively charged when they are filled with electrons and neutral when they are empty. Donor states are neutral when filled with electrons and positively charged when they are empty (or filled with holes).

Trap states impact the carrier transport properties but they also affect the electric field in the semiconductor layer when they are charged and induce carrier recombinations. The position of the trap state in the bandgap determines the nature of its impact. Shallow traps, usually distributed according to an exponential decay from the HOMO or LUMO DOS and known as tail states, have a strong impact on the carrier transport properties. On the other hand, when charges are trapped in deep energy levels, they have a higher probability to recombine with the carrier of opposite charge than being re-emitted in the transport level, decreasing the efficiency of solar cells and photodetectors. Figure 1.8 (b)

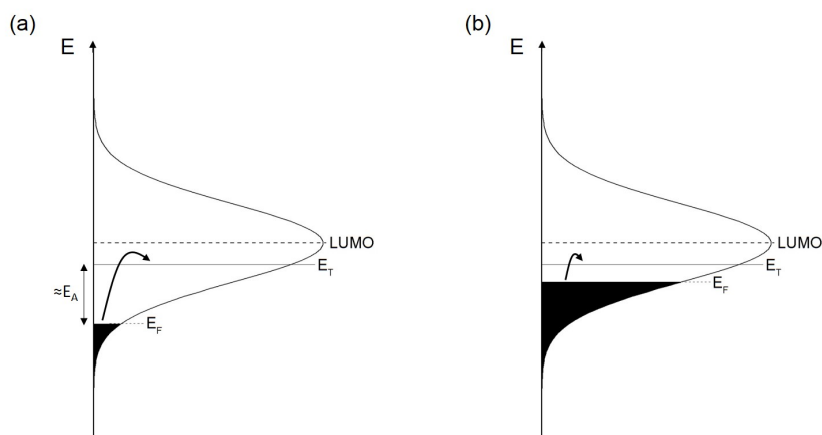


Figure 1.7: Schematic of a DOS Gaussian distribution with the center of the LUMO (LUMO level), the transport level E_T and the Fermi level E_F at low electron density (a) and high electron density (b). The energy difference between the Fermi and transport levels determines the activation energy for hopping transport.

shows a schematic of tail states and deep states in an organic semiconductor bandgap.

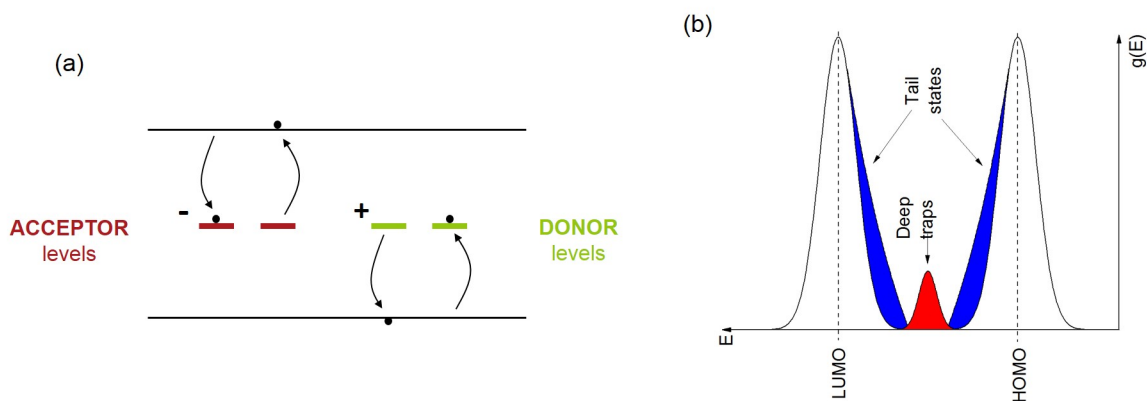


Figure 1.8: Schematic electron capture and emission in acceptor and donor energy levels situated in the middle of the semiconductor bandgap (a). Schematic representation of tail states extending from the HOMO and LUMO DOS and deep Gaussian density of trap states (b).

Charge carriers recombination can be divided in two categories, geminate and non-geminate [54]. Geminate recombination originate from the annihilation of an electron and a hole from the same exciton due to the Coulombic interaction. Geminate recombination are described by the Onsager-Braun model [55]. When an electron and a hole from two different excitons recombine, the process is called non-geminate. In this configuration, charges are dissociated before their recombination. A band-to-band recombination is

1.1. Principles of organic electronics: from the semiconductor to the device

known as Langevin or bimolecular recombination [54]. The low carrier mobility in organic semiconductors is responsible for high Langevin recombination losses [56]. Non-geminate recombination can also be trap-assisted with the capture of both electron and hole within the same energy level. Trap-assisted recombination are described by the Shockley-Read-Hall (SRH) model [57, 58]. Langevin and SRH models will be used in Chapters 4 and 5.

1.1.3 Toward the detection of photons

With the aim of using organic semiconductors in solar cells and photodetectors, we need to understand the processes enabling the detection of photons. Photons can be absorbed in organic materials through vibronic interactions in the internal dipoles of the molecule [13]. For a highly ordered organic material, sharp absorption bands are obtained with respect to the incident photon wavelength and associated with different vibronic features. Amorphous polymers exhibit broader Gaussian distribution of their absorption spectrum due to disorder in the film or solution.

When a photon is absorbed in a semiconductor, an electron is excited from the valence band (or HOMO) toward the conduction band (or LUMO) leaving a hole in the valence band as illustrated in Figure 1.9 (a). The electron-hole pair generated is called exciton. In organic materials, the exciton is tightly electrostatically bound due to the low permittivity ϵ_r of these materials (around 3) [13, 59] and is called Frenkel exciton. Due to the strong interaction between the electron and the hole, Frenkel excitons exhibit a short lifetime, and therefore a high recombination rate [60]. With an exciton binding energy typically around 200 or 300 meV in organic semiconductors, the thermal energy (26 meV at ambient temperature) is not sufficient to dissociate the exciton. For solar cells and photodetection applications, the photo-generated excitons need to be dissociated in order to collect electrons and holes separately.

The photogeneration efficiency was first enhanced by C. Tang in 1986 [61], who used a two-layer structure in small molecule organic solar cells. In 1992, the group of Prof. Heeger used two materials with appropriate energy levels creating an energy offset between the LUMO of both materials known as heterojunction of type II illustrated in Figure 1.9 (b) [62]. The photo-generated exciton can diffuse over a length of approximately 10 nm [60, 63]. If the exciton can reach the interface between the two types of materials, the electron is transferred on the other semiconductor. As the hole remains on the original material, the exciton is spatially separated increasing its lifetime and forms a polaron. The dissociation of the electron and hole is described by Braun model [55]. The photo-generated carriers can be transported and collected separately. The photo-generation of the exciton, its diffusion, transfer, dissociation and collection are illustrated in Figure 1.9 (b). The two types of organic semiconductors are named donor and acceptor according to their ability to give or accept an electron. One material can be either acceptor or donor depending on the complementary material chosen for the heterojunction.

The first organic solar cells processed with a bilayer structure as illustrated in Figure 1.10 (a) was proposed in 1986 by C. Tang [61] followed by the work of Sariciftci *et*

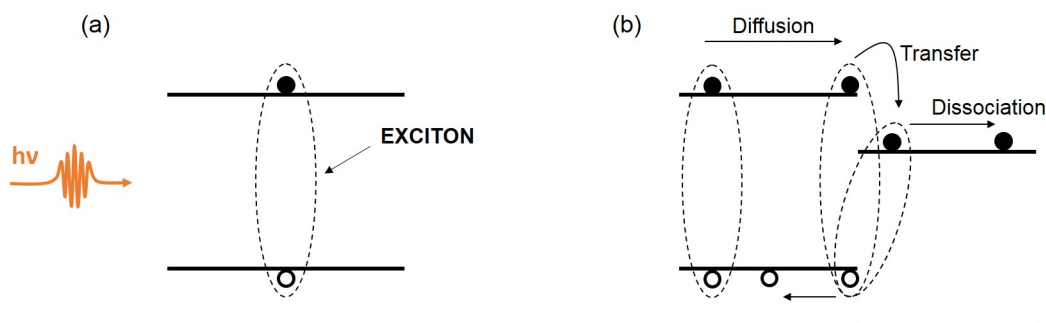


Figure 1.9: Exciton formation upon photon absorption in a semiconductor(a). Schematic of the processes involved in the dissociation of the exciton using an heterojunction of type II: exciton diffusion, electron transfer, exciton dissociation and carrier collection (b).

al. in 1993 [64]. However, the photon-electron conversion efficiency obtained for these device did not exceed 1% and 0.04% respectively. This limited efficiency is due to the low diffusion length of excitons in organic materials. All excitons photo-generated at a distance greater than 10 *nm* from the donor-acceptor interface indeed recombine (Figure 1.10 (b)). To address this issue, the groups of Prof. Heeger and Prof. Friend developed in 1995 a blend heterojunction of donor-acceptor materials [65, 66]. By mixing donor and acceptor molecules in solution prior to deposition, a blend of intermixing phases can be obtained enhancing the amount of donor-acceptor interfaces as shown in Figure 1.10 (c). The optimal structure is obtained when the size of the domains does not exceed 20 *nm* in order to dissociate all photo-generated excitons. An extensive body of work started with the aim of improving the solar cells performances through optimization of the blend heterojunction. In 2009, an exciton dissociation efficiency close to 100% was achieved by Park *et al.* [67]. Efficient percolation pathways need also to be generated in the heterojunction to enable the transport of carriers toward their respective electrode for collection.

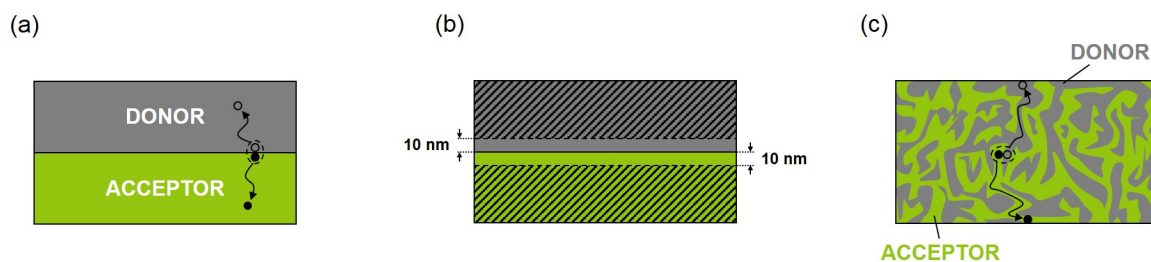


Figure 1.10: Schematic of a donor-acceptor bilayer structure with the exciton dissociation at the interface and the carrier transport toward the electrodes (a). Due to the limited exciton diffusion length, only the photons absorbed around the interface can be dissociated. Excitons absorbed in the striped area have a high probability to recombine (b). Schematic of a donor-acceptor bulk heterojunction with the exciton dissociation at the interface between donor and acceptor phases, and carrier transport along the percolation paths (c).

Donor materials in solution printed devices are usually π conjugated materials as described in Section 1.1.1. Acceptor materials require a lower lying LUMO and HOMO

1.2. Doping in organic semiconductors: how does it work?

than donor materials in order to enable charge transfer leading to the exciton dissociation. A soluble derivative of C_{60} , Phenyl- C_{61} -butyric acid methyl ester ($PC_{60}BM$), was the first acceptor material used in solution printed solar cells by Yu *et al.* [65]. Solar cells performances were then improved by replacing $PC_{60}BM$ with [6,6]-Phenyl- C_{71} -butyric acid methyl ester ($PC_{70}BM$), which exhibits a better absorption in the visible region [68]. New soluble derivative of C_{60} were developed as indene- C_{60} bisadduct ($IC_{60}BA$) and indene- C_{70} bisadduct ($IC_{70}BA$) with an increased LUMO compared to $PC_{60}BM$ and $PC_{70}BM$ [69, 70]. However, further improvements need to be done in acceptor molecules for solution printed solar cells, especially to replace $PCBM$ which is responsible for stability issues of the device through dimerization and formation of aggregates [71, 72]. One of the challenges for the years to come will be to develop efficient and stable non-fullerene acceptor molecules. The molecular structures of $PC_{60}BM$, $PC_{70}BM$, $IC_{60}BA$ and $IC_{70}BA$ are shown in Figure 1.11.

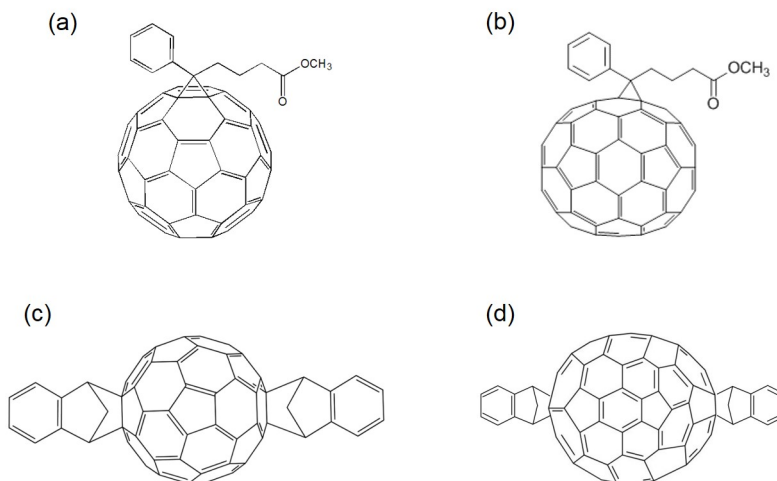


Figure 1.11: Molecular structure of Phenyl- C_{61} -butyric acid methyl ester ($PC_{60}BM$) (a), Phenyl- C_{71} -butyric acid methyl ester ($PC_{70}BM$) (b), indene- C_{60} bisadduct ($IC_{60}BA$) (c) and indene- C_{70} bisadduct ($IC_{70}BA$) (d).

1.2 Doping in organic semiconductors: how does it work?

Controlled p and n-doping was a key factor in the success of inorganic semiconductor devices. The ability to control the Fermi level position leads to improved transport and interface properties. Organic semiconductors are usually undoped and exhibit limited mobilities. Doping organic semiconductors is essential to reduce ohmic losses and obtain efficient contacts. Controlled doping can lower the electric field required to drive Organic Light Emitting Diodes (OLEDs), avoid voltage drops at the active layer-electrode interface of organic solar cells or reduce the contact resistance in Organic Field Effect Transistors (OFETs). Efficient ohmic contacts are required for all electronic devices. One of the major challenges in organic electronics for the years to come will be the development of efficient, controllable and stable n and p-doping.

1.2.1 Principles of the doping mechanisms

To introduce the basic principles of semiconductor doping we start by a short summary of inorganic semiconductor doping. Inorganic semiconductors as Silicon or Germanium are doped with impurity atoms. Phosphorous and Boron are typical dopants used for n and p-doping respectively. The Silicon atoms possess 4 valence electrons leading to the formation of 4 σ bounds with the neighboring atoms as illustrated in Figure 1.12 (a). Phosphorous and Boron atoms possess 5 and 3 valence electrons respectively. Therefore, the introduction of these impurities in the Silicon lattice leads to the addition of an electron or hole when they are ionized as shown in Figures 1.12 (b) and (c).

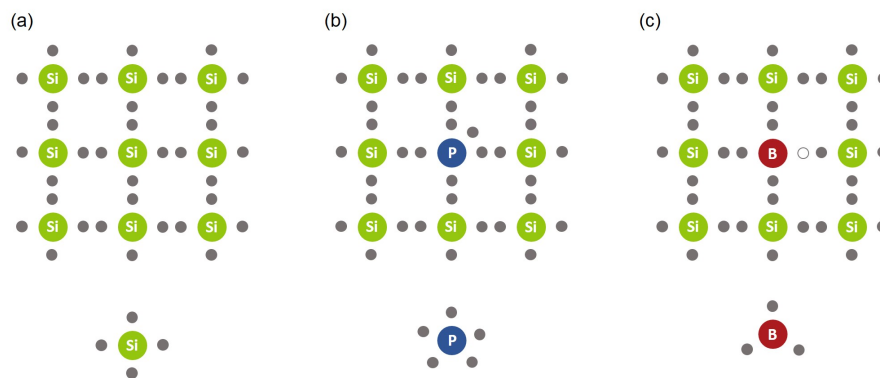


Figure 1.12: Schematic view of bonds formation in pure Silicon semiconductor (a), Phosphorous n-doped Silicon (b) and Boron p-doped Silicon (c).

The introduction of atom impurities doping the semiconductor lattice leads to the formation of states in the bandgap. Impurities giving an electron to the semiconductor are called donors and the associated energy level is situated a few tens of meV below the conduction band. Similarly, impurities adding a hole to the semiconductor matrix are called acceptors and the doping acceptor level is situated a few tens of meV above the valence band. The position of donor and acceptor levels in the semiconductor bandgap is illustrated in Figure 1.13. The levels introduced by efficient dopants, usually fully ionized at room temperature, are shallow states. The ionization of these impurities is associated with the formation of free carriers in the semiconductor. As a consequence of the addition of free carriers in the semiconductor, the Fermi level shifts toward the conduction band for n-doping and valence band for p-doping [23].

The probability of energy levels occupancy is given by the Fermi-Dirac distribution [23]:

$$f(E) = \frac{1}{1 + \exp[(E - E_F)/k_B T]} \quad (1.2)$$

with E the position in energy, E_F the Fermi level, k_B the Boltzmann constant and T the temperature. When the Fermi level gets closer to the dopant acceptor or donor level, the probability of occupancy of the dopant energy levels decreases leading to a lower proportion of ionized dopants. As a result, the position of the impurity energy level in the bandgap is of great importance for the doping efficiency. However, in inorganic semiconductors, all dopant atoms can be considered ionized at room temperature and

1.2. Doping in organic semiconductors: how does it work?

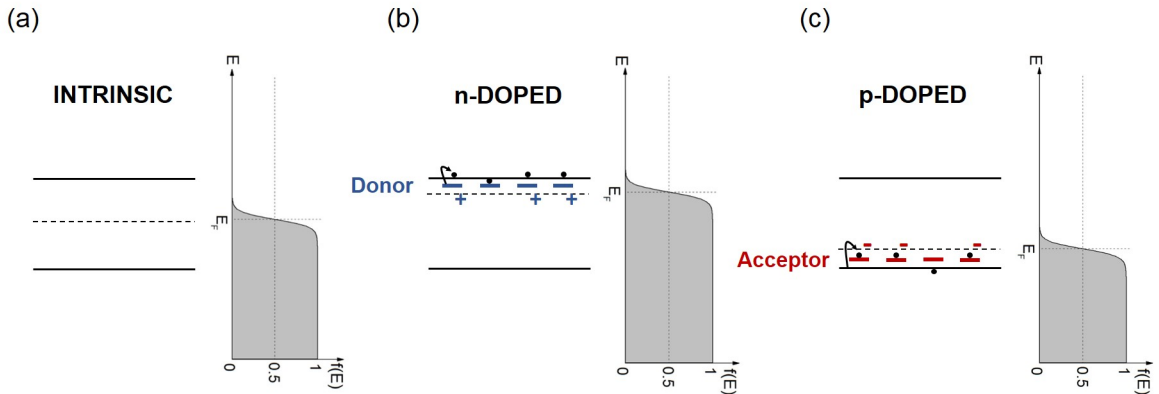


Figure 1.13: Evolution of the Fermi level position following Fermi-Dirac distribution for an intrinsic (a), n-doped (b) and p-doped (c) semiconductor. The donor and acceptor levels are shown in blue and red respectively.

concentrations of $10^{-6} - 10^{-3}$ dopant per semiconductor atom are sufficient to enhance significantly the transport properties and tune the Fermi level position [23]. Moreover, as impurities act as traps, a low doping concentration needs to be maintained to avoid a significant decline in the effective mobilities of carriers.

In organic semiconductors, n and p-doping is achieved by adding appropriate atoms or molecules to the polymer matrix. The doping process is usually described by a complete and direct transfer of an electron from the n-type dopant HOMO to the polymer LUMO for n-doping and from the polymer HOMO to the p-type dopant LUMO for p-doping as illustrated in Figure 1.14 [30, 73]. This process is called Integer Charge Transfer (ICT). Similarly to inorganic semiconductor doping, n-type dopants are called electron donors and p-type dopants electron acceptors. Considering this doping mechanism, simple requirements can be stated to obtain efficient charge transfer [74]:

$$IP_{Don} \leq EA_P \quad \text{for n-doping} \quad (1.3)$$

$$IP_P \leq EA_{Acc} \quad \text{for p-doping} \quad (1.4)$$

with IP_{Don} and IP_P the donor and polymer ionization potential respectively, EA_P and EA_{Acc} the polymer and acceptor electron affinity respectively. Moreover, it has been shown that the doping efficiency increases when the differences $EA_P - IE_{Don}$ and $EA_{Acc} - IE_P$ increase for n and p-doping respectively [75, 76, 77].

To quantify the efficiency of a given dopant in a semiconductor matrix, the doping efficiency is calculated as follows [78]:

$$\eta_{dop} = \frac{\text{Number of free charge carriers generated } (n/p)}{\text{Number of dopant atoms or molecules } (N_D/N_A)}. \quad (1.5)$$

N_D and N_A stand for the density of donor or acceptor dopants added to the semiconductor matrix respectively. Although dopant impurities result in a doping efficiency close to 100% in inorganic semiconductors, this is not the case in organic materials. An effective charge transfer between polymer and dopant does not necessarily lead to a free carrier. Indeed,

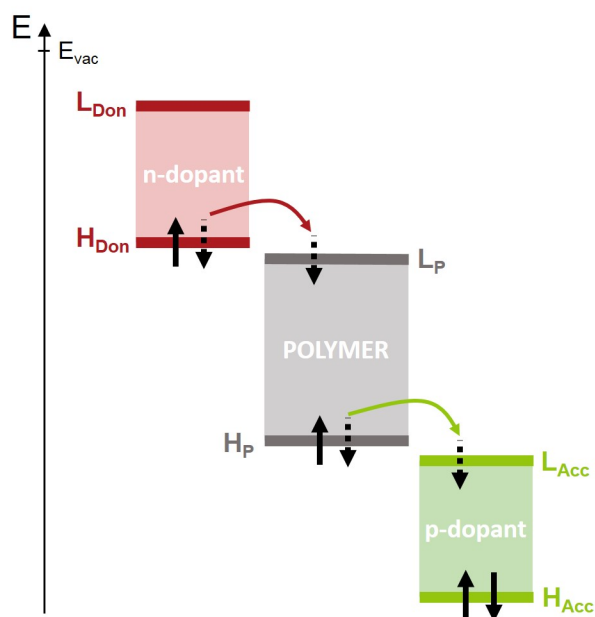


Figure 1.14: Schematic of organic semiconductor doping process through integer charge transfer from the donor molecule to the polymer for n-doping and from the polymer to the acceptor molecule for p-doping. L_{Don} and H_{Don} stand for the donor LUMO and HOMO levels, L_P and H_P for the polymer LUMO and HOMO levels and L_{Acc} and H_{Acc} for the acceptor LUMO and HOMO level.

due to the low relative permittivity of these materials (around 3-4) [59], the carriers are strongly bound to the dopant ion through Coulomb interactions [73]. As a result, achieving 100% charge transfer efficiency does not guarantee a good doping efficiency.

When a generated electron or hole is free in the polymer matrix, a polaron is created with the formation of two localized states inside the bandgap [30]. Figures 1.15 (a) and (b) exhibit a schematic representation of negative (electron) and positive (hole) polarons. The two energy levels shifted from the polymer HOMO and LUMO toward the polymer bandgap result from the distortion experienced by the polymer and due to the additional free charge [30]. Therefore, polarons are a signature of ionized organic semiconductor and is a consequence of the ICT mechanism.

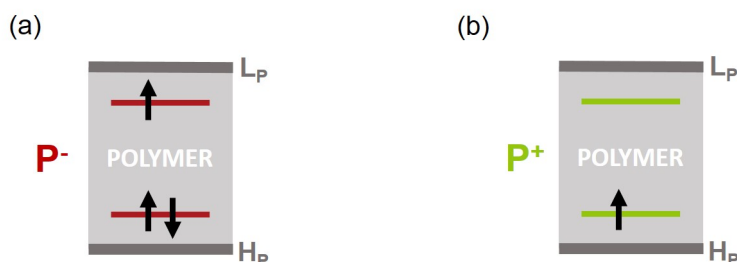


Figure 1.15: Schematic of negative P^- (a) and positive P^+ (b) polarons associated with additional free electrons and holes respectively.

1.2. Doping in organic semiconductors: how does it work?

Integer charge transfer (ICT) has been identified in multiple polymer-dopant mixtures (e.g. P3HT doped with TCNQ derivatives, F₄TCNQ doped PF) with the formation of sub-bandgap absorption peaks associated with the dopant ion or polarons in the polymer [79, 29, 80]. Polarons in the polymer have also been observed through the formation of an additional distribution of density of states (DOS) by Ultraviolet Photoemission Spectroscopy (UPS) for p-doping [81]. It has been shown that polaron states above the polymer HOMO leads to the saturation of the Fermi level shift, usually called Fermi level pinning [82]. Other groups have explained this Fermi level pinning with intrinsic tail states extending in the polymer bandgap [83, 84].

However, some studies carried out on polymer-dopant mixtures are not consistent with the ICT hypothesis. For MeO-TPD doped with C₆₀F₃₆ and F₆TCNNQ, Tietze *et al.* [85] have highlighted the Fermi level pinning a few hundreds of meV above the polymer HOMO and no additional states expected for polarons are measured [30]. Moreover, new occupied states have been measured in the polymer bandgap for some polymer-dopant blends [86, 87, 88]. It has also been shown that p-dopants with a LUMO level lying above the polymer HOMO can lead to effective p-doping [89, 85]. As ICT fails to explain some of the observations for a few polymer-dopant mixtures, an alternative model involving the formation of a Charge Transfer Complex (CTC) has been proposed by Prof. Koch and coworkers [90, 30].

1.2.2 Alternative model to explain organic semiconductor doping

An alternative to the Integer Charge Transfer (ICT) model consists in the formation of a Charge Transfer Complex (CTC) between the polymer and the dopant [30]. For n-doping, the orbital overlap between the dopant HOMO and polymer LUMO can lead to the energy-level splitting with the formation of supramolecular hybrid orbitals (SMHO) as illustrated in Figure 1.16 (a). The bonding state situated below the polymer LUMO is full with two electrons of opposite spin. The anti-bonding state situated above the dopant HOMO is empty. To n-dope the polymer, the electron needs to be transferred from the bonding state of the complex toward the polymer LUMO. This process requires energy ΔE_D and can be responsible for the limited doping efficiency around 10% obtained in organic semiconductors [78, 91, 92]. The analogy can be made for p-type doping shown in Figure 1.16 (b) with the formation of a CTC between the polymer HOMO and the dopant LUMO. The p-doping of the polymer is obtained with the electron transfer from the polymer HOMO to the anti-bonding state of the complex situated in the polymer bandgap. The doping activation energy required is given by ΔE_A .

Méndez *et al.* [92] have shown that a CTC formed between a polymer and a dopant can be described by a Hückel-like model with the gap of the complex E_{gap}^{CTC} given by the following equation for p-type doping:

$$E_{gap}^{CTC} = 2\sqrt{(IP_P - EA_{Acc})^2 + 4\beta^2} \quad (1.6)$$

where β is the resonance integral corresponding to the intermolecular electronic coupling between polymer and dopant. In order to decrease the activation energy required to dope

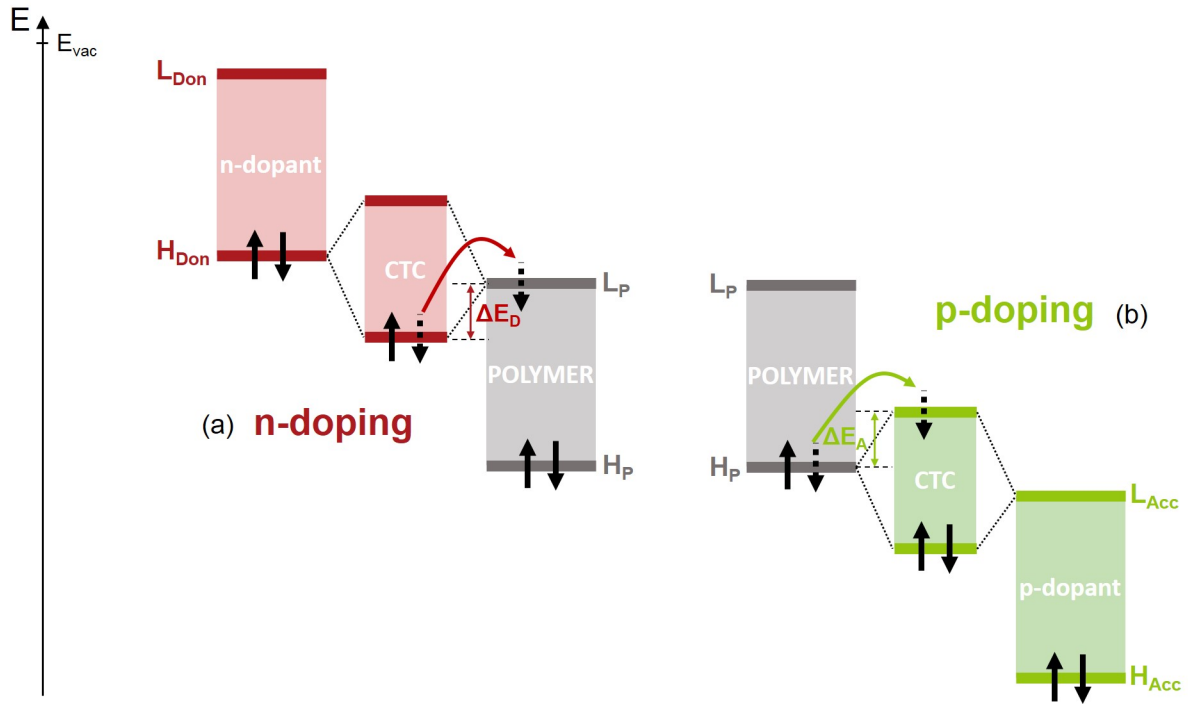


Figure 1.16: Schematic of organic semiconductor doping through Charge Transfer Complex (CTC) formation between the n-type dopant HOMO and polymer LUMO for n-doping (a) and between the polymer HOMO and p-type dopant LUMO for p-doping (b). ΔE_D and ΔE_A stand for the donor and acceptor activation energies.

the semiconductor, the gap of the complex needs to be reduced. According to relation 1.6, the gap of the complex can be reduced by decreasing the coupling β between both components. Moreover, this equation highlights the possibility of complex formation for p-dopant with a LUMO level lying above the polymer HOMO ($IP_P - EA_{Acc} > 0$) and therefore p-dope the polymer.

Density Functional Theory (DFT) calculations have been carried out on various polymer-dopant mixtures highlighting the formation of a charge transfer complex with a bonding and anti-bonding level, which lies several hundreds of meV above the polymer HOMO for p-doping [90, 93, 92]. These anti-bonding states have also been measured by Inverse Photoemission Spectroscopy (IPES) for F₄TCNQ doped 4T at a high doping concentration (1:1), which is closer to an alloy of semiconductor and dopant [29].

A doping donor or acceptor level situated a few hundreds of meV below the polymer LUMO or above the polymer HOMO for n and p-doping respectively leads to Fermi level pinning close to the dopant energy level [28]. Figure 1.17 illustrates the evolution of the Fermi level with the addition of p-dopant leading to doping through CTC formation. The probability of anti-bonding states (acceptor levels) to be filled with an electron is given by the Fermi-Dirac statistics (Equation 1.2). Therefore, as the Fermi level gets closer to the dopant acceptor levels, the probability of dopant ionization is reduced. The Fermi level is pinned between the polymer HOMO and the CTC anti-bonding state where a trade-off

1.2. Doping in organic semiconductors: how does it work?

is obtained between Fermi level shift and doping activation.

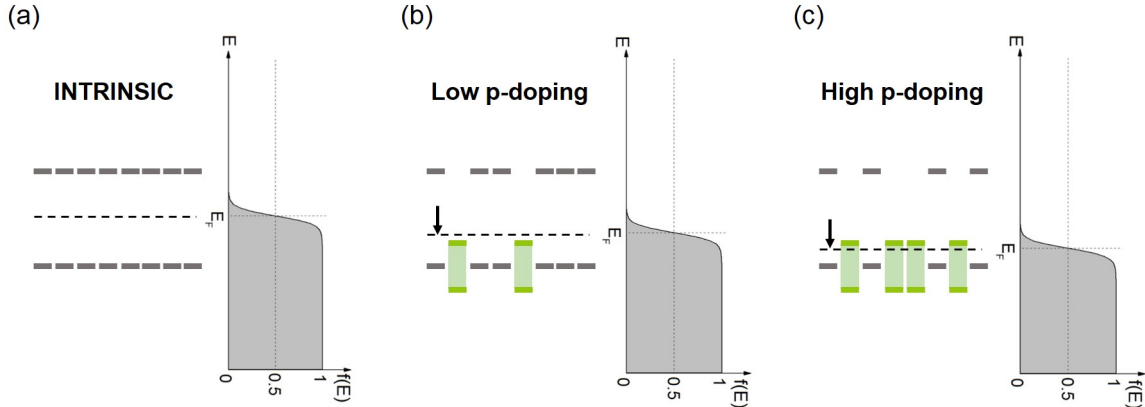


Figure 1.17: Schematic view of the band diagram for pure (a), lightly p-doped (b) and highly p-doped semiconductor (c) with the formation of CTC showing the Fermi-level shift with doping.

When the Fermi level is situated close or below the acceptor state for p-doping, a significant amount of dopant are not activated and act as trap states [85]. This regime is called impurity reserve regime [91]. When the impurity reserve regime is reached, the doping efficiency drops dramatically. Taking into account the Fermi-Dirac statistics described by equation 1.2, the doping efficiency η_{dop} can be described by the following relation [78]:

$$\eta_{dop} = \frac{p}{N_A} = \frac{1}{1 + \exp\left[\frac{(E_A - E_F)}{k_B T}\right]} \quad (1.7)$$

where E_A is the energy of the p-dopant acceptor level. According to this equation, when the Fermi level crosses the anti-bonding state, the doping efficiency is 50%. As the Fermi level continues to shift toward the polymer HOMO, the doping efficiency decreases dramatically and reaches 2% when the Fermi level is only 100 meV below the acceptor level. This behavior can explain the Fermi-level pinning a few hundreds of meV above the polymer HOMO or below the polymer LUMO and the limited efficiencies usually measured at high doping concentrations [85, 91].

I. Salzmann and G. Heimel [30] suggest that ICT and CTC concern different types of organic semiconductors. They suggest that ICT is related to the doping of conjugated polymer and CTC to the doping of films made of small conjugated organic molecules. However, the global picture of organic semiconductor doping and the origin for the different processes remain to be understood. Understanding the doping mechanisms and their limits is essential to push the boundaries of organic semiconductor doping performances. In the case of ICT, a simple condition on the position of the dopant energy levels needs to be fulfilled to achieve efficient charge transfer, but the Coulomb interaction binding the carrier to the dopant ion needs to be reduced to enable efficient doping. If CTC is involved in the doping process, a special care needs to be taken on the intermolecular electronic coupling between both components to reduce the energy level splitting. Moreover, it is crucial to determine the doping process involved in a polymer dopant mixture to further understand its behavior when incorporated in a complete device. For example,

ICT leads to dopant ions, which would be sensitive to the field applied to the device. As a result, a bias stress might cause the diffusion of dopants in the structure. In case of CTC formation, a strong interaction binds the dopant to the polymer host, which might prevent from dopant diffusion due to external electric field.

1.2.3 What do we use as dopant?

The rule to obtain efficient p and n-dopants is to design compounds with high electron affinity and low ionization potential respectively. The first dopants for organic semiconductor doping were simple atoms or di-atoms. The halides iodine (I_2) bromine (Br_2) and chloride (Cl_2) were perfect candidates to p-dope organic semiconductors with their high electron affinity [42, 94]. Similarly, alkali metals as lithium (Li), sodium (Na), potassium (K) and cesium (Cs) have been used as n-dopants [88, 95, 96, 97]. However, due to their size, dopant atoms and di-atoms exhibit a high tendency to diffuse in the organic semiconductor matrix leading to unstable doping properties [98, 88]. Studies on organic semiconductor doping led to metal oxides as molybdenum trioxide (MoO_3), vanadium oxide (V_2O_5) or rhenium trioxide (ReO_3) for p-dopants [99, 100, 101] and inorganic salts as cesium phosphate (Cs_3PO_4) or lithium nitride (Li_3N) for n-dopants [102, 103].

To further prevent the diffusion issues and converge toward solution processable dopants, small organic molecules have been developed. The TCNQ derivative (2,5-Cyclohexadiene-1,4-diyldiene)-dimalononitrile, 7,7,8,8-Tetracyanoquinodimethane (F_4TCNQ) is the most widely used molecular p-dopant (Figure 1.18 (a)) [104, 105]. F_4TCNQ can be co-evaporated with the host semiconductor or dissolved and processed in solution. The fluor atoms added to the TCNQ structure provide a high electron affinity of 5.24 eV [31]. More or less fluorinated TCNQ compounds have been synthesized with tunable electron affinity [106]. However, F_4TCNQ is highly volatile, exhibits a limited solubility and a strong tendency to diffuse due to its planar structure [107, 108, 109, 110]. Larger fluorinated molecules $C_{60}F_{36}$ (Figure 1.18 (b)) and $C_{60}F_{48}$ based on fullerene C_{60} have been developed showing good doping efficiencies, low volatility and good thermal stability [111, 85, 112]. The organo-metallic complex molybdenum tris[1,2-bis(trifluoromethyl)ethane-1,2-dithiolene] ($Mo(tfd)_3$) shown in Figure 1.18 (c) and its soluble derivatives have been developed by the group of Prof. Marder and offer promising performances for organic semiconductor p-doping [113, 114, 115]. In this study we use one of these soluble derivatives, tris[1-(trifluoroethanoyl)-2-(trifluoromethyl) ethane-1,2-dithiolene] ($Mo(tfd-COCF_3)_3$).

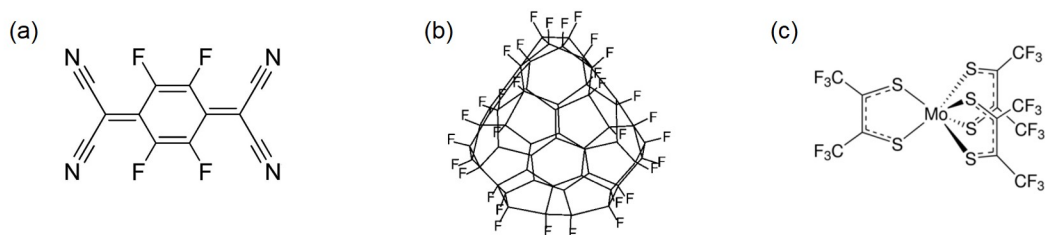


Figure 1.18: Chemical structure of p-dopants F_4TCNQ (a), $C_{60}F_{36}$ (b) and $Mo(tfd)_3$ (c).

The development of molecular n-dopant is constrained by the instability expected for

1.3. Doping to push the boundaries of organic electronic devices

materials with low ionization potentials upon air exposure [78]. Molecular n-type dopants comprise molecules as bis(ethylenedithio)-tetrathiafulvalene ((BEDT)-TTF), tetrathianaphthacene (TTN) or cobaltocene shown in Figure 1.19 (a)-(c) [116, 117, 118] and organic salts as pyronin B chloride (Figure 1.19 (d)) or 2-(2-methoxyphenyl)-1,3-dimethyl-1H-benzoimidazol-3-ium iodide (o-MeO-DMBI-I) [119, 120]. Another approach is to use air-stable dimers as rhodocene ($[\text{RhCp}_2]_2$) shown in Figure 1.19 (e) or ruthenium (pentamethylcyclopentadienyl) (1,3,5-triethylbenzene) ($[\text{Cp}^*\text{Ru}(\text{TEB})]_2$) [121, 122]. The objective for the years to come will be the design of more efficient, soluble and stable p and n-dopant molecules. Recently, Tang *et al.* [123] have overcome the problem of dedoping and dopant diffusion using counter-ions covalently bounded to the polymer for n and p-doping.

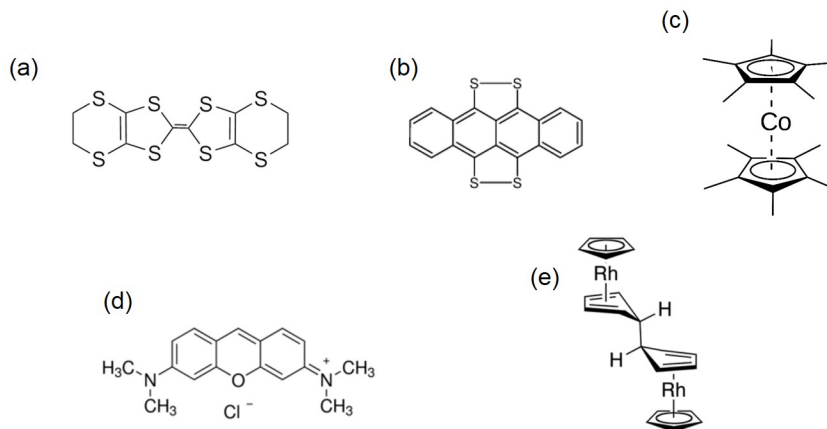


Figure 1.19: Chemical structure of n-dopants (BEDT)-TTF (a), TTN (b), cobaltocene (c), pyronin B chloride (d) and $[\text{RhCp}_2]_2$ (e).

1.3 Doping to push the boundaries of organic electronic devices

Semiconductor doping is an important tool to enhance the device performances. Bulk doping improves the transport properties while contact doping creates good ohmic contacts. Contact and transport properties are key parameters in the development of complete device structures and can be used to push the boundaries of organic electronics.

1.3.1 Enhancement of the transport properties

Efficient organic semiconductor doping leads to the increase of free carriers, holes for p-doping and electrons for n-doping. Therefore, the effect of dopants in organic semiconductors can be followed by measuring the free holes or electrons density through Mott-Schottky analysis, which will be developed in Chapter 2. Figure 1.20 exhibits the hole density with respect to the molar ratio of dopant F_4TCNQ in P3HT (a) and zinc phthalocyanine (ZnPc) (b) reprinted from the works of Pingel *et al.* [124] and Maenning *et al.* [105] respectively. F_4TCNQ leads to a hole density increase by 2 orders of magnitude

at low doping concentration (below 1% in molar ratio) and by 3 orders of magnitude at higher doping concentrations. Therefore, organic semiconductor with hole densities usually around 10^{15} cm^{-3} due to dopant impurities as oxygen can reach carrier densities of the order of 10^{18} cm^{-3} . Nevertheless, to reach carrier densities comparable to doped inorganic semiconductors, dopant concentrations of the order of a few percents in molar ratio are required for molecular doping, while densities below 0.1% are used in inorganic semiconductors.

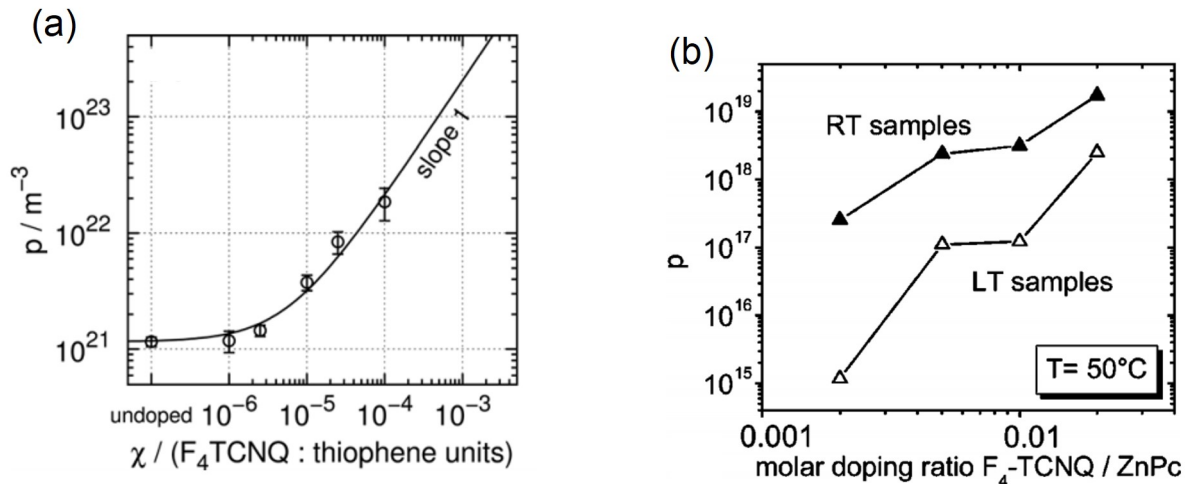


Figure 1.20: Hole density of undoped and doped P3HT layers (a). Reprinted with permission from [124]; Copyright (2012) by John Wiley and Sons. Hole density vs molar doping ratio for ZnPc layers 30 nm thick doped with F4-TCNQ (b). Reprinted with permission from [105]; Copyright (2001) by American Physical Society.

As the hole density p is directly related to the hole conductivity by the following relation:

$$\sigma_p = p\mu_p q \quad (1.8)$$

with μ_p the hole mobility and q the elementary charge, an increase of the hole density leads to the hole conductivity increase and therefore the improvement of the transport properties. Similarly, the electron density increase enhances the electron conductivity. The evolution of organic semiconductor conductivity upon dopant addition has been widely studied in the literature for various polymer-dopant mixtures [24]. The hole conductivity evolution for F_6TCNNQ doped ZnPc [91] and F_4TCNQ doped 4T [29] are shown in Figure 1.21. Depending on the dopant efficiency, the addition of molecular dopants increases the carrier conductivity by several orders of magnitude reaching values between 10^{-4} S/cm to 10^{-1} S/cm [76, 105, 125].

According to relation 1.8, we expect a linear dependency of the carrier conductivity with respect to the doping concentration. However, in most doped organic semiconductors, a superlinear conductivity increase is observed at low doping concentration [24]. This superlinear increase has been attributed to the progressive filling of trap states upon addition of carriers enhancing their mobility [126]. Indeed, a nonlinear evolution of the conductivity with the doping concentration indicates that the carrier mobility $\mu_{h/e}$ evolves

1.3. Doping to push the boundaries of organic electronic devices

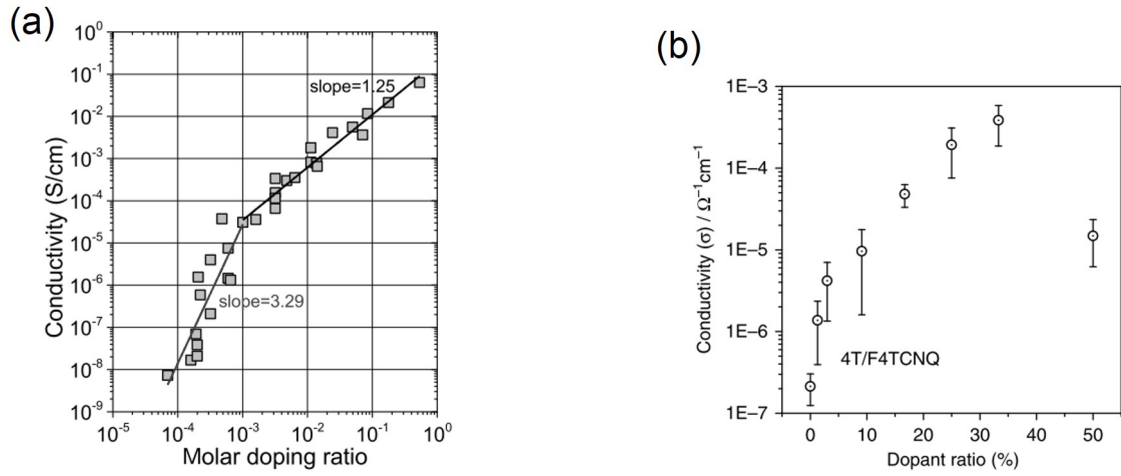


Figure 1.21: Conductivity of ZnPc:F₆TCNNQ thin films (a). Reprinted with permission from [91]; Copyright (2015) by John Wiley and Sons. Lateral thin-film conductivity as a function of the dopant ratio for vacuum co-deposited films of 4T and F₄TCNQ (b). Reprinted from the work of Méndez *et al.* [29].

with doping. Figure 1.22, reprinted from [126], compares the electron conductivity and mobility evolution with the addition of n-dopants [RuCp*(mes)]₂ in C₆₀. For doping concentrations leading to a superlinear increase of the electron conductivity (below 10^{-3} in Molar Ratio MR at 296 K), the electron mobility increases by 2 orders of magnitude. At higher doping concentrations, the mobility reaches a saturation regimes and the conductivity follows a linear increase. The filling of traps at low doping concentrations has been further studied by Lin *et al.* [127] with UPS analysis highlighting the filling of tail states and Gaussian density of states broadening for Mo(tfd)₃ doped CuPc.

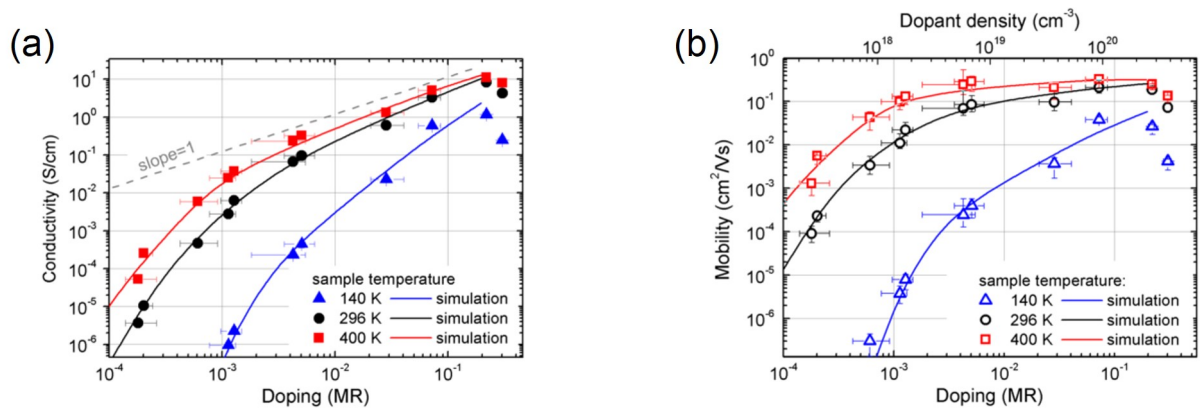


Figure 1.22: Experimental data (symbols) and simulation results (lines) for the conductivity of a C₆₀ layer as a function of doping with [RuCp*(mes)]₂ for three different temperatures; a line with a slope of unity is given as guide for the eye (a). Experimental data (symbols) and simulation results (lines) for the change in C₆₀ mobility upon trap filling deduced from the conductivity data shown in (a) using $\mu_e = \sigma_e/qn$ (b). Reprinted with permission from [126]; Copyright (2012) by American Physical Society.

Molecular doping is an important tool to improve the transport properties of organic semiconductors through carrier generation and trap filling. Although the conductivity evolution is well understood at low and moderate doping concentrations, its behavior at high doping concentration is still under debate. The conductivity saturation or decrease measured at high doping densities might be attributed to dopant aggregation or the addition of disorder in the polymer matrix [128, 129].

1.3.2 Ohmic contact for improved injection and collection

The improvement of charge carrier injection and extraction is one of the major challenges in organic electronic devices [73]. Good ohmic contacts are required in transistors, LEDs, solar cells and photodetectors. The energy level diagram for a metal electrode-semiconductor interface is illustrated in Figure 1.23 (a). The injection barriers for holes Φ_{inj}^p and electrons Φ_{inj}^n are given by the following relations [78]:

$$\Phi_{inj}^p = IP - W_f - \Delta, \quad (1.9)$$

$$\Phi_{inj}^n = W_f - EA + \Delta, \quad (1.10)$$

where W_f is the metal work-function, IP and EA the semiconductor ionization potential and electron affinity, and Δ the dipole formed at the interface between both materials.

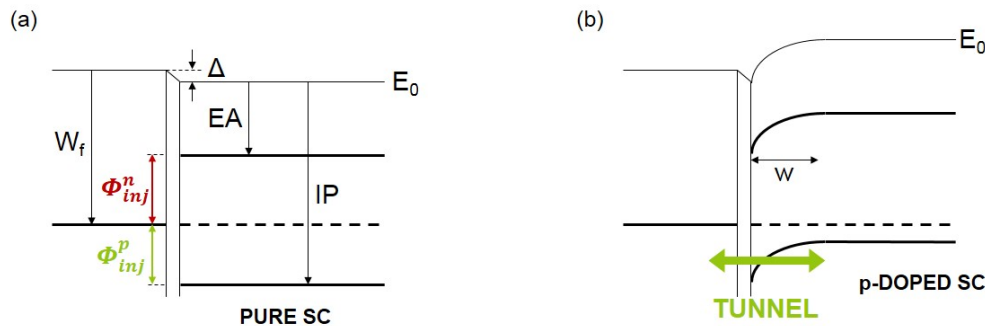


Figure 1.23: Schematic representation of the energy level diagram between a metal electrode and a pure (a) or p-doped (b) semiconductor layer.

According to relations 1.9 and 1.10, the hole injection can be improved by decreasing $IP - W_f$, and therefore, aligning the metal Fermi level with the polymer HOMO. This solution leads to the formation of an ohmic contact. Similarly, a good ohmic contact for electrons can be achieved by aligning the metal Fermi level with the polymer LUMO. However, the formation of an ohmic contact at metal electrode-semiconductor interface is limited by the metals work-functions available. Moreover, efficient electron contacts require electrodes with low work-function and therefore unstable in ambient atmosphere [78]. To tune the work-functions of stable materials, self-assembled monolayers (SAMs) have been developed forming a dipole at the metal interface and changing its work-function [130]. Another technique consists in using injection layers adjusting the electrode work-function as zinc oxide (ZnO), molybdenum oxide (MoO_x), titanium oxide (TiO_x) or PEDOT:PSS [131, 132, 133, 134]. More recently, a thin physisorbed layer

1.3. Doping to push the boundaries of organic electronic devices

of poly(ethylenimine) ethoxylated (PEIE) has been developed, reducing significantly the work-function of various electrode materials with the formation of a dipole at the interface [135].

Semiconductor doping at the interface with the metal electrode is an efficient solution to obtain good contacts [78]. The Fermi level alignment between a metal and a p-doped semiconductor leads to the formation of a space charge region over a depth w below the electrode with a band bending as illustrated in Figure 1.23 (b). The higher the doping concentration, the thinner the space charge region and the stronger the band bending. Therefore, at high doping concentrations, the holes can tunnel through the thin injection barrier leading to quasi-ohmic contacts [136]. The description and characterization of energy alignment at metal-semiconductor interface has been widely studied using Ultraviolet Photoelectron Spectroscopy (UPS) and Inverse Photoemission Spectroscopy (IPES) techniques, showing the formation of a band-bending at the interface with doping [84, 104, 137].

Pure dopant layers have been used to obtain quasi-ohmic contacts in organic electronic devices [138, 139, 140]. Guillain *et al* [141] have deposited a thin layer of pure F₄TCNQ on a solar cell active layer obtaining doped interface through thermally activated dopant diffusion. However, the deposition of pure dopant molecules on organic semiconductor layers might suffer from diffusion issues preventing from localization of doped areas. A mixture of doped semiconductor can also be used at the interface between pure semiconductor and the metal electrode. Doped layers have been introduced in organic electronics by co-evaporation of small molecules and dopants [142, 143, 144]. A stack of pure and doped semiconductor layers is more challenging with solution printed technologies but emerged over the last few years using orthogonal solvents or lamination techniques [26]. Indeed, the deposition of an organic layer dissolved in a compatible solvent with the semiconductor used underneath would lead to the dissolution of the previous layer. Using doped semiconductor as interface layers offers the possibility to use a wider range of metallic materials as electrode without constraints on their work-function.

1.3.3 Doping in organic devices: from evaporated OLED to solution printed solar cells

The operating principle of Organic Light Emitting Diodes (OLEDs) is simple: holes and electrons are injected in a semiconductor layer where excitons are formed and recombine, emitting photons. However, the structure of efficient OLEDs is complicated and involves p-i-n or multiple p-i-n stacks. Surrounding intrinsic layers of organic semiconductors with p and n-doped layers is essential to reduce the driving voltage [143]. Co-evaporation techniques enables the development of various OLEDs structures with stacks of pure and doped layers [145, 146, 147, 148].

The introduction of organic semiconductor doping in Organic Field Effect Transistors (OFETs) is significantly beneficial to reduce the source and drain contact resistances [149, 150, 151]. Localized doping at the interface with the electrodes has also been shown to improve the switching frequencies of transistors [152]. Channel doping can be used to

tune the threshold voltage and increase the devices stability [153, 154, 155]. Doping has also been used recently to fabricate inversion OFETs working with minority carriers [144].

Organic semiconductor doping is a useful tool for organic solar cells as well. p-i-n structures are used to decrease ohmic losses and obtain ohmic contacts at the active layer-electrode interface [156, 157]. Doped layers are also used as optical spacers optimizing the efficiency of the device [158]. The efficiency limit for single junction solar cell structures was estimated around 10-11% [159, 160]. In order to push the boundaries of solar cell technologies and harvest a broader part of the solar spectrum, tandem devices with stacked p-i-n junctions have been developed [161].

Therefore, organic semiconductor doping significantly contributed to the performance improvements of organic electronic devices over the last few years. However, the introduction of localized doped layers in complex structures requires deposition techniques enabling the superposition of multiple organic layers. Co-evaporation of host and dopant was mainly used in doped OLEDs, transistors and solar cells. Although solution printed organic doped layers have been processed, their introduction in complete devices is limited. In 2014, Dai *et al.* [26] used a lamination deposition technique to successfully replace the PEDOT:PSS hole transport layer with a solution processed doped polymer layer. This study opens a new way toward solution printed devices improvement.

2

Electrical characterization of molecular p-doping

Chapter contents

2.1	Molecular p-doping by solution processing	32
2.2	Impact of doping concentration on hole conductivity and hopping transport activation energy	34
2.2.1	Device processing and experimental set-up	35
2.2.2	Hole conductivity with varying doping concentration	36
2.2.3	Impact of p-doping on hole hopping transport activation energy	39
2.2.4	Trap filling and saturation regimes	41
2.3	Evolution of hole concentration with p-doping	42
2.3.1	Mott-Schottky law and Schottky diodes processing	42
2.3.2	Ionized dopant concentration	44
2.3.3	p-doping activation energy	49
2.4	Possible origin of limited doping efficiency at high concentration	51
2.4.1	Formation of aggregates with increasing doping concentration	51
2.4.2	Composition of the aggregates	56
2.4.3	Impact of doped polymer morphology on electrical performances	60
2.5	Effective barrier lowering at the organic/metal interface	63
2.5.1	Experiment	63
2.5.2	Injection regimes in polymer p-doped with varying concentrations	64
2.5.3	Enhancement of the organic/metal interface	66
2.6	Summary and outlook	68

In this study we have chosen to use molybdenum tris[1-(trifluoroethanoyl)-2-(trifluoromethyl) ethane-1,2-dithiolene] ($\text{Mo}(\text{tfd-COCF}_3)_3$) as p-dopant, a soluble derivative of $\text{Mo}(\text{tfd})$, synthesized by the group of Prof. Seth Marder at Georgia Institute of Technology. The polymer Poly[(4,8-bis-(2-ethylhexyloxy)-benzo(1,2-b:4,5-b')dithiophene)-2,6-diyl-alt-(4-(2-ethylhexanoyl)-thieno [3,4-b]thiophene)-2,6-diyl] (PBDTTT-c) is chosen for its promising performances in solar cells and photodetectors. As a first step we need to check the p-doping ability of $\text{Mo}(\text{tfd-COCF}_3)_3$ on the polymer PBDTTT-c. Conductivity and hole density will be measured to evaluate the p-doping efficiency and follow the evolution with the doping concentration. The analysis of different regimes has already been reported in the literature with trap filling at low doping concentration and a decline of the doping performances at higher doping concentrations [91]. Morphology and chemical analyses will be carried out to improve our understanding of the doping evolution. Finally, one of the main target of p-doped layers is their use as hole transport layers in organic electronic devices. Therefore, we will check the ability of $\text{Mo}(\text{tfd-COCF}_3)_3$ doped PBDTTT-c to act as efficient HTL in simple devices.

2.1 Molecular p-doping by solution processing

Thin films of pure and doped polymer will be processed throughout this work and integrated in a complete device structure. PBDTTT-c is chosen as donor material in our photodetectors and will be used to study the doping properties. The HOMO and LUMO levels of this polymer have been measured at 5.12 eV and 3.35 eV below the vacuum level respectively [162]. The chemical structure of PBDTTT-c is given in Figure 2.1 (a). We chose to p-dope PBDTTT-c with the molybdenum complex, $\text{Mo}(\text{tfd-COCF}_3)_3$. The electron affinity of $\text{Mo}(\text{tfd-COCF}_3)_3$ has not been measured directly as thin films of pure dopant are difficult to process. An approximation of the electron affinity has been obtained by cyclic voltammetry around 5.6 eV [163]. However, the uncertainty associated with cyclic voltammetry is significant (error margins larger than ± 0.1 eV [164]) and recent discussions with collaborators bring us to an estimation of the dopant electron affinity closer to 5.3 eV. Although further experiments are required to properly determine the electron affinity of the dopant, we consider a value of 5.3 eV throughout this thesis. An electron affinity of above 5.15 eV is suitable for PBDTTT-c p-doping. Contrary to the planar F_4TCNQ , the molybdenum complex offers a 3D structure, which should lead to improved spatial stability. Figure 2.1 (b) exhibits the chemical structure of the dopant molecule.

P-doped PBDTTT-c thin films are deposited by solution processing. As a first step, both components are dissolved separately in an appropriate solvent. PBDTTT-c and $\text{Mo}(\text{tfd-COCF}_3)_3$ show good solubility in ortho-xylene (o-Xylene), which was selected for

2.1. Molecular p-doping by solution processing

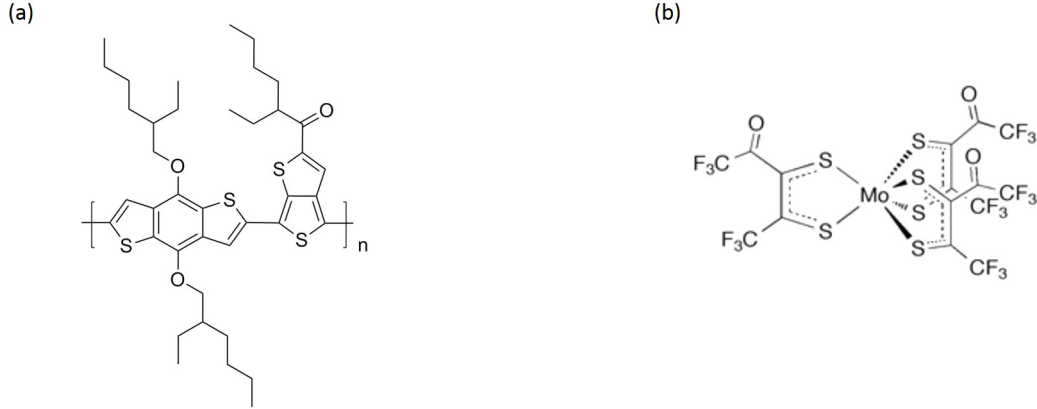


Figure 2.1: Chemical structure of PBDTTT-c (a) and $\text{Mo}(\text{tfd-COCF}_3)_3$ (b).

its non-chlorinated composition. The solutions of pure polymer and dopant are stirred overnight at 45°C . To obtain the solution of doped polymer, the appropriate volume of dopant solution is added to the polymer solution. The resulting mixture is stirred at 45°C for 4 hours.

The concentration of dopant in the polymer matrix is determined in Molar Ratio (MR). The Molar Ratio corresponds to the number of dopant molecules n_d added per monomer of PBDTTT-c n_p :

$$MR = \frac{n_d}{n_p} \quad [-]. \quad (2.1)$$

n_d and n_p depend on the dopant and polymer weight, m_d and m_p , as follows:

$$n_d = \frac{m_d}{M_d} \quad (2.2)$$

$$n_p = \frac{m_p}{M_p} \quad (2.3)$$

where M_d and M_p are the dopant and polymer molecular weights. The molecular weights of $\text{Mo}(\text{tfd-COCF}_3)_3$ and PBDTTT-c monomer are 858 g/mol and 710.4 g/mol respectively. As solutions of polymer and dopant are mixed to obtain the final ink, we need to express m_d and m_p with respect to the concentrations (C_d and C_p) and volumes (V_d and V_p) of both components:

$$m_d = C_d V_d \quad (2.4)$$

$$m_p = C_p V_p. \quad (2.5)$$

As a result, the Molar Ratio is given by the following relation:

$$MR = \frac{C_d V_d M_p}{C_p V_p M_d}. \quad (2.6)$$

Different printing techniques have been developed to process thin films from solution: spincoating, inkjet printing, screen printing and roll-to-roll (R2R) or sheet-to-sheet compatible techniques like slot die or gravure coating [165]. In this work we have chosen,

as a first proof of concept, to deposit our thin films using spincoating. This deposition technique consists in applying a high rotational speed to a substrate, which is maintained by vacuum. When the solution of polymer is dropped on the substrate, a homogenous thin film is formed and the solution in excess is ejected from the substrate as shown in Figure 2.2. Most of the solvent is evaporated during the coating but an annealing step is usually required to obtain the final solvent-free polymer thin film. The solvent evaporation is indeed critical for the film morphology. Although one of the drawbacks of this technique is the significant waste of solution, spincoating is particularly appreciated at the laboratory scale when no patterning is required. The layer thickness can be tuned by the polymer concentration and the rotational speed applied to the substrate.

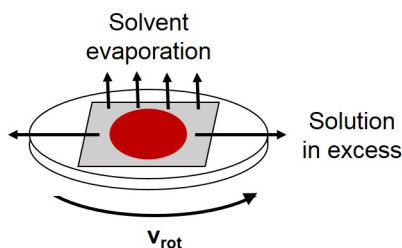


Figure 2.2: Schematic view of the spincoating deposition technique.

All solution deposition techniques face a challenge when a stack of several organic layers is required. The deposition of the top layer may lead to the dissolution of the bottom thin film. To avoid this issue and enable multilayer processing, orthogonal solvents are chosen for successive depositions [166]. However, finding appropriate orthogonal solvents for several organic compounds is not straightforward [167, 168]. To overcome this limitation, a deposition technique of thin films in their solid form has been first reported by Gränstrom *et al.* [169] and further developed by Dai *et al.* [26] to deposit p-doped polymer thin film on solar cell active layer. This technique called Soft Contact Transfer Lamination technique is illustrated in Figure 2.3. As a first step the top layer is spincoated on a UV-ozone treated silicon wafer (Step (a)). After annealing, the thin film is brought into contact with a Polydimethylsiloxane (PDMS) stamp (step (b)). To transfer the top layer on the PDMS stamp, the whole sample is dipped in deionized (DI) water (step (c)). The top layer, in its solid form, is then deposited on the bottom layer previously spincoated on the device (step (d)). The lamination is completed by carefully removing the PDMS stamp (step (e)). This technique will be used throughout this work in various experiments.

2.2 Impact of doping concentration on hole conductivity and hopping transport activation energy

As introduction of this chapter we start by reproducing the work of A. Dai to show the evolution the hole conductivity and hopping transport activation energy with doping [25]. As it has been mentioned in Chapter 1, p-doping leads to the increase of the hole conductivity through the addition of charge carriers in the transport level. Conductivity measurements are therefore a convenient way to verify the p-doping ability of

2.2. Impact of doping concentration on hole conductivity and hopping transport activation energy

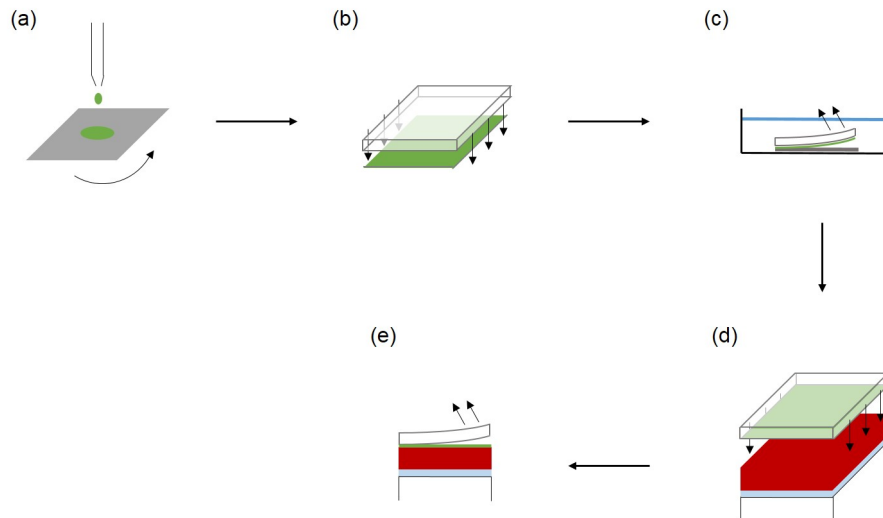


Figure 2.3: Schematic of SCTL process: spincoating of the top layer on silicon substrate (a), PDMS stamp brought into contact with top layer (b), lamination of top layer on PDMS stamp in DI water (c), lamination of top layer on bottom layer (d) and removal of PDMS stamp (e).

Mo(tfd-COCF₃)₃ on PBDTTT-c. Moreover, it will help identify the doping concentrations required to observe significant improvements induced by the addition of dopant. Comparing these concentrations with the literature will give an idea of the efficiency of this dopant. From temperature measurements, it is also possible to follow the impact of p-doping on the hole transport mechanism. The determination of the hopping transport activation energy for holes will highlight the improvement of the transport properties with doping.

2.2.1 Device processing and experimental set-up

To study the lateral transport of holes we use a hole-only structure with a polymer layer deposited on inter-digitated gold electrodes. A schematic of the electrode pattern is given in Figure 2.4 and in Appendix A as Structure 1. This device consists in 15 channels of 150 μm in length and 5 mm in width.

The gold electrodes are evaporated on a glass substrate using a shadow mask to reach a thickness of 100 nm . A thin layer of titanium (10 nm) is evaporated prior to gold to ensure a good adhesion of the electrode on glass. Pure and Mo(tfd-COCF₃)₃ doped PBDTTT-c with 8 doping concentrations from 0.5% MR to 8% MR are spincoated on the patterned gold electrodes and annealed at 150°C for 10 min in glovebox. The thicknesses of the layers are measured using an Atomic Force Microscope (AFM) and range between 30 and 225 nm . This significant thickness inhomogeneity is due to the difficulty to obtain polymer-dopant mixtures with similar viscosity at different doping concentrations. A strong variability in the layer thicknesses might have a non-negligible impact on the conductivity measurements and need to be considered. The thickness control of p-doped layers has been improved for further experiments presented in Chapter 3.

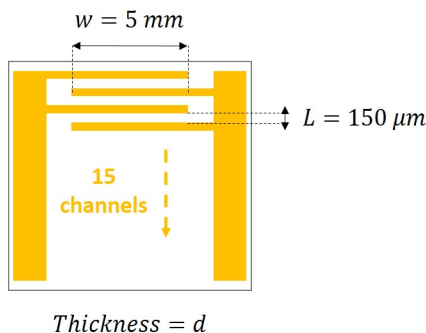


Figure 2.4: Schematic of the gold inter-digitated structure used for conductivity measurements with variable temperatures (Structure 1).

After processing, the device is transferred to a vacuum chamber (base pressure of 2×10^{-10} Torr) for measurements. A sample holder is used to ensure electrical contact and apply variable temperatures to the substrate. In this experiment, the temperature is varied from 200 K to 390 K with a step of 5 K using a closed-cycle He refrigerator combined with a heater. Current-Voltage (I(V)) measurements are carried out from -50 V to +50 V with a step of 2 V using a Keithley 2400 source meter.

2.2.2 Hole conductivity with varying doping concentration

To extract the hole conductivity for each doping concentration, we measure the I(V) characteristics for the hole only devices. With a work-function around 5.1 eV [170], gold is chosen as the electrode material to ensure ohmic contact with the PBDTTT-c polymer, which exhibits an ionization potential of 5.12 eV. Transmission Line Measurement (TLM) has been used to determine the contact resistance with the gold electrode for pure PBDTTT-c. The plot showing the resistance values measured for various channel widths and lengths is given in Appendix B. The sample exhibits a contact resistance of the order of $10^{10} \Omega$ while the resistance of the polymer layer is measured around $10^{12} \Omega$. Therefore, the contact resistance can be neglected at 0% MR. With doping, we expect a decrease of the contact resistance as an ohmic contact is formed at the electrode interface. This evolution will be verified in Section 2.5. Assuming a negligible contact resistance, the resistance of the film R is related to the material resistivity ρ by the following relation:

$$R = \rho \frac{L}{S} \quad (2.7)$$

where L is the channel length ($150 \mu\text{m}$) and S the surface of the channel cross section:

$$S = w \times d \times 15. \quad (2.8)$$

w corresponds to the channel width (5 mm) and the thickness d is given by the layer thickness when it is lower than the electrode thickness (110 nm) and by the electrode when it is higher. The conductivity is inversely proportional to the material resistivity. As a result, the conductivity σ can be extracted from the resistance R using the following

2.2. Impact of doping concentration on hole conductivity and hopping transport activation energy

relation:

$$\sigma = \frac{L}{15Rwd}. \quad (2.9)$$

The $I(V)$ measurements for the pure PBDTTT-c and the 5% MR samples are given in Figure 2.5. The extraction of the layer resistance R must be done where the current is linearly dependent on the bias corresponding to the ohmic regime. The $I(V)$ characteristics of the pure sample is linear from -10 V to +10 V. When doping at 5% MR, the sample exhibits an ohmic regime in a broader range, from -25 V to +25 V. These concentration dependent behaviors are taken into account for the resistance extraction. We can also notice that for the pure PBDTTT-c sample, $I(V)$ measurements are only available for temperatures above 330 K. Below this temperature, the signal is too low to be analyzed due to the limited amount of carriers thermally activated toward the transport levels.

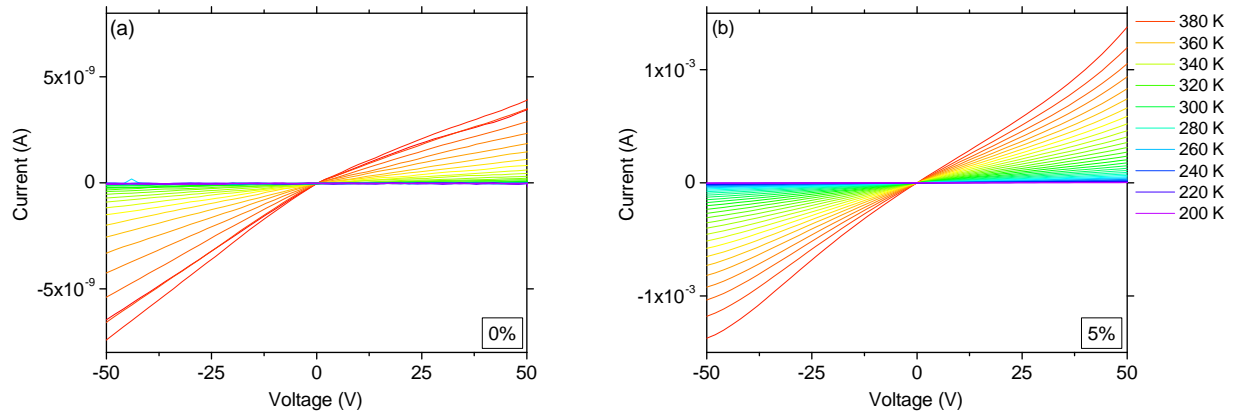


Figure 2.5: $I(V)$ measurements for temperatures varying from 390 to 200 K for pure PBDTTT-c (a) and doped PBDTTT-c at 5% MR (b).

Figure 2.6 exhibits the current density with respect to the electric field in a logarithmic scale at 300 K. Only 4 doping concentrations are shown for clarity, although the complete evolution follows the trend suggested by the arrows. The current density is calculated taking into account the surface of the channel cross section S and the electric field is determined from the channel length L . This graph highlights the current evolution by almost 3 orders of magnitude for doping concentrations varying from 0.5% MR to 2.5% MR. The current density decreases then by one order of magnitude between 2.5% MR and 8% MR.

By extracting R for a given temperature, we can determine the conductivity σ using relation 2.9. To calculate the uncertainty associated with the conductivity we take into account the error of the extracted resistance ΔR from the fit and the uncertainty of the layer thickness estimated around 10 nm from the AFM measurements. The conductivity uncertainty $\Delta\sigma$ is therefore given by the following equation:

$$\Delta\sigma = \sigma \left[\frac{\Delta R}{R} + \frac{\Delta d}{d} \right]. \quad (2.10)$$

The evolution of PBDTTT-c conductivity at 300 K with $\text{Mo}(\text{tfd-COCF}_3)_3$ doping is

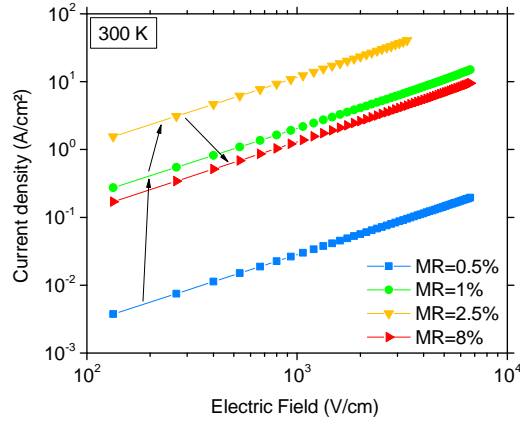


Figure 2.6: Current density with respect to the electric field in a logarithmic scale for 4 doping concentrations at 300 K.

given in Figure 2.7 (a) with error bars corresponding to the calculated uncertainties. Two regimes can be observed in this graph. From 0.5% to 2.5% MR the conductivity follows a superlinear increase with the doping concentration reaching a conductivity around $8 \times 10^{-4} \text{ S/cm}$ at 2.5% MR. This superlinear increase has been attributed to trap filling and has been observed in several polymer-dopant mixtures [24, 125, 126]. However, the fitting of the superlinear regime can be discussed as the conductivity for 1% MR is slightly above the expected value. This discrepancy might be due to the thickness inhomogeneity of the layers. For doping concentrations above 2.5% MR, a slight decrease is observed with a power law of -0.5. A decline in conductivity at high doping concentration has been reported in the literature and is probably due to the creation of new traps in the polymer [128, 171, 172]. The possible origin for this decline will be further developed in Section 2.4.

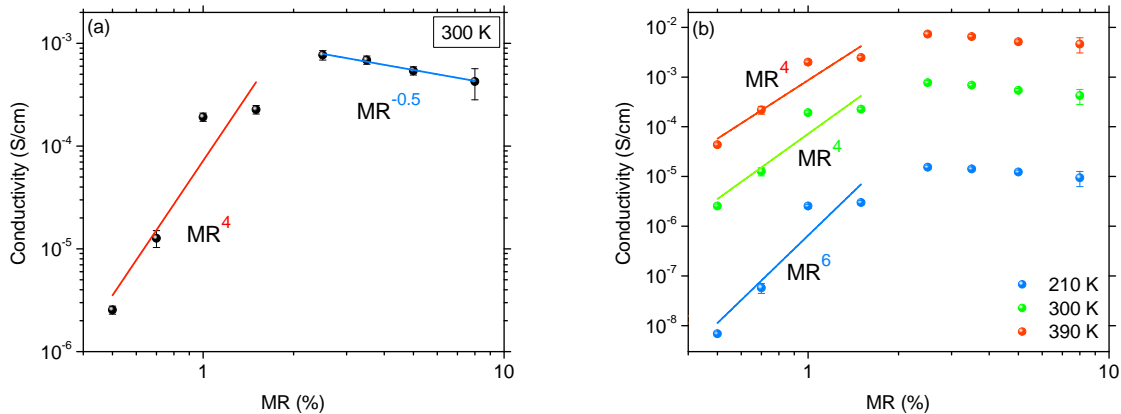


Figure 2.7: Conductivity of PBDTTT-c with respect to $\text{Mo}(\text{tfd-COCF}_3)_3$ molar ratio in a logarithmic scale at 300 K (a) and at 3 different temperatures (b).

2.2. Impact of doping concentration on hole conductivity and hopping transport activation energy

The hole conductivity σ_p is related to the hole density p and hole mobility μ_p by the following relation:

$$\sigma_p = p\mu_p q \quad (2.11)$$

with q the elementary charge. Considering a constant mobility, the conductivity should increase linearly with the hole density driven by the doping concentration. A superlinear increase of the conductivity is therefore related to an increase of the hole mobility with doping. A mobility enhancement is associated with the filling of trap states above the HOMO level enhancing the hole transport properties [173]. When all traps are filled, the conductivity can follow a linear dependency with the doping concentration as the mobility reaches a saturation regime [126]. However, this linear regime is not observed in the case of Mo(tfd-COCF₃)₃ doped PBDTTT-c. Olthof *et al.* [126] explain that the impact of traps is temperature dependent leading to a varying power law with respect to temperature. It is therefore possible that the trap filling regime overcomes the linear regime at 300 K. If we compare the conductivity evolution at 210 K, 300 K and 390 K, we can notice that the power law is effectively reduced at higher temperature as shown in Figure 2.7 (b). However, even at 390 K, no linear regime is reached.

The conductivity of pure PBDTTT-c has not been extracted at 300 K due to a low signal. However, at 330 K, a conductivity of $2 \times 10^{-9} S/cm$ is obtained for pure PBDTTT-c. As a result, Mo(tfd-COCF₃)₃ enables a hole conductivity increase close to 6 orders of magnitude for PBDTTT-c highlighting its p-doping ability. By comparison, F₄TCNQ leads to an increase of hole conductivity by 4 orders of magnitude at a molar ratio of 17% for P3HT [171] and slightly more than 3 orders of magnitude at a molar ratio of 30% for 4T [29].

Hole conductivity measurements of Mo(tfd-COCF₃)₃ doped PBDTTT-c at different doping concentration highlights the p-doping ability of Mo(tfd-COCF₃)₃. The conductivity evolution with the doping concentrations exhibits two regimes: a superlinear increase at low concentration and a slight decline above 2.5% MR. The superlinear increase is associated with trap filling and the decrease might be induced by additional traps due to the addition of dopant. Around 2.5% MR, the hole conductivity reaches a maximum value reaching $8 \times 10^{-4} S/cm$, almost 6 orders of magnitude above the hole conductivity of the pristine material. To our knowledge, this doping efficiency at 2.5% MR is among the best results reported in the literature.

2.2.3 Impact of p-doping on hole hopping transport activation energy

As mentioned in Chapter 1, the transport mechanism identified in organic semiconductors is thermally activated and known as hopping transport between localized states [174]. Carriers are strongly influenced by trap states situated above the HOMO level or below the LUMO level altering the transport rate. Considering a Gaussian distribution of Density of States (DOS), we can identify an energy level E_T within this distribution where the most efficient transport of carriers takes place (see Section 1.1.2) [53]. For carriers trapped below

the transport level, energy is required to activate these charges toward E_T . Therefore, temperature measurements give insight into the energy required for trapped carriers to reach the transport level.

The hole conductivity is described by an Arrhenius law with E_A the activation energy of hopping transport [175, 76]:

$$\sigma_p = \sigma_0 \exp\left(-\frac{E_A}{k_B T}\right) \quad (2.12)$$

with σ_0 a pre-factor, k_B the Boltzmann constant and T the temperature. Therefore, hole conductivity measurements at variable temperatures leads to the determination of the hopping transport activation energy E_A for holes.

Figure 2.8 (a) shows the conductivity with respect to $1000/T$ in a semi-logarithmic scale for pure PBDTTT-c and the 8 doping concentrations studied. This representation enables a direct control of the Arrhenius law through a linear fitting with the extraction of the activation energy E_A from the slope and the pre-factor σ_0 from the intercept. The corresponding activation energy evolution with doping concentration is given in Figure 2.8 (b).

We can observe in Figure 2.8 (a) a decrease of the slope with increasing doping concentration. This evolution is directly linked with the activation energy decrease shown in Figure 2.8 (b). For pure PBDTTT-c, an activation energy of 570 meV is extracted. This energy strongly decreases with doping up to 2.5% MR reaching 240 meV. Above this threshold, the decrease of the activation energy is much lower and reaches 230 meV at 8% MR.

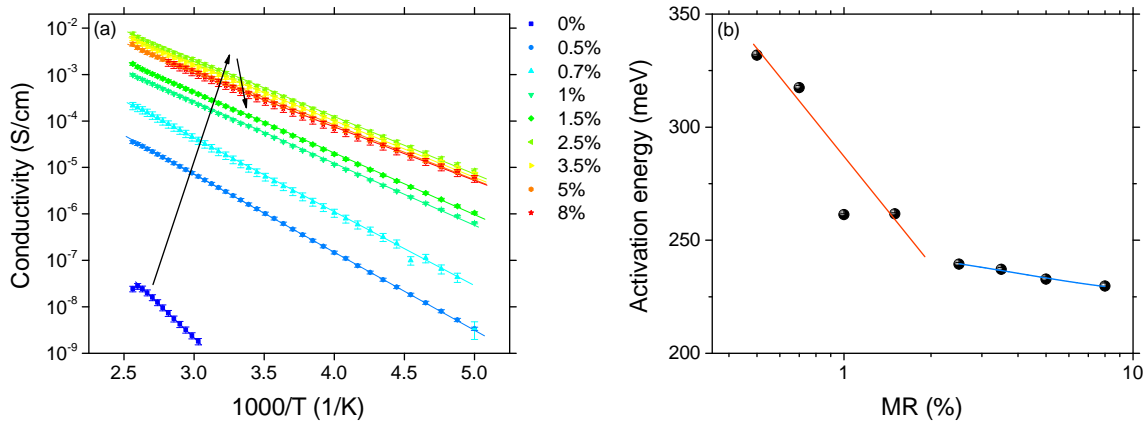


Figure 2.8: Arrhenius plot of conductivity for pure and $\text{Mo}(\text{tfd-COCF}_3)_3$ doped PBDTTT-c with respect to the inverse of temperature in a semi-logarithmic scale (a) and corresponding hole hopping transport activation energy with respect to the doping molar ratio (b).

A reduction of the activation energy is due to a lower impact of traps on the transport of carriers and the shift of the Fermi level toward the transport level [126]. As a result, the strong decrease of the activation energy observed up to 2.5% MR for $\text{Mo}(\text{tfd-COCF}_3)_3$

2.2. Impact of doping concentration on hole conductivity and hopping transport activation energy

doped PBDTTT-c and for several other polymer-dopant blends in the literature is associated with the gradual filling of trap states above the HOMO level with holes [76, 176, 177]. This is consistent with the superlinear increase of hole conductivity observed up to 2.5% MR. The hopping transport mechanism for holes is enhanced as the Fermi level shifts toward the transport level increasing the occupation probability of the Gaussian DOS and filling progressively the trap states with holes.

The saturation of the activation energy at high doping concentration has been attributed to the creation of new trap states by Olthof *et al.* [126]. This hypothesis explaining the slower evolution observed above 2.5% MR would be consistent with the conductivity decline observed above this threshold.

2.2.4 Trap filling and saturation regimes

I(V) measurements at variable temperatures has enabled the study of both hole conductivity and hopping transport activation energy evolution with doping concentration. This experiment demonstrated the p-doping ability of the Molybdenum complex Mo(tfd-COCF₃)₃ on PBDTTT-c but also highlighted the presence of two distinct regimes for doping concentrations below and above 2.5% MR.

The superlinear increase of the conductivity and the strong decrease of the hopping transport activation energy are attributed to trap filling. This regime is illustrated in Figure 2.9 (a) and (b). When a p-dopant is added to a semiconductor, electrons from the polymer HOMO are transferred toward the dopant. If the semiconductor exhibits trap states above its HOMO level, the first electrons to be transferred to the dopant come from these energy levels. As electrons are removed from donor traps, we talk about trap filling mechanism. As a result, holes from the transport level will not be attracted by the donor traps, which are positively charged when filled with a hole. This process enhances the hole mobility leading to a superlinear increase of the conductivity.

The activation energy decrease is driven by the shift of the Fermi level toward the HOMO level upon addition of new carriers, filling trap states with holes and enhancing hopping transport. A saturation of the activation energy above 2.5% MR can therefore be attributed to the creation of new defects altering the transport mechanism or to a saturation of the Fermi level shift. This regime is illustrated in Figure 2.9 (c).

The conductivity saturation or low decline above 2.5% MR could be consistent with the creation of new trap states with the addition of dopants. These new energy levels are often attributed to strong Coulomb interaction with the ionized dopant [173] or changes in the polymer morphology [129, 178]. This hypothesis will be considered in Section 2.4. It has also been observed that the Fermi level shift in organic semiconductor doping is limited and saturates several hundreds of meV above the HOMO [91, 84]. In the case of Mo(tfd-COCF₃)₃ doped PBDTTT-c, the Fermi level lies 400 meV above the polymer HOMO for a doping concentration as high as 10% MR [25].

There are still unknowns regarding the behavior of organic semiconductor doping at high doping concentration. Understanding the mechanisms leading to the saturation or

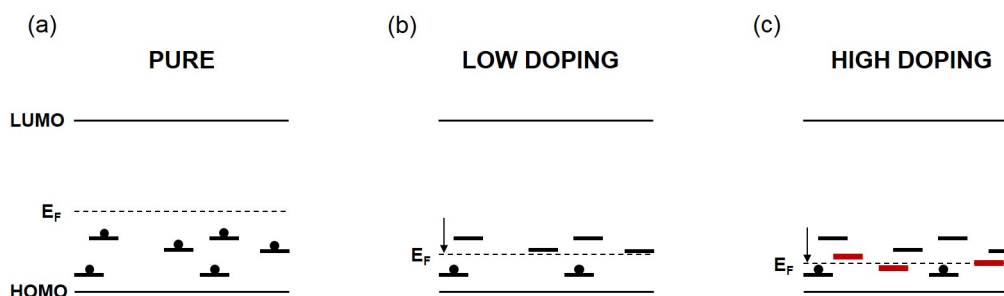


Figure 2.9: Schematic of a polymer band diagram with donor traps above the HOMO (a). Upon doping the Fermi level shifts toward the HOMO and traps are progressively filled with holes (b). At high doping concentrations, new defect states are created (donor or acceptor) and the Fermi level saturates several hundreds of meV above the HOMO.

decline of the conductivity and hopping transport activation energy would help finding some solutions and overcome this efficiency barrier. Also, it is still unclear why concentrations of several % MR are required to reach significant doping impact while concentrations as low as 10^{-5} MR are required in inorganic semiconductor doping [74].

2.3 Evolution of hole concentration with p-doping

The major impact of semiconductor p-doping is the increase of hole concentration in the valence band (or HOMO for organic semiconductors). This density increase results in the shift of the Fermi level toward the valence band. Therefore, p-doping leads to the conductivity increase as well as the effective lowering of injection barriers through energy level alignment. This effect will be studied in Section 2.5 of this chapter.

Looking at the evolution of the hole concentration in the polymer with the molar ratio of dopant added can give information about the effective impact of doping and its efficiency. Hole and electron densities in p and n-doped semiconductor respectively are generally extracted from capacitance measurements either on MIS (Metal Oxide Semiconductor) capacitors [99] or Schottky diodes [179]. In this study we will use the Mott-Schottky extraction technique on Schottky diodes, which will be used for further experiments in Chapter 3.

2.3.1 Mott-Schottky law and Schottky diodes processing

The theory of Mott and Schottky has been demonstrated in inorganic semiconductors doped with variable doping concentrations [180]. It relies on the formation of a charge depletion zone upon doping to follow Poisson's equation. Capacitance measurements of appropriate diodes are carried out with variable applied bias to extract the density of ionized dopants using the Mott-Schottky relation.

Capacitance measurements require the application of a small oscillating AC signal

2.3. Evolution of hole concentration with p-doping

with a typical amplitude around 10-100 mV added to a constant DC bias. Upon doping, charges in the semiconductor layer can oscillate to follow the AC component of the applied signal. Therefore, the charges induced by doping participate to the overall capacitance. By applying a reverse bias, a charge depletion zone is formed and the charges are progressively extracted from the semiconductor layer. For a homogeneous doping in the semiconductor layer, the evolution of capacitance C with the applied DC bias V follows the Mott-Schottky law (for p-type doping here) [181]:

$$\frac{1}{C^2} = \frac{2}{q\epsilon_0\epsilon_r p A^2} (V_{bi} - V). \quad (2.13)$$

In this equation, q is the elementary charge, ϵ_0 the vacuum permittivity, ϵ_r the relative permittivity, p the free holes density, A the diode area and V_{bi} the diode built-in voltage. Therefore we can extract the hole density p from $C(V)$ measurements on a Schottky diode.

To carry out the $C(V)$ measurements and extract the hole density in PBDTTT-c (p-type semiconductor) with and without doping, we need to fabricate hole-only devices with one ohmic contact for holes on one side and one Schottky contact on the other side to create a depletion zone in reverse bias regime. We will show in Section 2.5 of this chapter that p-doping PBDTTT-c decreases the injection barrier for holes leading to a good ohmic contact for an electrode work-function of 4.5 eV. Therefore, we decided to surround the doped layers by two pure layers avoiding any interface effects and ensure effective Schottky contact on the aluminum side. PEDOT:PSS is used as bottom electrode and aluminum as top electrode. The complete structure and the band diagram of the device studied are presented in Figure 2.10 and in Appendix A as Structure 2. Devices with pure PBDTTT-c and p-doped PBDTTT-c with 0.5%, 1%, 2% and 5% MR are fabricated.

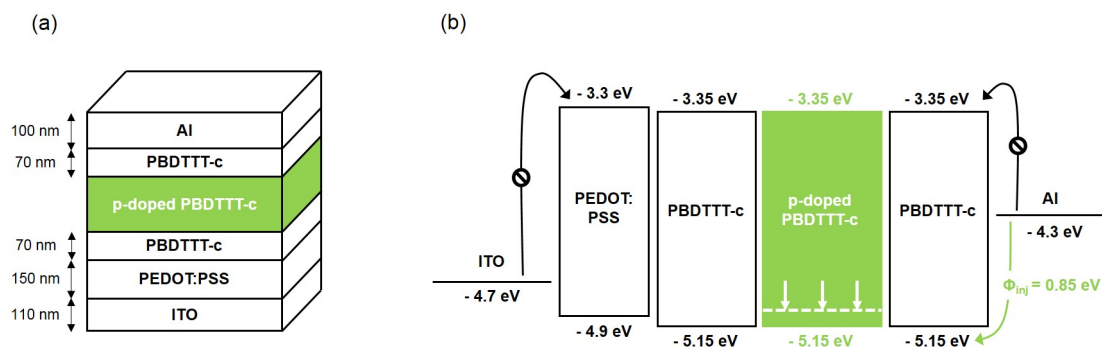


Figure 2.10: Structure (a) and band diagram (b) of the Schottky diode processed for Mott-Schottky analysis (Structure 2).

The diodes are processed on ITO/coated glass substrates. The 110 nm thick ITO is patterned by photolithography and the substrates are cleaned in ultrasonic baths of acetone and isopropanol for 15 minutes each. PEDOT:PSS is spin-coated on UV-ozone treated ITO and annealed at 115°C under nitrogen for 10 minutes to reach a thickness of 150 nm. A thin layer (70 ± 10 nm) of PBDTTT-c is then spin-coated on PEDOT:PSS and annealed at 115°C under nitrogen for 10 minutes as well. The layer of interest, pure or doped, is deposited on a cleaned silicon substrate, annealed at 115°C under nitrogen

for 10 minutes and laminated following the SCTL process described in Section 2.1. The thicknesses of pure and doped layers are summarized in Table 2.1. Another 70 nm thick layer of pure PBDTTT-c is laminated on top of the structure. After the two lamination steps required in this process, a 100 nm thick aluminum top electrode is evaporated through a shadow mask in a vacuum chamber. To limit the impact of oxygen on the hole density extraction, the diodes are encapsulated in glovebox with glass using an epoxy glue.

The references and suppliers information of all the materials used for processing are summarized in Appendix C.

Table 2.1: Thicknesses of pure and doped layers of PBDTTT-c processed in the Schottky diodes for hole density extraction and measured with a contact profilometer.

MR (%)	Thickness (nm)
0	165 ± 10
0.5	100 ± 10
1	110 ± 10
2	165 ± 10
5	165 ± 10

C(V) measurements are carried out in the dark using a probe-station and an LCR meter Agilent E4980A. The capacitance is measured for a DC bias varying from -5 V to +2 V with an AC signal of 100 mV in amplitude and a frequency of 100 Hz. A relatively low frequency is chosen to enable the charges generated by doping to follow the oscillating signal and participate to the measured capacitance.

2.3.2 Ionized dopant concentration

The C(V) measurement at 100 Hz and ambient temperature for the pure polymer is given in Figure 2.11 (a). In reverse bias, the diode is progressively depleted leading to the decrease of the capacitance. When the diode is completely depleted, the capacitance reaches the geometric capacitance C_{geo} :

$$C_{geo} = \frac{\epsilon_0 \epsilon_r A}{d}. \quad (2.14)$$

Knowing the diode area A and layer thickness d , this relation can be used to extract the polymer relative permittivity ϵ_r , which is necessary to determine the hole density. The sample with pure PBDTTT-c exhibits a geometric capacitance of $(3.90 \pm 0.02) \times 10^{-10} F$ reached around -3 V. The accuracy of the permittivity is limited by the uncertainty of the effective surface area A . For photodetectors, we usually measure the active area by scanning the photocurrent on the diode. Since no blend heterojunction is used in our device, this technique cannot be used. However, for similar processes we obtain effective areas between 4.7 and 5.1 mm^2 . Taking into account a layer thickness of 305 nm, which is measured by contact profilometer, we obtain a permittivity of 2.8 ± 0.1 , consistent with values around 3 usually obtained for organic semiconductors [59].

2.3. Evolution of hole concentration with p-doping

The Mott-Schottky plot for the pure polymer corresponding to the plot of $1/C^2$ with respect to the applied bias is shown in Figure 2.11 (b). According to equation 2.13, it is possible to extract the hole density p by taking the slope of this plot in the linear regime into account:

$$p = -\frac{2}{q\epsilon_0\epsilon_r A^2 \frac{d(\frac{1}{C^2})}{dV}}. \quad (2.15)$$

This equation is only valid when the diode is not fully depleted. In the case of pure PBDTTT-c, the Mott-Schottky extraction can be carried out around 0 V. Below -1 V, the Mott-Schottky plot saturates as the depletion width reaches the active layer thickness. From this fit we obtain a hole concentration p of $(5.4 \pm 0.7) \times 10^{15} \text{ cm}^{-3}$ for pure PBDTTT-c. Usually, p-doping in organic semiconductors is attributed to unintentional oxygen doping or defects [182, 183]. However, Kirchartz *et al.* [184] have highlighted the limits of the Mott-Schottky extraction technique at low doping densities. They determined that, for a diode with a schottky contact and a layer thickness around 300 nm, the Mott-Schottky extraction technique is not appropriate for hole concentrations below $4 \times 10^{15} \text{ cm}^{-3}$ because the depletion approximation is not valid. With a hole density around $5 \times 10^{15} \text{ cm}^{-3}$, it is difficult to consider the value extracted using the Mott-Schottky relation as reliable.

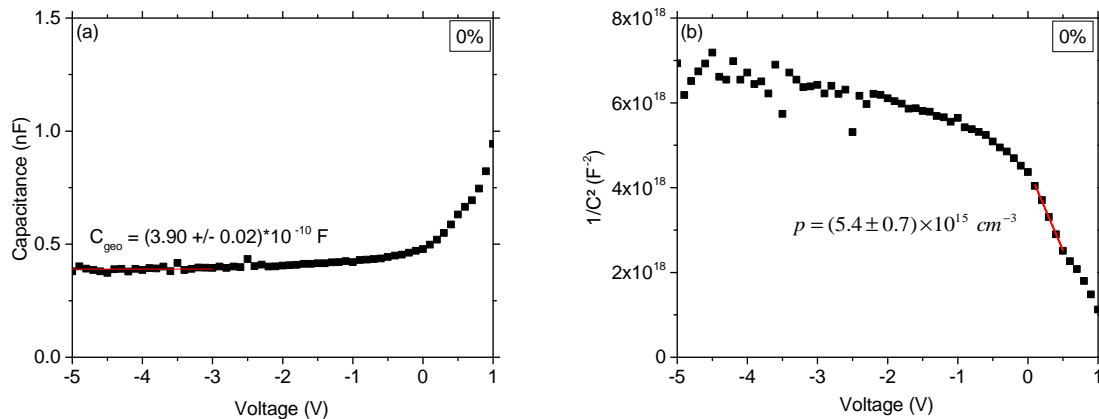


Figure 2.11: $C(V)$ characteristic (a) and Mott-Schottky plot (b) for pure PBDTTT-c. The geometric capacitance and hole densities are indicated.

The $C(V)$ characteristics for 0.5%, 1%, 2% and 5% MR are shown in Figure 2.12 (a), (c), (e) and (g) respectively. To extract the hole density we use the Mott-Schottky representation given in Figure 2.12 (b), (d), (f) and (h). For a homogeneous doping, the hole density p can be extracted from the linear dependency of $1/C^2$ in reverse bias. Homogeneity is respected for the sample with the pure polymer. For the doped samples, no linear behavior can be obtained over the full bias range as the doping is not homogeneous in the device. At low reverse bias, the pure PBDTTT-c layer at the aluminum electrode layer is depleted. The hole density extracted in this regime corresponds to the pure layer. At higher reverse bias, the pure layer is totally depleted and the depletion reaches the doped central layer of polymer. Therefore, it is important to determine at what biases the Mott-Schottky analysis needs to be carried out.

Chapter 2. Electrical characterization of molecular p-doping

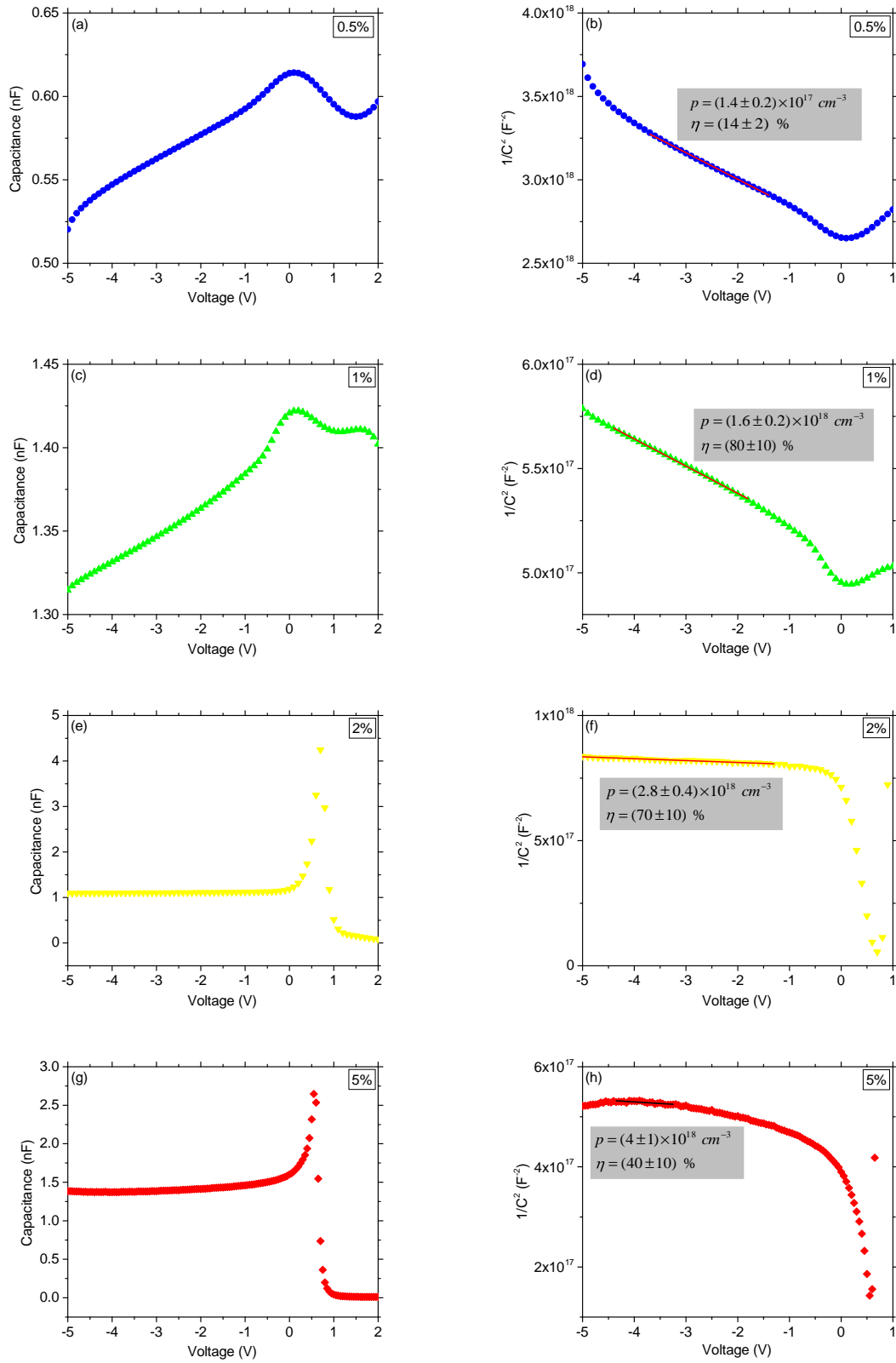


Figure 2.12: C(V) characteristic (a), (c), (e), (g) and Mott-Schottky plot (b), (d), (f), (h) for doped PBDTTT-c at 0.5%, 1%, 2% and 5% MR.

2.3. Evolution of hole concentration with p-doping

According to Khelifi *et al.* [182], the hole density profile in the semiconductor layer can be obtained from the Mott-Schottky law generalized for inhomogeneous doping:

$$\frac{d(1/C_j^2)}{dV} = -\frac{2}{qA^2\epsilon_0\epsilon_r p(w)} \quad (2.16)$$

where q is the elementary charge and w the depth in the semiconductor layer given by the capacitance at a given voltage C_j :

$$C_j = \frac{A\epsilon_0\epsilon_r}{w}. \quad (2.17)$$

As an example, the profile of the hole density is given for the 1% MR sample at 300 K in Figure 2.13. A plateau is reached above 87.5 nm (from the aluminum electrode). Below 87.5 nm, the hole density of the pure polymer should be measured as only the pure layer is depleted. This threshold corresponds to an applied bias of -1 V. When the applied bias is lower than -1 V, the depletion reaches the doped layer leading to the desired value of p . This graph illustrates the origin of the two slopes observed in the Mott-Schottky plots for the samples with a doped layer.

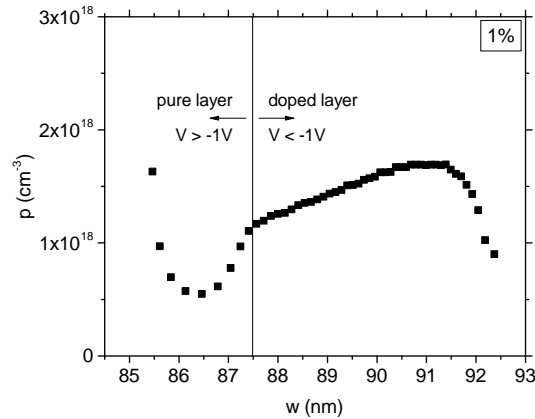


Figure 2.13: Hole density profile in the semiconductor layer for the 1% MR sample measured at ambient temperature.

Therefore, only the second slope is taken into account for the Mott-Schottky analysis for each doping concentration as shown in Figure 2.12 (b), (d), (f) and (h). The hole densities extracted vary from $(1.4 \pm 0.2) \times 10^{17} \text{ cm}^{-3}$ for MR=0.5% to $(4 \pm 1) \times 10^{18} \text{ cm}^{-3}$ for MR=5%. The determination of the linear region for the highest doping concentration (5% MR) is not straightforward. As a result, caution needs to be taken about the extracted value of p at 5% MR.

In order to evaluate and quantify the efficiency of the polymer p-doping by $\text{Mo}(\text{tfd-COCF}_3)_3$, the ratio between the density of free holes p and the total density of molecular dopants N_A called doping efficiency η is considered:

$$\eta = \frac{p}{N_A}. \quad (2.18)$$

The total density of molecular dopants N_A is obtained by multiplying the polymer total site density N_V by the molar ratio MR :

$$N_A = N_V \times MR. \quad (2.19)$$

To determine the total site density in PBDTTT-c we have measured its mass density. By determining the volume of a fluid (e.g. water) displacement upon addition of a certain quantity of polymer, we can determine its volume. Combined with the measurement of its mass, we obtain a PBDTTT-c mass density $\rho_{\text{PBDTTT-c}}$ of 0.242 g/cm^3 . Considering the monomer molecular weight $M_{\text{PBDTTT-c}}$ of 710.4 g/mol and that one monomer leads to one available site as it is usually considered in organic materials [124], we calculate the total site density using the following relation:

$$N_V = \frac{\rho_{\text{PBDTTT-c}}}{M_{\text{PBDTTT-c}}} \times N_{\text{AV}} \quad (2.20)$$

with N_{AV} the Avogadro number. We obtain a total site density of $2.05 \times 10^{20} \text{ cm}^{-3}$ for PBDTTT-c. This value is consistent with the total site density usually measured for organic semiconductors around $10^{20} - 10^{21} \text{ cm}^{-3}$ [124, 185]. The hole density and the corresponding doping efficiency for each doping concentration measured are summarized in Table 2.2.

Table 2.2: Hole density extracted using the Mott-Schottky relation and corresponding doping efficiency for each sample.

MR (%)	$p \text{ (cm}^{-3}\text{)}$	$\eta \text{ (%)}$
0	$(5.4 \pm 0.7) \times 10^{15}$	
0.5	$(1.4 \pm 0.2) \times 10^{17}$	14 ± 2
1	$(1.6 \pm 0.2) \times 10^{18}$	80 ± 10
2	$(2.8 \pm 0.4) \times 10^{18}$	70 ± 10
5	$(4 \pm 1) \times 10^{18}$	40 ± 10

The evolution of the hole density and the doping efficiency with the doping concentration are shown in Figure 2.14. The hole density exhibits a superlinear increase below 1% MR and a sublinear increase above 1% MR. The superlinear increase at low doping concentration is probably related to the trap filling phenomenon identified through conductivity measurements. This regime is accompanied with a low doping efficiency ($14 \pm 2 \%$ at 0.5% MR) as most of the molecular dopants added to the polymer contribute to trap filling. The doping efficiency reaches a maximum value of $80 \pm 10 \%$ at 1% MR for the samples measured. A doping efficiency around 80% is around the best doping efficiencies reported in the literature for organic semiconductor doping [59, 78]. This result illustrates the p-doping ability of $\text{Mo}(\text{tfd-COCF}_3)_3$ on PBDTTT-c.

The doping efficiency decreases slightly between 1% and 2% MR and drops above 2% MR to reach $40 \pm 10 \%$ at 5% MR, although the hole density is not determined with good accuracy at 5% MR. A decrease of the doping efficiency above 1% MR is consistent with a sublinear increase of the hole density and can be explained either by the formation of dopant aggregates limiting the interaction with the polymer host or a saturation of the Fermi level below the acceptor state [181, 91]. When the Fermi level crosses the acceptor

2.3. Evolution of hole concentration with p-doping

state responsible for p-doping, the probability of dopant ionization is reduced. This regime is called impurity reserve regime in inorganic semiconductors. In this case, the increase of empty acceptor states upon doping can be related to the increase of trap states. Both dopant aggregates and formation of trap states with doping have been suggested to explain the conductivity decrease above 2.5% MR. A decrease of the doping efficiency at higher doping concentration has already been reported in the literature for various polymer-dopant mixtures [181, 186]. Tietze *et al.* [85] have highlighted the relation between the doping efficiency decrease and the position of the acceptor state in the bandgap. This hypothesis will be further developed in Chapter 3.

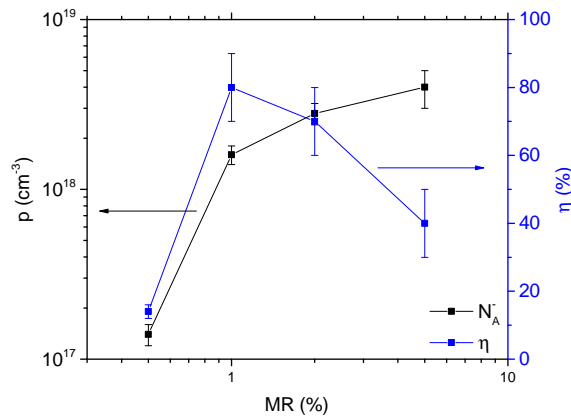


Figure 2.14: Hole density and doping efficiency with respect to the molar ratio.

The determination of the hole density with doping reaching values around $3 \times 10^{18} \text{ cm}^{-3}$ confirmed the p-doping ability of $\text{Mo}(\text{tfd-COCF}_3)_3$ on PBDTTT-c. By comparing the density of free holes with the total dopant density added to the polymer host, we extracted the doping efficiency of this polymer-dopant mixture. The efficiency of 80% measured at 1% MR is among the best doping efficiencies reported in the literature for organic semiconductor doping. However, above 1% MR the doping efficiency decreases significantly highlighting the limits of the doping process. This decrease might be explained by the formation of dopant aggregates or the entry in the impurity reserve regime with the saturation of the Fermi level below the acceptor state. Further work will be carried out to understand the origin of this limited efficiency at high doping concentration.

2.3.3 p-doping activation energy

In inorganic semiconductors, doping with impurities leads to the formation of energy levels within the bandgap. For n-doping donor states are introduced a few tens of meV below the conduction band. Similarly, acceptor states are formed a few tens of meV above

the valence band for p-doping. The energy required to dope the semiconductor is called ionization energy or thermal dopant activation energy. A schematic of the semiconductor bandgap with neutral and charged donor and acceptor states is shown in Figure 2.15.

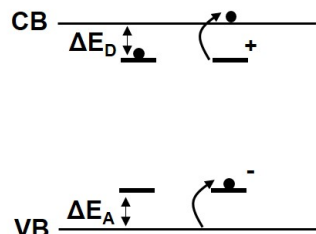


Figure 2.15: Schematic of the donor and acceptor states in their neutral and charged form.

The thermal dopant activation energy for holes ΔE_A can be determined from hole density p extraction at different temperatures. An Arrhenius relation links the hole density with the thermal dopant activation energy [181]:

$$p \propto \exp\left(-\frac{\Delta E_A}{qk_B T}\right). \quad (2.21)$$

Therefore, ΔE_A can be obtained from an Arrhenius plot of $\ln(p)$ with respect to $q/k_B T$.

This extraction technique is limited to a small temperature range for Mo(tfd-COCF₃)₃ doped PBDTTT-c. Below 0°C, capacitance measurements with respect to the applied bias indeed exhibit a very low signal. Moreover, we have chosen to limit temperature measurements of these devices at 40°C to avoid potential dopant diffusion issues in the pure layers. As a result, the evolution of the hole density with temperature is carried out from 5°C to 40°C on the Schottky device shown in Figure 2.10.

The Mott-Schottky plots at different temperatures for 1% MR is shown in figure 2.16 (a). We can observe a slight decrease of the slope in the reverse bias regime with temperature. The corresponding Arrhenius plot is shown in Figure 2.16 (b). A linear fit of these data leads to a thermal dopant activation energy of 33 ± 2 meV. However, the thermal dopant activation energy extraction is limited by the significant uncertainty obtained for the hole density and the short temperature range studied.

The thermal dopant activation energy obtained for Mo(tfd-COCF₃)₃ doped PBDTTT-c is consistent with the values reported in the literature. Pahner *et al.* [181] have measured activation energies of 54 meV and 19 meV for PEN:C₆₀F₃₆ and PEN:F₆TCNNQ respectively. A value of 32 meV has been obtained for F₆TCNNQ doped MeO-TPD by Tietze *et al.* [85].

However, the interpretation of ΔE_A in doped organic semiconductor is not straightforward. In impurity doped inorganic semiconductors, ΔE_A is defined as the energy difference between the valence band and the acceptor state associated with the impurity as illustrated in Figure 2.15. This description is valid for a sharp valence band and a well-defined single acceptor state [85]. Organic semiconductors exhibit broad Gaussian density of states and potential exponential tail states while doping acceptor levels are also

2.4. Possible origin of limited doping efficiency at high concentration

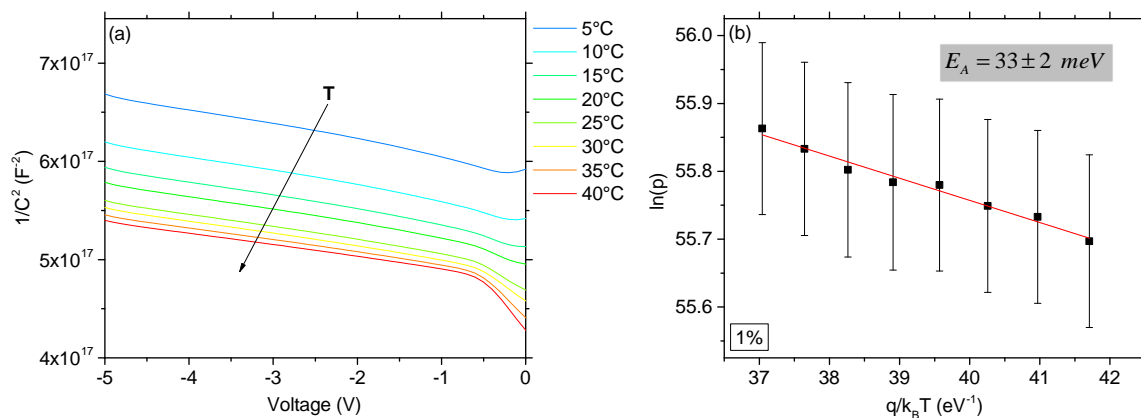


Figure 2.16: Mott-Schottky representation of capacitance measurements from 5°C to 40°C for 1% MR (a) and corresponding Arrhenius plot of the doping activation with temperature (b).

distributed in the bandgap. Therefore, it is unclear whether we can directly link ΔE_A with the position of the acceptor state above the HOMO. The question of doping acceptor states will be developed in Chapter 3.

2.4 Possible origin of limited doping efficiency at high concentration

In Sections 2.2 and 2.3 we have highlighted the p-doping ability of $\text{Mo}(\text{tfd-COCF}_3)_3$ in PBDTTT-c through conductivity and hole density extraction with respect to the doping concentration. However, both parameters highlight the limited doping ability at high doping concentration. A slight reduction of the conductivity above 2.5% MR has been observed accompanied with a saturation of the hole hopping transport activation energy. Such behavior are usually attributed to the creation of trap states upon doping or the formation of dopant aggregates limiting the interaction with the polymer host [129, 128]. The decrease of the doping efficiency observed above 1% MR would be consistent with both hypotheses.

In this section we will study potential morphology changes with the formation of aggregates in the polymer-dopant mixture. Scanning Electron Microscopy (SEM) and Transmission Electron Microscopy (TEM) techniques will be used to follow the evolution of $\text{Mo}(\text{tfd-COCF}_3)_3$ doped PBDTTT-c layers with doping concentration. Chemical analyses will also be carried out to deepen our understanding of the morphology evolution.

2.4.1 Formation of aggregates with increasing doping concentration

Regarding the previous results, we would like to determine whether aggregates of dopant or polymer-dopant mixture are formed in the layer with doping. SEM is relevant to carry

out this study as the Molybdenum atomic number ($Z_{Mo} = 42$) is much higher than the atomic number of the organic elements in the polymer ($Z_C = 6$, $Z_O = 8$, $Z_S = 16$ and $Z_H = 1$). Although SEM is a surface analysis technique, if aggregates containing the Molybdenum complex are formed in the polymer matrix, we should be able to observe differences in the SEM images.

The samples of pure PBDTTT-c and $\text{Mo}(\text{tfd-COCF}_3)_3$ doped PBDTTT-c with 7 different doping concentrations from 0.5% MR to 6% MR are prepared on Borosilicate glass substrates. The layers are processed by spin-coating and annealed at 115°C for 10 min under nitrogen. A few monolayers of platinum are deposited on the pure or doped layer to evacuate the charges generated during the SEM measurements and avoid charge build-up in the substrate.

Measurements are carried out with a SEM Leo 1530 from Zeiss at an accelerating voltage of 3 kV. Secondary electrons are used for this analysis and the working distance varies from 2.7 to 3.5 mm. Figures 2.17 (a) to (h) exhibit the SEM images of the samples from 0% MR to 6% MR.

From 0% MR to 1% MR, the layer is uniform and no particular modification can be observed on the SEM images. At a doping concentration of 2% MR, some nanoparticles can be identified on the layer in lighter grey. The increase of brightness can be due to an increase of the atomic number Z of the components. An increase of Z would be consistent with the formation of aggregates containing the Molybdenum complex. Above 2% MR, the density of aggregates increases.

Images with a higher magnification are recorded to have a more precise view of the aggregates and their evolution with doping concentration. Figure 2.18 (a) to (c) shows the SEM images for the doping concentrations 2%, 3% and 4% MR. The size of the aggregates are estimated with two cursors. All aggregates exhibit a diameter around 20 nm and their size is not influenced by the doping concentration between 2% and 4% MR, only the density of particles on the surface increases with doping.

The formation of aggregates or phase segregation have been reported in the literature for several doped organic semiconductors. Deschler *et al.* [129] have reported the formation of dopant rich domains in F_4TCNQ doped P3HT and PCPDTBT. They correlated the phase separation with the conductivity saturation observed for both polymer-dopant blends. The aggregation of doped polymer domains has been identified in F_4TCNQ doped PBTTT-C₁₄ by Cochran *et al.* [187].

In order to analyze the composition of the aggregates we have carried out TEM measurements. A FEI Tecnai Osiris TEM microscope is used and operated at an accelerating voltage of 200 kV. A solution of $\text{Mo}(\text{tfd-COCF}_3)_3$ doped PBDTTT-c at 5% MR is prepared in ortho-xylene and 2 μL of the solution is deposited on a metal grid. Aggregates with varying shape and sizes are observed in TEM images as shown in Figure 2.19 (a) to (d). Small aggregates with a diameter around 20-30 nm are recorded surrounded by larger aggregates reaching 100-500 nm. We believe that the bigger aggregates are due to the formation of clusters with the smaller aggregates observed in SEM images. Admittedly, differences can occur in the size of the aggregates between SEM and TEM analyses as one

2.4. Possible origin of limited doping efficiency at high concentration

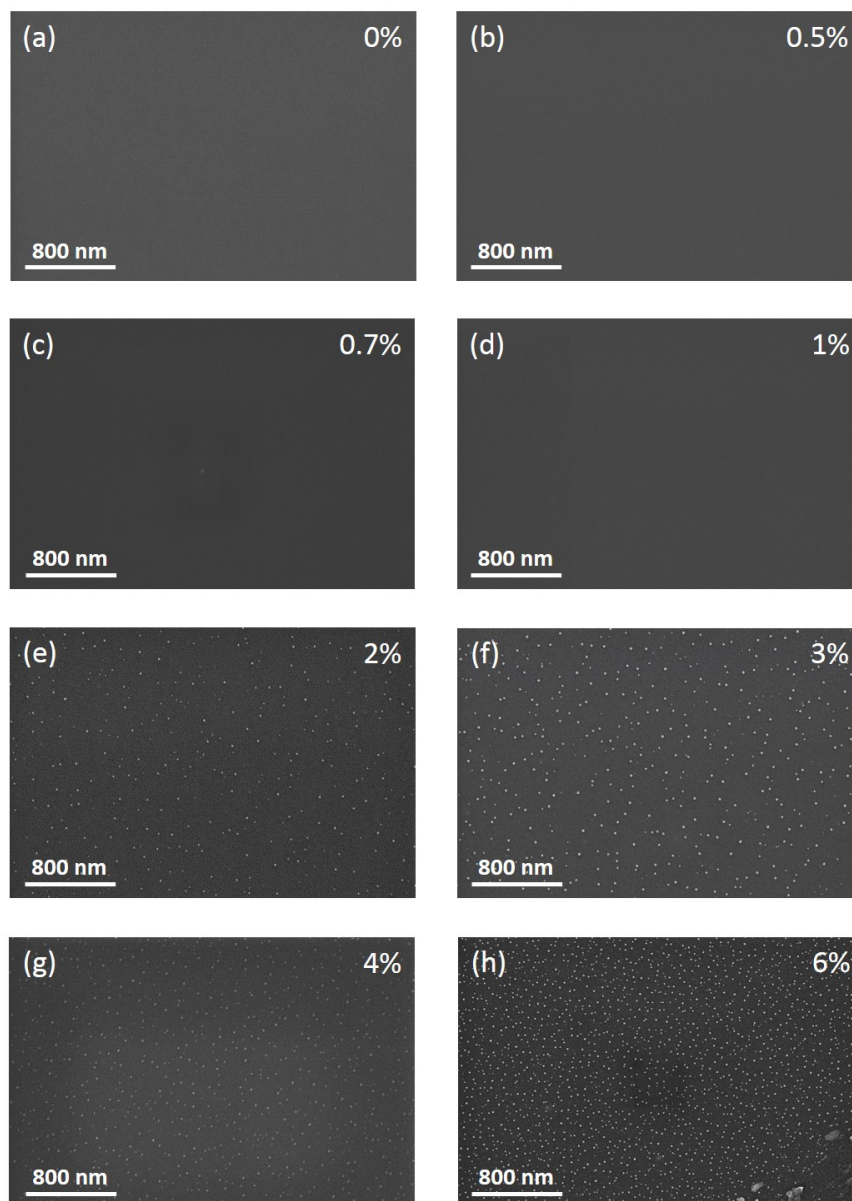


Figure 2.17: Scanning Electron Microscopy (SEM) images of the pure PBDTTT-c (a) and $\text{Mo}(\text{tfd-COCF}_3)_3$ doped PBDTTT-c at 0.5% MR (b), 0.7% MR (c), 1% MR (d), 2% MR (e), 3% MR (f), 4% MR (g) and 6% MR (h).

experiment is carried out on annealed thin films while the other analysis is conducted on solution. However, the composition should not be affected by the film formation and the annealing step. Therefore, TEM analysis is a useful tool to determine the composition of the aggregates.

An energy-dispersive X-ray (EDX) analysis is carried out on a cluster shown in Figure 2.20 (a) to determine their composition using an X-ray detector. The EDX spectrum is shown in Figure 2.21. We observe the peaks corresponding to the expected organic compounds Carbon, Sulfur and Oxygen. Those 3 components are found in the polymer

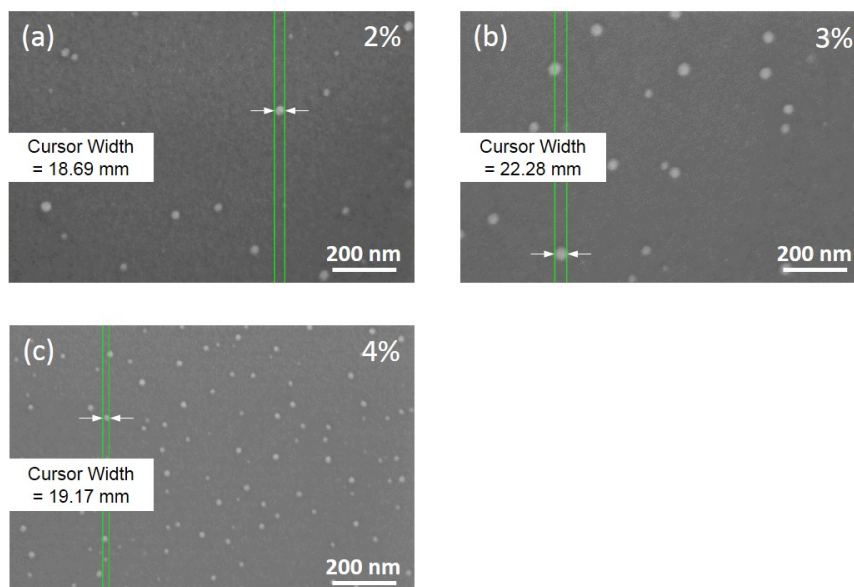


Figure 2.18: Scanning Electron Microscopy (SEM) images of the $\text{Mo}(\text{tfd-COCF}_3)_3$ doped PB-DTTT-c at 2% MR (a), 3% MR (b) and 4% MR (c).

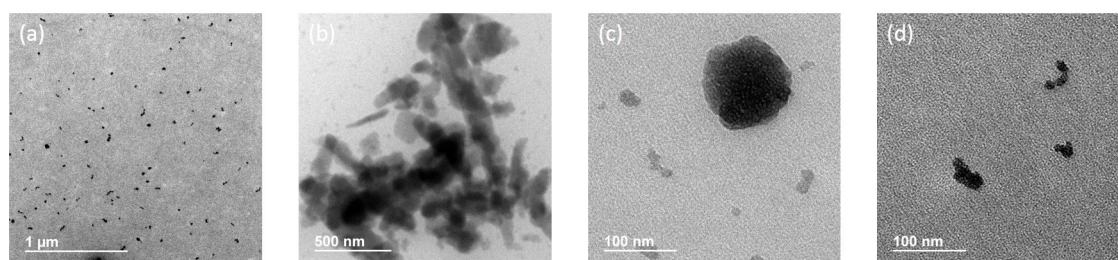


Figure 2.19: TEM images of the 5% MR sample obtained with an acceleration voltage of 200 kV for different spots on the grid at 4 different magnifications: $8.9\text{k}\times$ (a), $13.5\text{k}\times$ (b) and $64\text{k}\times$ for (c) and (d).

and the dopant. Moreover we can observe the peaks corresponding to Fluor and Molybdenum, which are only found in the dopant. However, the Molybdenum cannot be taken into account in this study as this component might be present in the TEM microscope.

The Figures 2.20 (b), (c) and (d) show the map of Fluor, Sulfur and Oxygen respectively on the area scanned by the X-ray detector. Sulfur and Oxygen are found on the whole area, although the cluster exhibits a higher density of both components. Fluor is mainly observed in the cluster indicating that $\text{Mo}(\text{tfd-COCF}_3)_3$ dopant is probably mostly situated in the aggregates and clusters of aggregates. However, we cannot determine whether the aggregates contain some PB-DTTT-c molecules as no atom (except Hydrogen) is specific to the polymer.

2.4. Possible origin of limited doping efficiency at high concentration

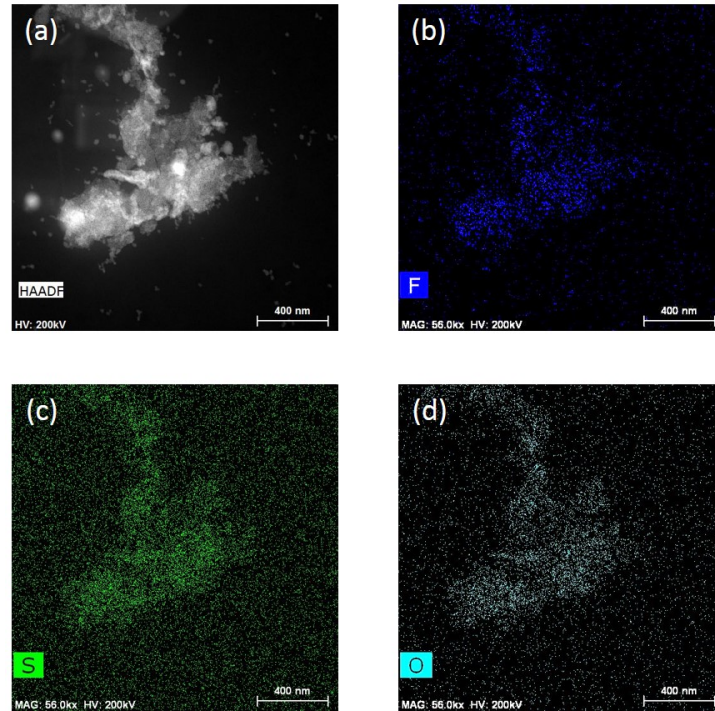


Figure 2.20: TEM images of the 5% MR sample obtained with a magnifications of 56k \times (a) and the Fluor (b), Sulfur (c) and Oxygen (d) maps obtained by EDX.

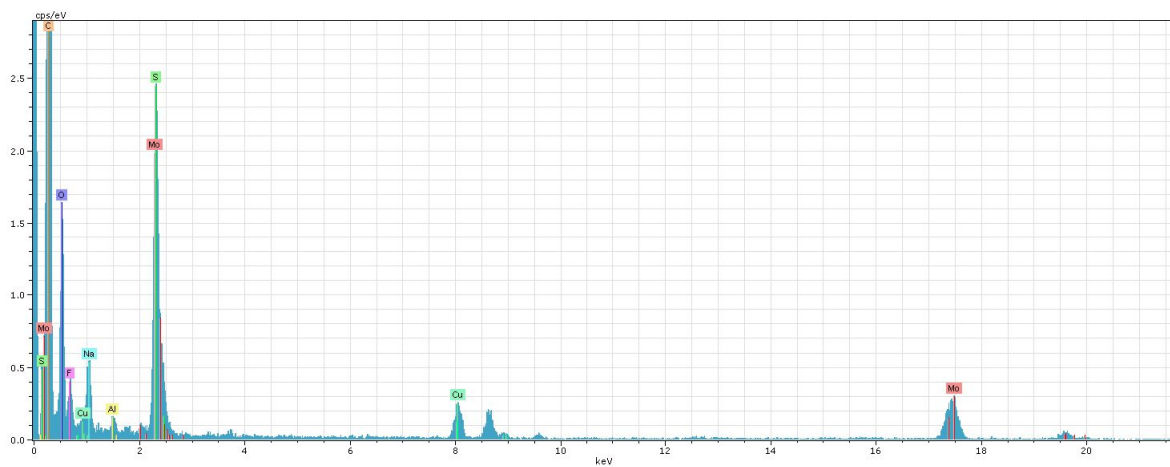


Figure 2.21: EDX spectrum of the aggregates cluster analyzed for the 5% MR sample.

Regarding the Scanning Electron Microscope (SEM) images obtained on pure and Mo(tfd-COCF₃)₃ doped PBDTTT-c, we can conclude that aggregates of approximately 20 nm in diameter are formed in the polymer matrix for doping concentrations exceeding 2% MR. This threshold is consistent with the conductivity and hole hopping transport activation energy measurements suggesting that their respective decline and saturation could be related to the formation of aggregates. Transmission Electron Microscope (TEM) images and energy-dispersive X-ray (EDX) analysis showed that Mo(tfd-COCF₃)₃ dopants are only situated in the aggregates and clusters of aggregates. However further analyses are required to distinguish between pure dopant or polymer-dopant aggregates.

2.4.2 Composition of the aggregates

In order to determine whether the aggregates observed in the Mo(tfd-COCF₃)₃ doped PBDTTT-c above 2% MR are composed of dopant only or polymer-dopant blends, we have chosen to carry out Nuclear Magnetic Resonance (NMR) spectroscopy analysis on pure and doped PBDTTT-c. NMR is an interesting characterization technique to get information on the physical and chemical properties of atoms or molecules in which they are contained. The resonance frequency depends on the magnetic field around an atom in a molecule and the evolution of the frequency value gives insight into the electronic structure of a molecule as it is sensitive to changes in chemical bonds as well as modifications in the chemical environment of the atoms probed. NMR spectroscopy relies on splitting of nuclei spin states upon application of a magnetic field for atoms with a non zero spin quantum number. Hydrogen and Carbon isotopes ¹H and ¹³C are the most commonly studied isotopes in NMR analysis. In this study we will also consider the Fluor isotope ¹⁹F. NMR principles are not detailed in this report as it is outside the scope of this thesis. However, further details can be found in the literature [188, 189].

We have carried out liquid-state NMR measurements using a 400 MHz NMR spectrometer from Bruker for a solution of pure Mo(tfd-COCF₃)₃ and Mo(tfd-COCF₃)₃ doped PBDTTT-c at a doping concentration of 5% MR. The components are dissolved in deuterated o-xylene. Liquid-state NMR has been chosen to obtain NMR spectra of pure dopant using small quantities. Indeed, experiments in solid-state NMR require a significant amount of dopant powder.

In order to make sure that the polymer-dopant interaction is similar in solution and solid thin film, we have carried out ¹³C spectra for pure and 5% MR doped PBDTTT-c in liquid and in solid-state using Magic Angle Spinning (MAS) to increase the resolution of the NMR spectrum. The ¹³C spectra of pure and doped PBDTTT-c obtained in solid-state MAS NMR using a BRUKER AVANCE DSX 500 MHz spectrometer are shown in Figure 2.22. A detailed experimental protocol is given in Appendix D. The chemical shifts of carbons have been simulated for a monomer of PBDTTT-c using the open source software nmrdb.org developed at Ecole Polytechnique Fédérale de Lausanne (EPFL) and reported in the table given as inset in Figure 2.22. With doping, the ¹³C spectrum is

2.4. Possible origin of limited doping efficiency at high concentration

mainly modified between 110 and 160 ppm. In this region, the peaks corresponding to the carbon atoms contained in the thiophene rings are attenuated. The disappearance of peaks in NMR spectra are usually due to the actual broadening of the peak. Such broadening can be due to the paramagnetic influence of Molybdenum leading to a faster spin relaxation [190]. It is unlikely that PBDTTT-c thiophene rings are broken upon dopant addition as it would lead to major changes on UV-visible absorption spectra. UV-visible absorption spectroscopy results will be presented in Chapter 3 and exhibit no evolution that would be due to such changes in the molecule.

The addition of $\text{Mo}(\text{tfd-COCF}_3)_3$ dopant in the PBDTTT-c matrix also leads to modifications in the peaks corresponding to the alkyl chains. The interaction of the dopant with the alkyl chains might disturb the cross-polarization used for this measurement. As cross-polarization involves dipolar interactions, modifications in the geometry of the side chains induce changes in the NMR signal. Moreover, a thin peak appears around 18 ppm but its origin has not been identified.

Solid-state MAS NMR highlights the interaction between the polymer and the dopant suggesting that the interaction is localized on the thiophene rings of the polymer. As the double CO bound around 200 ppm is not impacted by the addition of dopant, we believe that the dopant molecule might be situated as illustrated with a red circle on the molecular structure of PBDTTT-c given as inset in Figure 2.22.

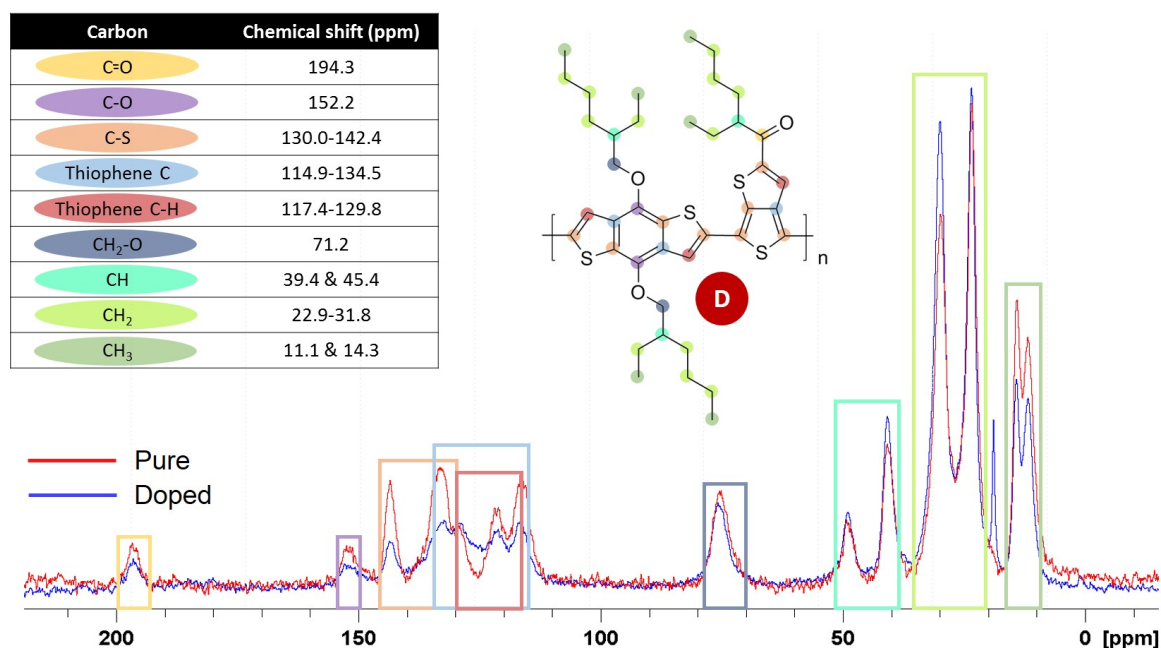


Figure 2.22: ^{13}C spectra of solid-state MAS NMR for pure (red) and $\text{Mo}(\text{tfd-COCF}_3)_3$ doped PBDTTT-c (blue). The carbon chemical shifts simulated for a monomer of PBDTTT-c using nmrdb.org are given in the table as inset. Colors are used to highlight the peaks corresponding to the carbon atoms in the PBDTTT-c chemical structure given as inset.

Figures 2.23 (a) and (b) exhibit the liquid-state NMR ^{13}C spectra for pure and 5% MR doped PBDTTT-c respectively. As the deuterated solvent o-xylene contains carbon atoms, we have measured the ^{13}C spectrum of the solvent shown in Figure 2.23 (c). By comparing the spectra of both solvent and polymer, we can show that the thin peaks observed at 18, 125, 129 and 135 ppm in the polymer spectrum are attributed to the solvent. As observed in solid-state MAS NMR, the addition of $\text{Mo}(\text{tfd-COCF}_3)_3$ dopants leads to the disappearance, or broadening, of the peaks corresponding to the carbon atoms in the thiophene rings. Moreover, we can notice a significant decrease of both CO and CH_2O peaks indicating that both types of side-chains are affected by the presence of dopant, suggested by the red circle in the molecular structure. This difference between solid and liquid-state NMR is probably due to the ability of both dopant and polymer to move in liquid-state, while their position is fixed in solid-state.

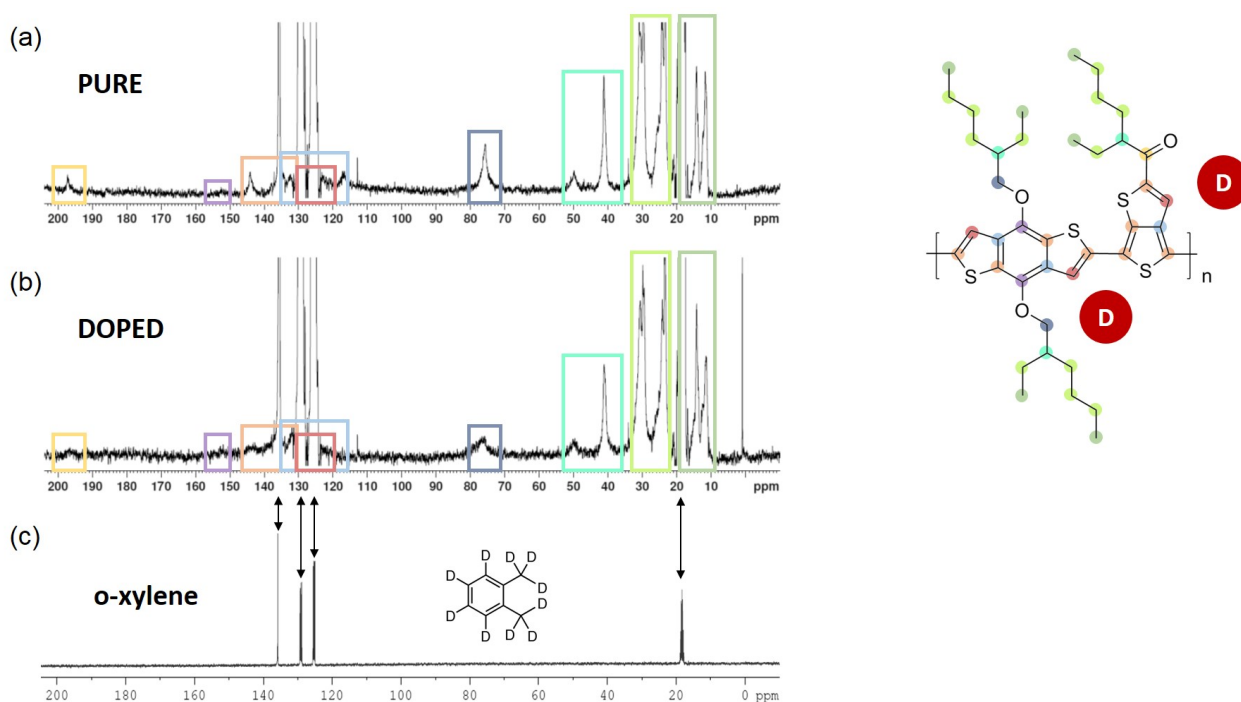


Figure 2.23: ^{13}C spectra of liquid-state NMR for pure PBDTTT-c (a), $\text{Mo}(\text{tfd-COCF}_3)_3$ doped PBDTTT-c (b) and deuterated o-xylene (c). Colors are used to highlight the peaks corresponding to the carbon atoms in the PBDTTT-c chemical structure given as inset.

The comparison of solid and liquid state NMR for pure and doped PBDTTT-c shows that the polymer-dopant interaction already takes place in solution. Therefore, we can carry out NMR spectroscopy of pure dopant and polymer-dopant mixture in liquid-state to determine whether all molecular dopants interact with the polymer. Figure 2.24 exhibits the ^{19}F spectra of the pure $\text{Mo}(\text{tfd-COCF}_3)_3$ dopant and of the doped polymer blend at 5% MR. For the pure dopant, two peaks are observed around -55 and -73 ppm. The integration of both peaks leads to a ratio close to 1:1. Therefore, the two peaks are probably associated with the two types of carbon-fluor bonds (green and blue in the chemical structure given as inset in Figure 2.24). The presence of the carbonyl group close to the carbon-fluor bonds colored in green might lead to a different chemical shift

2.4. Possible origin of limited doping efficiency at high concentration

of ^{19}F . When the dopant is mixed with the polymer, the two peaks combine to form one broad peak centered around -62 ppm . To make sure that the broader peak obtained after addition of the dopant in the polymer matrix is not due to a probe noise, we have measured the ^{19}F spectra of the pure $\text{Mo}(\text{tfd-COCF}_3)_3$ dopant and of the doped polymer blend at 5% MR with the exact same experimental conditions. Figure 2.25 shows that no peak is observed around -62 ppm for the polymer-dopant mixture when the same experimental conditions are used. The remaining peaks are probably due to impurities or ligands separated from the complex. Although the modifications in the molecular structure of the dopant are not identified, this major modification in the ^{19}F spectrum is the signature of the dopant interaction with the polymer. If some molecular dopants did not interact with the polymer host, we would expect small peaks around -55 and -73 ppm , which are not observed in the doped polymer. Therefore, we can conclude that all molecules of dopant added to the polymer have reacted. It is then unlikely that aggregates of pure dopant are formed. As a result, we believe that the aggregates observed in SEM and TEM images are composed of polymer-dopant mixture.

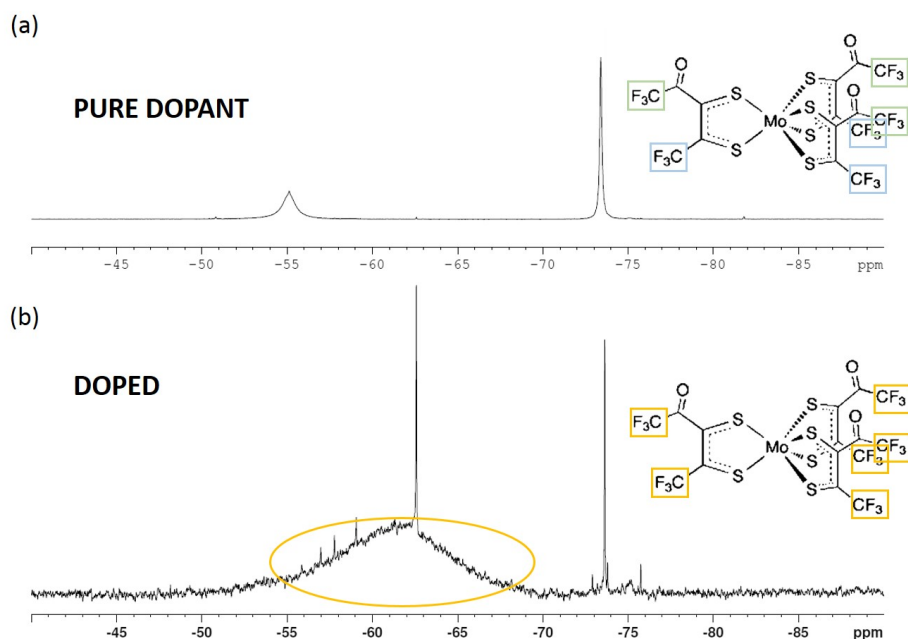


Figure 2.24: Liquid-state ^{19}F NMR spectra for pure $\text{Mo}(\text{tfd-COCF}_3)_3$ dopant (a) and 5% MR doped PBDTTT-c with $\text{Mo}(\text{tfd-COCF}_3)_3$ (b). The chemical structure of $\text{Mo}(\text{tfd-COCF}_3)_3$ is given as inset.

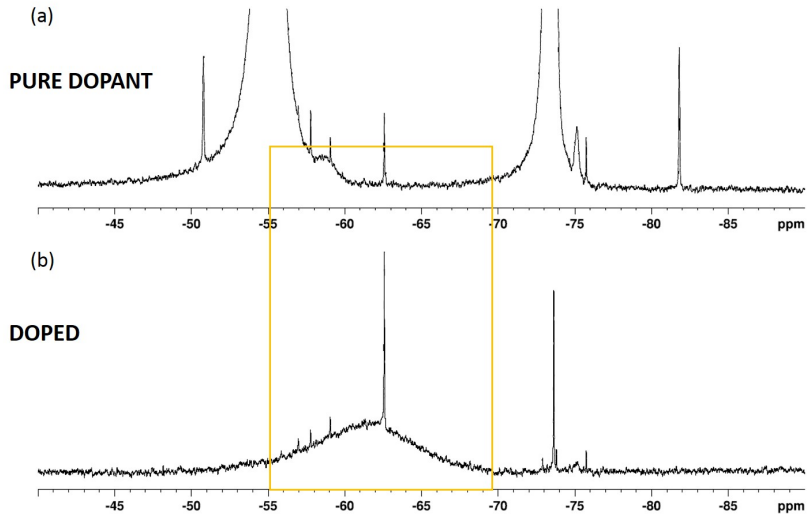


Figure 2.25: ^{19}F spectra of liquid-state NMR for pure $\text{Mo}(\text{tfd-COCF}_3)_3$ (a) and $\text{Mo}(\text{tfd-COCF}_3)_3$ doped PBDTTT-c (b) carried out with the same experimental conditions.

Nuclear Magnetic Resonance (NMR) measurements on pure PBDTTT-c, pure $\text{Mo}(\text{tfd-COCF}_3)_3$ and $\text{Mo}(\text{tfd-COCF}_3)_3$ doped PBDTTT-c at 5% MR highlighted the chemical interaction between the polymer and the dopant. The interaction between both components is more likely to take place around a thiophene ring of the polymer body. Moreover, ^{19}F NMR on pure dopant and polymer-dopant blend suggests that all dopant molecule added to the polymer matrix react with the host. Therefore, the aggregates observed above 2% MR are more likely composed of polymer-dopant mixture than pure dopant.

2.4.3 Impact of doped polymer morphology on electrical performances

Conductivity, hopping transport activation energy and ionized dopant density measurements on pure and doped PBDTTT-c at different doping concentrations highlighted the p-doping ability of $\text{Mo}(\text{tfd-COCF}_3)_3$ on PBDTTT-c. Moreover, different behaviors are observed between low and high doping concentration with a threshold around 1-2% MR. At low doping concentration, a superlinear increase in hole conductivity σ_p and density p and a decrease of the hole hopping transport activation energy E_A are measured. In the literature, such behavior has been associated with trap filling in the semiconductor [24, 125, 126].

Once all traps are filled, we expect the hole conductivity and density to increase linearly with the doping concentration as one dopant would lead to one hole created in the polymer matrix. The addition of new carriers in the HOMO should lead to a continuous decrease of the hole hopping transport activation energy E_A as the Fermi level would shift toward the HOMO level. However, we observe a slight decline of the conductivity and

2.4. Possible origin of limited doping efficiency at high concentration

a sublinear increase of the hole density with the doping concentration accompanied by a strong decrease of the hole doping efficiency above 1-2% MR. Moreover, the hole hopping transport activation energy saturates above 2% MR indicating a saturation of the Fermi level shift. An Dai [25] has measured the position of the Fermi level in $\text{Mo}(\text{tfd-COCF}_3)_3$ doped PBDTTT-c using Ultraviolet Photoemission Spectroscopy (UPS). She showed that doping PBDTTT-c at 1% MR leads to a strong shift of the Fermi level from 1.45 eV to 0.80 eV above the HOMO level. However, at 4% and 10% MR the Fermi level shift seems reduced and measured at 0.60 and 0.40 eV above the HOMO level respectively.

This decline of the doping efficiency at high doping concentration can be attributed to two phenomena: the formation of dopant aggregates or the creation of trap states in the polymer bandgap. Through SEM and TEM images we have highlighted the formation of aggregates of approximately 20 nm in diameter above 2% MR. However, the NMR study carried out on pure and doped PBDTTT-c indicated that all molecular dopants added to the polymer matrix seem to interact. If dopant aggregates are formed, a significant fraction of dopant should remain in its pristine form. Therefore, we believe that the aggregates observed above 2% MR are made of polymer-dopant mixture. Polymer-dopant aggregates can lead to a decline in the transport properties as the layer is made of sparse highly doped clusters with a high hole mobility in a pure polymer phase, which exhibits a limited mobility. This configuration is illustrated in Figure 2.26.

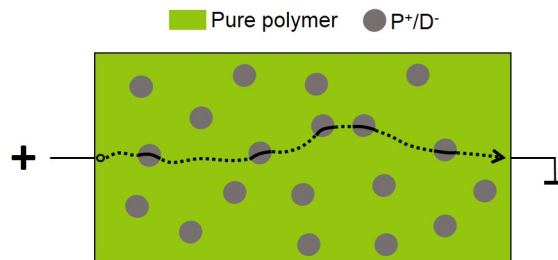


Figure 2.26: Schematic of the PBDTTT-c layer (in green) with aggregates of $\text{Mo}(\text{tfd-COCF}_3)_3$ doped PBDTTT-c (in gray). The morphology impact on hole transport is illustrated with dashed and solid lines in pure (low mobility) and doped (high mobility) areas respectively.

Although the conductivity and hole hopping transport activation energy evolutions can be explained by the formation of polymer-dopant aggregates altering the transport properties of the layer, the sublinear increase in hole density associated with a significant decrease in doping efficiency are not properly described by this hypothesis. As all molecular dopants added to the polymer matrix seem to interact with the host, we expect a continuous creation of holes in the HOMO. A decline in the generation of holes upon dopant addition indicates a reduction in the p-doping ability of the dopant. This decline can be attributed to the transition to the dopant reserve regime. Tietze *et al.* [91] explain that 3 regimes can be observed in the organic semiconductor doping process: trap filling, dopant saturation and dopant reserve. The dopant saturation regime corresponds to the impurity saturation regime in inorganic semiconductor doping and is observed if the Fermi level lies above the acceptor state (for p-doping) leading to a complete dopant activation. In this regime illustrated in Figure 2.27 (a), a linear evolution of the conductivity and hole density should be observed. When the Fermi level crosses the acceptor state, the

dopant activation is incomplete causing a sublinear increase of both conductivity and hole density. This regime called dopant reserve is associated with the impurity reserve regime in inorganic semiconductor doping. As shown in Figure 2.27 (b), in the dopant reserve regime we expect the Fermi level to saturate between the acceptor and transport levels.

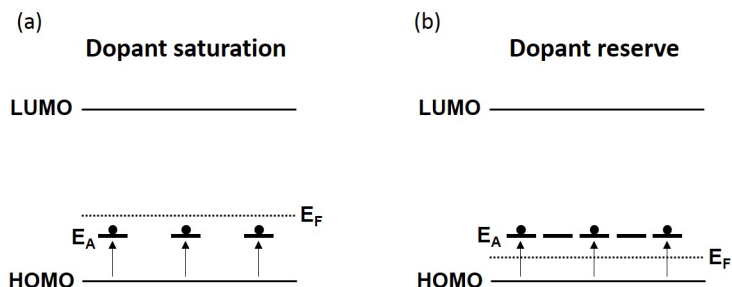


Figure 2.27: Schematic of the dopant saturation (a) and dopant reserve (b) regimes for p-doped organic semiconductor.

The entry in the dopant reserve regime would explain a saturation (but not decline) of the hole conductivity, the sublinear increase of the hole density accompanied by the doping efficiency decrease and the saturation of the hopping transport activation energy due to the saturation of the Fermi level shift. Considering that the dopant reserve regime is achieved above 2% MR, the UPS measurements carried out by An Dai on Mo(tfd-COCF₃)₃ doped PBDTTT-c indicate that the acceptor state would be several hundreds of meV above the polymer HOMO. The origin of such deep acceptor level remains to be understood and will be studied in Chapter 3.

The presence of polymer-dopant aggregates observed by SEM and TEM images have probably an impact on the transport properties. Therefore they can explain the hole conductivity and hopping transport activation energy evolution above 2% MR. However, polymer-dopant aggregates fail to explain the sublinear increase in hole density above 1% MR associated with a strong decrease of the doping efficiency. The entry in the dopant reserve regime at high doping concentration might be the origin of the different behaviors observed by electrical characterization. Further work will be carried out in Chapter 3 to deepen our understanding about the doping process involved and determine whether the entry in dopant reserve regime might effectively be responsible for the limited doping efficiency at high doping concentration.

Doping is used to enhance the transport properties of the semiconductor but also to improve or even create an ohmic contact between the semiconductor and metal electrode layers. As a last step of electrical characterization on the p-doped layer, we need to make sure that the addition of Mo(tfd-COCF₃)₃ effectively lowers the injection barrier between the metal electrode and organic semiconductor layer. This property is required to use the p-doped layer as interface layer in organic devices like photodetectors (Chapter 4).

2.5. Effective barrier lowering at the organic/metal interface

2.5 Effective barrier lowering at the organic/metal interface

In inorganic electronic devices, doping is widely used to improve the interface properties between the semiconductor and the electrode. Such improvement is due to the formation of a good ohmic contact between the highly doped semiconductor and the metal or semiconductor used as electrode. Doping leads to the shift of the Fermi level toward the valence band for p-doping and conduction band for n-doping. The Fermi level alignment induced when two materials are brought into contact generates a strong band bending in the doped layer. This band bending enables the injection or extraction of charges by tunneling as explained in Chapter 1.

In organic electronics, the carrier injection improvement has been demonstrated with the use of doped interface layers [191, 104, 32], which are integrated in various organic devices [26, 192]. An Dai followed the injection barrier evolution for different doped polymer layers [25, 26]. In this section we will reproduce this work to verify that Mo(tfd-COCF₃)₃ doped PBDTTT-c effectively lowers the injection barrier transforming a Schottky contact into a good ohmic contact. This experiment is the first step toward its integration in complete electronic devices like photodetectors.

2.5.1 Experiment

This study has been carried out on 3 types of devices illustrated in Figure 2.28 and in Appendix A as Structures 3A, 3B and 3C. All devices are based on an ITO-coated glass with a PEDOT:PSS layer to provide good ohmic contact for holes. The ITO-coated glass substrates are cleaned in ultra-sonic bath of soap water, acetone and isopropanol for 15 minutes each. PEDOT:PSS is spin-coated on the UV-ozone treated substrates and annealed at 160°C for 5 min. A thickness of 40 nm is measured by Atomic Force Microscopy (AFM). The following layers depend on the structure studied. The suppliers and references information of all materials are given in Appendix C.

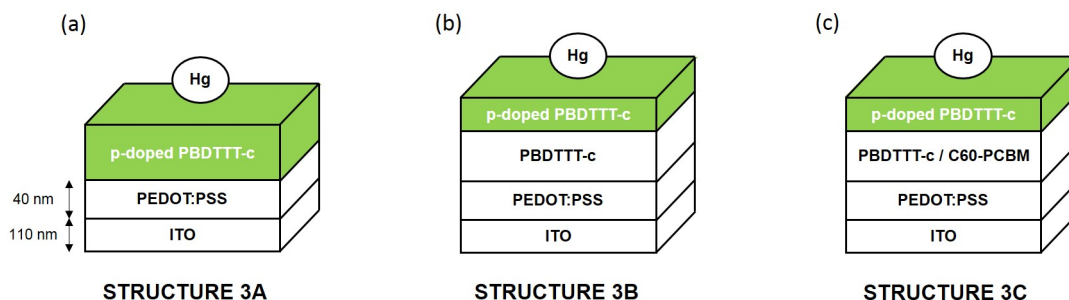


Figure 2.28: Schematic of the structures fabricated to study the injection barrier evolution with doping: Structure 3A (a), Structure 3B (b) and Structure 3C (c).

Structure 3A is a simple Schottky diode with the ohmic contact provided by PEDOT:PSS, the pure or doped layer of PBDTTT-c and the Schottky contact obtained with Mercury. Devices with pure PBDTTT-c and 4 different doping concentrations rang-

ing from 0.5% MR to 5% MR are fabricated by spin-coating and annealed at 150°C for 15 min in glovebox. The layer thicknesses are given in Table 2.3. The top electrode is obtained directly from the mercury probe used for the I(V) measurements. This first structure will be used to study the different injection regimes from ohmic and Schottky contact in pure and doped layers with varying doping concentrations.

Table 2.3: Thickness of the pure and doped layers deposited in Structure 3A and measured by AFM.

MR	Thickness
0%	$(130 \pm 10) \text{ nm}$
0.5%	$(95 \pm 5) \text{ nm}$
1%	$(185 \pm 10) \text{ nm}$
1.5%	$(220 \pm 10) \text{ nm}$
5%	$(120 \pm 10) \text{ nm}$

In structure 3B, a thin doped layer of PBDTTT-c ($35 \pm 5 \text{ nm}$) with varying concentrations is laminated on a $160 \pm 10 \text{ nm}$ thick layer of pure polymer. This structure will give insight in the injection barrier lowering induced by the doped interface layer. This study is further developed by replacing the pure layer of polymer with a $90 \pm 5 \text{ nm}$ thick donor/acceptor blend in structure 3C. A blend of PBDTTT-c with C₆₀-PCBM will be used in organic photodetectors studied in Chapter 4. This characterization will make sure that doped PBDTTT-c can act as hole transport layer in a photodetector or solar cell. All layers are annealed at 150°C for 15 min in glovebox. The top layer is deposited by Soft Contact Transfer Lamination (SCTL) technique outside the glovebox as explained in Section 2.1.

Electrical characterization are carried out in an N₂ flow box using a mercury probe station. In this setup, the top electrode is provided by controlled growth mercury drop at the end of a capillary tube and deposited on the device surface. The diameter of the mercury drop at the layer surface is measured using a camera and kept at 0.96 mm for all measurements. The mercury electrode and the bottom contact in ITO are connected to an Agilent 4155 sourcemeter. Mercury probes are convenient to obtain rapid I(V) characterization on devices without the evaporation of a top electrode.

2.5.2 Injection regimes in polymer p-doped with varying concentrations

Structure 3A is used to study the injection regimes from ohmic and Schottky contact in pure and doped PBDTTT-c with varying doping concentrations. Figure 2.29 (a) exhibits the current density with respect to the electric field in the layer in a semi-logarithmic plot. The injection from the mercury electrode (Schottky contact) is shown in dotted line and the injection from the PEDOT:PSS electrode (ohmic contact) in solid line.

Three different injection regimes can be observed from the PEDOT:PSS electrode depending on the electric field in the layer and the doping concentration: ohmic regime, Trap Charge Limited Current (TCLC) regime and Space Charge Limited Current (SCLC) regime. At low electric field, the intrinsic hole density p_0 for a p-type semiconductor

2.5. Effective barrier lowering at the organic/metal interface

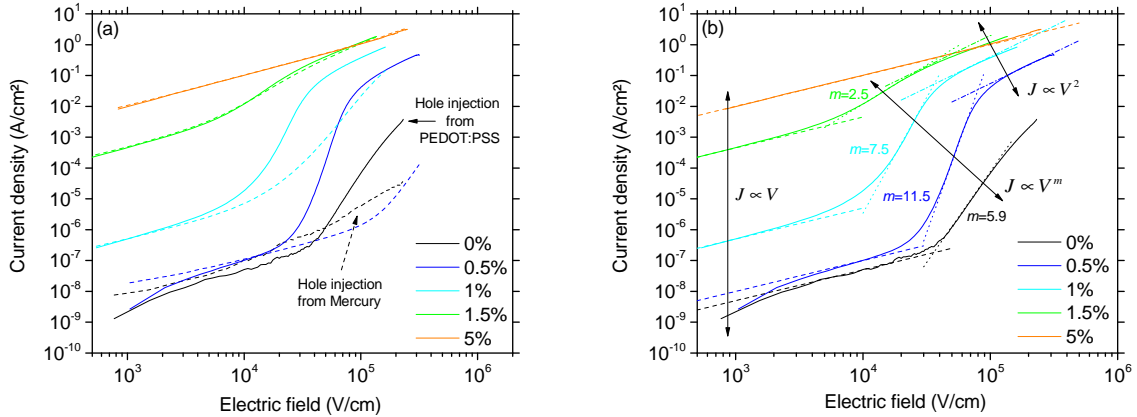


Figure 2.29: Current density with respect to the electric field in the device structure for 0%, 0.5%, 1%, 1.5% and 5% MR (a). The hole injection from the Mercury electrode is shown in dotted line and the hole injection from the PEDOT:PSS in solid line. Ohmic, TCLC and SCLC fitting for the current density injected from the PEDOT:PSS electrode for the same devices (b).

exceeds the amount of holes injected from the electrode. This configuration describes the ohmic regime where the current density J_{ohmic} evolves linearly with the applied bias V [193]:

$$J_{ohmic} = q\mu_h p_0 V/L \quad (2.22)$$

where μ_h is the majority carrier mobility (holes in a p-type semiconductor) and L the layer thickness. At higher electric field, the amount of injected charges exceeds the intrinsic hole density generating a space charge region in the layer. This non uniform electric field results in the formation of a Space Charge Limited Current (SCLC) where the current density J_{SCLC} is given by the Mott and Gurney law [194]:

$$J_{SCLC} = \frac{9}{8}\epsilon_0\epsilon_r\mu_h \frac{V^2}{L^3} \quad (2.23)$$

with ϵ_0 the vacuum permittivity and ϵ_r the relative permittivity. Ohmic regimes followed by SCLC regimes have been widely observed in the literature for pure and doped polymers [195, 196, 194].

When the semiconductor exhibits trap states, a third regime is observed between ohmic and SCLC regimes. This regime called Trap Charge Limited Current (TCLC) is described by a power law evolution of the current density $J \propto V^m$, with m depending on the amount of trap states [197]. By increasing the electric field in the layer, the trap states are progressively filled by the injected charges leading to the increase of the carrier mobility. This mobility evolution justifies a superlinear increase of the current density. The different regimes are indicated in Figure 2.29 (b).

From the mercury electrode, the injection current is mainly limited by the injection barrier for holes estimated at 650 meV. As a result, a difference of 2 orders of magnitude is observed in the injected current density from both electrodes for an electric field of

2×10^5 V/cm. This discrepancy illustrates the difference in the hole injection ability between PEDOT:PSS and mercury electrodes.

With the addition of a small amount of dopants in the polymer layer (0.5% MR), the injection from the mercury electrode remains stable while the injection from PEDOT:PSS is strongly improved with a current density increase of 2 orders of magnitude at 2×10^5 V/cm. This strong current density increase in the SCLC regime is mainly due to the improved mobility at low doping concentrations. We have shown in Section 2.2 that doping concentrations below 2.5% MR leads to a superlinear increase of the hole conductivity and a drop in the hole hopping transport activation energy. Both evolutions have been attributed to the progressive filling of trap states with the addition of dopant resulting in a strong mobility increase. According to relation 2.23, an increase in mobility leads to an increase in current density in the SCLC regime.

By further increasing the doping concentration from 0.5% MR to 1.5% MR, we observe a current density increase in the injection regime accompanied by a strong improvement of the current density injected from the mercury electrode. At 1.5% MR, the injection current from both electrodes overlap. Both observations can be explained by the formation of free carriers upon addition of p-dopants. Doping at the interface leads to a reduction of the injection barrier increasing the hole current density. Moreover, a decrease of the TCLC power law m from 11.5 to 2.5 is highlighted, emphasizing the progressive filling of trap states with holes.

When a doping concentration of 5% MR is reached, the current density follows the ohmic law over the whole range of electric field measured indicating that a high density of free carriers has been generated in the layer allowing a good ohmic contact from both electrodes. Therefore, Figure 2.29 illustrates the p-doping ability of Mo(tfd-COCF₃)₃ in PBDTTT-c leading to an effective barrier lowering at the Schottky electrode, the filling of traps at low doping concentration and the increase in hole carrier density.

2.5.3 Enhancement of the organic/metal interface

Now that we have highlighted the ability of Mo(tfd-COCF₃)₃ doped PBDTTT-c to decrease the effective injection barrier, we can try to use this polymer-dopant mixture as hole transport layer in electronic devices in order to improve the injection of holes. One target of this layer is the replacement of PEDOT:PSS in organic photodetectors or solar cells which is known to be responsible for some stability issues in these devices [37, 38, 39]. Chapter 4 will be devoted to the replacement of PEDOT:PSS by Mo(tfd-COCF₃)₃ doped PBDTTT-c in organic photodetectors. However, as a first step we propose to check the effective barrier lowering in simple devices. Structures 3B and 3C are used to study the evolution of the hole injection barrier between the mercury electrode and pure PBDTTT-c for structure 3B and a polymer-fullerene blend in structure 3C using a doped interface layer.

Figure 2.30 (a) exhibits the J(V) characteristics for structure 3B with the injection from mercury in dotted line and from PEDOT:PSS in solid line. As expected we observe an improvement in the injection current from the Schottky contact with increasing doping

2.5. Effective barrier lowering at the organic/metal interface

concentration in the interface layer. At 1.5% MR the current density injected from both electrodes overlaps and at a doping concentration of 5% MR, the current injected from the mercury electrode exceeds the current injected from the PEDOT:PSS electrode. We can also notice that the current density injected from the ohmic PEDOT:PSS contact remains relatively stable in the SCLC regime. This regime is indeed driven by the hole density and mobility in the layer. However, in structures 3B and 3C, the doped layer is thin compared to the pure polymer and blend layers. As a result, the hole density and mobility are mainly determined by the thicker unchanged layer.

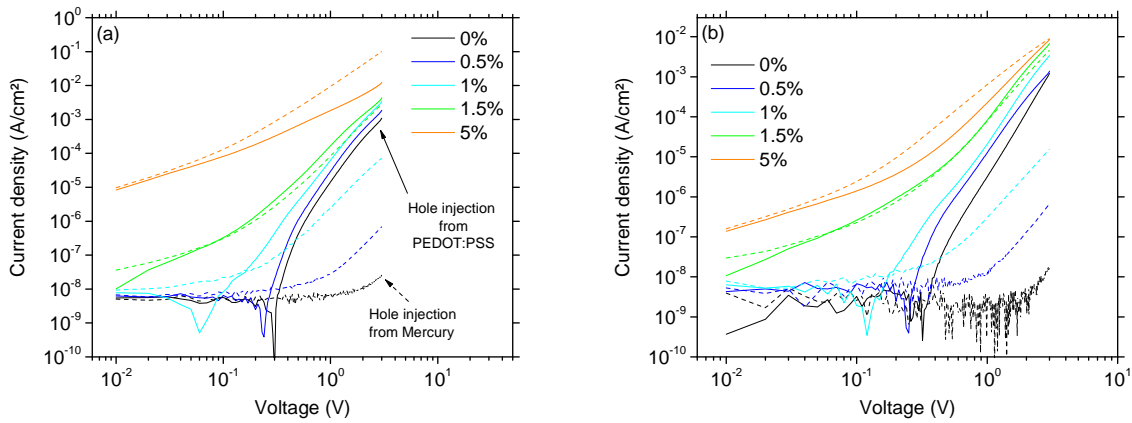


Figure 2.30: Current density with respect to the applied bias for structure 3B with pure PB-DTTT-c (a) and structure 3C with the blend of polymer:fullerene (b).

The $J(V)$ characteristics for structure 3C are shown in Figure 2.30 (b). The same evolution of the injection barrier is observed with the overlap of the injected current at 1.5% MR. Therefore, we can obtain an efficient ohmic contact between a polymer-fullerene blend and a mercury electrode with a work-function of 4.5 eV by using $\text{Mo}(\text{tfd-COCF}_3)_3$ doped PB-DTTT-c as interface layer. This result is promising for the replacement of the hole transport layer PEDOT:PSS in photodectors.

The integration of the p-doped layer with varying doping concentrations in 3 simple structures have highlighted the different impacts of $\text{Mo}(\text{tfd-COCF}_3)_3$ p-doping in PBDTTT-c. Electrical characterization of the doped layer between one ohmic contact and one Schottky contact further confirmed the hypothesis of trap filling at low doping concentration leading to a strong increase of the hole mobility. Moreover, this experiment illustrated the ability of this p-doped layer to reduce the effective injection barrier for holes at the Schottky contact. Above 1.5% MR, the energy barrier of 650 meV is overcome leading to the overlap of the injected current from both ohmic and Schottky contacts.

By using $\text{Mo}(\text{tfd-COCF}_3)_3$ doped PBDTTT-c as interface layer between the mercury electrode and the undoped polymer or blend layer we have illustrated the possibility to use this polymer-dopant mixture as hole transport layer in organic electronic devices. This major property will be further developed in Chapter 4.

2.6 Summary and outlook

As a first step in our study we needed to verify the p-doping ability of $\text{Mo}(\text{tfd-COCF}_3)_3$ in the polymer PBDTTT-c and follow the evolution of the electrical characteristics with the doping concentration.

We demonstrated that the addition of $\text{Mo}(\text{tfd-COCF}_3)_3$ in the polymer matrix leads to the increase in hole conductivity and hole density, the decrease in hole hopping transport activation energy and the effective barrier lowering for holes. All these evolutions are characteristic of p-doping. Moreover, the improvement in hole conductivity between pure and 2.5% MR doped polymer is among the best results reported in the literature.

Two regimes have been identified with the doping concentration. Up to 2.5% MR, doping leads to the filling of trap states in the semiconductor resulting in a superlinear conductivity and hole density increase, a drop of the hopping transport activation energy, a doping efficiency increase and a decrease in the TCLC slope. Trap filling has been observed in various polymer-dopant mixtures and can be used to reduce the impact of trap states on the transport properties of the device.

Above 2.5% MR, a saturation or decline of doping can be observed. Indeed, a decrease in hole conductivity and doping efficiency, a saturation of the hopping transport activation energy and a sublinear increase in hole density indicate that the doping impact of additional $\text{Mo}(\text{tfd-COCF}_3)_3$ molecules in the polymer is reduced. We have highlighted the formation of polymer-dopant aggregates above 2.5% MR, which could be responsible for the degradation of the transport properties leading to the conductivity decrease and the saturation of the hopping transport activation energy. However, polymer-dopant aggregates fail to explain the sublinear increase in hole density and the doping efficiency drop above 1% MR. NMR characterizations indeed indicate that all molecular dopants added to the matrix react with the polymer. Therefore, the doping efficiency might be limited by another parameter. The entry in dopant reserve regime could explain both

2.6. Summary and outlook

observations but involves the saturation of the Fermi level below the dopant acceptor state.

Chapter 3 will focus on the doping mechanisms involved in our polymer-dopant mixture in order to deepen our understanding of the doping limitations at high doping concentration. This study will help determine whether the entry in dopant reserve regime is a consistent hypothesis and suggest ideas to improve the doping efficiency. In Chapter 4 we will take advantage of the effective barrier lowering induced by p-doping at the interface to replace PEDOT:PSS in organic photodetectors.

3

Analysis of the doping mechanism involved in Mo(tfd-COCF₃)₃ doped PBDTTT-c

Chapter contents

3.1	Sub-bandgap absorption with p-doping	73
3.1.1	Experiment	73
3.1.2	Formation of sub-bandgap absorption peaks with doping concentration	74
3.1.3	Sub-bandgap peaks related to Charge Transfer Complex (CTC) formation	77
3.2	Doping induced fluorescence quenching	84
3.2.1	Experiment	86
3.2.2	Photoluminescence quenching	88
3.2.3	Static or Dynamic quenching?	91
3.3	Characterization of gap states related to organic semiconductor p-doping	97
3.3.1	Admittance spectroscopy	97
3.3.2	Samples and experimental set-up	101
3.3.3	Trap states formation with p-doping	102
3.3.4	Trap concentration and Density of States	106
3.3.5	From UV-visible absorption spectroscopy to admittance spectroscopy	109
3.4	How to explain the effective p-doping?	110
3.4.1	Density of States broadening	110
3.4.2	Light assisted p-doping	112
3.5	Summary and outlook	114

In the previous chapter we provided evidence of the effective PBDTTT-c p-doping with the complex Mo(tfd-COCF₃)₃. We highlighted the limited doping efficiency at high doping concentration through conductivity, hopping transport activation energy and hole density measurements. Although the observed formation of polymer-dopant aggregates for doping concentrations above 2% MR can be responsible for the saturation of conductivity and activation energy by altering the transport properties in the layer, it fails to explain the limited charge generation efficiency. Moreover, it has been demonstrated in the literature that the Fermi level shift saturates at high doping concentration lying a few hundreds of meV above the HOMO for p-type doping [29, 91, 198].

Improving the molecular doping efficiency is a major requirement to achieve better performances in organic electronic devices. The need for high doping concentrations results in the degradation of transport properties [172, 59]. As a consequence, we need to deepen our understanding of the mechanisms involved in doping processes between polymers and molecular dopants. By identifying the origin of the poor efficiency in organic semiconductor doping, we should be able to provide clues for dopant design improvement and push the boundaries of this new technology.

In the literature, two doping mechanisms are discussed for different polymer-dopant mixtures. Historically, doping is described with the ground-state Integer Charge Transfer (ICT) model [73, 24, 32]. This mechanism relies on direct and complete transfer of the electron from the polymer HOMO to the dopant LUMO for p-doping as shown in Figure 3.1 (a). An alternative model has been proposed by Salzmann *et al.* involving the formation of an hybrid Charge Transfer Complex (CTC) between the polymer HOMO and dopant LUMO for p-doping [90]. This mechanism is illustrated in Figure 3.1 (b). To effectively p-dope the polymer, the electron needs to be transferred from the polymer HOMO level to the anti-bonding state of the CTC [59]. A partial charge transfer is then attributed to this process which could explain the low doping efficiencies.

Although a few studies have been conducted to determine what model is involved in different polymer-dopant blends, the underlying origins and consequences remain to be understood [30]. Moreover, there is a lack of a global picture of the doping processes in organic materials (printed or evaporated).

In this chapter we try to understand which model corresponds to our doped polymer. Complementary optical and electrical characterization techniques are used to strengthen our hypothesis and deepen our understanding of the mechanism involved. As a last step, a model is proposed to explain the Mo(tfd-COCF₃)₃ p-doping process of PBDTTT-c and its consequences on the electrical performances presented in Chapter 2.

3.1. Sub-bandgap absorption with p-doping

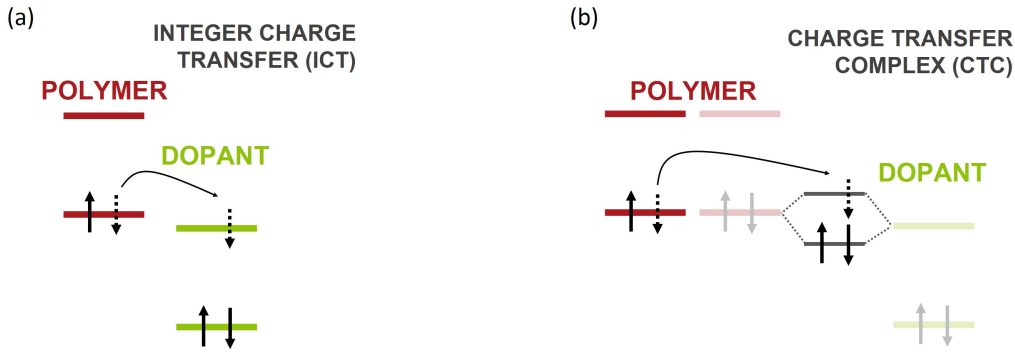


Figure 3.1: Schematic of the Integer Charge Transfer (ICT) (a) and Complex Charge Transfer (CTC) (b) models used to describe the doping process in organic semiconductors, here in the case of p-type doping.

3.1 Sub-bandgap absorption with p-doping

It has been demonstrated that both ICT and CTC result in the polymer absorption spectrum modification in the sub-bandgap region [74]. The formation of F_4TCNQ anions through charge transfer from P3HT leads to the creation of peaks in the near infra-red originating from the singly negatively charged dopant [79]. Moreover, the cation formed on the polymer leads to polarons also creating absorption peaks in the sub-bandgap region. When a hybrid CTC is formed between the polymer and the dopant, a transition is expected from the bonding to the anti-bonding level of the complex. As the CTC gap is usually lower than the polymer bandgap, an absorption peak can be observed in the sub-bandgap region [29].

UV-visible absorption spectroscopy is then carried out on $Mo(tfd-COCF_3)_3$ doped PBDTTT-c with varying doping concentrations to observe the impact of the polymer-dopant interaction in the sub-bandgap absorption. This analysis will provide information on the model involved in our polymer-dopant blend.

3.1.1 Experiment

Pure and p-doped PBDTTT-c with $Mo(tfd-COCF_3)_3$ are deposited on glass substrates to carry out UV-visible absorption spectroscopy from 300 to 2000 nm. Eight different molar concentrations are processed from 0.5% to 6% to cover the different regimes observed through electrical characterization in Chapter 2. The concentrations of PBDTTT-c and $Mo(tfd-COCF_3)_3$ in o-xylene have been carefully chosen to obtain similar thicknesses. The solutions are spin-coated on borosilicate glass substrates and annealed at 115°C for 10 minutes under nitrogen. The thicknesses are measured with a contact profilometer and summarized in Table 3.1. The average thickness for all layers is estimated at $390\text{ nm} \pm 10\%$.

Borosilicate has been selected as glass substrate for its high transparency in the wavelength range of interest in this study (from 700 to 2000 nm). The absorption spectrum

Table 3.1: Thicknesses of polymer layers used for UV-visible absorption spectroscopy.

MR (%)	Thickness (nm)	Inhomogeneity (nm)
0	405	20
0.5	395	10
0.7	355	10
1	380	10
2	420	20
3	385	10
4	350	10
5	415	10
6	430	10

of the 0.7 mm thick borosilicate substrate used in this study is shown in Figure 3.2. The absorption is close to 0% from 400 to 2000 nm ensuring a good analysis of the doped polymer in the sub-bandgap region.

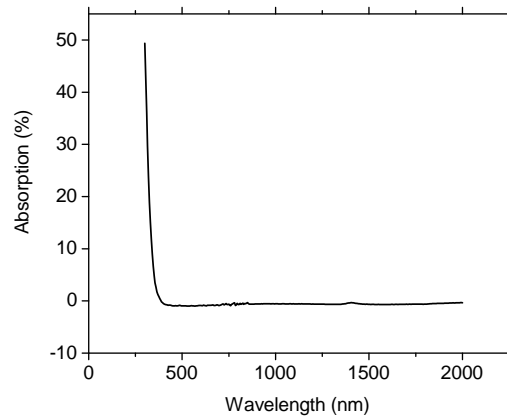


Figure 3.2: Absorption spectrum of 0.7 mm thick borosilicate substrate.

The absorption spectra are obtained from reflection and transmission measurements using a LAMBDA 950 UV/Vis/NIR Spectrophotometer from Perkin Elmer with an integrating sphere. The sample is located outside the sphere enabling the measurements of the diffuse components of the transmission and reflection spectra.

3.1.2 Formation of sub-bandgap absorption peaks with doping concentration

The transmission and reflection spectra are measured for each doping concentration from 300 to 2000 nm with a step of 5 nm. This wavelength range is equivalent to an energy varying from 4.1 to 0.62 eV. The absorption A is calculated with respect to the transmission T and reflection R using the following relation:

$$A = 1 - T - R \quad [-]. \quad (3.1)$$

3.1. Sub-bandgap absorption with p-doping

The absorption spectra for doping concentrations ranging from 0 to 6% MR are presented in Figure 3.3 (a). As absorption is thickness dependent special care has been taken to achieve layers with relatively close thicknesses. However, a variation of 10% was measured around the average thickness. In order to eliminate the thickness dependency and enable a direct comparison of the spectra, we chose to calculate the absorption coefficient for each layer. The absorption coefficient α is a property of the material describing its ability to attenuate an incident light intensity. Its value is wavelength dependent and is related, at a given wavelength, to the incident I_0 and output I light intensities by Beer-Lambert law:

$$I = I_0 e^{-\alpha d} \quad (3.2)$$

with d the layer thickness. In the case of a polymer thin film deposited on a glass substrate, Beer-Lambert law does not lead directly to the absorption coefficient knowing the absorption, as we need to take into account the interferences between layers. In order to properly determine the absorption coefficient we have simulated the extinction coefficient k for each concentration using the OptiChar module of OptiLayer Thin Film Software. The absorption coefficient α is related to the extinction coefficient k as follows:

$$\alpha = \frac{4\pi k}{\lambda} \quad (3.3)$$

with λ the wavelength of the incident photons.

Figure 3.3 (b) exhibits the absorption coefficient spectra for each doping concentration. This extraction confirms the formation of absorption peaks in the bandgap of the polymer around 1100 nm with doping and their intensity increase with the doping concentration.

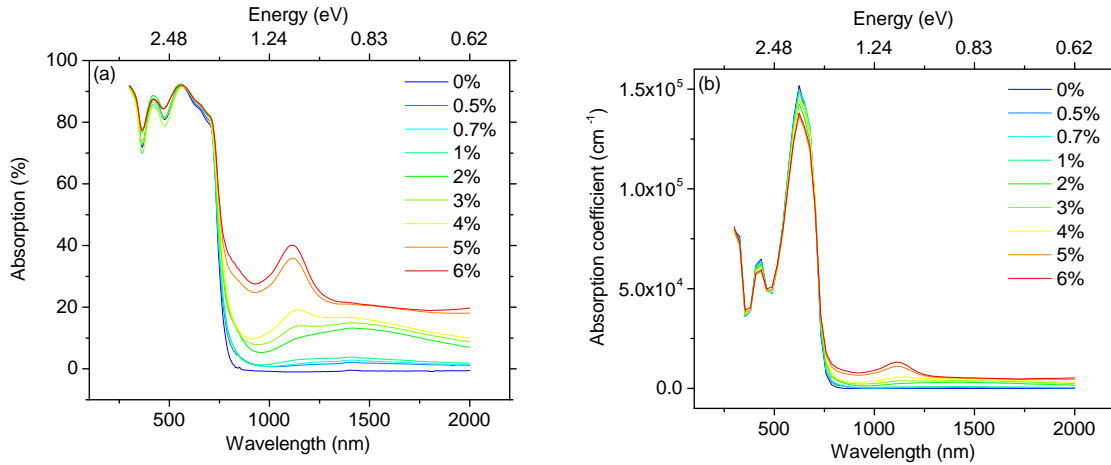


Figure 3.3: Absorption (a) and absorption coefficient (b) spectra for the pure polymer and 8 doping concentrations varying from 0.5 to 6%.

Although the formation of a peak with a Gaussian distribution is clearly visible around 1.1 eV, the absorption increases in the whole near infra-red range and could be related to diffusion issues. As the equipment set-up includes an integrating sphere, if total transmission and reflection measurements are properly carried out, diffusion is taken into account in the absorption calculation. However, to make sure that diffusion is not involved in the

sub-bandgap absorption increase with doping concentration due to potential modifications in the doped layer morphology, we decided to study the evolution of diffusion with doping concentration.

The total transmission T_{total} is divided into specular ($T_{specular}$) and diffuse ($T_{diffuse}$) components:

$$T_{total} = T_{diffuse} + T_{specular}. \quad (3.4)$$

The diffuse component of transmission is compared to the total transmission of the layers in Figure 3.4 (a). The PBDTTT-c layer exhibits a very low diffuse transmission (lower than 1%) and the diffusivity of the polymer is not influenced by the doping concentration.

To quantify the diffusivity of the material, the Haze factor H can be calculated:

$$H = \frac{T_{diffuse}}{T_{total}} * 100 \quad [\%]. \quad (3.5)$$

The Haze factors determined for each wavelength are shown in Figure 3.4. In the near infra-red region the Haze factor is very low (around 0.5%) and similar for all doping concentrations. Therefore, we cannot explain the absorption increase in the sub-bandgap region by diffusion.

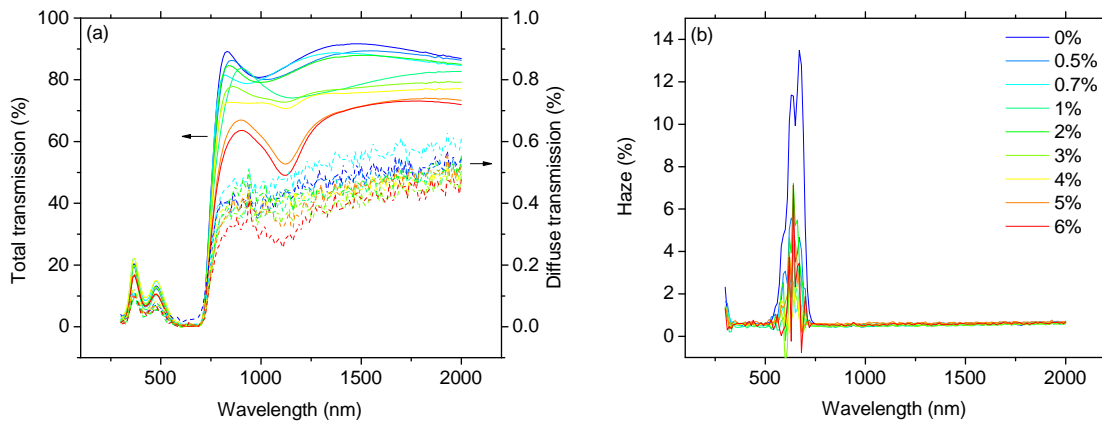


Figure 3.4: Total and diffuse transmission spectra (a) and Haze factor (b) for the pure polymer and 8 doping concentrations varying from 0.5 to 6%.

As both ICT and CTC models result in the formation of sub-bandgap absorption peaks, we need to study both possibilities. If ICT is involved in the $\text{Mo}(\text{tfd-COCF}_3)_3$ interaction with PBDTTT-c, the absorption increase would be due to the dopant in its ionized form or to polarons in the polymer. Mohapatra *et al.* have measured the absorption spectra of $\text{Mo}(\text{tfd-COCF}_3)_3$ in neutral, monoanionic and dianionic oxidation states [199]. Figure 3.5 exhibits the absorption spectra of the $\text{Mo}(\text{tfd-COCF}_3)_3$ doped PBDTTT-c layers studied during this thesis (a) and of the different dopant oxidation states extracted from literature (b). The monoanionic form of $\text{Mo}(\text{tfd-COCF}_3)_3$ presents a broad and low absorption peak in the near infra-red region but neither the monoanionic nor the dianionic oxidation states of the dopant correspond to the absorption peaks created

3.1. Sub-bandgap absorption with p-doping

in the doped polymer. However, there is still a chance that the peaks observed are due to polarons in the polymer. Further analyses are required to distinguish between ICT and CTC.

In the following section we will consider that the absorption peaks result from the formation of an hybrid CTC between the polymer HOMO and the dopant LUMO. Further experiments will be carried out to test this hypothesis and discuss the possibility of CTC compared to polarons to explain the formation of sub-bandgap absorption peaks.

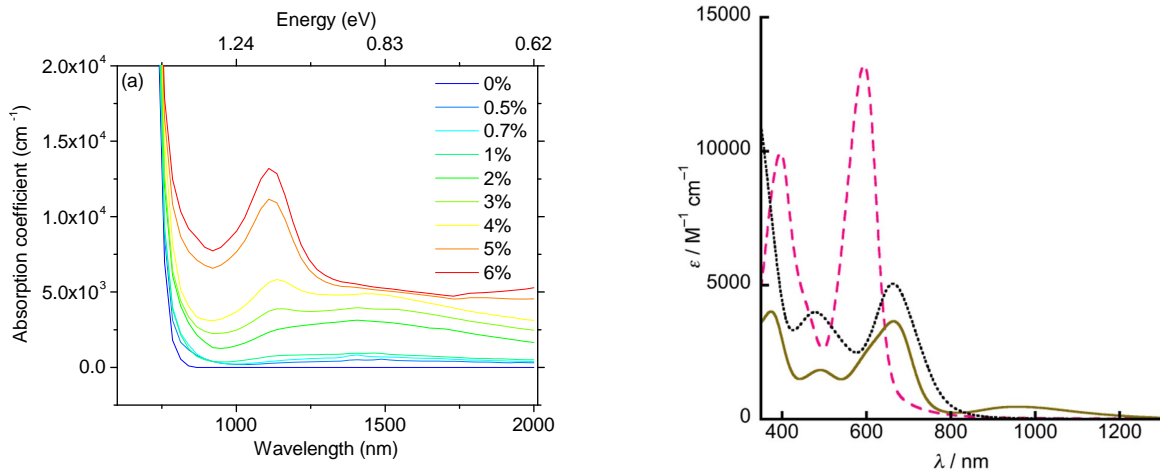


Figure 3.5: Absorption coefficient spectra for the pure polymer and 8 doping concentrations varying from 0.5 to 6% (a). Electronic absorption spectra in CH₂Cl₂ for Mo(tfd-COCF₃)₃ in neutral (broken line), monoanionic (solid line), and dianionic (dotted line) oxidation states (b). Reprinted with permission from [199]; Copyright (2016) by Elsevier.

3.1.3 Sub-bandgap peaks related to Charge Transfer Complex (CTC) formation

Figure 3.6 shows the evolution of the absorption peaks with the doping concentration in the near infrared region. In this graph the x-axis is given in energy to facilitate the extraction of the energy levels. Different steps can be observed in the evolution of the sub-bandgap absorption. From 0 to 1% MR, a slight and broad increase is observed. The absorption peaks start to be stronger above 2% MR with a broad Gaussian distribution centered around 860 meV and a thinner Gaussian distribution centered around 1.1 eV. From 2 to 4% MR, the peak around 860 meV increases more strongly than the second one, but above 4% the peak centered at 1.1 eV prevails. This threshold of 2% MR has already been observed in the electrical characterizations carried out in Chapter 2. Hole conductivity and hopping transport activation energy measurements suggest that this concentration marks the transition from the trap filling regime to a saturation regime explained by the formation of new traps or changes in the morphology.

To follow the evolution of the absorption peaks in the sub-bandgap region we fit the spectra with Gaussian functions. We chose not to subtract the baseline as it will change the amplitude value which carries important information for our analysis. Although

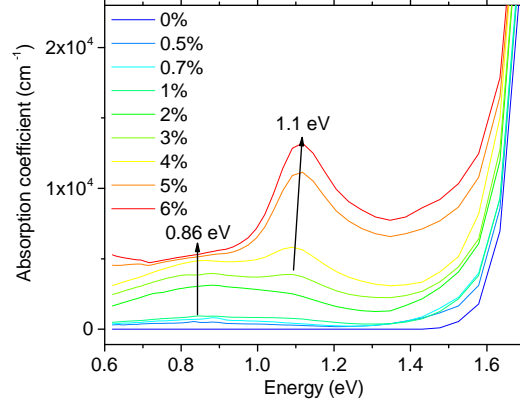


Figure 3.6: Absorption coefficient spectra with respect to the photon energy for the pure polymer and 8 doping concentrations varying from 0.5 to 6%.

it would be more accurate to fit the absorption coefficient spectra obtained from the extinction coefficient simulation, the wavelength resolution is too poor to obtain a good fit. Therefore, we chose to analyze directly the absorption spectra, considering a thickness variation of 10% around the average thickness. The Gaussian function used to fit the two peaks is described as follows:

$$y = y_0 + \frac{A}{w\sqrt{\frac{\pi}{4\ln(2)}}} \exp\left(\frac{-4\ln(2)(x - x_c)^2}{w^2}\right) \quad (3.6)$$

where x_c represents the center of the Gaussian distribution and w the FWHM of the peak. The amplitude of the peak is given by the following equation:

$$Amplitude = y_0 + \frac{A}{w\sqrt{\frac{\pi}{4\ln(2)}}}. \quad (3.7)$$

Figure 3.7 (a) shows the fitting with Gaussian distributions for the sample at 0.7% MR. An artifact due to the equipment also visible in the baseline in Figure 3.7 (b) is observed around 0.88 eV for low doping concentrations. To take this peak into account in the cumulative fit determination, we use a third Gaussian function.

The fitting with Gaussian functions for all samples are given in Figure 3.8 (a) to (h). The peak centered around 860 meV is called peak 1, the artifact peak 2 and the peak centered around 1.1 eV peak 3. The cumulative fit is also given showing good fitting of the absorption spectra in the sub-bandgap regime.

The amplitude, x_c and the FWHM are extracted from the fits and summarized in Table 3.2. From these data we determine the positions of peaks 1 and 3 at $860 \pm 30 \text{ meV}$ and $1.09 \pm 0.05 \text{ meV}$ respectively.

We make the hypothesis that the peaks observed at 860 meV and 1.1 eV originate from the formation of a hybrid charge transfer complex between the polymer HOMO

3.1. Sub-bandgap absorption with p-doping

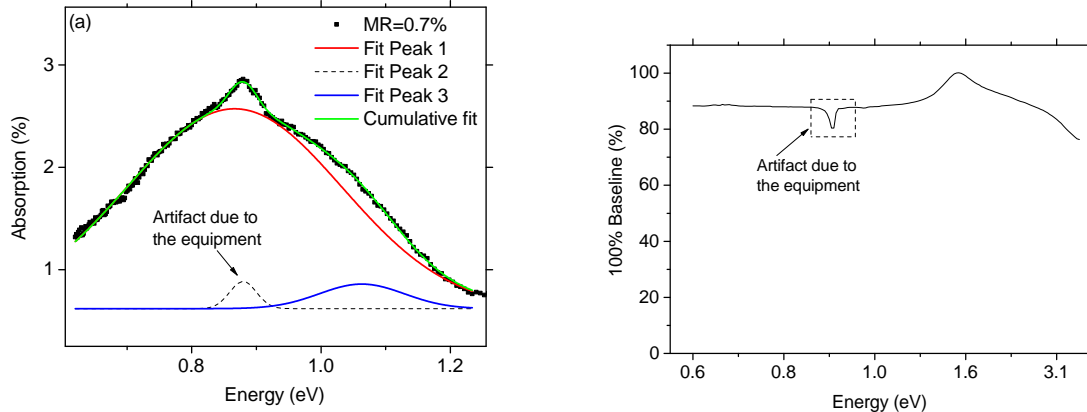


Figure 3.7: Absorption spectrum for MR=0.7% and Gaussian fitting for peaks 1, 2 and 3 (a). 100% baseline spectrum with respect to the photon energy (b).

Table 3.2: Amplitude, position and FWHM extracted from the Gaussian fits for peaks 1 and 3.

MR (%)	Peak 1			Peak 3		
	Amplitude (%)	x_c (meV)	FWHM (meV)	Amplitude (%)	x_c (meV)	FWHM (meV)
0.5	1.86 ± 0.01	832 ± 4	329 ± 8	0.94 ± 0.01	1052 ± 4	180 ± 10
0.7	2.57 ± 0.05	866 ± 4	390 ± 10	0.86 ± 0.06	1063 ± 4	150 ± 20
1	1.24 ± 0.02	883 ± 2	372 ± 5	1.98 ± 0.03	1094 ± 2	171 ± 5
2	13.0 ± 0.2	851 ± 1	388 ± 6	6.7 ± 0.2	1111 ± 3	236 ± 4
3	7.07 ± 0.08	859 ± 1	338 ± 4	11.72 ± 0.08	1104 ± 1	192 ± 2
4	9.63 ± 0.07	863 ± 2	277 ± 4	17.81 ± 0.08	1099 ± 1	202 ± 2
5	20.8 ± 0.1	863 ± 2	230 ± 10	35.9 ± 0.1	1119.6 ± 0.5	181 ± 1
6	21.17 ± 0.09	871 ± 3	170 ± 10	40.2 ± 0.2	1122.2 ± 0.4	191 ± 1

and dopant LUMO. The transition between the bonding and anti-bonding levels of the complex leads to the formation of absorption peaks, which positions are determined by the gap of the complex E_{gap}^{CTC} . We believe that the narrower peak observed at 1.1 eV corresponds to the gap of the complex. Méndez *et al.* explain that the magnitude of the energy-level splitting in the complex is described by a Hückel-like model [92]. The gap of the complex depends on the polymer ionization potential IP_P and dopant electron affinity EA_D but also on the intermolecular electronic coupling described by the resonance integral β [29]:

$$E_{gap}^{CTC} = 2\sqrt{(IP_P - EA_D)^2 + 4\beta^2} \quad [eV]. \quad (3.8)$$

The PBDTTT-c ionization potential has been measured by UPS around 5.15 eV [200] and the Mo(tfd-COCF₃)₃ electron affinity has been estimated at 5.3 eV, but further experiments are required to confirm this value. Taking into account a E_{gap}^{CTC} gap value of 1.1 eV we obtain an intermolecular resonance integral of 0.26 eV. In the case of F₄TCNQ doped 4T, β has been evaluated at 0.42 eV [29]. The intermolecular coupling between Mo(tfd-COCF₃)₃ and PBDTTT-c is then weaker than between F₄TCNQ and 4T and

Chapter 3. Analysis of the doping mechanism involved in $\text{Mo}(\text{tfd-COCF}_3)_3$ doped PBDTTT-c

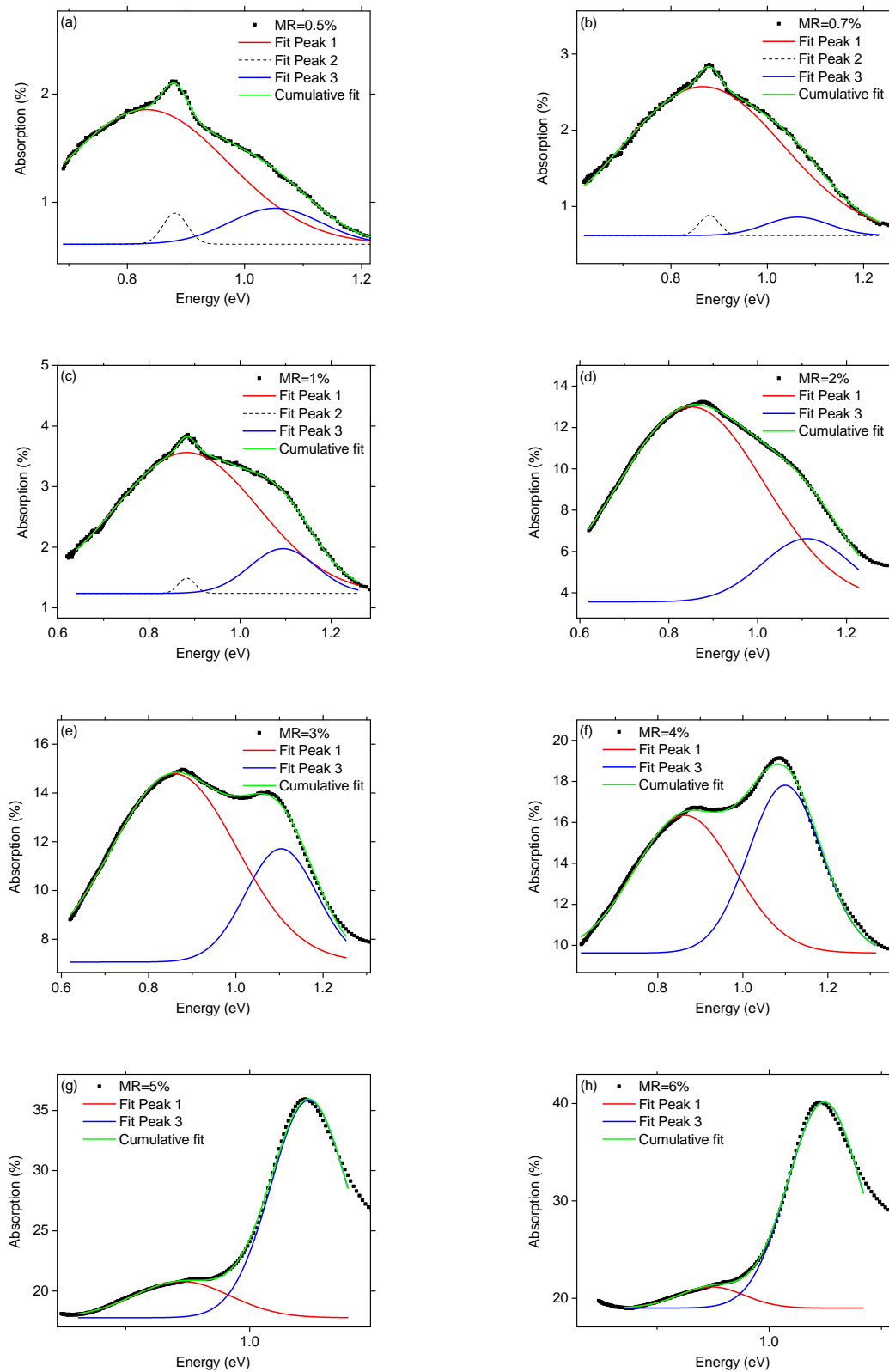


Figure 3.8: Absorption spectra for MR=0.5% (a), 0.7% (b), 1% (c), 2% (d), 3% (e), 4% (f), 5% (g) and 6% (h) with Gaussian fitting for peaks 1, 2 and 3.

3.1. Sub-bandgap absorption with p-doping

should lead to a better doping efficiency as the anti-bonding state is closer to the polymer HOMO enabling improved partial charge transfer.

In a Hückel-like model, the values of the complex bonding E_{gap}^B and anti-bonding E_{gap}^A levels are given by the following relation [74]:

$$E_{gap}^{B/A} = \frac{IP_P + EA_D}{2} \pm \sqrt{(IP_P - EA_D)^2 + 4\beta^2}. \quad (3.9)$$

With an intermolecular resonance integral of 0.26 eV we obtain bonding and anti-bonding levels situated 5.78 eV and 4.68 eV below the vacuum level respectively. The energy levels extracted from the absorption peak centered at 1.1 eV are summarized in Figure 3.9.

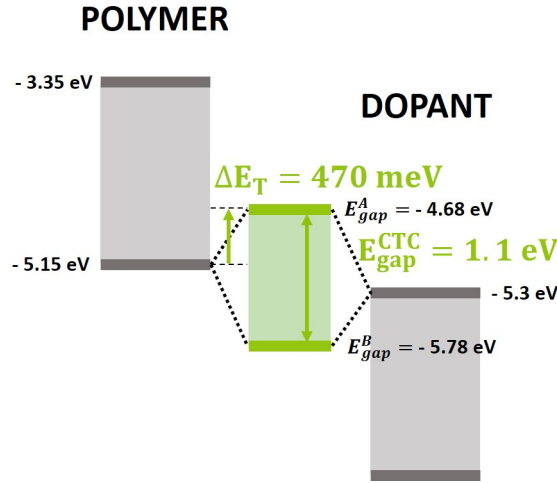


Figure 3.9: Schematic of the hypothetical CTC formed between the PBDTTT-c HOMO and the Mo(tfd-COCF₃)₃ LUMO with the energy levels obtained from the Hückel-like model.

Considering a Hückel-like model to extract the energy levels of the hybrid CTC, an anti-bonding level is identified 470 meV above the polymer HOMO. As a result, the energy required for the electron to reach the acceptor level and p-dope the polymer is high compared to the thermal energy available at ambient temperature (26 meV). Although this high energy requirement is used to justify the partial charge transfer expected with CTC, it seems insufficient to explain the density of ionized dopants measured in Chapter 2 and reaching 10^{18} cm^{-3} . This discrepancy will be further developed in this chapter.

We still need to understand the origin of the peak at 860 meV in the sub-bandgap regime. This peak is not observed in the pure polymer (Figure 3.6). As a consequence, it must be related to the dopant or the formation of the hybrid CTC. At this stage we make the hypothesis that this peak originates from the transition between the bonding level of the complex and a trap level intrinsic to the polymer and situated in the bandgap as illustrated in Figure 3.11. This assumption is strengthened by UV-visible absorption spectroscopy measurements carried out on a previous batch of PBDTTT-c. The absorption spectra of the 2% MR with this previous batch of polymer is shown in Figure 3.10. The peak around 1.1 eV attributed to the CTC is measured but the transition around 860 meV is not observed. As the only difference between this measurement and the previous results lies in the batch of polymer used, we suggest that this peak originates from

an impurity in the polymer leading to a trap state that would be situated 230 meV above the polymer HOMO. Further experiments will be carried out to check this hypothesis.

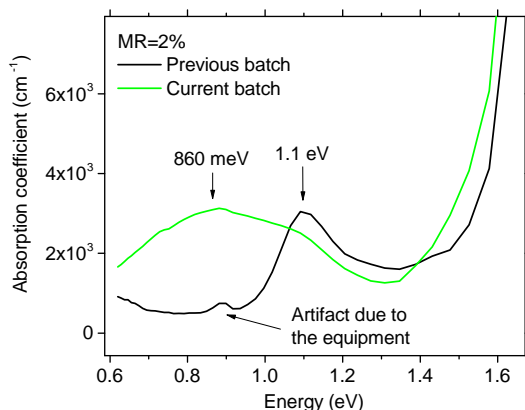


Figure 3.10: Absorption coefficient spectra for two batches of PBDTTT-c doped at 2% MR.

Figure 3.11 summarizes the hypothesis of CTC formation determined from the UV-visible absorption spectroscopy measurements. An energy level lying 230 meV above the polymer HOMO is suggested to explain the peak appearing around 860 meV. Considering a Hückel-like model, the anti-bonding level of the CTC lies 470 meV above the polymer HOMO.

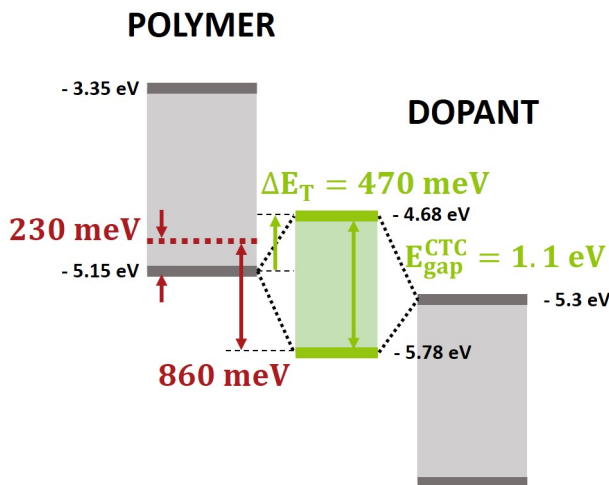


Figure 3.11: Schematic of the hypothetical CTC formed between the PBDTTT-c HOMO and the $\text{Mo}(\text{tfd-COCF}_3)_3$ LUMO with the energy levels obtained from the Hückel-like model and the intrinsic trap level suggested in PBDTTT-c.

The evolution of the peaks amplitude is studied using the fitting parameters given in Table 3.2. The amplitude with respect to the doping concentration is given in Figure 3.12 (a) and (b). Although both peaks increase with doping, their evolution follows a different tendency. By using a semi-logarithmic scale we can see that the peak around 1.1 eV increases with a power law close to 2 in the full range of MR measured. The amplitude of

3.1. Sub-bandgap absorption with p-doping

the peak centered at 860 meV shows two steps in its evolution with an evolution similar to the previous peak for $MR < 2\%$ and a square root dependency at higher concentrations.

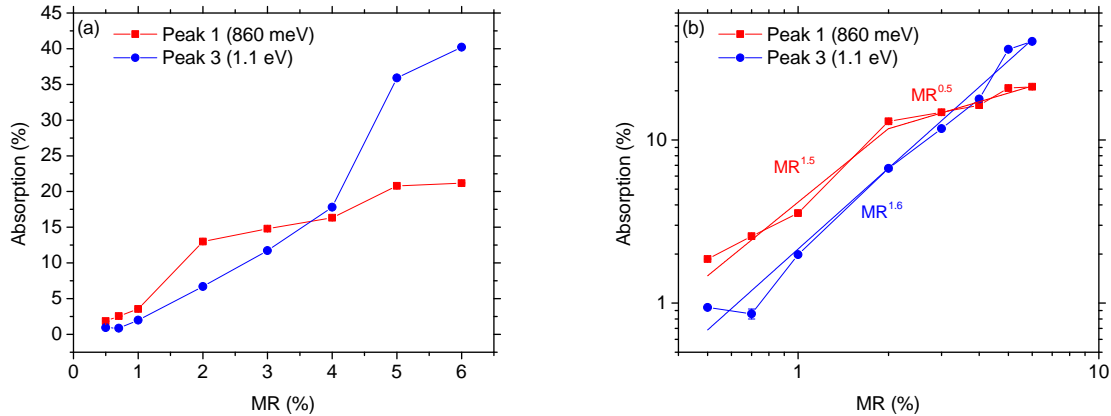


Figure 3.12: Amplitude evolution with doping concentration for peaks 1 and 3 in linear (a) and semi-logarithmic (b) scale.

The amplitude evolution of the peak around 860 meV reminds the conductivity evolution with doping presented in Chapter 2 (Figure 2.7 (a)). The conductivity exhibits a super-linear increase up to 2% MR followed by a decline. As the amplitude saturates at similar concentrations, it is possible that both parameters are linked. If the peak around 860 meV is effectively due to a trap level intrinsic to the polymer, we expect that p-doping fills these states with holes at low concentration. This behavior can explain the super-linear increase of the conductivity. The filling of donor traps induces the transfer of electrons from the donor level to the acceptor level of the dopant as shown in Figure 3.13 (black arrow). As a consequence, the donor level is free of electrons and a transition from the bonding level of the complex to the trap level of the polymer is enabled (red arrow in Figure 3.13). When all traps are filled with holes, the addition of dopants does not increase the absorption further. This hypothesis could explain the amplitude saturation of the peak around 860 meV at high concentration. Moreover, the estimated doping concentration of 2% MR required to reach a total trap filling in the polymer is similar according to conductivity and absorption spectroscopy measurements.

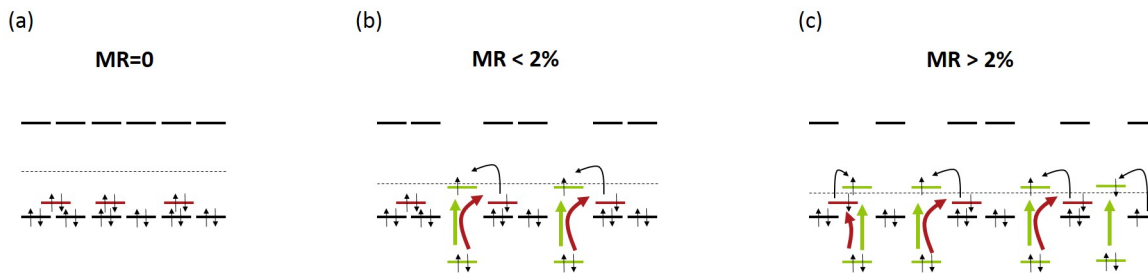


Figure 3.13: Schematic of the PBDTTT-c HOMO, LUMO and Fermi levels with the donor traps suggested 230 meV above the HOMO (a). With doping and for $\text{MR} < 2\%$, the formation of CTC leads to trap filling with holes (black arrow) enabling the optical transition from the bonding state of the CTC to the trap level (red arrow) (b). For $\text{MR} > 2\%$, all traps are filled with holes and the addition of dopants only increases the optical transitions between the bonding and anti-bonding levels of the CTC (green arrow) (c).

UV-visible absorption spectroscopy has been carried out on pure PBDTTT-c and $\text{Mo}(\text{tfd-COCF}_3)_3$ doped PBDTTT-c with 8 different doping concentrations. This study highlighted the formation of two sub-bandgap absorption peaks. Diffusion and ionized dopant have been ruled out as potential origin for these peaks. Polarons in the polymer and the formation of a Charge Transfer Complex between the polymer and the dopant remain to be considered. The hypothesis of a CTC formation between the polymer HOMO and dopant LUMO has been formulated. Considering a Hückel-like model the energy levels of the potential complex have been calculated. However, an estimated value has been taken into account for the dopant electron affinity. Further experiments are required to properly determine the position of the dopant LUMO and validate the assumptions formulated in this chapter. The anti-bonding level would lie 470 meV above the polymer HOMO. An hypothesis has been proposed to explain the second peak involving a trap state intrinsic to the polymer and lying 230 meV above the HOMO. Measurements on a different batch of polymer and the amplitude evolution of the peak strengthen this hypothesis.

3.2 Doping induced fluorescence quenching

In this study we will use static and Time Resolved Photoluminescence (TRPL) measurements to follow the evolution of PBDTTT-c fluorescence with doping concentration to determine what doping mechanisms (ICT or CTC) might be involved in $\text{Mo}(\text{tfd-COCF}_3)_3$ doped PBDTTT-c. If we consider that hole polarons are formed upon dopant addition in the polymer matrix through ICT mechanism, we would expect to observe fluorescence quenching with increasing doping concentration. The absorption of a photon by the polymer leads to the creation of an exciton, which can diffuse over a path of approximately 10 nm [60, 63]. As it was mentioned in Chapter 1, a polaron created by the ionization of the polymer shifts the corresponding HOMO and LUMO in the bandgap. If the exciton reaches a hole polaron, a non-radiative path will be allowed and will compete with the

3.2. Doping induced fluorescence quenching

radiative recombination normally observed in the pure polymer. This quenching mechanism is illustrated in Figure 3.14 (a). Yu *et al.* [201] have observed fluorescence quenching in MEH-PPV due to polarons created by charge injection in the layer.

The formation of a charge transfer complex between the polymer HOMO and dopant LUMO can induce fluorescence quenching as well. We have showed in Chapter 2 that the doping efficiency decreases with increasing doping concentration. As a consequence, we expect a significant amount of anti-bonding states to be empty. The availability of an energy level in the bandgap can lead to fluorescence quenching as described previously. Moreover, the presence of non-radiative complexes contributes to the photoluminescence decrease as some photons are directly absorbed by the complex. Both mechanisms leading to fluorescence quenching in case of CTC are illustrated in Figure 3.14 (b). Tyagi *et al.* [202] have shown that the photoluminescence of Alq₃ is quenched when the dopant F₄TCNQ is added. This observation confirmed their hypothesis of CTC formation formulated according to UV-visible absorption spectroscopy measurements.

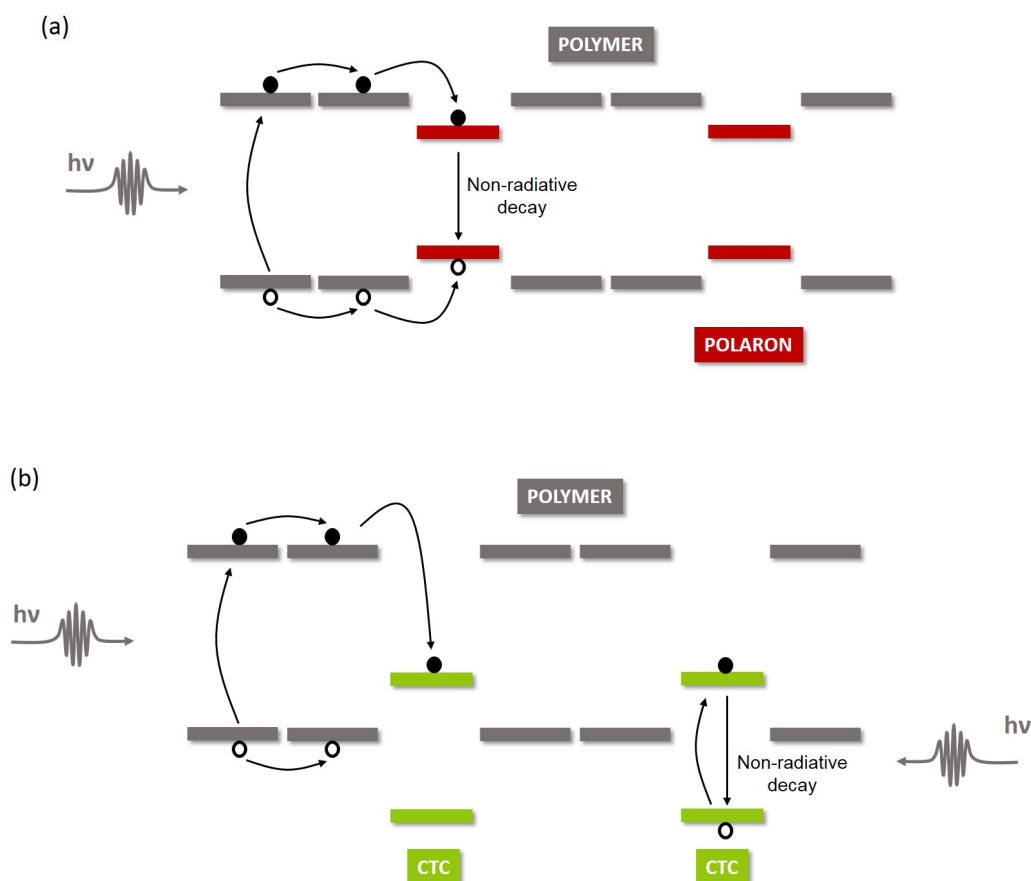


Figure 3.14: Schematic showing the fluorescence quenching due to hole polarons in the polymer matrix (a) and due to the formation of CTC between the polymer and the dopant (b).

3.2.1 Experiment

The same samples have been used for UV-visible absorption and photoluminescence spectroscopy. Photoluminescence measurements have been carried out with a modular Fluorolog FL 3-22 spectrofluorimeter from Horiba-Jobin Yvon-Spex with a near infra-red photomultiplier from Hamamatsu (T5509-73). The schematic of the experimental setup is given in Figure 3.15 showing the light source, the excitation and emission monochromators, the slits, the filter, the IR detector and the position of the sample.

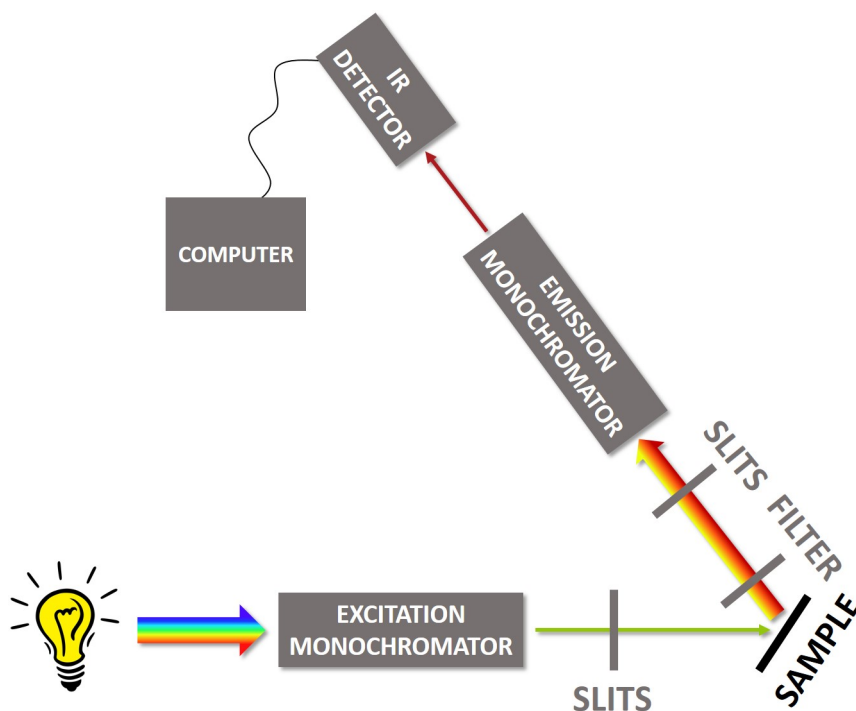


Figure 3.15: Schematic of the experimental setup used for photoluminescence spectroscopy.

The size of the slits and the orientation of the sample have been optimized with the MR=0% sample and kept constant for all measurements. The emission and excitation spectra of PBDTTT-c are shown in Figure 3.16. For excitation wavelengths varying from 367 to 550 nm, the normalized emission spectra are similar with a peak around 810 nm and a shoulder around 890 nm. We chose 810 nm as emission wavelength to perform the excitation spectrum of PBDTTT-c. This measurement shows that a maximum PL intensity will be reached for excitation wavelengths between 350 and 400 nm. Using these preliminary results, the measurement conditions for the emission spectra are set for all samples and presented in Table 3.3.

For excitation and emission spectra measurements a filter needs to be added to the setup between the sample and the emission slits. The filter wavelength is chosen to block the excitation wavelength and its harmonics and allow the emission wavelength range of interest for the measurement. For the emission spectra, an excitation wavelength of 350 nm is chosen and the emission range starts at 415 nm and ends at 1500 nm. A

3.2. Doping induced fluorescence quenching

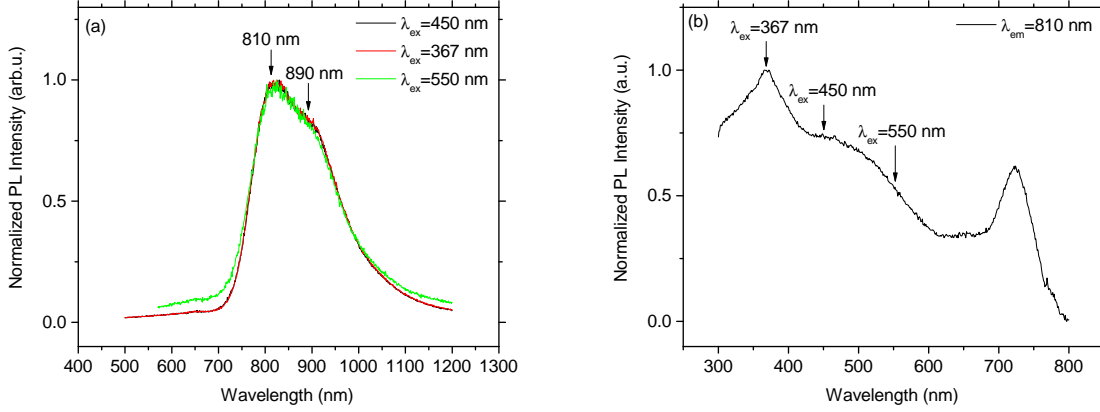


Figure 3.16: PL spectra of PBDTTT-c for different excitation wavelengths (a) and excitation spectrum for $\lambda_{em} = 810 \text{ nm}$ (b).

high-pass filter cutting below 400 nm can be used to block the excitation wavelength and its harmonics without blocking the emission wavelengths measured. For the excitation spectra, the emission wavelength of interest is 810 nm. As the excitation wavelength varies from 275 to 780 nm we need to take into account the wavelength leading to a second harmonic at 810 nm. We chose therefore a high-pass filter cutting below 550 nm, blocking the excitation wavelengths around 405 nm.

Table 3.3: Measurements conditions for emission and excitation spectra on pure and doped PBDTTT-c.

Spectrum	λ_{ex} (nm)	λ_{em} (nm)	Filter (nm)	Slits (mm)	Sample
Emission	350	415-1500	400	5.0/1.5	Front Face 60°
Excitation	275-780	810	550	5.0/3.0	Front Face 60°

Time Resolved Photoluminescence (TRPL) measurements have been carried out to follow the evolution of the polymer excited state lifetime with increasing doping concentration. As the lifetime of pure PBDTTT-c is short (below 1 ns), we had to use a titanium-sapphire laser in pulse mode. The laser emits pulses at a wavelength of 810 nm with a duration of 200 fs. The laser has been set to emit a pulse every microseconds (frequency of 1 MHz). According to the excitation spectrum of pure PBDTTT-c shown in Figure 3.16 (b), TRPL measurements need to be carried out with an excitation wavelength between 350 and 500 nm. Therefore, we use a nonlinear crystal to obtain the second harmonic at 405 nm.

The laser beam with a diameter around $1 \mu\text{m}$ is directed toward the sample and the average power is measured just before the sample. We have noticed that a high power density degrades our samples as the fluorescence signal decreases over time. Therefore, we have optimized the laser average power to obtain sufficient and stable fluorescence signal. The laser average power was set at 65 nW for all samples.

A monochromator is used to select the emission wavelength of interest for the TRPL

study. To optimize the signal-to-noise ratio we have chosen to measure the TRPL signal for an emission wavelength corresponding to the maximum of the peak in the photoluminescence spectra around 810 nm. A silicon avalanche photodiode (APD) with a time resolution of 300 ps is used.

3.2.2 Photoluminescence quenching

Figure 3.17 (a) exhibits the excitation, emission and absorption spectra for pure PBDTTT-c. The excitation spectrum presents a maximum around 350-400 nm and a peak at 700 nm. The wavelength range covered by the excitation spectrum is consistent with the absorption spectrum of the polymer. The emission spectrum is situated in the near infra-red from 700 to 1200 nm with a maximum around 810 nm and a shoulder around 900 nm. The red shift, also called Stokes shift, of the emission spectrum with respect to the excitation spectrum is due to non-radiative vibrational relaxations preceding the radiative transition to the ground state. Figure 3.18 shows the electronic transition from the ground state to an excited state of the molecule upon excitation with a photon. According to Kasha's rule, molecules quickly relax in the lowest excited state through non-radiative vibrational transitions [203]. The fluorescent decay to the ground state is therefore red shifted compared to the incident photon absorbed by the molecule.

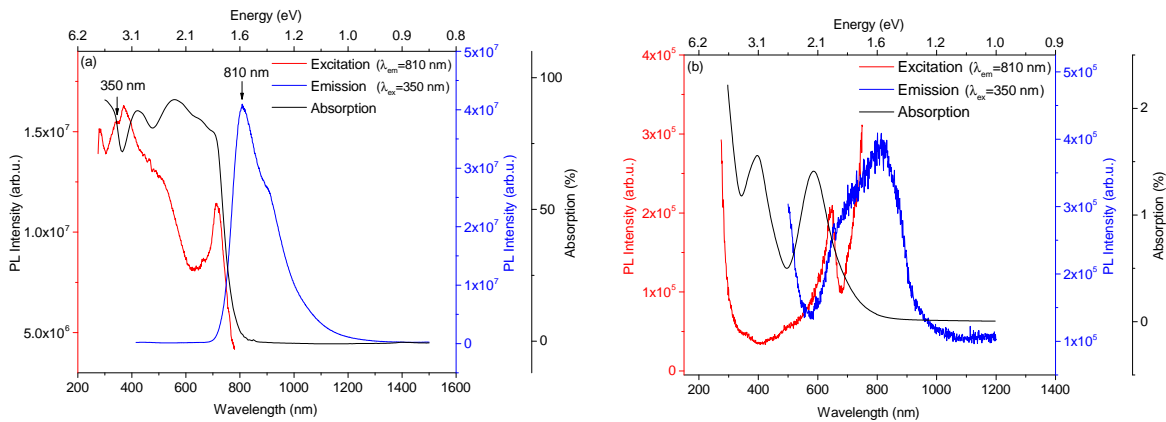


Figure 3.17: Emission, excitation and absorption spectra of pure PBDTTT-c (a) and $\text{Mo}(\text{tfd-COCF}_3)_3$ (b).

The excitation, emission and absorption spectra of the pure dopant $\text{Mo}(\text{tfd-COCF}_3)_3$ are given in Figure 3.17 (b). All spectra have been obtained in solution as solid thin films of dopant were difficult to obtain. The photoluminescence intensity is very low for an excitation wavelength of 350 nm and situated between 600 and 900 nm.

To study the impact of $\text{Mo}(\text{tfd-COCF}_3)_3$ on the PBDTTT-c fluorescence we measure the PL emission spectra for 8 doping concentrations varying from 0.5 to 6%. As the PL intensity is low for an excitation wavelength of 350 nm for $\text{Mo}(\text{tfd-COCF}_3)_3$ we can consider that the PL intensity measured is only due to PBDTTT-c fluorescence. To compare the spectra we took special care to prepare samples with similar thicknesses.

3.2. Doping induced fluorescence quenching

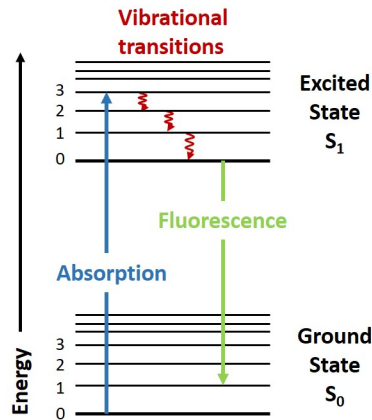


Figure 3.18: Schematic of the radiative and non-radiative transitions between the ground and excited states of the polymer describing the fluorescence red-shift with respect to the excitation.

The thickness of the layers are given in Table 3.1 and the mean thickness is estimated at $390 \text{ nm} \pm 10\%$.

Figure 3.19 (a) shows the PL spectra of pure and doped PBDTTT-c and the PL spectra are magnified to follow the evolution at high doping concentrations (b). The shape of the PBDTTT-c emission spectrum is maintained with doping but the PL intensity is strongly quenched with the addition of dopant. For $\text{MR} > 4\%$ the PL intensity reaches the PL spectrum of the borosilicate substrate. This fluorescence quenching has also been observed for F_4TCNQ doped Tris-(8-hydroxyquinoline)aluminum (Alq_3) and has been attributed to the formation of a complex charge transfer [202]. However, we need to verify whether the formation of polarons is responsible for the fluorescence quenching observed.

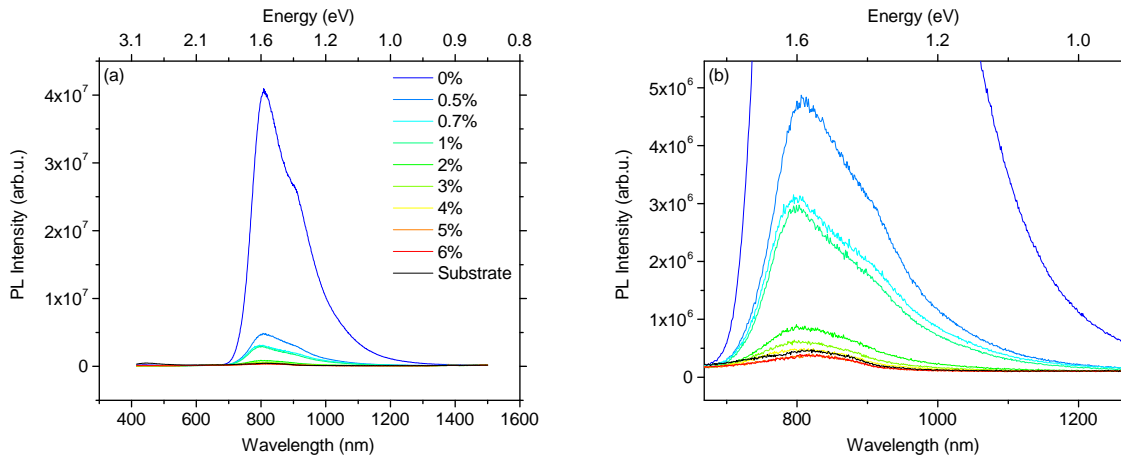


Figure 3.19: PL emission spectra for pure and doped PBDTTT-c and for the borosilicate substrate (a). Magnified view of the PL spectra for doped PBDTTT-c (b).

Fluorescence quenching can be explained by different mechanisms divided into 2 categories: dynamic and static quenching [204]. Dynamic quenching includes various mechanisms like fluorescence resonance energy transfer (FRET) and collisional quenching.

FRET or Förster type energy transfer involves the transfer of the excited state energy from the fluorophore to the quencher as illustrated in Figure 3.20 (a) [205]. The FRET energy transfer is allowed through long-range dipole-dipole interaction. As a consequence, the distance between both molecules plays an important role in the quenching efficiency. Moreover, a spectral overlap is required between the fluorophore emission and quencher absorption to allow the energy transfer. Collisional quenching is due to the non-radiative decay of the excited state fluorophore induced by contact with another molecule called quencher [204]. This process is illustrated in Figure 3.20 (b). Diffusion of the fluorophore or generated exciton toward the quencher is involved in the model. Polarons induced fluorescence quenching as illustrated in Figure 3.14 (a) corresponds to collisional and, therefore, dynamic quenching [201]. Static quenching results from the formation of a ground state charge transfer complex between the fluorophore and the quencher. The part of the incident photons absorbed in the complex leads to non-radiative recombinations as illustrated in Figure 3.20 (c), decreasing the overall photoluminescence signal [204]. Moreover, the presence of a ground-state complex between the fluorophore and the quencher can lead to collisional quenching induced by the exciton diffusion toward the anti-bonding state of the complex. If we can show that the fluorescence quenching of PBDTTT-c with $\text{Mo}(\text{tfd-COCF}_3)_3$ possesses a static component, we will strengthen the hypothesis of CTC formation between both components. If the quenching is purely dynamic, it will strengthen the hypothesis of polarons and, therefore, of ICT.

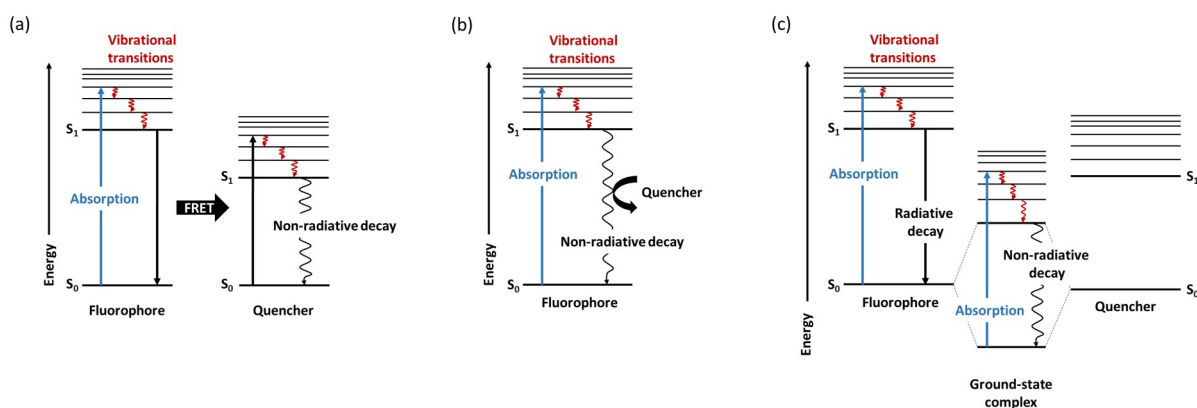


Figure 3.20: Schematic of fluorescence quenching mechanisms: FRET (a), collisional quenching (b) and static quenching (c).

We can determine if the quenching is due to FRET by analyzing the PBDTTT-c emission and $\text{Mo}(\text{tfd-COCF}_3)_3$ absorption spectra shown in Figure 3.21. As mentioned above, fluorescence quenching through energy transfer requires a spectral overlap between the fluorophore emission and the quencher absorption. For $\text{Mo}(\text{tfd-COCF}_3)_3$ doped PBDTTT-c, this spectral overlap is limited. It is therefore unlikely that a FRET mechanism is responsible for the fluorescence quenching observed. Therefore, we need to distinguish between collisional and static quenching.

3.2. Doping induced fluorescence quenching

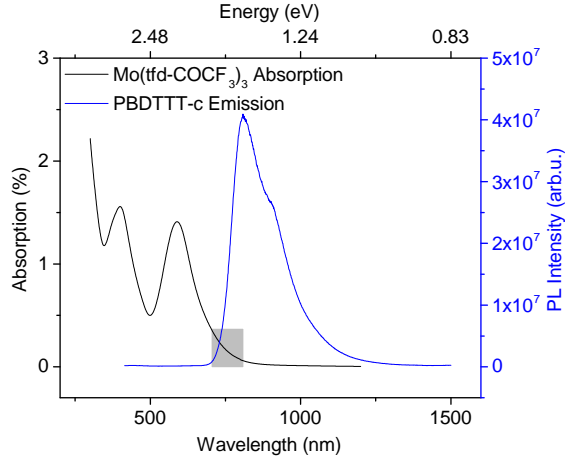


Figure 3.21: Absorption spectrum of $\text{Mo}(\text{tfd-COCF}_3)_3$ and emission spectrum of PBDTTT-c for an excitation wavelength of 350 nm.

3.2.3 Static or Dynamic quenching?

Collisional and static fluorescence quenching are described by the Stern-Volmer equation [204]:

$$\frac{I_0}{I} = 1 + K_{SV}[Q] \quad (3.10)$$

where I_0 and I are the emission intensities in the absence and presence of quencher respectively, K_{SV} is the Stern-Volmer constant and $[Q]$ the molar concentration of quencher. By plotting the ratio I_0/I with respect to the concentration of quencher $[Q]$ we should obtain a straight line for static and dynamic quenching. In the case of dynamic quenching, K_{SV} is the Dynamic constant K_D , which is given by the product of the bimolecular quenching constant k_q and the fluorophore excited state lifetime in the absence of quencher τ_0 :

$$K_D = k_q\tau_0 \quad [\text{mol}^{-1}]. \quad (3.11)$$

For static quenching, K_{SV} is the association constant for complex formation K_S given by the following equation:

$$K_S = \frac{[F - Q]}{[F][Q]} \quad [\text{mol}^{-1}] \quad (3.12)$$

with $[F - Q]$ the complex concentration and $[F]$ the concentration of uncomplexed fluorophore.

To extract properly the emission intensities of pure PBDTTT-c (I_0) and with various concentrations of dopant (I), we fit the spectra with Gaussian distributions. In this analysis we chose to subtract the baseline before fitting as the signal to noise ratio is low at high doping concentration. The Gaussian functions used for the fit and the determination of the amplitude are similar to the one used for the absorption spectra and is given by Relations 3.6 and 3.7. The emission spectra are fitted with two Gaussian functions centered at 1.42 (Peak 1) and 1.55 eV (Peak 2). The position of both peaks has been determined with a free fit for the pure PBDTTT-c sample and kept constant for the doped

polymer spectra. Figure 3.22 exhibits the Gaussian fitting for both peaks for MR=0%. The fits of the spectra for the doped samples are shown in Figure 3.23 (a) to (h).

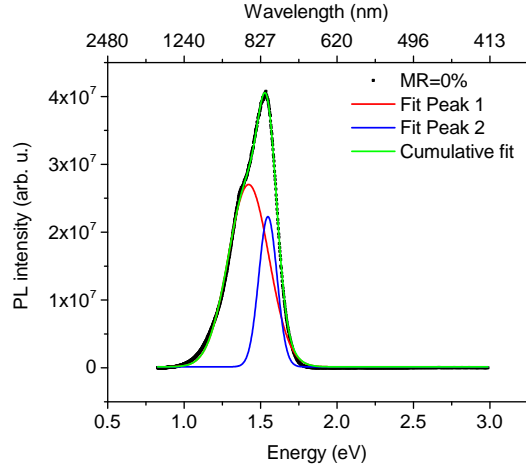


Figure 3.22: Emission spectra of PBDTTT-c and Gaussian fitting.

The area under the curve is determined for the cumulative fit for pure PBDTTT-c (I_0) and for the various doping concentrations (I). Figure 3.24 (a) shows the Stern-Volmer plot with $[Q]$ determined with respect to the concentration of fluorophore $[I_0] = 1$. Although we expect a linear dependence for static or dynamic quenching as suggested by equation 3.10, a positive deviation from the Stern-Volmer plot is observed for doping concentrations above 2%. A positive deviation can be explained by combination of static and dynamic quenching or by a large extent of quenching called sphere of action [204].

When the presence of the quencher involves static and dynamic quenching of the fluorophore, the Stern-Volmer equation is modified as follows [204]:

$$\frac{I_0}{I} = (1 + K_D[Q]) (1 + K_S[Q]) = 1 + (K_D + K_S) [Q] + K_D K_S [Q]^2. \quad (3.13)$$

The dynamic constant K_D is usually determined using TRPL measurements and the constant for complex formation K_S can be deduced from a modified representation of the Stern-Volmer plot. Equation 3.13 can be rewritten as follows:

$$\left(\frac{I_0}{I} - 1\right) / [Q] = (K_D + K_S) + K_D K_S [Q]. \quad (3.14)$$

Therefore, the plot of $(I_0/I - 1) / [Q]$ with respect to the concentration of quencher $[Q]$ leads to a straight line with the slope $K_D K_S$ and the intercept $K_D + K_S$.

Figure 3.24 (b) shows the modified representation of the Stern-Volmer plot, which exhibits a straight line indicating that both dynamic and static mechanisms might be involved in the quenching of PBDTTT-c.

To verify that the quenching contains a dynamic component and determine the dynamic constant K_D , we analyze the evolution of the fluorophore lifetime with doping. The

3.2. Doping induced fluorescence quenching

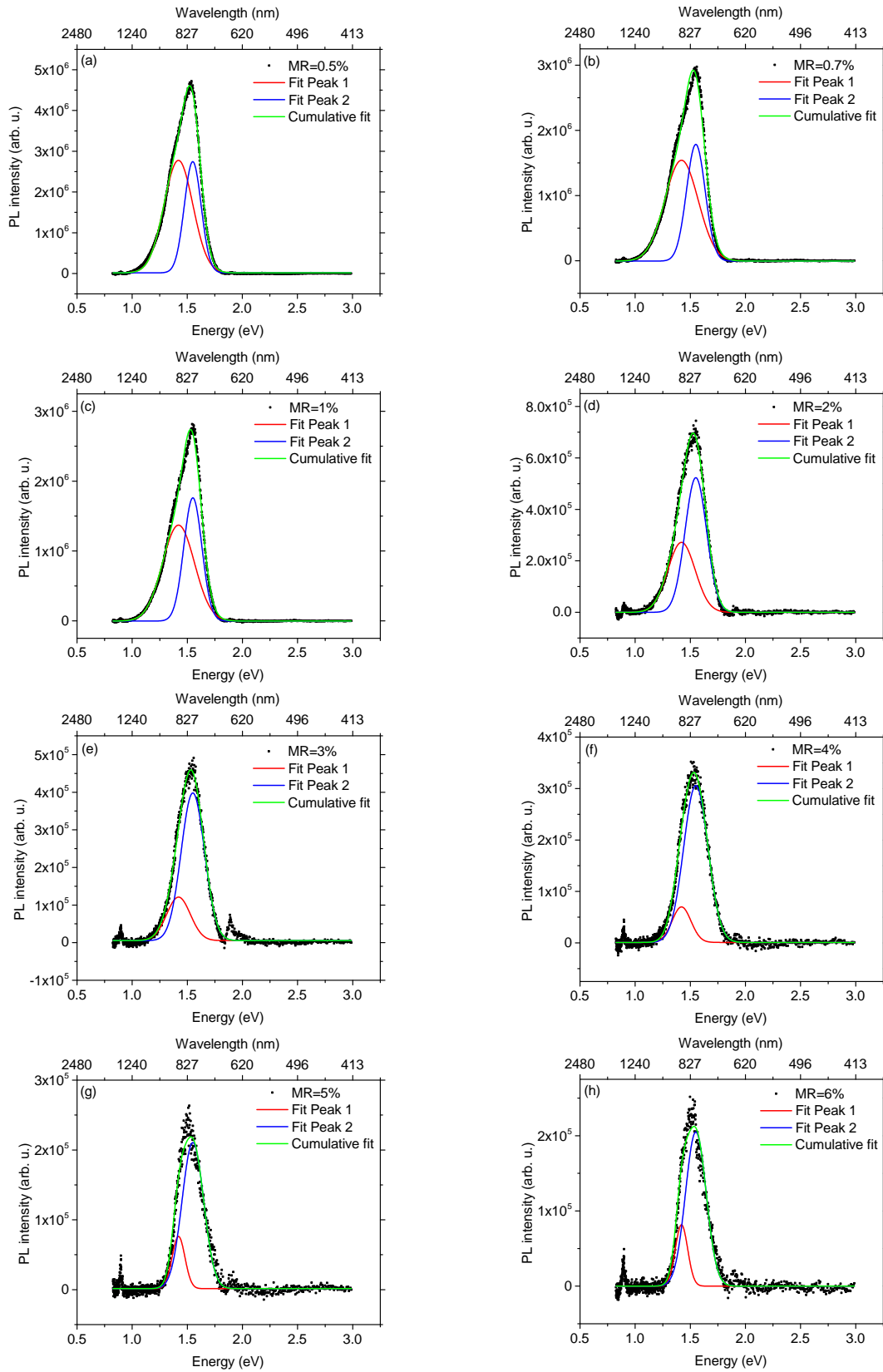


Figure 3.23: Emission spectra of MR=0.5% (a), 0.7% (b), 1% (c), 2% (d), 3% (e), 4% (f), 5% (g) and 6% (h) with Gaussian fitting.

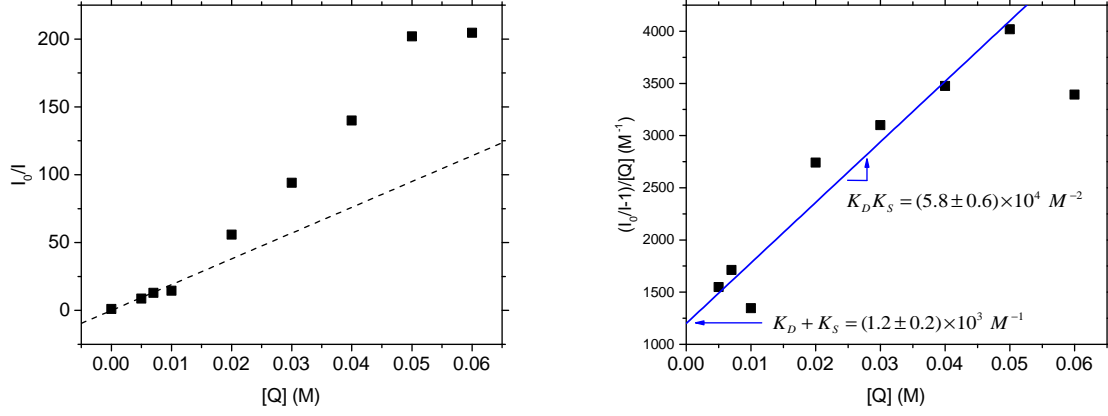


Figure 3.24: Stern-Volmer plot determined with the total area under the curve and linear function (dotted line) (a). Corrected Stern-Volmer plot to separate dynamic and static constants (b).

fluorophore excited state lifetime τ depends on the radiative τ_R and non-radiative τ_{NR} lifetimes as follows:

$$\frac{1}{\tau} = \frac{1}{\tau_R} + \frac{1}{\tau_{NR}}. \quad (3.15)$$

For collisional quenching, the addition of quenchers offers non-radiative pathways to the excited fluorophore decreasing τ_{NR} and, therefore, the fluorophore lifetime τ . In the absence of quencher the fluorophore decay rate γ is given by:

$$\tau_0^{-1} = \gamma. \quad (3.16)$$

Since collisional quenching depopulates the fluorophore excited state, an additional decay rate defined by the bimolecular constant needs to be taken into account:

$$\tau = (\gamma + k_q[Q])^{-1}. \quad (3.17)$$

As a consequence, for collisional quenching the fluorophore excited state lifetime with and without quencher is related to I_0/I as follows:

$$\frac{\tau_0}{\tau} = 1 + k_q\tau_0[Q] = \frac{I_0}{I}. \quad (3.18)$$

Fluorescence quenching due to the formation of non-radiative complex does not affect any of the radiative and non-radiative lifetimes of the fluorophore. Therefore, the observed fluorescence results only from the radiative and non-radiative decay in the uncomplexed fluorophore, which excited state lifetime is given by τ_0 . For static quenching, the ratio τ_0/τ is unity. If we measure the fluorophore excited state lifetime for the pure PBDTTT-c and doped PBDTTT-c with different doping concentration we can distinguish between dynamic and static quenching.

Figure 3.25 shows the TRPL spectra for pure, 0.5%, 1%, 2% and 4% MR doped PBDTTT-c. The 5 and 6% MR doped samples have not been analyzed due to their

3.2. Doping induced fluorescence quenching

low photoluminescence intensity. Moreover, we have noticed in Figure 3.19 that the photoluminescence intensity reaches the one of the substrate for doping concentrations above 4% MR. Therefore, at high concentrations, we are not sure whether we measure the photoluminescence of the polymer or the substrate. To extract the excited state lifetime, we fit the TRPL spectra with a double exponential function as follows:

$$y = y_0 + A_1 \exp(-x/\tau_1) + A_2 \exp(-x/\tau_2). \quad (3.19)$$

As intensity values evolve over several orders of magnitude, we weight the data using standard deviation. We also avoid to fit the tail of the signal where the signal-to-noise ratio is low. The black lines in Figure 3.25 correspond to the double exponential fit and the extracted lifetimes are given in Table 3.4.

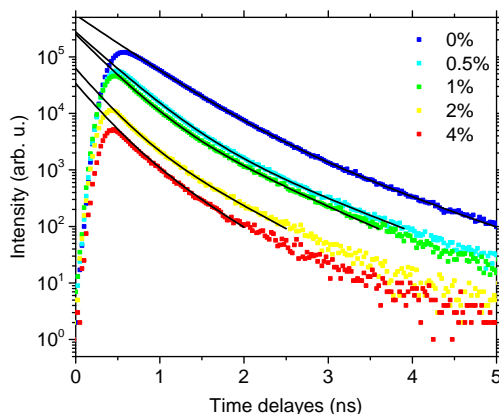


Figure 3.25: TRPL spectra for 0%, 0.5%, 1%, 2% and 4% doped PBDTTT-c and double exponential fit (black lines) in a semi-logarithmic scale.

The extracted values of τ_1 and τ_2 are short (below 1 ns) and close to the time response of the APD (between 300 and 350 ps). The values of τ_1 extracted during the first nanosecond of decay and lower than 350 ps for doped polymer are probably related to the APD response. The lifetime τ_2 corresponds to the excited state in pure and doped PBDTTT-c and needs to be deconvoluted from the APD response. If we consider the APD response time τ_{APD} and the PBDTTT-c excited state lifetime $\tau_{\text{PBDTTT-c}}$ as two independent variables, the measured lifetime τ is given by:

$$\tau^2 = \tau_{\text{APD}}^2 + \tau_{\text{PBDTTT-c}}^2. \quad (3.20)$$

Using this relation, the PBDTTT-c lifetime $\tau_{\text{PBDTTT-c}}$ is extracted for each doping concentration and given in Table 3.4.

The evolution of the polymer lifetime is shown in Figure 3.26 (a). The excited state lifetime of PBDTTT-c decreases linearly from 0% to 2% MR as expected for dynamic quenching. The value obtained at higher doping concentration (4% MR) deviates from the linear law, probably due to the APD response time. If we take into account the linear fit obtained between 0% and 2% MR, we would indeed expect a lifetime around 50 ps at

Table 3.4: Lifetimes extracted from the TRPL spectra fitting with a double exponential.

MR (%)	Extracted τ_1 (ps)	Extracted τ_2 (ps)	Corrected τ_2 (ps)
0	419	850	780 ± 10
0.5	320	750	680 ± 10
1	280	660	570 ± 10
2	240	550	440 ± 20
4	230	480	350 ± 20

4% MR. Since the APD response time is given by the supplier between 300 and 350 ps, it is very likely that the lifetime extracted is mostly due to the equipment.

As suggested by equation 3.18, by plotting τ_0/τ with respect to the concentration of quencher $[Q]$ given in Figure 3.26 (b), we can extract the dynamic constant $K_D = k_q\tau_0$ of $36 \pm 2 M^{-1}$. Considering an excited state lifetime τ_0 of 780 ± 10 ps for the pure polymer, we obtain a bimolecular quenching constant k_q of $(4.6 \pm 0.3) \times 10^{10} M^{-1}s^{-1}$. Bimolecular quenching constants of the order of $10^{10} M^{-1}s^{-1}$ are typical for dynamic quenching due to diffusion [204].

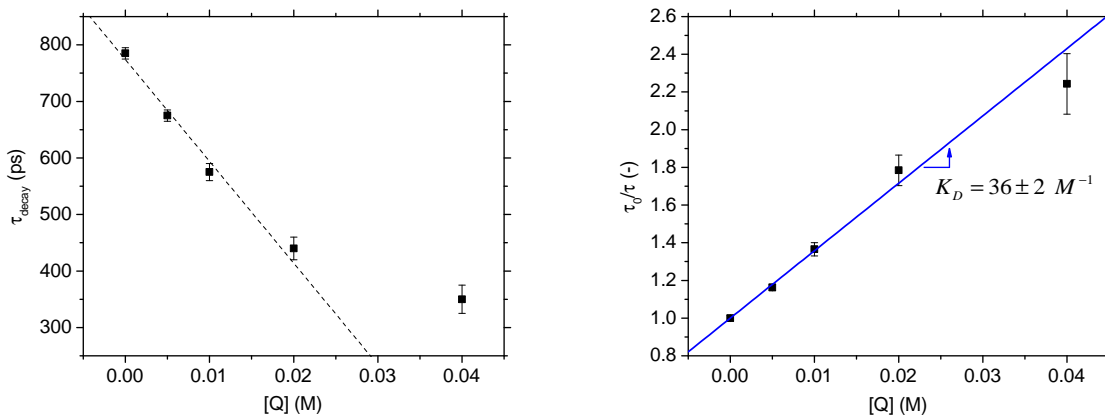


Figure 3.26: Evolution of PBDTTT-c excited state decay time with doping concentration and linear function (dotted line) (a). Plot of τ_0/τ with respect to the doping concentration and extraction of the dynamic constant K_D (b).

The upward curvature of the Stern-Volmer plot suggested a combination of static and dynamic quenching involved in Mo(tfd-COCF₃)₃ doped PBDTTT-c. We verified the presence of dynamic quenching with TRPL measurements and extracted the dynamic constant K_D . Using the modified version of the Stern-Volmer plot, we can determine the constant for complex formation K_S of $(1.4 \pm 0.3) \times 10^3 M^{-1}$. This value is of the same order of magnitude as MEH-PPV complexed with C₆₀ with a constant of $2.5 \times 10^3 M^{-1}$ [206]. However, the constant for complex formation is 2 orders of magnitude higher for Mo(tfd-COCF₃)₃ doped PBDTTT-c than for F₄TCNQ doped Alq₃ with a constant of $13.8 M^{-1}$ [202]. This is consistent with the fact that the electron affinity of F₄TCNQ of 5.2 eV is lower than the ionization potential of Alq₃ determined at 5.7 eV. This result shows that

3.3. Characterization of gap states related to organic semiconductor p-doping

the probability of complex formation between $\text{Mo}(\text{tfd-COCF}_3)_3$ and PBDTTT-c is high.

Using photoluminescence spectroscopy we have shown that the addition of the dopant $\text{Mo}(\text{tfd-COCF}_3)_3$ in PBDTTT-c quenches the polymer fluorescence. FRET has been excluded as potential origin for fluorescence quenching and lifetime measurements have been performed to distinguish collisional and static quenching. With an increasing τ_0/τ ratio, Time Resolved Photoluminescence (TRPL) measurements have shown that dynamic quenching is involved in the photoluminescence quenching with doping. However, the upward curvature obtained in the Stern-Volmer plot indicates a combination of dynamic and static quenching mechanisms. The dynamic constant and constant for complex formation have been extracted and are consistent with the literature. The involvement of both static and collisional quenching strengthens the hypothesis of Charge Transfer Complex formation (CTC).

3.3 Characterization of gap states related to organic semiconductor p-doping

UV-visible absorption spectroscopy and photoluminescence measurements suggest the formation of a charge transfer complex between the polymer HOMO and the dopant LUMO. The anti-bonding level of this complex would lie 470 meV above the HOMO (see Figure 3.11) and might correspond to the doping acceptor state. Moreover, an additional trap level is suspected in the polymer bandgap lying 230 meV above the HOMO. To validate these assumptions we want to probe the existing energy levels in the bandgap and confirm their position. In this study we use admittance spectroscopy to probe the trap levels in pure and doped PBDTTT-c. Molar concentrations of 2% and 5% MR are chosen to cover the trap filling and high doping concentration regimes identified with conductivity measurements in Chapter 2.

3.3.1 Admittance spectroscopy

Different characterization techniques have been developed to probe the energy levels in the bandgap of semiconductors. These techniques include Deep Level Transient Spectroscopy (DLTS), Modulated Photocurrent (MPC), Photoconductivity (PC), Thermally Stimulated Current (TSC) and admittance spectroscopy [207]. It has been reported that DLTS is not suitable for organic semiconductors because of their low mobility and TSC probes only the shallow states (typically below 0.4 eV from the valence or conduction band) [208, 209]. In this study we choose to use admittance spectroscopy to probe the potential trap states in the pure and doped polymer.

The admittance spectroscopy technique consists in analyzing the capacitance C and conductance G with the frequency at different temperatures. To measure the capacitance and conductance, we apply a DC voltage V and an additional AC voltage with a small

amplitude (typically 10 mV) around the DC component and measure the polarization current. The complex admittance of a diode structure is given by the following equation [182]:

$$Y = G(\omega) + i\omega C(\omega), \quad (i^2 = -1) \quad [S] \quad (3.21)$$

with $\omega = 2\pi f$ the angular frequency of the applied bias AC component. Defects in the bandgap will impact both conductance and capacitance due to the response of additional charges to the oscillating signal. This impact is frequency and temperature dependent and enables the extraction of parameters related to the traps.

Figure 3.27 (a) represents the band diagram of a Schottky diode at 0 V with two energy levels in the bandgap E_{T1} and E_{T2} . A band-bending is formed on the Schottky contact to satisfy Poisson's equation. In this configuration, the Fermi level of the semiconductor crosses the trap levels at two different depths in the layer. When a small AC voltage is added to the DC bias, the charges in the trap levels oscillate to follow the position of the Fermi level. The answer of charges to the sinusoidal signal are equivalent to a RC circuit with $R_1 C_1 = \tau_1$ and $R_2 C_2 = \tau_2$. τ_1 and τ_2 are the time constant of the trap levels [210]. Figure 3.27 (b) depicts the equivalent circuit of the Schottky diode with two RC circuits in parallel. The third component C_d corresponds to the space charge.

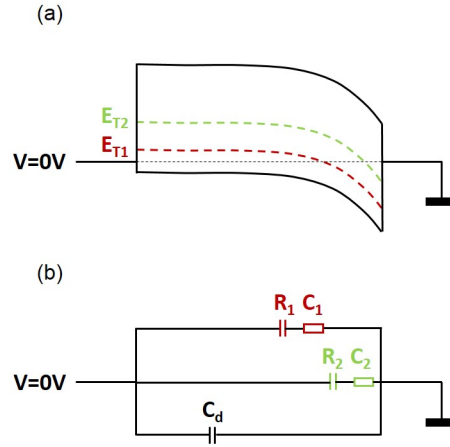


Figure 3.27: Energy level diagram (a) and equivalent circuit (b) of a Schottky diode with two trap levels in the bandgap. C_1 , C_2 , R_1 and R_2 represent the equivalent capacitance and resistance of the trap levels and C_d the capacitance related to the space charge.

The charges response to the AC voltage depends on the frequency of the oscillating signal. At high frequency, the carriers cannot follow the AC signal and do not contribute to the total capacitance. The capacitance of the diode measured at a given frequency and DC bias is given by the following equation [182]:

$$C(\omega) = C_d + C_t(\omega) \quad (3.22)$$

where C_d represents the contribution of the depletion region and is frequency independent and $C_t(\omega)$ corresponds to the charges in the trap levels responding to the AC signal. If we consider a single energy level in the bandgap, the total capacitance can be expressed

3.3. Characterization of gap states related to organic semiconductor p-doping

as follows [211]:

$$C(\omega) = C_{hf} + \frac{1}{1 + \omega^2\tau^2}(C_{lf} - C_{hf}) \quad (3.23)$$

with C_{hf} and C_{lf} the high and low frequency capacitances. At high frequency, the trapped carriers cannot respond to the signal and $C_{hf} = C_d$. As a consequence, $C_{lf} - C_{hf}$ corresponds to the trap contribution and τ drives the dynamics of the energy level. The trap capacitance $C - C_d$ of a Schottky diode with one single trap level in the bandgap will follow a step-like function as shown in Figure 3.28 (a). With increasing temperature, the position of the step shifts toward higher frequencies as temperature facilitates the trapping-detraping process. The position of the step at a given temperature is given by $\omega\tau = 1$. Therefore, by identifying the inflection point of the step-like function we can determine the time constant of the trap $\tau_T = \omega_T^{-1}$.

Considering the similar structure, the evolution of the total conductance can be expressed with respect to the angular frequency:

$$\frac{G - G_0}{\omega} = (C_{lf} - C_{hf}) \frac{\omega\tau}{1 + \omega^2\tau^2} \quad (3.24)$$

where G_0 is the dc conductance. To be as close as possible to the conductance without AC signal, we take the value of the conductance at the lowest frequency measured (20 Hz) for G_0 . A trap level in the bandgap of the semiconductor leads to the formation of a peak centered at ω_T in the conductance spectrum as shown in Figure 3.28 (b). The maximum of the peak corresponds to $C_T/2$ and the peak shifts in frequency with varying temperature following the position of the step in the capacitance spectrum.

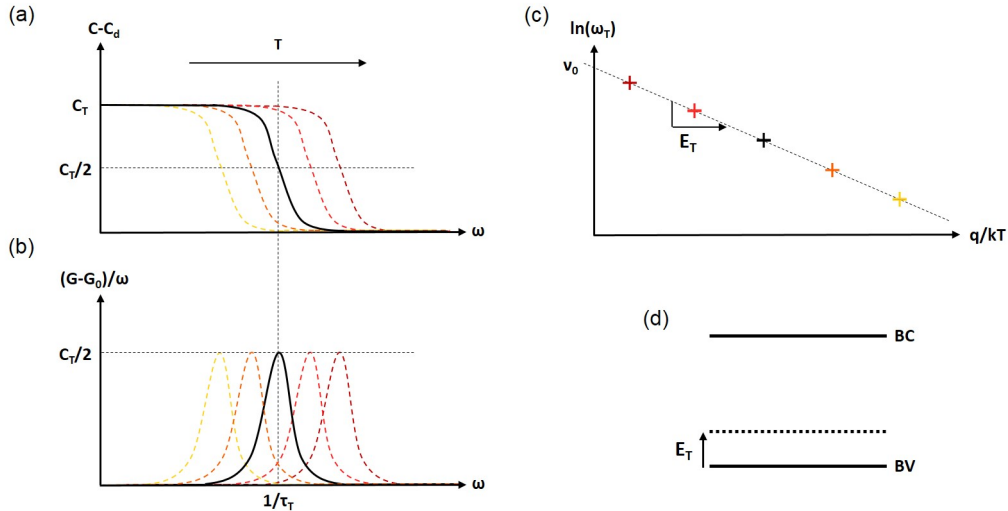


Figure 3.28: Schematic of capacitance $C - C_d$ (a) and conductance $(G - G_0)/\omega$ (b) versus frequency plots at different temperatures for a Schottky diode with a single energy level in the bandgap. Schematic of the Arrhenius plot derived from the temperature dependency of the conductance spectra (c) and band diagram show the position of the trap state from the activation energy extracted (d).

The temperature dependent time constant of the trap τ_T follows an Arrhenius law

[212]:

$$\frac{1}{\tau_T} = p\nu_{th}\sigma_p \exp\left(-\frac{E_T}{k_B T}\right) \quad (3.25)$$

for a p-type semiconductor with p the hole density of states, ν_{th} the thermal velocity, σ_p the capture cross-section for holes and E_T the activation energy of the trap. The prefactor of the Arrhenius law is called attempt-to-escape frequency ν_0 [212]:

$$\nu_0 = p\nu_{th}\sigma_p. \quad (3.26)$$

The attempt-to-escape frequency is related to the dynamics of the trap emission and the maximum rate of the detrapping process. In inorganic semiconductors, the attempt-to-escape frequency is temperature dependent. However, the temperature dependency of the Arrhenius prefactor can usually be neglected with respect to the exponential component [213]. As a result, Equation 3.25 can be simplified to:

$$\frac{1}{\tau_T} = \nu_0 \exp\left(-\frac{E_T}{k_B T}\right). \quad (3.27)$$

The plot of $\ln(\omega_T)$ with respect to $/k_B T$ shown in Figure 3.28 (c) can be fitted with a straight line which slope corresponds to the activation energy of the trap E_T , as illustrated on the band diagram in Figure 3.28 (d). The attempt-to-escape frequency can be extracted from the intercept of the fit with the y-axis.

The extraction of the trap activation energy with admittance spectroscopy measurements is not sufficient to determine whether the trap is situated below the conduction band or above the valence band (Figure 3.29 (a)). The electrode work-functions can help identifying the position of the trap in the bandgap. A defect in the semiconductor bandgap is probed by admittance spectroscopy when the trap level is crossed by the Fermi level at equilibrium or the quasi-Fermi levels when a bias is applied to the diode. In a diode structure, the quasi-Fermi levels are necessarily situated between the cathode and the anode work-functions. As a consequence, states below the anode and above the cathode cannot be probed by this technique [207]. Depending on the energy level extracted, the position of the trap level can be distinguished by considering the electrode work-functions as shown in Figure 3.29 (b).

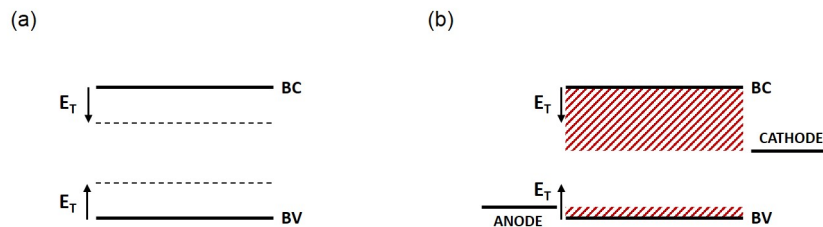


Figure 3.29: Band diagram of the semiconductor showing the two potential position of the trap level determined by admittance spectroscopy (a). Band diagram of the Schottky diode used, showing the bandgap areas which cannot be probed by admittance spectroscopy (hatched area) (b).

3.3. Characterization of gap states related to organic semiconductor p-doping

Using admittance spectroscopy, the activation energy and the time constant of traps in semiconductor bandgaps can be extracted. The position of the energy level with respect to the conduction or the valence band can be determined depending on the electrode work-functions. However, complementary analyses like Mott-Schottky measurements need to be carried out to distinguish between donor and acceptor states.

We will use this characterization technique to probe potential trap state in pure and doped polymer and compare the energy levels with the anti-bonding state calculated previously and suggested by UV-visible spectroscopy.

3.3.2 Samples and experimental set-up

As we want to probe trap states above the polymer HOMO for pure and doped PBDTTT-c, we need to fabricate hole-only devices with one ohmic contact for holes and one Schottky contact to create a depletion zone in reverse bias regime. We can therefore use the Schottky diodes described in Chapter 2 for hole concentration extraction through Mott-Schottky analysis and called Structure 2 in Appendix A. The structure of this diode is shown in Figure 3.30 and the experimental description can be found in Section 2.3.1. Devices with pure PBDTTT-c and p-doped PBDTTT-c with 2 and 5% MR are studied in this section.

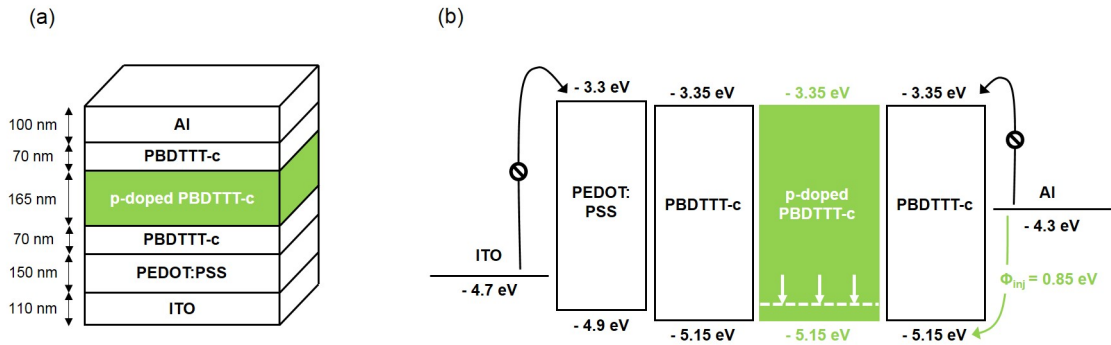


Figure 3.30: Structure (a) and band diagram (b) of the Schottky diode processed for admittance spectroscopy measurements (Structure 2).

For admittance spectroscopy analysis, we need to carry out capacitance measurements at variable temperatures from 100 to 350 K. The measurements have been performed in a vacuum chamber with a chuck cooled down to 77 K with liquid nitrogen. The chuck is then heated to the required temperature. An impedance analyzer Keysight E4990A is used for the capacitance measurements. The complete setup is shown in Figure 3.31. For this study, $C(f)$ and $G(f)$ characteristics have been carried out from 20 Hz to 10 MHz with an AC signal amplitude of 10 mV and a bias of 0 V.

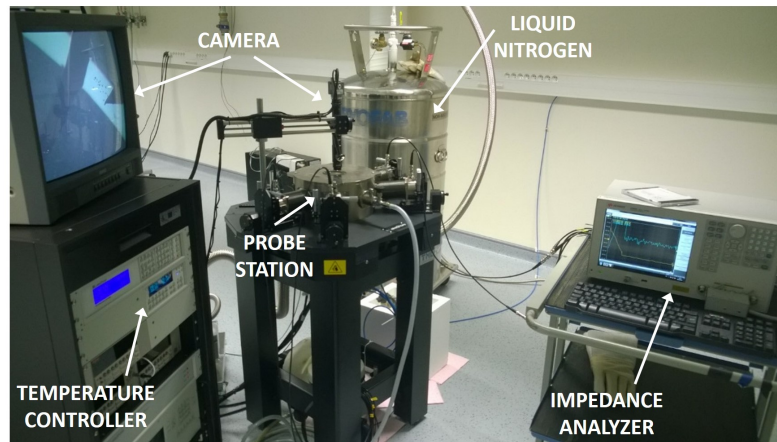


Figure 3.31: Admittance spectroscopy setup with the liquid nitrogen and temperature controller for variable temperature measurements, the camera, the probe station and the impedance analyzer.

3.3.3 Trap states formation with p-doping

Figure 3.32 (a), (c) and (e) exhibits the capacitance spectra with varying temperature for 0%, 2% and 5% MR. While two steps can be observed for the doped samples with transition frequencies increasing with temperature, the pure sample shows only a slight capacitance increase at low frequency for temperatures above 260 K. The conductance spectra are shown in Figure 3.32 (b), (d) and (f) highlighting the formation of two peaks with doping associated with two trap states in the bandgap.

The position of the peaks (ω_T) with temperature needs to be extracted to derive the activation energy of the trap. The Arrhenius plots of $\ln(\omega_T)$ with respect to $q/k_B T$ are shown in Figure 3.33. Linear fittings are used to extract the activation energies and attempt-to-escape frequencies of the traps for the 0%, 2% and 5% MR samples.

For the pure polymer, the peak is visible only for temperatures above 300 K. To obtain a fit of the Arrhenius plot we measured the conductance spectra up to 350 K in steps of 10 K. The data suggest a trap with an activation energy around 200 meV. However, precautions need to be taken on this value regarding the low conductance signal. As shown in Figure 3.29, the electrode work-functions can help us determine whether the activation energy is given with respect to the HOMO or LUMO levels. In the device studied, the anode and cathode work-functions are 4.9 and 4.3 eV respectively (as shown in Figure 3.30). As a consequence, potential traps situated less than 150 meV above the HOMO or 1.05 eV below the LUMO cannot be probed by admittance spectroscopy. The trap probed with an activation energy of 200 meV is therefore situated above the PBDTTT-c HOMO as illustrated in Figure 3.35 (a).

When the polymer PBDTTT-c is doped with the dopant $\text{Mo}(\text{tfd-COCF}_3)_3$ at a concentration of 2% MR, two peaks can be observed in the conductance spectra. In order to properly determine the position of both peaks with temperature, the spectra are fitted with two Gaussian functions as shown in Figure 3.34 at 280 K. The position of the peak

3.3. Characterization of gap states related to organic semiconductor p-doping

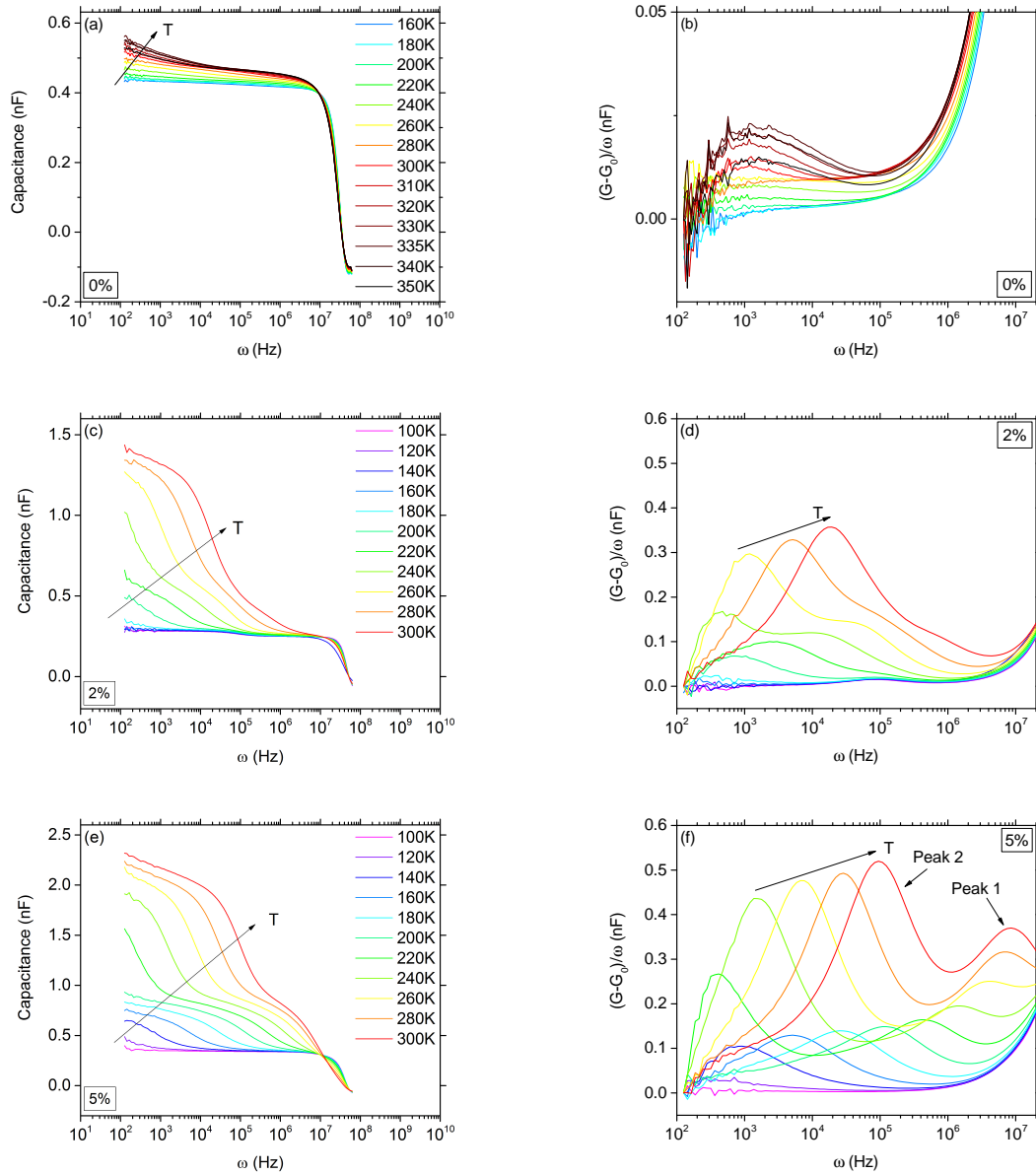


Figure 3.32: Capacitance (a), (c) and (e) and $(G - G_0)/\omega$ (b), (d), (f) vs angular frequency ω as a function of temperature at 0 V for MR=0%, 2% and 5% respectively.

Chapter 3. Analysis of the doping mechanism involved in $\text{Mo}(\text{tfd-COCF}_3)_3$ doped PBDTTT-c

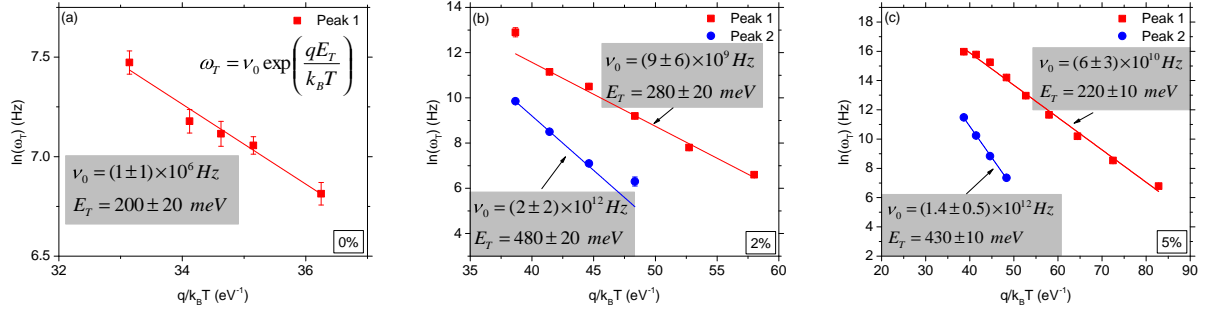


Figure 3.33: Arrhenius plot derived from the admittance spectroscopy measurements on the samples with doping concentrations of 0% (a), 2% (b) and 5% MR (c). The activation energies and attempt-to-escape frequencies are extracted with a linear fit.

with lower intensity, called peak 1, is shown in red in Figure 3.33 (b) and the peak with higher intensity, peak 2, in blue. Two activation energies can be extracted at 280 ± 20 and 480 ± 20 meV. According to the electrode work-functions, both peaks are situated above the HOMO. Figure 3.35 (b) shows the position of the trap levels extracted for this sample. The level obtained for the pure polymer around 280 meV above the HOMO is also observed with doping. Moreover, an additional trap state can be identified deeper in the bandgap when PBDTTT-c is doped with $\text{Mo}(\text{tfd-COCF}_3)_3$.

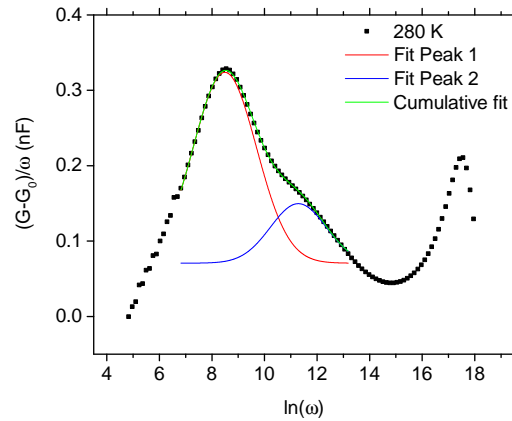


Figure 3.34: $(G - G_0)/\omega$ vs angular frequency ω at 280 K for the 2% MR sample and Gaussian fitting for peaks 1 and 2.

Increasing the doping concentration from 2% to 5% MR does not lead to major changes in the trap position. The trap attributed to the polymer is extracted at 220 ± 10 meV above the HOMO and the energy level associated with the addition of dopant is obtained at 430 ± 10 meV above the HOMO for the 5% MR sample. Figure 3.35 summarizes the energy levels probed by admittance spectroscopy in the three samples studied.

3.3. Characterization of gap states related to organic semiconductor p-doping

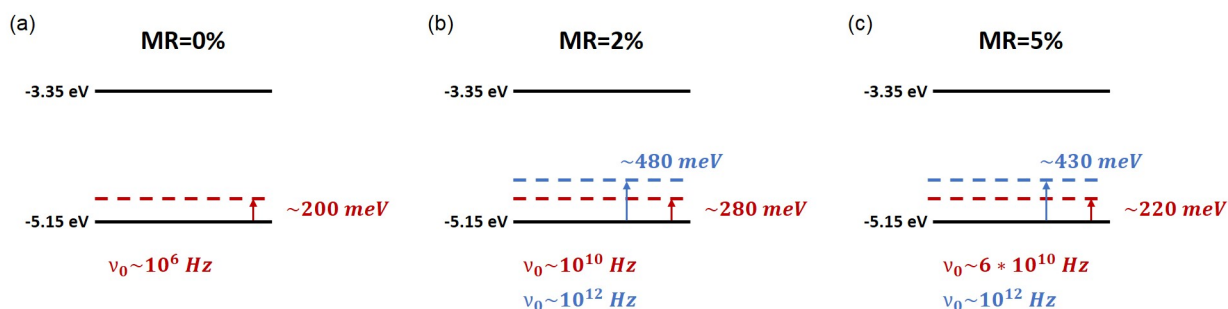


Figure 3.35: PBDTTT-c band diagram showing the energy levels probed by admittance spectroscopy and their attempt-to-escape frequency for the MR=0% (a), 2% (b) and 5% (c).

Admittance spectroscopy measurements have been carried out on pure and Mo(tfd-COCF₃)₃ doped PBDTTT-c to probe potential trap states in the polymer bandgap. One trap state is identified in the pure polymer approximately 200-280 meV above the HOMO. This energy level is intrinsic to the polymer and is also probed in the doped samples. With doping an additional trap state is identified 430-480 meV above the HOMO. Both energy levels probed by admittance spectroscopy are consistent with the hypothesis of Charge Transfer Complex formation suggested from UV-visible absorption spectroscopy results if we consider a dopant electron affinity of 5.3 eV and summarized in Figure 3.36. The trap closer to the HOMO probed in the pure and doped polymer would correspond to the trap state intrinsic to the polymer suggested to explain the peak at 860 meV in UV-visible absorption spectroscopy measurements. The second trap state probed deeper in the bandgap is consistent with the hypothesis of an anti-bonding level situated approximately 470 meV above the polymer HOMO.

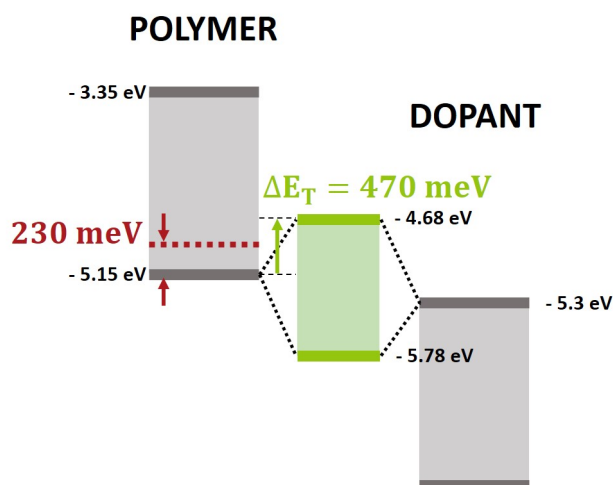


Figure 3.36: Schematic of the hypothetical CTC formed between the PBDTTT-c HOMO and the Mo(tfd-COCF₃)₃ LUMO with the energy levels of the anti-bonding and trap levels according to UV-visible absorption spectroscopy measurements.

Figure 3.35 also summarizes the attempt-to-escape frequencies extracted for both peaks for each doping concentration. We can notice that, for the trap intrinsic to the polymer, the attempt-to-escape frequency increases by several orders of magnitude with doping. This might be due to the hole density increase in the polymer. Equation 3.26 shows that the attempt-to-escape frequency for holes depends on the hole concentration p , the thermal velocity ν_{th} and the capture cross-section for holes σ_p . The thermal velocity and the capture cross-section are independent of the doping concentration. However, p is directly related to the quantity of molecular dopants added to the polymer, as shown by the hole density p increase with doping presented in Chapter 2. As a consequence, the attempt-to-escape frequency increases for both traps with the concentration of holes available in the HOMO.

In the following section we will determine the trap density and their Density of States (DOS). The evolution of the trap density with doping will be analyzed and compared with the hole density.

3.3.4 Trap concentration and Density of States

Two methods can be used to extract the trap concentration N_T for each trap probed in the bandgap. The density of traps can be obtained from the capacitance C_T extracted from the peak amplitude in the conductance spectra [212]:

$$N_T = \frac{4k_B T C_T}{e^2 A \Delta w} \quad [cm^{-3}] \quad (3.28)$$

with A the area of the device and Δw the depletion thickness variation induced by the oscillating signal. Δw can be extracted from the C(V) measurements of the device at a given bias and temperature. A frequency of 100 Hz is chosen for the C(V) measurements to ensure the response of traps to the sinusoidal voltage. The capacitance of the device is related to the depletion thickness w as follows:

$$C = \frac{\epsilon_0 \epsilon_r A}{w} \quad [F]. \quad (3.29)$$

At a given bias V and an AC signal amplitude dV , the depletion thickness variation Δw is obtained from the difference between the depletion thickness at $V + dV$ and $V - dV$. The permittivity ϵ_r of PBDTTT-c has been determined from the geometric capacitance C_{geo} in Chapter 2 at 2.8 ± 0.1 .

Table 3.5 summarizes C_T , Δw and the trap concentrations for both peaks calculated at 0 V. The trap concentrations are compared with the hole concentration p extracted in Chapter 2.

We can observe that the concentration of the traps situated 430-480 meV above the HOMO increases by a factor 2.5 between the 2% and 5% MR samples. This evolution is consistent with the molecular doping concentration evolution. However, we also notice a strong evolution of the trap density corresponding to the level 200-280 meV above the HOMO, which has been attributed to the polymer. If this trap is intrinsic to PBDTTT-c,

3.3. Characterization of gap states related to organic semiconductor p-doping

its density shouldn't be influenced by the addition of dopants. This behavior can be explained by the amount of available carriers in the HOMO. To obtain a signal of the trap in the conductance spectra, charges need to be trapped and detrapped in the defect following the oscillating signal. If the amount of free carriers in the HOMO available for trapping/detrapping process is limited, the resulting capacitance will be lower. In the pure polymer, the doping concentration is very low ($\leq (5 \pm 0.1) \times 10^{15}$) limiting the fraction of traps probed by admittance spectroscopy. By doping the polymer, the number of carriers increases leading to a more complete probing of the defects. As the trap concentration continues to increase between 2% and 5% MR we cannot conclude whether we reached the total concentration of this trap state. It is therefore unclear whether the concentration extracted by admittance spectroscopy for the trap level attributed to the addition of dopant corresponds to the real amount of trap states.

Table 3.5: Trap concentration extraction from Equation 3.28 with the capacitance of the peak in conductance spectra C_T and the depletion thickness variation Δw . The hole density p extracted in Chapter 2 are also indicated.

MR (%)	Δw (nm)	N_T Peak 1 (cm^{-3})	N_T Peak 2 (cm^{-3})	p (cm^{-3})
0	1.4	$(1.4 \pm 0.1) \times 10^{16}$		$\leq (5.4 \pm 0.7) \times 10^{15}$
2	0.6	$(5.28 \pm 0.08) \times 10^{16}$	$(1.6 \pm 0.1) \times 10^{17}$	$(2.8 \pm 0.4) \times 10^{18}$
5	0.34	$(2.9 \pm 0.2) \times 10^{17}$	$(4.0 \pm 0.3) \times 10^{17}$	$(4 \pm 1) \times 10^{18}$

By using the capacitance measurements, it is also possible to extract the trap Density of States (DOS) profile. According to Khelifi *et al.* [182], the density of trap states D_t at an energy E_ω above the valence band is given by the following relation:

$$D_t(E_\omega) = -\frac{V_{bi}}{AW} \frac{dC}{d\omega} \frac{\omega}{k_B T} \quad [cm^{-3}eV^{-1}] \quad (3.30)$$

where E_ω is defined as follows:

$$E_\omega = k_B T \ln \left(\frac{2\nu_0}{\omega} \right) \quad [eV]. \quad (3.31)$$

In Equation 3.30, the attempt-to-escape frequency ν_0 is taken from the Arrhenius fit shown in Figure 3.33 and V_{bi} corresponds to the built-in voltage of the device. The Mott-Schottky analysis can be used to extract V_{bi} for a homogeneous doping profile. This condition is only satisfied for the pure sample. However, Krichartz *et al.* have shown that the V_{bi} extraction using Mott-Schottky analysis is not accurate at low doping concentration [184]. As a consequence we choose to use the theoretical built-in voltage defined by the difference between the electrode work-functions. Considering PEDOT:PSS and aluminum work-functions of 4.9 and 4.3 eV respectively, a built-in voltage of 0.6 V is taken into account.

For this analysis we should only consider the depletion thickness where the traps are probed by this technique. When a doped layer is surrounded by two pure layers of polymer, the increased capacitance induced by traps is mainly due to the defects in the doped layer where a sufficient amount of free carriers are available. Therefore, we need to determine the depletion width in the doped layer W_d .

As a first step we determine the depletion width W_p in the pure layer situated between the aluminum electrode and the doped layer. Considering a homogeneous doping in this layer, W_p is calculated using the following relation:

$$W_p = \sqrt{\frac{2\epsilon_0\epsilon_r}{qp}(V_{bi} - V)}. \quad (3.32)$$

With a hole concentration p of $(5.0 \pm 0.1) \times 10^{15} \text{ cm}^{-3}$ in the pure polymer and a built-in voltage estimated at 0.6 V, a depletion width of $190 \pm 20 \text{ nm}$ is obtained at 0 V. As the pure layer is thinner than the depletion width calculated, a part of the built-in potential is absorbed by the doped layer forming a depletion region W_d , which will be used in the determination of the DOS profile. To calculate W_d , we first need to determine the depletion width that has not been absorbed in the pure layer ΔW :

$$\Delta W = W_p - t_{pure} \quad (3.33)$$

with t_{pure} the thickness of the pure layer measured at $70 \pm 10 \text{ nm}$. We obtain a difference ΔW of $120 \pm 20 \text{ nm}$. Using Relation 3.32 we can now determine the voltage drop $V_{bi} - V$ that has not been absorbed in the pure layer of polymer:

$$V_{bi} - V = \frac{\Delta W^2 qp}{2\epsilon_0\epsilon_r}. \quad (3.34)$$

We obtain a voltage drop of $0.23 \pm 0.08 \text{ V}$. As a last step, the depletion thickness in the doped layer W_d can be calculated using Equation 3.32 with the voltage drop ($V_{bi} - V$) calculated previously and the hole density p in the doped layer. For the 2% and 5% MR samples we obtain depletion widths W_d of $6 \pm 1 \text{ nm}$ and $4.5 \pm 0.8 \text{ nm}$ respectively. Using those depletion widths we can reconstruct the DOS profile for each trap in the bandgap. For the sample with pure polymer, the depletion width is W_p ($190 \pm 20 \text{ nm}$).

Figure 3.37 exhibits the DOS profiles for the pure polymer and the doped polymer at 2% and 5% MR. Although the uncertainty is significant with this technique, we can identify gaussian-like profiles for both trap states measured by admittance spectroscopy. The Gaussian distribution for peak 2 is consistent with the sub-bandgap absorption peak attributed to the charge transfer complex formation. By fitting the peak density D_t with Gaussian functions, we can determine the total trap density N_T , the center of the DOS with respect to the HOMO E_T and the FWHM of the peak [182]:

$$D_t = \frac{N_T}{\sqrt{2\pi}\delta} \exp\left[-\frac{(E_T - E_\omega)^2}{2\delta^2}\right] \quad (3.35)$$

where δ is the energy dispersion related to the FWHM of the DOS and E_ω the position in the bandgap with respect to the HOMO level.

Except for the pure sample, the total trap concentrations N_T are of the same order of magnitude for both extraction techniques (from C_T and from the DOS). However, regarding the significant density uncertainty obtained through the DOS calculation, we prefer to consider the values given in Table 3.5. The position of the Gaussian distributions are indeed directly influenced by the attempt-to-escape frequency extracted with the linear fit on the Arrhenius plot. Uncertainties on this value can lead to shifts of the peak position.

3.3. Characterization of gap states related to organic semiconductor p-doping

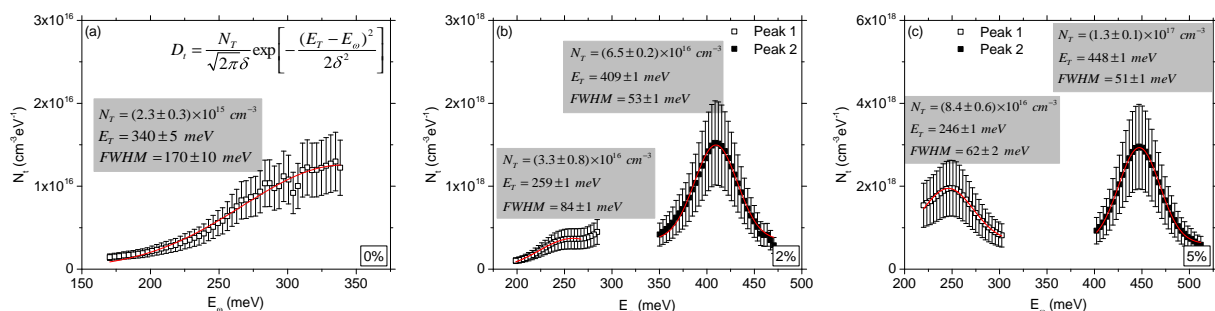


Figure 3.37: DOS profiles at 300 K for MR=0% (a), 2% (b) and 5% (c). The fitting parameters are indicated.

The trap densities have been extracted using the capacitance amplitude of the peaks in the conductance spectra. We have shown that the density of the energy levels attributed to the addition of dopant increases by a factor 2.5 between 2% and 5% MR, consistent with the doping evolution. However, it is unclear whether the total amount of defects has been probed with this technique as the trap response is limited by the free carriers available in the polymer HOMO. This limitation can explain the strong evolution with doping of the trap density associated with the defect intrinsic to the polymer. Finally, the DOS profile has been reconstructed for all samples highlighting the gaussian-like distribution of both traps. This observation is consistent with the Gaussian profiles obtained for the sub-bandgap peaks in the UV-visible absorption spectra.

3.3.5 From UV-visible absorption spectroscopy to admittance spectroscopy

Figures 3.38 (a) and (b) summarize the main results of the admittance spectroscopy study on pure and $\text{Mo}(\text{tfd-COCF}_3)_3$ doped PBDTTT-c. A trap level situated approximately 200 meV above the polymer HOMO has been probed for the pure sample. This trap is also measured in the doped samples with activation energies varying between 220 and 280 meV depending on the doping concentration. The addition of dopant leads to the formation of an additional energy level in the bandgap situated around 430-480 meV above the polymer HOMO. The density evolution of this trap is proportional to the doping concentration evolution.

We can consider that the trap 200-280 meV above the HOMO is intrinsic to the polymer. In case of CTC formation, the absorption peak at 860 meV (section 3.1) would be consistent with electron emission from the bonding state of the complex to this trap. The schematic related to this hypothesis is reminded in Figure 3.38 (c).

The trap probed 430-480 meV above the polymer HOMO is attributed to the addition of dopant. The position of this energy level is consistent with the anti-bonding state of the

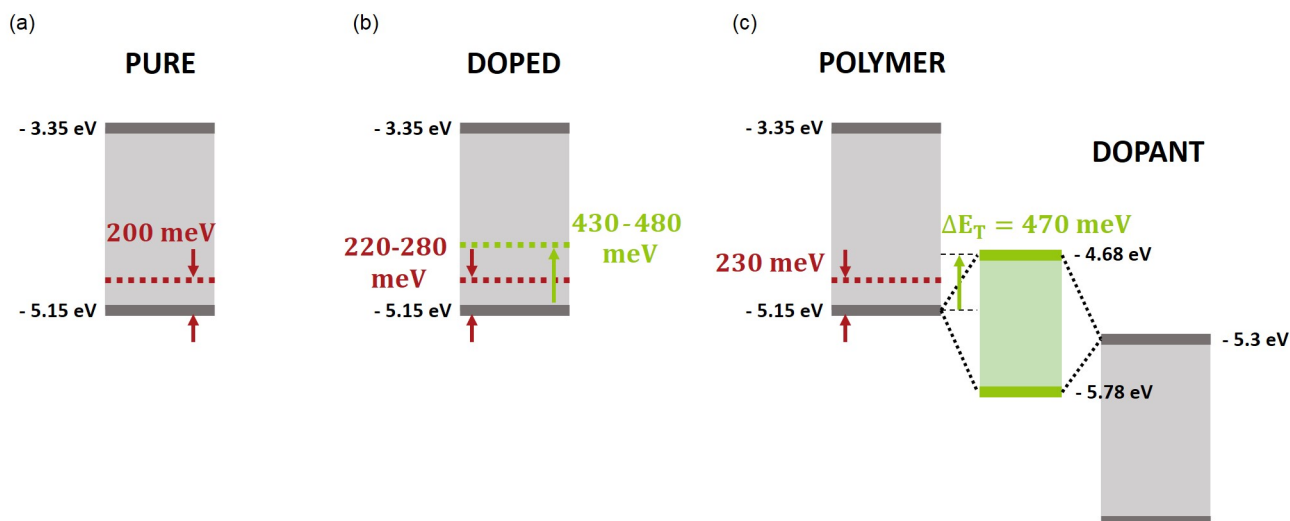


Figure 3.38: PBDTTT-c band diagram summarizing the trap states probed by admittance spectroscopy for pure (a) and doped (b) samples. Schematic of the hypothetical CTC formed between the PBDTTT-c HOMO and the $\text{Mo}(\text{tfd-COCF}_3)_3$ LUMO with the energy levels obtained from UV-visible absorption spectroscopy considering a Hückel-like model (c).

the potential complex formed between the polymer HOMO and the dopant LUMO. Considering a Hückel-like model, this anti-bonding state is situated approximately 470 meV above the polymer HOMO.

3.4 How to explain the effective p-doping?

Although our experiments strongly suggest that the formation of a Charge Transfer Complex is involved in the p-doping process of PBDTTT-c by $\text{Mo}(\text{tfd-COCF}_3)_3$, it is unclear how an acceptor level situated several hundreds of meV above the HOMO can lead to doping densities as high as 10^{18} cm^{-3} . Further work needs to be carried out to understand what mechanism allows this transition from the HOMO level to the anti-bonding state of the complex as illustrated in Figure 3.39. Over the last few years, several studies have reported a broadening of the HOMO Density of States with doping. This phenomenon might be involved in the doping process. Also, as it is known for photo-oxidation, light could enable the transition needed toward the acceptor states. In this section we detail both hypothesis and present an outlook to this study.

3.4.1 Density of States broadening

Arkhipov *et al.* have shown that the addition of dopant leading to strong Coulombic interactions induces a Density of States (DOS) broadening with an increase of the deep states in the tail of the Gaussian distribution [173]. Figure 3.40 illustrates the DOS distribution of the Gaussian HOMO with additional tail states. The potential anti-bonding state of the complex is added to the schematic at approximately 470 meV above the HOMO. Two

3.4. How to explain the effective p-doping?

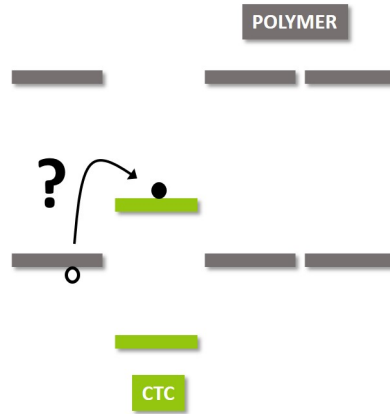


Figure 3.39: Schematic of the transition required from the polymer HOMO to the anti-bonding state of the CTC to p-dope the polymer.

FWHM are considered for the Gaussian distribution of the acceptor level. In Figure 3.40 (a), a FWHM of 70 meV is taken into account regarding the Gaussian fit carried out on admittance spectroscopy measurements. The Gaussian distribution associated with the sub-bandgap peak observed in UV-visible absorption spectroscopy measurements exhibits a FWHM around 180 meV. The discrepancy between both values remains to be understood. This potential Gaussian distribution is shown in Figure 3.40 (b). In both schematics we can see that a broadening of the tail states results in a superposition of the HOMO with the acceptor level distributions. Such phenomenon could explain how electrons from the polymer HOMO can be accepted on the dopant level approximately 470 meV above the HOMO.

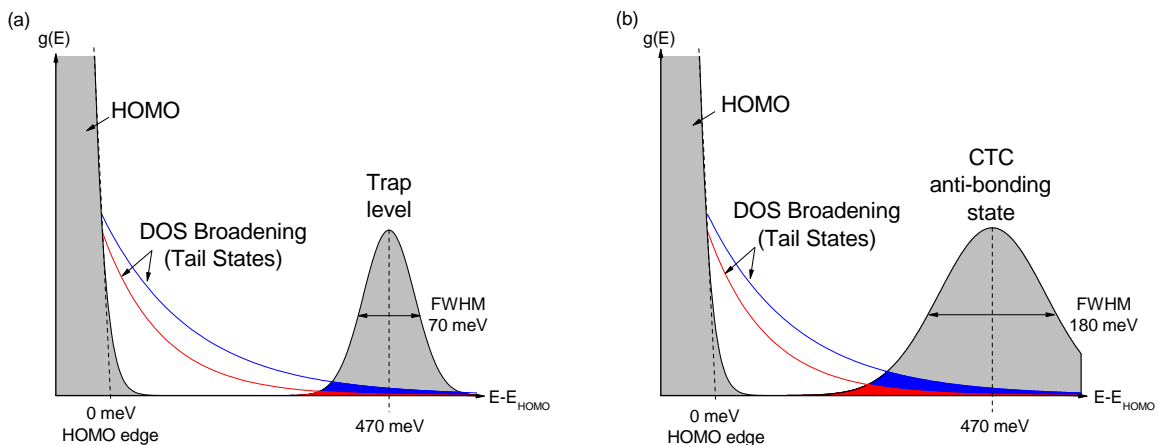


Figure 3.40: Schematic of the HOMO DOS and the trap Gaussian distribution with two different FWHM: 70 meV (a) and 180 meV (b) corresponding to the admittance spectroscopy and UV-visible absorption spectroscopy extractions respectively.

Recent studies have reported experimental results of DOS broadening with doping through Ultraviolet Photoelectron Spectroscopy (UPS) measurements. Pahner *et al.* have measured an increase of the tail states distribution with doping for $C_{60}F_{36}$ doped PEN

[181]. This tail states evolution has also been observed by Zuo *et al.* in F_4TCNQ doped P3HT and they developed a model showing good consistency with the data and highlighting the role of deep trap tail in the DOS evolution of the HOMO [214]. Lin *et al.* have also observed an evolution of the HOMO Density of States for $\text{Mo}(\text{tfd})_3$ doped CuPc [127]. However, they showed that the addition of small amounts of dopant in CuPc leads to broadening of the main Gaussian distribution while the trap states in the tail distribution are progressively filled with doping.

To further explore this hypothesis, it would be interesting to carry out UPS measurements in order to follow the evolution of the HOMO distribution of PBDTTT-c upon $\text{Mo}(\text{tfd-COCF}_3)_3$ addition. Moreover, we could use UPS and IPES measurements to probe the bonding and anti-bonding distributions of the complex by dramatically increasing the doping concentration to reach a 50:50 ratio between polymer and dopant.

3.4.2 Light assisted p-doping

The p-doping ability of oxygen in organic semiconductors has been highly reported in the literature [215, 216, 217]. Although the mechanisms behind oxygen doping is not totally understood, the impact of light on the doping effectiveness has been highlighted [183, 218]. Light-assisted oxygen p-doping is explained by the excitation of the electron from the HOMO to the LUMO of the polymer followed by the electron transfer in the oxygen acceptor level situated in the polymer bandgap as illustrated in Figure 3.41 (a). The hole associated with the excited electron trapped by the oxygen level does not recombine and increases the hole density of the polymer. Liao *et al.* followed the current evolution in a symmetric two terminal device in the dark and under light exposure with and without high oxygen pressure [219]. They highlighted the increased oxygen doping efficiency under light exposure.

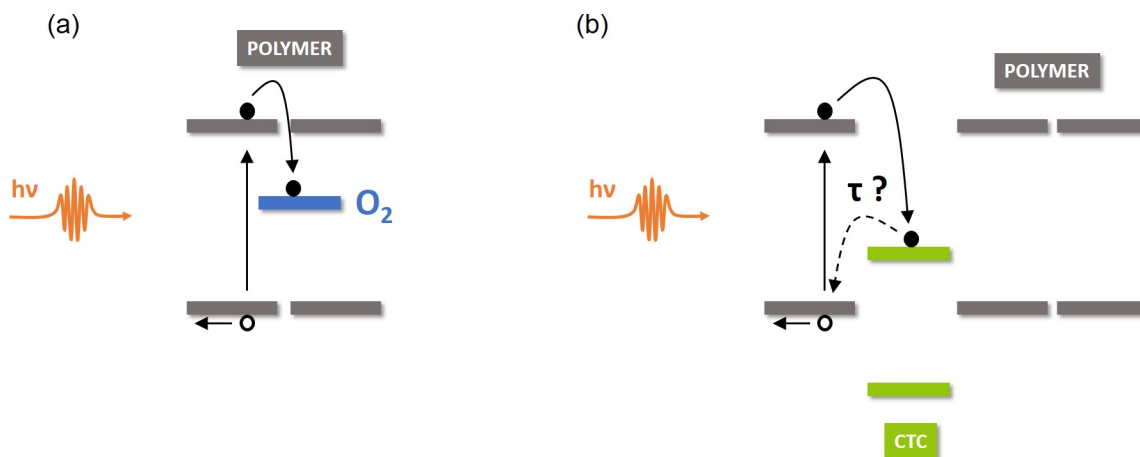


Figure 3.41: Schematic of light-assisted oxygen p-doping in polymers (a). Illustration of the potential role of light in the doping activation leading to the transition of an electron from the HOMO to the LUMO of polymer followed by the transition to the anti-bonding state of the complex (b).

3.4. How to explain the effective p-doping?

With an acceptor level situated several thousands of meV above the polymer HOMO, light might also play a role in the doping of PBDTTT-c with Mo(tfd-COCF₃). As shown in Figure 3.41 (b), we can consider that the photo-excited electron is trapped in the anti-bonding level of the complex. This phenomenon is suggested by dynamic fluorescence quenching determined in this chapter. If the decay time τ from the anti-bonding state to the polymer HOMO is long, the generated hole can lead to relatively stable PBDTTT-c p-doping. In Figure 3.42, we show the current evolution of a simple gold/doped PBDTTT-c (MR=5%)/gold sample over time in the dark and under ambient illumination. The device has been encapsulated in the glovebox to avoid the potential effect of oxygen. The current exhibits a constant and slow decrease over 60 hours of storage in the dark. An increase of the current can be observed when the sample is exposed to ambient illumination.

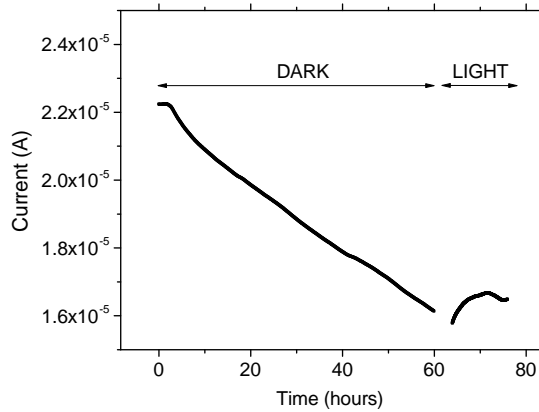


Figure 3.42: Current density at 2 V versus time in the dark for 60 hours followed by 10 hours under ambient illumination.

This preliminary experiment suggests that light could be involved in the doping of Mo(tfd-COCF₃) in PBDTTT-c. A longer monitoring of the device when stored in the dark needs to be carried out to follow the complete decrease and the potential saturation of the current. If light enables PBDTTT-c p-doping, we expect to reach a current close to the pure sample, as we will be limited by thermal activation. Further experiments need also to be done under controlled illumination to determine the dynamic of the doping activation. It would be interesting to reproduce this experiment with varying wavelengths. If the photon energy is lower than the polymer bandgap, the transition illustrated in Figure 3.41 (b) is not allowed. However we can expect a direct transition from the polymer HOMO to the anti-bonding state of the complex. Therefore, by illuminating the device with a photon energy lower than the activation energy of the trap associated with the anti-bonding state (430-480 meV), the device behavior should be similar to the dark storage condition.

3.5 Summary and outlook

In this Chapter we aimed at determining which mechanism is involved in PBDTTT-c p-doping with $\text{Mo}(\text{tfd-COCF}_3)_3$ in order to deepen our understanding of the limitations observed in organic semiconductor doping. Due to poor doping efficiency, the concentration required to achieve significant electrical performance improvement is of the order of a few percent in molar ratio for molecular doping. As the need for high doping concentrations leads to the degradation of transport properties, further work is required to understand the limits of this process and give clues for dopant design improvement.

As a first step, we carried out UV-visible absorption spectroscopy measurements on pure and doped PBDTTT-c with 8 doping concentrations highlighting the formation of sub-bandgap absorption peaks with doping. Diffusion and ionized dopant have been ruled out as potential origin for these peaks. Polarons and the formation of a Charge Transfer Complex (CTC) between the polymer HOMO and the dopant LUMO remained to be considered. The energy levels of the potential CTC have been calculated considering a Hückel-like model suggesting an anti-bonding level situated approximately 470 meV above the polymer HOMO if we consider a dopant electron affinity of 5.3 eV. Further work is required to verify the position of the dopant LUMO and validate our CTC assumption.

To distinguish between polarons and CTC, we used photoluminescence spectroscopy showing the fluorescence quenching upon dopant addition. The fluorescence intensity and excited state lifetime evolutions with doping highlighted the involvement of both dynamic and static quenching. This observation strengthened the hypothesis of CTC formation.

Finally, we carried out admittance spectroscopy measurements on pure and doped polymer in order to probe the anti-bonding state of the CTC and strengthen our hypothesis. With doping, the formation of a trap state in the bandgap has been identified. The activation energy of the trap obtained from variable temperature measurements is consistent with the UV-visible absorption spectroscopy results. The Density of States profile has been reconstructed from the capacitance measurements showing Gaussian-like distributions, consistent with the Gaussian absorption peaks observed in the sub-bandgap regime.

The combination of optical and electrical characterization techniques suggests that the formation of a Charge Transfer Complex is involved in $\text{Mo}(\text{tfd-COCF}_3)_3$ p-doping of PBDTTT-c. This hypothesis could be further verified by using a different molecular dopant, like F_4TCNQ , and comparing UV-visible absorption spectroscopy and admittance spectroscopy measurements.

Considering a CTC process, the limited efficiency of p-doping might be explained by the significant energy required for the transfer of the electron from the polymer HOMO to the anti-bonding state of the complex. In order to improve the p-doping ability of the dopant, the gap of the CTC must be reduced. This can be achieved by reducing the intermolecular electronic coupling described by the resonance integral β . However, further work needs to be carried out to understand how an acceptor state situated several hundreds of meV above the HOMO can lead to hole densities as high as 10^{18} cm^{-3} for

3.5. Summary and outlook

dopant molar concentrations of 5%.

In the previous Chapter we have demonstrated that Mo(tfd-COCF₃) effectively p-dopes PBDTTT-c. We also carried out further experiments to improve our understanding of the mechanisms involved in the doping process. In the following Chapter we will integrate this doped layer in a complete device, an organic photodetector. The doped layer will replace the common HTL PEDOT:PSS and provide good ohmic contact between the blend and the anode electrode.

4

P-doped organic semiconductor as potential replacement for PEDOT:PSS in organic photodetectors

Chapter contents

4.1	Experiment	119
4.2	p-doped polymer versus PEDOT:PSS as HTL in OPDs figures of merit	122
4.2.1	I(V) characteristics	122
4.2.2	External Quantum Efficiency	125
4.2.3	Similarities between both HTLs	125
4.3	Deeper analysis on the impact of p-doped polymer as HTL	127
4.3.1	Photocurrent dependency on light intensity	127
4.3.2	Active area localization induced by p-doped polymer	133
4.4	Preliminary ageing studies on OPDs with p-doped PBDTTT-c as HTL	135
4.4.1	Reduced humidity impact on series resistance	135
4.4.2	Thermal ageing with p-doped polymer as HTL	137
4.4.3	Establishment of a detailed experimental design for future works	139
4.5	Summary and outlook	140

Nowadays, organic photodetectors (OPDs) show good performances competing with amorphous silicon-made devices and can be fully processed using printing techniques on transparent and flexible substrates [220, 221, 222]. The OPD active layer is typically made of a thick (ca. 500 nm) blend layer composed of a donor (polymer) and an acceptor (fullerene) material [221]. To selectively extract one type of carriers and block the other type on each electrode, different inter-layers are engineered. To extract electrons and block holes, PEIE coated ITO [135] and ITO covered with a zinc oxide layer [223] are widely used cathodes. The anode is mostly made of solution processable PEDOT:PSS [224]. Its high work function around 4.8-5 eV enables a good energy alignment with the blend HOMO and its wide band gap is convenient for electron blocking. As degenerate p-type semiconductor, PEDOT:PSS benefits from a high conductivity (ca. 500 S/cm) [225] leading to its use as transparent conducting tracks. Figure 4.1 depicts the typical layers in the OPD stack.

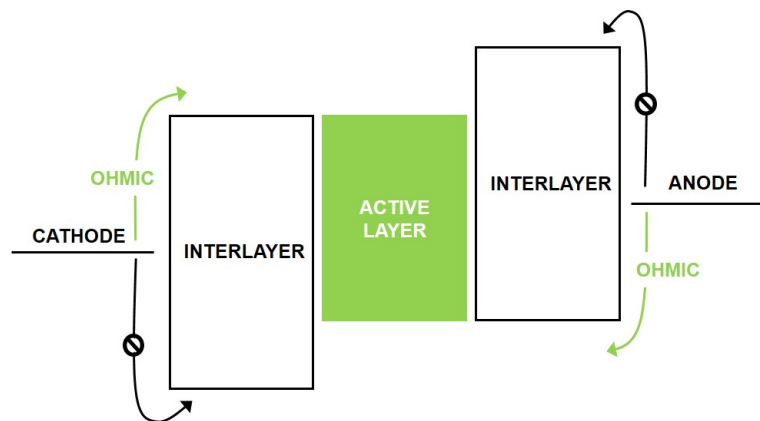


Figure 4.1: Schematic of the OPD band diagram showing the active layer surrounded by the anode and cathode. Interlayers are used to enable selective carrier injection and blocking.

However, as aging becomes the main issue of organic devices to allow their large scale industrialization [226, 223, 20], PEDOT:PSS has been identified as responsible for several degradation mechanisms in organic photodetectors and solar cells. PEDOT:PSS was originally used as HTL in standard structures where it is deposited on ITO. It has been observed that the acidic property of PSS groups leads to ITO degradation and indium migration in the PEDOT:PSS layer [227]. This issue was solved by reversing the structure with the deposition of PEDOT:PSS as top electrode [228]. But PEDOT:PSS is also known to be sensitive to humidity, oxygen and UV. When exposed to humidity the PEDOT:PSS layer swells leading to OPD series resistance increase by making the interface layer insulating and by forming interfacial voids [37]. The exposure of PEDOT:PSS to oxygen causes phase segregation in the HTL between PEDOT and PSS components and the sheet resistance of PEDOT:PSS is increased when exposed to UV [38, 39].

4.1. Experiment

Attempts to remove PEDOT:PSS from the organic devices structure has already been suggested by Ramuz *et al.* [40]. Although its removal enhances ageing performances of the device, when no HTL is proposed as replacement for PEDOT:PSS, the dark current density is highly impacted since no electron blocking layer is introduced. This evolution might not be detrimental for organic solar cells, but low dark current density over a wide bias range is essential for photodetection applications.

One solution to properly replace the PEDOT:PSS layer consists in doping the donor type semiconductor at the interface. With this technique, the injection barrier is effectively reduced and no constraint is given on the top electrode work function. As the donor type material electron affinity is lower than the acceptor ionization potential, the electron blocking property of the HTL can also be maintained. The replacement of PEDOT:PSS in organic solar cells with a p-doped organic layer deposited by SCTL has been introduced by An Dai *et al.* showing similar performances [26]. Another technique consists in spin-coating a thin layer of dopant on the active layer surface leading to the interface doping by diffusion [141]. However, the use of diffusion does not enable controlled p-doping of the active layer. The group of Prof. Bernard Kippelen suggests a post-process immersion into a phosphomolybdic acid solution leading to good OPV performances and improved air stability [229].

In this work we propose to replace PEDOT:PSS by a thin p-doped polymer layer in an OPD and study the evolution of the electrical performances of the devices. After the analysis of the OPD figures of merit, a deeper study will be made to follow the impact of the p-doped layer on the OPD performances.

4.1 Experiment

The structures studied in this Chapter are shown in Figure 4.2 (a) with the corresponding band diagram (b) and in Appendix A as Structure 4. In this study, OPDs using inverted structure with two different HTLs, PEDOT:PSS and p-doped polymer, are compared.

The diodes are processed on ITO-coated glass substrates. ITO electrodes are patterned using photolithography. In order to reduce the ITO work-function and enable a good electron injection in the active layer, a monolayer of Polyethylenimine (PEIE) is spin-coated on ITO, annealed at 100°C and rinsed. The 500 nm thick active layer is composed of PBDTTT-c:C60-PCBM with a 1:1.5 ratio in weight and dissolved in chlorobenzene(CB):trichlorobenzene(TCB) with a 90:10 ratio in volume. TCB is an additive used to improve the bulk heterojunction morphology. The solution is stirred for 12 hours at 45°C, filtered at 0.2 μm and spin-coated on the ITO/PEIE electrode. The resulting layer is annealed at 115°C under nitrogen for 15 minutes. The hole transport layer is then deposited on the active layer. Two different HTLs are studied, PEDOT:PSS and p-doped PBDTTT-c, and their respective processing will be detailed below. The active and HTL layers are then removed from the contacts. Since the HTL is deposited as a full layer, a patterned top electrode is required to define the active area of the diode. A 100 nm thick aluminum top electrode is then evaporated through a shadow mask in a vacuum chamber for both types of devices. Although the top electrode is not processed in solution

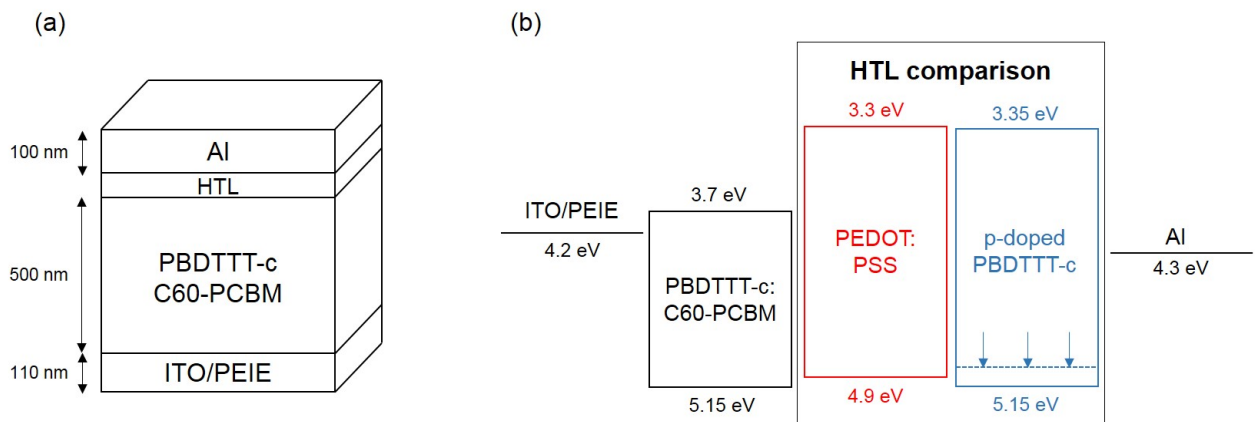


Figure 4.2: Stack of the OPD layers (a) and energy level diagram of the different components (b). The blue dotted line illustrates the Fermi level shift toward the polymer HOMO. (Structure 4)

in this study, we can imagine for further works to use new high conductive inks as top electrode like silver nanoparticles or graphene [230, 231]. To limit the impact of oxygen and humidity on the OPDs performances, the devices are encapsulated with glass in the glovebox using an epoxy glue. The successive steps are summarized in Figure 4.3.

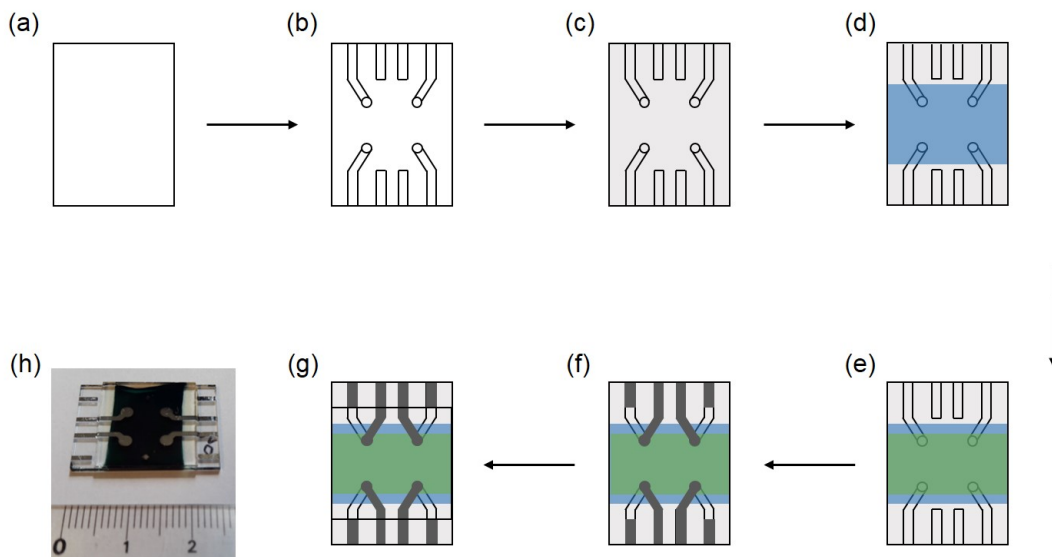


Figure 4.3: Schematic of the successive OPD processing steps: ITO-coated glass substrate (a), ITO patterning by photolithography (b), PEIE spin-coating (c), active layer spin-coating and wiping (d), HTL lamination and wiping (e), aluminum evaporation (f) and encapsulation (g). Picture of the final OPD device (h).

The first type of device is processed with PEDOT:PSS as HTL. As Soft Contact Transfer Lamination (SCTL) will be used for p-doped PBDTTT-c deposition, we chose to laminate PEDOT:PSS on the active layer as well and ensure good comparison of the electrical characteristics between both diodes. To laminate PEDOT:PSS on the active

4.1. Experiment

layer we followed the processing technique described by Gupta *et al.* [232] and illustrated Figure 4.4. PEDOT:PSS is filtered at $0.45 \mu\text{m}$ and spin-coated on an O_2 plasma treated PDMS stamp. The plasma treatment is required to change the surface tension of the stamp from hydrophobic to hydrophilic. The PEDOT:PSS layer is then left in air for 20 minutes for drying before bringing into contact the PEDOT:PSS coated PDMS with the active layer. The full stack is annealed at 85°C for 5 minutes to change back the surface tension of the PDMS stamp to hydrophobic. After cooling down the substrate at ambient temperature the PDMS stamp is carefully removed. A special care needs to be taken in the PEDOT:PSS wiping on the contacts. As we will see in this chapter, the diode surface area is determined by the superposition of the ITO and PEDOT:PSS electrodes. Therefore, the wiping of PEDOT:PSS determines the surface area. To take into account the surface variations between samples, the active area will be properly measured and the current density will be calculated.

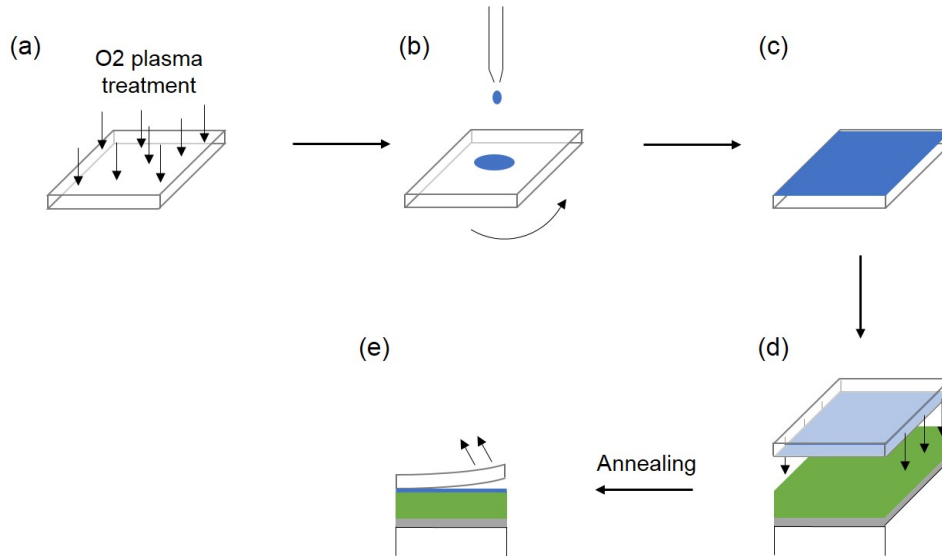


Figure 4.4: Schematic of PEDOT:PSS lamination on PBDTTT-c:C60-PCBM active layer: O_2 plasma treatment on PDMS (a), PEDOT:PSS spin-coating on PDMS stamp (b), PEDOT:PSS drying in air (c), PEDOT:PSS and active layer brought into contact and annealed (d), PDMS stamp removal (e).

To compare the PEDOT:PSS HTL with a p-doped polymer we chose the molybdenum complex $\text{Mo}(\text{tfd-COCF}_3)_3$ studied in Chapters 2 and 3 as dopant. A thin layer ($45 \pm 10 \text{ nm}$) of PBDTTT-c: $\text{Mo}(\text{tfd-COCF}_3)_3$ is then deposited on top of the active layer. As direct spin-coating of this solution would lead to the dissolution of the active layer, SCTL is used to deposit the HTL. The SCTL technique for doped layers has been described in Chapter 2. Contrary to PEDOT:PSS lamination, the doped layer is spin-coated on a silicon wafer prior to its lamination on a PDMS stamp. With regard to the study of the doping concentration impact on hole injection barrier presented in Chapter 2 (Figure 2.7 (a)) a molar concentration of 5% is chosen. This concentration ensures a good ohmic contact for holes between the top electrode and the active layer. The references and suppliers information of all the materials used for processing are summarized in Appendix C.

The only varying parameters between both structures studied in this chapter are the nature of the HTL material and its thickness. The band diagram with the energy levels of each layer is shown in Figure 4.2 (b). The ITO/PEIE and PEDOT:PSS work functions are measured by kelvin probe. The PEDOT:PSS work function (equivalent to the ionization potential for a p-type degenerate semiconductor) has been measured on both laminated layer surfaces using kelvin probe. The work function of the PEDOT:PSS surface in contact with the active layer in our OPD has been measured around 4.9 eV. The HOMO level of PBDTTT-c has been measured by Atmospheric Photoemission Spectroscopy (APS) at 5.15 eV. The values of PBDTTT-c and PEDOT:PSS electron affinities and aluminum work function are taken from the literature [162, 233, 170].

4.2 p-doped polymer versus PEDOT:PSS as HTL in OPDs figures of merit

The goal of this work is to present an alternative to the use of PEDOT:PSS as HTL in printed organic photodetectors. As a first step we need to find a layer that fulfills the same role in order to obtain a working diode with similar or better performances. The electrical characterizations of OPDs with both HTLs will be compared and analyzed.

4.2.1 I(V) characteristics

The main figure of merit for OPDs is current versus voltage I(V) in the dark and under illumination. The I(V) measurements for a typical OPD is shown in Figure 4.5 in linear scale (a) and in semi-logarithmic scale (b). Three regimes can be observed:

1. **At positive voltage and current: injection regime.** OLEDs are used in this regime to generate light by recombination of holes and electrons.
2. **At positive voltage and negative current: photovoltaic regime.** Solar cells operate in this regime leading to a negative power (generated power) when exposed to light. Three parameters of the solar cell can be extracted in this regime: V_{OC} , J_{SC} and FF. The open-circuit voltage V_{OC} is defined as the voltage when photo-generated and injection currents cancel each other out. The short-circuit current J_{SC} represents the maximum current density when no external bias is applied to the solar cell. From the maximum power generation, V_{OC} and J_{SC} , we can calculate the fill factor FF:

$$FF = \frac{P_{max}}{J_{SC}V_{OC}} \quad [-]. \quad (4.1)$$

The fill factor informs about the quality of the solar cell by taking into account the electrical losses in the device. The closer to 1 it is, the more ideal the diode is.

3. **At negative voltage and current: reverse bias regime.** In this operating region, dark and light current densities saturate and remain stable over a wide range of voltages with the current density proportional to the incident light intensity.

4.2. p-doped polymer versus PEDOT:PSS as HTL in OPDs figures of merit

For OPD application, the dark and light current densities need to be quasi-electric field independent to allow for small voltage variations around the bias set by the electronic. The semi-logarithmic scale is useful to observe the field-dependency of current density and its evolution over several decades with light intensity. One of the main parameters of photodetectors is the sensitivity S given by the ratio of the current I with the light power P_{light} for a given bias and wavelength:

$$S = \frac{I}{P_{light}} \quad A/W. \quad (4.2)$$

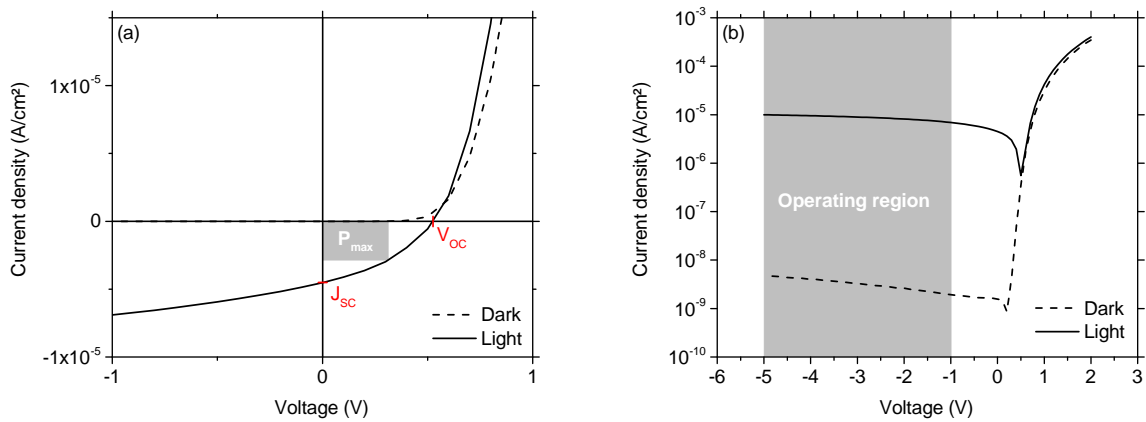


Figure 4.5: Current density versus voltage figure of merit in the dark and under illumination for an organic photodetector in linear scale (a) and semi-logarithmic scale (b). The ITO/PEIE electrode is grounded and the potential is applied to the aluminum electrode.

In order to compare $I(V)$ characteristics for devices with PEDOT:PSS and p-doped polymer as HTL we first need to fix the HTL thickness. The thickness of the p-doped polymer has been set to approximately 45 nm, consistent with the experiments described in Chapter 2 for injection barrier lowering. To set the PEDOT:PSS thickness, we processed diodes with PEDOT:PSS layers of 40 ± 10 nm and 180 ± 10 nm. The $J(V)$ (current density) characteristics of both devices are shown in Figure 4.6 and compared to the $J(V)$ characteristics of the diode with 45 nm p-doped polymer. The thickness of PEDOT:PSS has a significant impact on the $J(V)$ characteristics. An increase of the PEDOT:PSS thickness decreases the current density in the injection regime probably due to the series resistance. In the reverse regime, the use of a thicker PEDOT:PSS layer leads to photo-generated and dark currents decrease. This evolution can also be attributed to a series resistance increase. A compromise needs to be done between low dark current density and high sensitivity. As low reverse current density in the dark is a major requirement for photodetectors, we chose to select the diode with a thicker PEDOT:PSS layer. Moreover, this device leads to similar injection and photogenerated currents as 45 nm p-doped PBDTTT-c HTL. We observe in Figure 4.6 similar $J(V)$ characteristics for 180 nm thick PEDOT:PSS and 45 nm p-doped polymer.

After setting the HTL thickness we can compare the $J(V)$ characteristics in the dark and under illumination for both structures. To take into account the surface variations

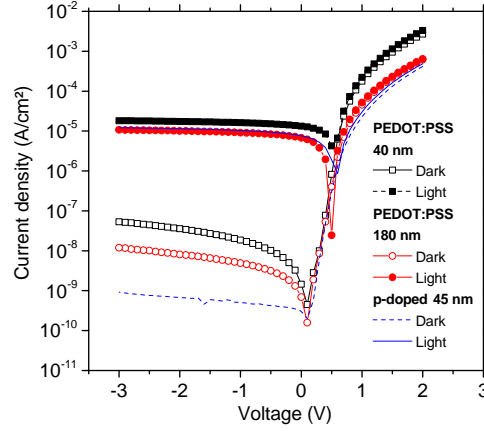


Figure 4.6: Current density in the dark and under illumination (530 nm, 650 mW/m²) in a semi-logarithmic scale for diodes with 40 nm (black squares) PEDOT:PSS, 180 nm (red circles) PEDOT:PSS and 45 nm (black line) p-doped polymer.

between both samples, we chose to plot the current density J . Figure 4.7 (a) exhibits the $J(V)$ figure of merit in semi-logarithmic scale for the diode with PEDOT:PSS HTL in red and with p-doped PBDTTT-c in blue. Performances under illumination are similar for both devices with almost identical light current densities in the reverse bias regime ($-1.1 \times 10^{-5} \text{ A/cm}^2$ with PEDOT:PSS and $-1.2 \times 10^{-5} \text{ A/cm}^2$ with p-doped polymer at -3 V). The injection regime is also similar for both devices reaching current densities of $6.1 \times 10^{-4} \text{ A/cm}^2$ and $4.9 \times 10^{-4} \text{ A/cm}^2$ for PEDOT:PSS and p-doped polymer respectively. However, we observe the decrease of the dark current density in the reverse bias regime when p-doped PBDTTT-c is used as HTL. At -3 V the dark current density is reduced by one order of magnitude reaching $-9.2 \times 10^{-10} \text{ A/cm}^2$. To illustrate the impact of the HTL on $J(V)$ characteristics, we measured the current density in the dark and under illumination for a similar structure processed without HTL shown in Figure 4.7 (black line). We can notice that the removal of the HTL leads to an increase of the dark current density in the reverse bias regime. This evolution is due to the lack of electron blocking layer. Since the work-function of aluminum is 4.3 eV and the electron affinity of the active layer is 3.7 eV, the electron injection barrier is reduced to 0.6 eV. When PEDOT:PSS or p-doped PBDTTT-c is added between the active layer and the top electrode, the electron injection barrier is around 1 eV. Moreover, the poor injection regime obtained for the diode without HTL has also an impact on the photo-generated current between -0.5 and 0 V leading to a low fill factor. This comparison shows that a simple removal or the PEDOT:PSS layer to improve lifetime is not feasible for OPD application.

The $J(V)$ characteristics under illumination are shown in linear scale in Figure 4.7 (b). We observe a slight shift of V_{OC} and J_{SC} between both devices. The open-circuit voltage increases from 0.50 V to 0.57 V when PEDOT:PSS is replaced by p-doped PBDTTT-c. The short-circuit current increases slightly from $6.7 \times 10^{-6} \text{ A/cm}^2$ with PEDOT:PSS to $7.6 \times 10^{-6} \text{ A/cm}^2$ with p-doped PBDTTT-c. The fill factor has been calculated around 33% with PEDOT:PSS and 37% with p-doped PBDTTT-c.

4.2. p-doped polymer versus PEDOT:PSS as HTL in OPDs figures of merit

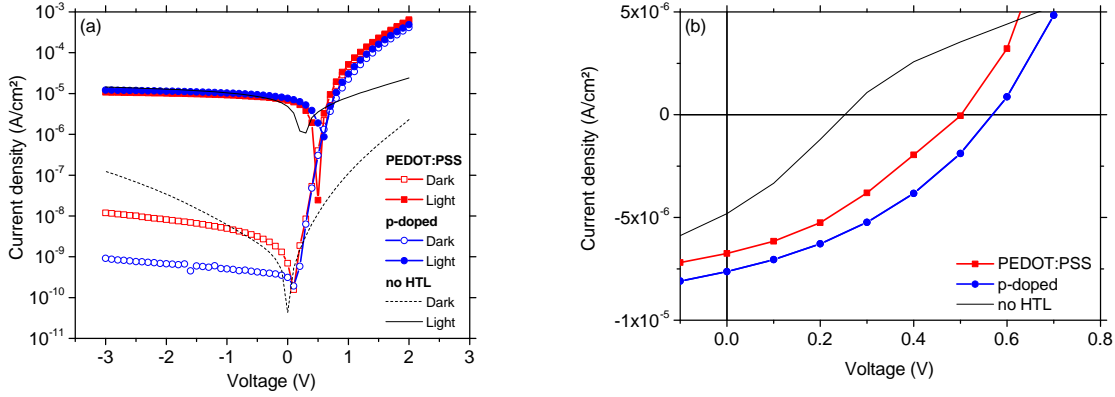


Figure 4.7: Current density in the dark and under illumination (530 nm, 650 mW/m²) for the diode with PEDOT:PSS (red), p-doped PBDTTT-c (blue) and without HTL (black) in semi-logarithmic scale (a) and linear scale (b).

We have shown that replacing PEDOT:PSS with appropriate thickness by a p-doped PBDTTT-c layer leads to similar performances under illumination and decreases the dark current density in the reverse regime. We also highlighted the impact of the HTL in $J(V)$ characteristics showing that replacing the PEDOT:PSS layer by a material with similar properties is required for OPD application.

4.2.2 External Quantum Efficiency

The External Quantum Efficiency (EQE) is the figure of merit used to quantify the efficiency of the diode to create a photo-generated current and its dependency at a specific voltage. This parameter takes into account optical losses (by reflexion or incomplete absorption) and carriers recombination. The EQE is defined as the ratio between the incident photons flow and the collected carriers flow:

$$EQE(\lambda) = \frac{hcI_{ph}}{qP_{light}\lambda} \quad [-] \quad (4.3)$$

where λ is the wavelength of the incident light and I_{ph} the photo-generated current calculated from dark I_{dark} and light I_{light} currents:

$$I_{ph} = I_{light} - I_{dark}. \quad (4.4)$$

The EQE figure of merit for the devices with PEDOT:PSS and p-doped polymer are shown in Figure 4.8. Both devices show essentially identical EQE characteristics reaching 70% between 400 and 700 nm at -2 V.

4.2.3 Similarities between both HTLs

In order to compare the performances of these diodes with those reported in the literature, we determine the specific detectivity of the diodes at -2 V and 530 nm. The specific

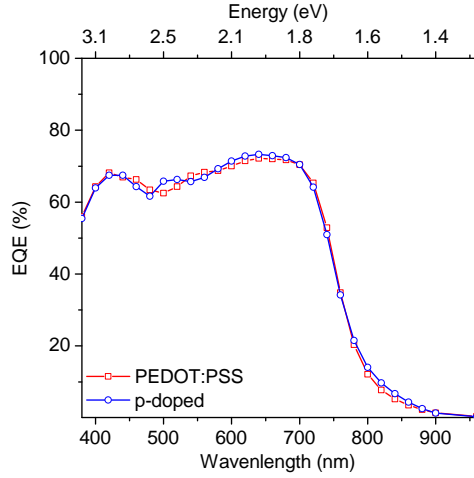


Figure 4.8: EQE at -2 V for the devices with PEDOT:PSS (red) and p-doped PBDTTT-c (blue) as HTL in linear scale.

detectivity D^* given in $cmHz^{1/2}W^{-1}$ or Jones allows to quantify the signal to noise ratio of the photodetector with an active area of $1 cm^2$ and an incident light intensity of $1 W$ detected at a bandwidth of $1 Hz$. This parameter can be calculated from EQE and noise measurements using the following relation [234]:

$$D^* = \frac{q\lambda EQE}{hc} (2qJ_d + N_{other\ noise})^{-1/2} \quad (4.5)$$

with J_d the dark current density and $N_{other\ noise}$ the power spectra density in $A^2Hz^{-1}cm^{-2}$ of other noise sources. To properly determine the specific detectivity of photodetectors, we should take into account the different sources of noise: shot noise from the dark current, Johnson noise or thermal fluctuations and flicker noise [235]. In most paper, shot noise is considered as the major contribution for noise while others are neglected [221, 236, 237]. However, taking only the shot noise into account can lead to an underestimation of the noise current and an overestimation of the specific detectivity which makes difficult the comparison of different photodetector performances [238].

However, due to the lack of noise measurement setup in the laboratory and the common assumption that Johnson and flicker noises can be neglected over shot noise, we decided to determine a first approximation of the specific detectivity by simplifying relation 4.5:

$$D^* = \frac{q\lambda EQE}{hc} (2qJ_d)^{-1/2}. \quad (4.6)$$

Detectivities of 5.5×10^{12} and $1.9 \times 10^{13} cmHz^{1/2}W^{-1}$ are obtained for the devices with PEDOT:PSS and p-doped PBDTTT-c respectively at -2 V and 530 nm. The improvement of the dark current density with the use of p-doped PBDTTT-c as HTL enhances the specific detectivity by one order of magnitude. Moreover, this value is among the best detectivities reported in the literature when Johnson and flicker noises are neglected [234] and competes with those of silicon-made devices with typical detectivities around $10^{13} cmHz^{1/2}W^{-1}$ for imaging applications.

4.3. Deeper analysis on the impact of p-doped polymer as HTL

The main parameters extracted from $J(V)$ and EQE measurements for both OPDs are summarized in Table 4.1.

Table 4.1: Parameters extracted from $J(V)$ and EQE characteristics for the devices with PEDOT:PSS and p-doped PBDTTT-c as HTL.

HTL	V_{OC} (V)	J_{SC} (A/cm ²)	FF (%)	EQE @ -2 V, 640 nm (%)	S @ -2 V, 530 nm (A/W)	D^* @ -2 V, 530 nm (cmHz ^{1/2} W ⁻¹)
PEDOT:PSS	0.50	-6.7×10^{-6}	33	72	0.26	5.5×10^{12}
p-doped	0.57	-7.6×10^{-6}	37	73	0.26	1.9×10^{13}

The main goal of this study is to replace PEDOT:PSS by a material leading to similar or better performances for photodetection. Using usual photodetectors figures of merit we show that devices with p-doped PBDTTT-c as HTL exhibit similar performances under illumination as with PEDOT:PSS HTL, with the EQE reaching 70% at -2 V. Injection performances are also maintained between both HTLs while the replacement of PEDOT:PSS by p-doped PBDTTT-c results in the enhancement of the OPD specific detectivity with a reduction of the dark current density in the reverse bias regime.

Although we have shown that PEDOT:PSS can be successfully replaced by p-doped PBDTTT-c in OPD, we need to carry out a deeper analysis on the impact of a laminated doped polymer on electrical transport at the interface.

4.3 Deeper analysis on the impact of p-doped polymer as HTL

To study the impact of a laminated p-doped polymer layer on the interface electrical characteristics, further analyses have been carried out. The behavior of the OPD characteristics at different light intensities is studied and a sensitivity scanning method is used to show a major advantage of p-doped polymer over PEDOT:PSS as HTL.

4.3.1 Photocurrent dependency on light intensity

In the previous section, we studied $J(V)$ characteristics measured at a light intensity of 650 mW/m^2 . However, photodetectors need to cover a wide range of light intensities with comparable performances to ensure photocurrent linearity. In order to evaluate this ability to respond to the light intensity, the photocurrent is measured for different light intensities at a given voltage. A power law is used to describe the photocurrent dependency on light intensity:

$$J_{ph} = P_{light}^{\alpha} \quad (4.7)$$

where J_{ph} and P_{light} are the photocurrent and light intensity respectively. α is close to unity when all generated carriers are extracted prior to their recombination. A photocurrent deviation from linearity with respect to the light intensity is indicative of photo-generated carrier losses. Two phenomena can lead to this non-linearity:

- Space Charge Limited Photocurrent (SCLP) [239, 240]
- Langevin recombination [241].

The linearity measurements at 0 V for the diodes with PEDOT:PSS and p-doped PBDTTT-c are shown in Figure 4.9 in a logarithmic scale. A halogen lamp has been used as source and the light intensity has been varied from 10 to 10^6 mW/m^2 (approximately 1 Sun AM1.5) with optical densities. To verify the linearity of the diodes, a linear fit is added to the graph. We can notice that the photocurrent deviates from linearity for light intensities above 10^4 mW/m^2 and the deviation is slightly more important with the p-doped PBDTTT-c as HTL. Although linearity is commonly verified in the reverse bias regime, electrical transport weaknesses are highlighted when no potential is applied to the device. We will investigate both possibilities (SCLP and Langevin) to understand the origin of the linearity deviation for each device.

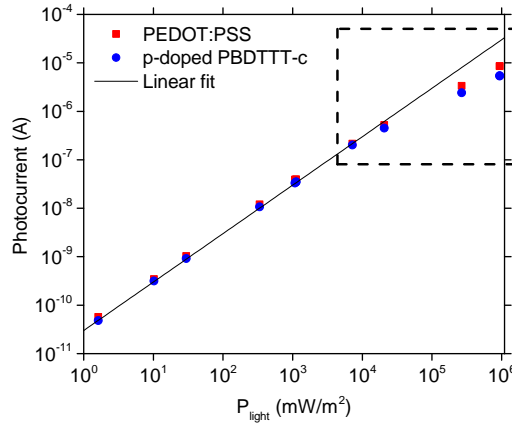


Figure 4.9: Linearity measurements of the photocurrent with respect to the light intensity for the diodes with PEDOT:PSS (red) and p-doped PBDTTT-c (blue) as HTL for a bias of 0 V. A linear fit is added to the graph.

- **Space Charge Limited Photocurrent (SCLP)**

Space Charge Limited Photocurrent (SCLP) is observed when the extraction of one type of carriers is less efficient than the other. This phenomenon leads to the creation of a space charge region in the active layer. This model has been introduced by Goodman and Rose [242]. Two distinct origins can explain the formation of a space charge region [243]:

4.3. Deeper analysis on the impact of p-doped polymer as HTL

- Unbalanced mobilities between electrons and holes
- Extraction barriers.

The OPD processed in this study should not exhibit any extraction barrier since the PEIE-coated ITO work-function is higher than the blend electron affinity and an ohmic contact is provided by the PEDOT:PSS or p-doped layer on the anode side (see Figure 4.2 (b)). In the PBDTTT-c:C₆₀-PCBM blend heterojunction, the electron and hole mobilities have been measured by CELIV (Charge Extraction in a Linearly Increasing Voltage) around $6 \times 10^{-4} \text{ cm}^2\text{s}^{-1}\text{V}^{-1}$ and $1 \times 10^{-3} \text{ cm}^2\text{s}^{-1}\text{V}^{-1}$ respectively [200]. Although mobilities of holes and electrons are almost equivalent we cannot put aside this hypothesis.

In order to determine whether the deviation from linearity is caused by SCLP, we need to derive the photocurrent dependency on light intensity. For $V < V_{OC}$, the photocurrent is mainly driven by the electric field and diffusion current can be neglected. The hole and electron current densities $J_{drift,e/h}$ are then described by the following relations:

$$J_{drift,h} = qp\mu_h E \quad (4.8)$$

$$J_{drift,e} = qn\mu_e E \quad (4.9)$$

where p and n are the hole and electron densities, μ_h and μ_e the hole and electron mobilities, E the electric field in the active layer and q the elementary charge. If the metal/semiconductor contacts are considered ohmic, SCLP can be caused by an unbalanced mean free path L between holes and electrons with one of them being lower than the active layer thickness w . The mean free path for electrons and holes is given by the following relation:

$$L_{e/h} = \mu_{e/h}\tau_{e/h}E \quad (4.10)$$

where τ_e and τ_h are the electron and hole lifetimes. Since the hole mobility is slightly lower than the electron mobility in the active layer studied, we consider $L_h < L_e$ and assume $L_h < w$. The mean free path in organic semiconductors usually ranges from 0.1 nm to 10 nm [244, 245]. Therefore, with an active layer of 500 nm, the assumption $L_h < w$ is reliable.

If the holes present a lower mobility than the electrons they will accumulate at the anode interface as their mean free path is reduced compared to electrons (Figure 4.10 (a)). In order to keep an equilibrium between electron and hole flows and satisfy Poisson's equation, the potential distribution in the active layer is modified. With the formation of a band bending on the anode side, the extraction of holes is facilitated with a higher electric field. On the cathode side, the electric field is reduced decreasing the electron collection. A space charge region is then created as shown in Figure 4.10 (b) with an inhomogeneous electric field in the active layer. The space charge region extends along the length L_1 with a voltage drop V_1 .

Taking into account this hypothesis, it is possible to derive the equation of the photocurrent with respect to the voltage drop in the active layer as described by Mihailetschi *et al.* [240]. The length L_1 of the space charge region is given by equation 4.10 for holes

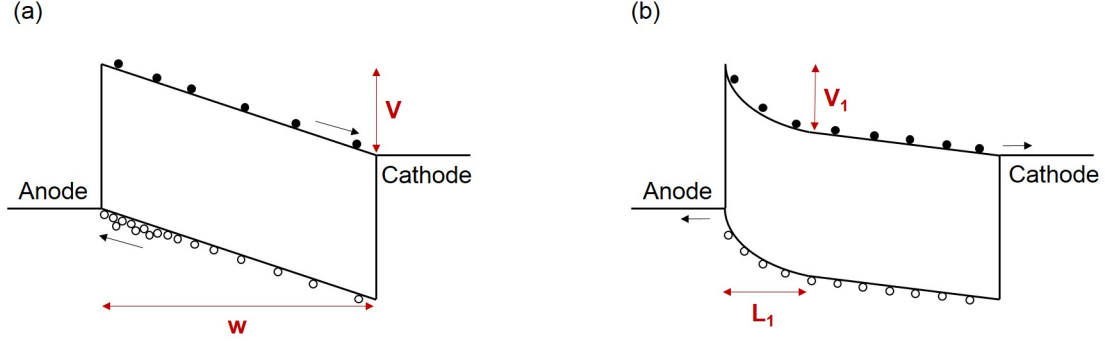


Figure 4.10: Schematic of the band diagram showing the hole accumulation at the anode due to unbalanced mobilities (a) and the space charge formation to satisfy Poisson's equation (b).

and the electric field E_1 is defined by:

$$E_1 = \frac{V_1}{L_1} \quad (4.11)$$

with V_1 the voltage drop in the space charge region. We can consider that the voltage drop is entirely situated in the space charge region and V_1 can be replaced by the total voltage drop V . By combining Equations 4.10 and 4.11 the length of the space charge region L_1 can be determined with respect to the voltage drop V in the active layer:

$$L_1 = \sqrt{\mu_h \tau_h V}. \quad (4.12)$$

The photocurrent generated in the active layer is proportional to the electron-hole generation rate G in the active layer:

$$J_{ph} = qGw. \quad (4.13)$$

We can consider that most of the photocurrent is generated in the space charge region as the electric field is close to 0 elsewhere leading to a high recombination rate. The photocurrent is then described by:

$$J_{ph} = qGL_1 = qG\sqrt{\mu_h \tau_h V}. \quad (4.14)$$

Goodman and Rose [242] explain that the space charge region impact is given by the difference between the effective photocurrent and the maximum photocurrent the active layer can handle. If the generated photocurrent is small compared to the limitation of the space charge region, SCLP can be neglected. The Space Charge Limited Current J_{SCLC} when holes are the limiting carriers is given by the following relation [240]:

$$J_{SCLC} = \frac{9}{8} \epsilon_0 \epsilon_r \mu_h \frac{V^2}{L_1^3} \quad (4.15)$$

where ϵ_0 and ϵ_r are the vacuum and relative permittivity respectively. By equating Equations 4.14 and 4.15, we extract a condition on the length of the space charge region L_1 necessary to observe SCLP:

$$L_{max} = \left(\frac{9\epsilon_0 \epsilon_r \mu_h}{8qG} \right)^{1/4} \sqrt{V}. \quad (4.16)$$

4.3. Deeper analysis on the impact of p-doped polymer as HTL

When the length of the space charge region reaches L_{max} , the impact of SCLP cannot be neglected and the photocurrent is described by the following relation:

$$J_{ph} = q \left(\frac{9\epsilon_0\epsilon_r\mu_h}{8q} \right)^{1/4} G^{3/4}\sqrt{V}. \quad (4.17)$$

As a result, we have shown that SCLP leads to a non-linear photocurrent dependency with the generation rate G . In our structure, we can consider that $G \propto P_{light}$ [240]. This assumption is strengthened by the linear dependency of the photocurrent with the light intensity at low intensities. To determine whether the non-linearity observed at high light intensities in our devices are due to SCLP, we added a $I \propto P_{light}^{3/4}$ to the linearity measurements in Figure 4.11 (a). At 0 V bias the photocurrent follows a linear dependency up to 10^4 mW/m^2 and a good fit with $I \propto P_{light}^{3/4}$ is obtained for the diode with PEDOT:PSS at higher light intensities.

Regarding these data, it is unclear whether the SCLP can explain the linearity deviation for the diode with p-doped PBDTTT-c as photocurrent measurements slightly deviate from the 3/4 power law. In order to verify this hypothesis, we measured the photocurrent with respect to the light intensity at $V > 0 \text{ V}$. When the applied bias gets closer to the open-circuit voltage, the internal electric field is reduced enhancing the recombination losses. Figure 4.11 (b) and (c) exhibits the linearity measurements at 0.3 V and 0.5 V respectively. Although SCLP can explain the linearity deviation for the diode with PEDOT:PSS, the photocurrent for the diode with p-doped PBDTTT-c deviates from the 3/4 power law at high light intensities and this deviation is emphasized when the internal electric field is reduced to reach a power law of 0.54 for a bias of 0.5 V. We need to consider Langevin recombination to explain this behavior.

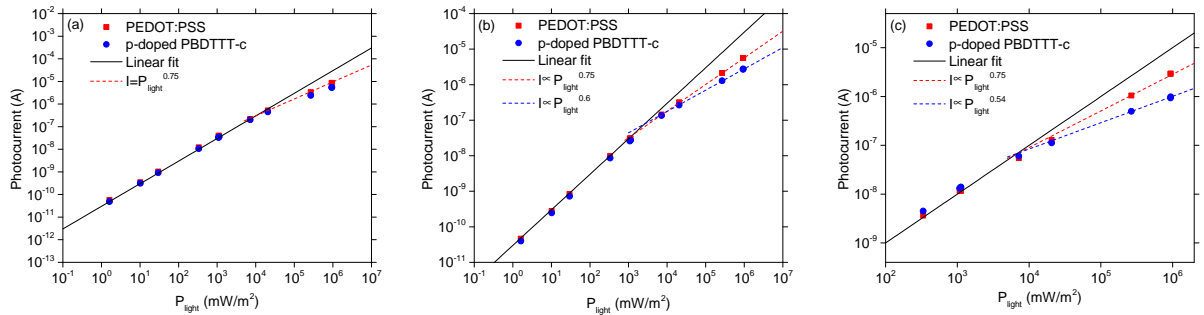


Figure 4.11: Linearity measurement of the photocurrent with respect to the light intensity for the diodes with PEDOT:PSS in red and p-doped PBDTTT-c in blue at 0 V (a), 0.3 V (b) and 0.5 V (c). Linear fit and $I = P_{light}^\alpha$ fit are added to the graphs.

- **Langevin or bimolecular recombination**

The bimolecular recombination process with the rate given by Langevin theory has been introduced in organic photodiodes and solar cells by Koster *et al.* [246]. This

mechanism induces electrical losses through band-to-band recombination. The Langevin recombination rate R_L is described by the following relation:

$$R_L = \frac{q(\mu_e + \mu_h)}{\epsilon} (np - n_i^2) \quad (4.18)$$

with μ_e and μ_h the electron and hole mobilities, ϵ the permittivity ($\epsilon = \epsilon_r \epsilon_0$), n and p the electron and hole densities, n_i the intrinsic carrier density and q the elementary charge. As the Langevin recombination rate is proportional to the np product, increasing the light intensity induces an increase of the recombination rate. A light intensity dependent recombination rate leads to a photo-current deviation from linearity. With increasing light intensity, the coefficient α decreases and, for a 100% bimolecular recombination efficiency, the coefficient α approaches 0.5 [247]. The Langevin recombination rate needs to be considered if the carrier mobilities (μ_e and μ_h) or the carrier density (np) are high.

At reverse bias condition, the electric field is high in the active layer facilitating the extraction of generated carriers. When the internal electric field is reduced, the time required for the carriers to reach the electrodes is increased. As a result, the carrier densities n and p in the active layer is higher, increasing Langevin recombination rate R_L and its dependency in light intensity and leading to the reduction of the coefficient α [246]. This behavior can explain that the deviation from linearity is emphasized when the applied bias gets closer to V_{OC} for the sample with doped polymer as HTL. However, we still need to understand why the photocurrent evolution with light intensity depends on the HTL material.

The main difference between both HTL material is their conductivity. The hole conductivity of PEDOT:PSS has been measured using the four point probe method at 425 S/cm while the hole conductivity for a 5 % doped PBDTTT-c with $\text{Mo}(\text{tfd-COCF}_3)_3$ exhibits a conductivity around 10^{-4} S/cm . Although the difference of 6 orders of magnitude between both conductivities is not detrimental for injection properties as effective barrier lowering is probably involved at the interface between doped polymer and aluminum, it can explain the increase in bimolecular recombination. Indeed, an external series resistance $R_{S,ext}$ induces a voltage drop outside the active layer leading to the reduction of the internal electric field [248]. As the electric field is reduced in the active layer, the probability of bimolecular recombination increases due to higher carrier densities. Street *et al.* [249] found that an external series resistance equivalent to or above $5 \text{ }\Omega\text{cm}^2$ reduces significantly the photocurrent density J_{ph} .

To evaluate the impact of the HTL material on the photocurrent density, we estimated the external series resistance due to this layer:

$$R_{S,ext} = \frac{A}{d\sigma_h} \quad (4.19)$$

with d the HTL thickness, σ_h the hole conductivity in the HTL and A the effective diode area. As a first approximation, external series resistance around $5 \text{ }\Omega\text{cm}^2$ and $10^7 \text{ }\Omega\text{cm}^2$ are obtained for PEDOT:PSS and p-doped PBDTTT-c HTLs respectively. The high conductivity of PEDOT:PSS provides a sufficiently low series resistance while the limited conductivity of p-doped PBDTTT-c involves significant external series resistance. The

4.3. Deeper analysis on the impact of p-doped polymer as HTL

series resistance around $10^7 \Omega\text{cm}^2$ for p-doped PBDTTT-c is 7 orders of magnitude higher than the threshold value suggested by Street *et al.* [249]. It is then probable that the external series resistance caused by the p-doped PBDTTT-c HTL is responsible for the linearity deviation due to Langevin recombination.

In order to support this hypothesis, we measured the $J(V)$ characteristics for both diodes with varying light intensities. If an external series resistance is responsible for the linearity deviation we expect the formation of an S-shape around V_{OC} in the $J(V)$ characteristics [250, 251]. Figures 4.12 (a) and (b) exhibit the $J(V)$ measurements under different light intensities for the diodes with PEDOT:PSS and p-doped PBDTTT-c respectively. For light intensities above $10^5 \text{ mW}/\text{m}^2$ an inflexion appears around V_{OC} for the diode with p-doped PBDTTT-c while no inflexion is observed with PEDOT:PSS as HTL. This result is consistent with the previous hypothesis.

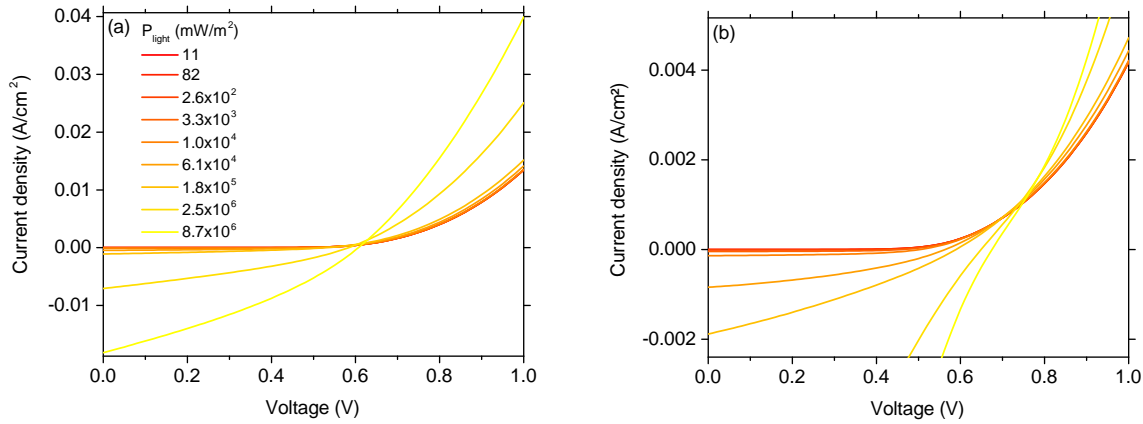


Figure 4.12: Current density under illumination with different intensities from 11 to $8.7 \times 10^6 \text{ mW}/\text{m}^2$ for the device with PEDOT:PSS (a) and p-doped PBDTTT-c (b).

This study of the light intensity impact on the OPD performances highlights the need to improve the p-doped layer conductivity. As it has been mentioned in the previous chapters, the increase in conductivity with the doping concentration in organic semiconductors is probably limited by the low doping efficiency. Enhancing the doping efficiency is necessary to reduce the doping concentration required for injection but will also improve the conductivity of the polymer leading to appropriate external series resistances for detection or solar applications.

4.3.2 Active area localization induced by p-doped polymer

To carry out this study on the PEDOT:PSS replacement by p-doped PBDTTT-c, we had to use Soft Contact Transfer Lamination to deposit the HTL. To make sure that this new deposition technique does not introduce inhomogeneities on the active area, we need to

map the sensitivity of the OPD. This analysis was done using a $150\ \mu\text{m}$ diameter spot light with a $530\ \text{nm}$ LED from Thorlab. The spot light scans the surface on a $4\times 4\ \text{mm}$ area with a pitch of $0.2\ \text{mm}$. For each position of the spot light, the current density is measured and the sensitivity of the diode is calculated using Equation 4.2. The light power is measured with a calibrated photodiode. This characterization technique is also useful to properly determine the active surface area for each diode. The effective area is then taken into account to calculate the current density in the diode.

The 2D sensitivity representations of the OPDs are shown in Figure 4.13 for PEDOT:PSS (a) and p-doped PBDTTT-c (b) as HTL. The sensitivity reaches $0.26\ \text{A/W}$ for both devices. Obtaining similar sensitivities is consistent with the light current density and EQE measurements presented previously. We can also notice that no sensitivity inhomogeneities are detected on the OPD active area. As a result, we show that SCTL deposition technique used for PEDOT:PSS and p-doped polymer is not detrimental for the sensitivity uniformity at a scale of $2 - 4\ \text{mm}^2$.

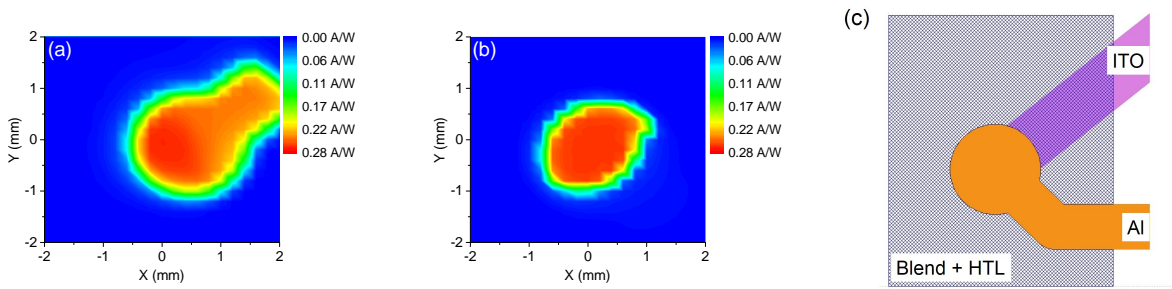


Figure 4.13: Sensitivity map at $530\ \text{nm}$ with a light power of $16.7\ \text{mW}/\text{m}^2$ for the device with PEDOT:PSS (a) and p-doped PBDTTT-c (b). OPD top view representation with the electrodes, the blend and the HTL (c).

The sensitivity scanning highlights a strong difference between both diodes. The device processed with p-doped PBDTTT-c as HTL displays a sensitivity only on the diode area defined by the overlay of patterned ITO and aluminum electrodes. On the other hand, the use of PEDOT:PSS as HTL leads to a wider active area since this HTL can act as an electrode. As a consequence, the effective area is defined by the superposition of patterned ITO and PEDOT:PSS which is deposited as a full layer. To help visualizing the different layers of the OPD on the sensitivity map, we add a top view representation showing the electrodes, the blend and the HTL in Figure 4.13 (c).

These different behaviors are presumably due to the 6 orders of magnitude difference between the conductivities of both HTL materials. The doped polymer is used to lower the effective barrier for holes between the blend HOMO and the aluminum work-function. However, its conductivity around $10^{-4}\ \text{S}/\text{cm}$ is insufficient to transport the extracted holes laterally over a few millimeters to be collected by the aluminum. This limitation induces the definition of the active area by the superposition of the two electrodes. On the other hand, PEDOT:PSS exhibits a conductivity measured at $425\ \text{S}/\text{cm}$, sufficiently high to act as a conducting track and is widely used in printed electronics as a transparent electrode. The extracted holes can diffuse laterally before being collected by the aluminum electrode. The effective area when PEDOT:PSS is used as HTL is then given by the superposition

4.4. Preliminary ageing studies on OPDs with p-doped PBDTTT-c as HTL

of ITO and PEDOT:PSS.

This sensitivity map characterization was important to make sure that SCTL deposition technique does not introduce inhomogeneities. But most importantly, it highlights a significant advantage of p-doped layers over PEDOT:PSS as HTL. When the latter is used it needs to be patterned to avoid the extension of the OPD active area. If we replace this HTL by a doped polymer, its localization is not necessary as it allows charge injection and extraction only through effective barrier lowering at the active layer/electrode interface. The top electrode chosen with no constraint on its workfunction is then patterned on the p-doped polymer HTL and defines the OPD effective area with the bottom electrode.

4.4 Preliminary ageing studies on OPDs with p-doped PBDTTT-c as HTL

The need to replace PEDOT:PSS in organic photodetectors and solar cells is related to its impact on the device stability. As PEDOT:PSS is sensitive to humidity, oxygen and UV, we suggested its replacement by a p-doped polymer layer. Ageing studies are required to check the device enhancement regarding those three external parameters but it is also necessary to take into account the limiting factor when small molecules are locally introduced in a structure: diffusion. Diffusion is indeed one of the main problem related to organic semiconductor doping and can be driven by temperature and electric field. It has been shown that F_4TCNQ diffuses in organic semiconductors like P3HT, 4,4',4''-tris(N,N-diphenyl-amino)triphenylamine (TDATA) or 4,4'-bis(N-carbazolyl)biphenyl (CBP) [110, 252]. The p-dopant $Mo(tfd-COCF_3)_3$, a derivative of $Mo(tfd)_3$, has been synthesized by the group of Prof. Seth Marder to improve doping efficiency [114, 115] and is less prone to diffusion with its 3D structure. As a result we expect limited diffusion induced by temperature in our OPD structure.

Although a complete ageing study was not carried out during this thesis, preparatory experiments were used to give clues on the ageing behavior of the OPD with p-doped PBDTTT-c as HTL. In this report, we present the reduced humidity impact on the OPD without PEDOT:PSS and introduce temperature ageing results showing good device stability. As those results are not sufficient to conclude on the temperature instability of OPD with p-doped layers, a detailed experimental design is presented for future works.

4.4.1 Reduced humidity impact on series resistance

Humidity is the main external parameter influencing PEDOT:PSS related device degradation [37, 38]. To make sure that the replacement of PEDOT:PSS by a p-doped polymer reduces the impact of humidity on the device stability, we carried out a short ageing study on both devices in humid atmosphere.

The diodes with PEDOT:PSS and p-doped PBDTTT-c as HTL are stored in the dark in a climate chamber where relative humidity (RH) and temperature can be tuned. As the diodes are encapsulated to avoid the fast degradation of the top aluminum electrode with oxygen, strong ageing conditions are used to accelerate the water diffusion in the devices. The humidity was set at 80% RH while the temperature was kept at 25°C to avoid potential dopant diffusion issues. No bias is applied to the diodes during the ageing and I(V) measurements are carried out in the dark and under illumination regularly for 286 hours.

Figure 4.14 exhibits dark (a) and light (b) J(V) measurements for the diode with PEDOT:PSS as HTL over time. The dark and light current densities remain stable in the reverse bias regime while the injection current is reduced by a factor two after 286 hours at 80% RH and 25°C. The linear scale used in Figure 4.15 emphasizes the injection current decrease with time exposure to humidity. This evolution is consistent with the series resistance increase expected for PEDOT:PSS when exposed to humidity.

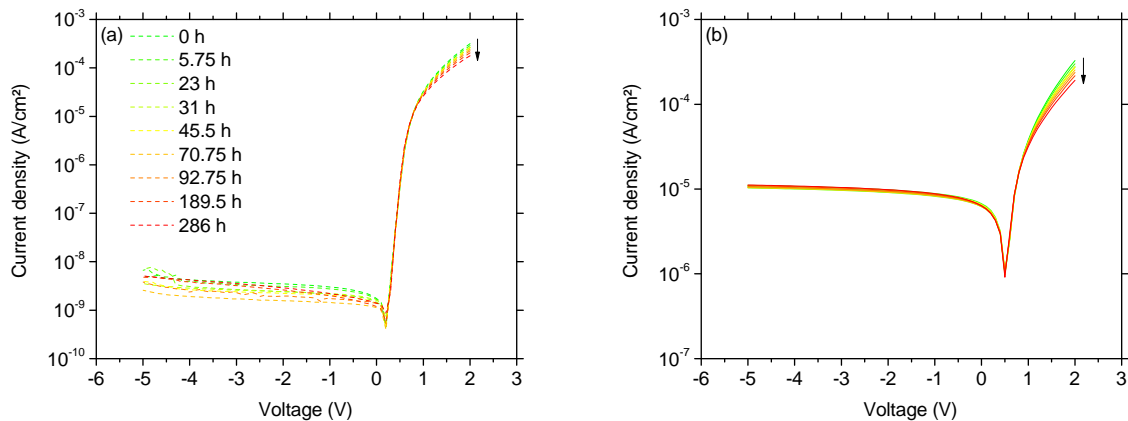


Figure 4.14: Current density in the dark (a) and under illumination (530 nm, 650 mW/m²) (b) over time when stored in the dark at 25°C and 80% RH for the diode with PEDOT:PSS as HTL.

In contrast to PEDOT:PSS, the use of p-doped PBDTTT-c as HTL does not induce degradations of the injection current as shown in Figure 4.16 (a) and (b). This observation strengthens the hypothesis of series resistance increase due to absorbed water in PEDOT:PSS and highlights the responsibility of PEDOT:PSS in OPD and OPV degradation due to humidity. After 286 hours of storage in a strong humid atmosphere of 80% RH, no changes in the J(V) characteristics can be observed for the diode with p-doped PBDTTT-c as HTL.

The 286 hours of storage in the dark at 80% RH and 25°C emphasizes the impact of PEDOT:PSS sensitivity to humidity on OPD characteristics and highlights the stability enhancement by replacing this layer with a p-doped polymer. A longer ageing study would be necessary to confirm this trend and make sure that the p-doped polymer is not impacted by humidity at a slower rate. This experiment could be accelerated by removing the encapsulation of the diode. However, to enable the encapsulation removal, the use of

4.4. Preliminary ageing studies on OPDs with p-doped PBDTTT-c as HTL

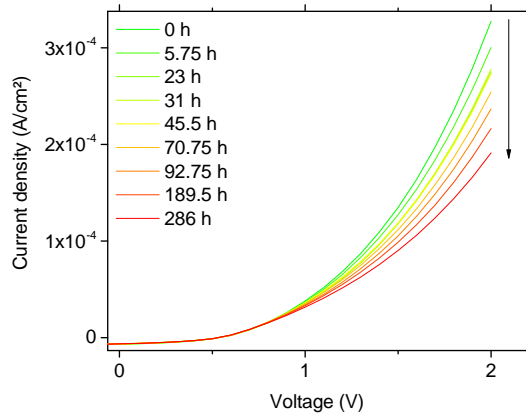


Figure 4.15: Current density under illumination (530 nm , 650 mW/m^2) over time in linear scale when stored in the dark at 25°C and 80% RH for the diode with PEDOT:PSS.

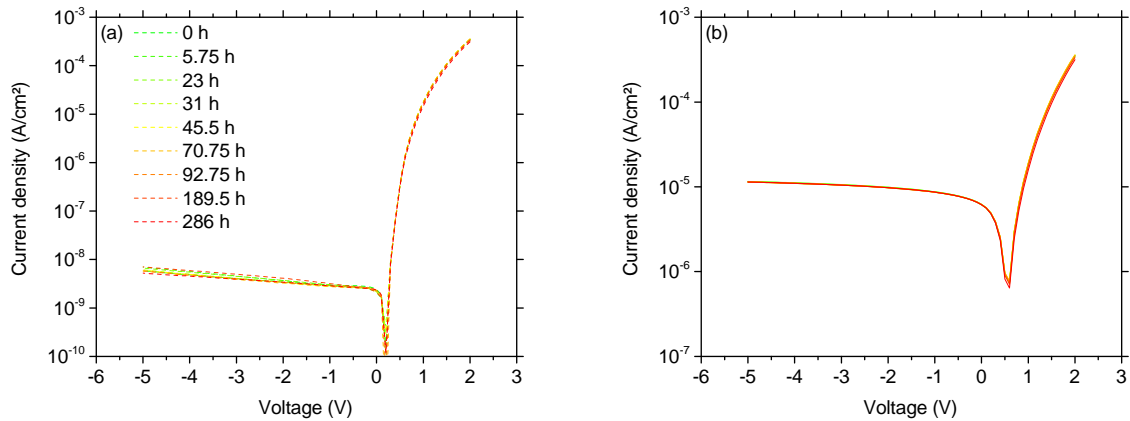


Figure 4.16: Current density in the dark (a) and under illumination (530 nm , 650 mW/m^2) (b) over time when stored in the dark at 25°C and 80% RH for the diode with p-doped PBDTTT-c as HTL.

a top electrode that is not sensitive to oxygen and water, like gold, is required.

4.4.2 Thermal ageing with p-doped polymer as HTL

As temperature is expected to be the limiting factor for the stability of devices containing localized dopants, a thermal ageing study needs to be carried out on those devices. We present preliminary results about the impact of temperature on the OPD with p-doped PBDTTT-c as HTL. This experiment will give clues about the OPD behavior with temperature and will help designing a proper ageing study.

An Dai has shown that the p-dopant $\text{Mo}(\text{tfd-COCF}_3)_3$ diffuses in a 100 nm pure PB-

DTTT-c layer at 70°C within one hour and diffusion starts to be effective at 50°C [25]. Further experiments on p-doped P3HT suggest a lower diffusivity of dopants in a bulk heterojunction due to the reduction of diffusion paths. A temperature of 50°C is then chosen for a thermal ageing of one week on the OPD containing p-doped PBDTTT-c as HTL. A heating resistance is used to maintain the diode at a constant temperature. To follow the impact of temperature on OPD characteristics, the device has been characterized before and after ageing.

Figure 4.17 (a) exhibits the $J(V)$ characteristics of the OPD before and after thermal ageing. If diffusion of dopant occurs from the doped layer to the blend, we expect a degradation of the injection regime. However, after one week of storage at 50°C, the injection regime is not degraded. A slight decrease of the dark current density in the reverse bias regime can be observed. The origin of this enhancement remains to be understood. If we consider that the holes and electron energy barriers remain unchanged in the reverse bias regime, a decrease of the dark current density can be explained by a lower density of traps. A long exposure at 50°C can lead to a rearrangement of the active layer reducing the SRH (Shockley Read Hall) recombination and generation.

The EQE spectra measured at 0, -2 and -5 V before and after thermal ageing are shown in Figure 4.17 (b). The stability of EQE levels obtained before and after thermal ageing are consistent with the unchanged light current density in the reverse bias regime. A small change in the shape can be noticed with slightly lower values around 650 nm. This tendency needs to be confirmed with longer studies.

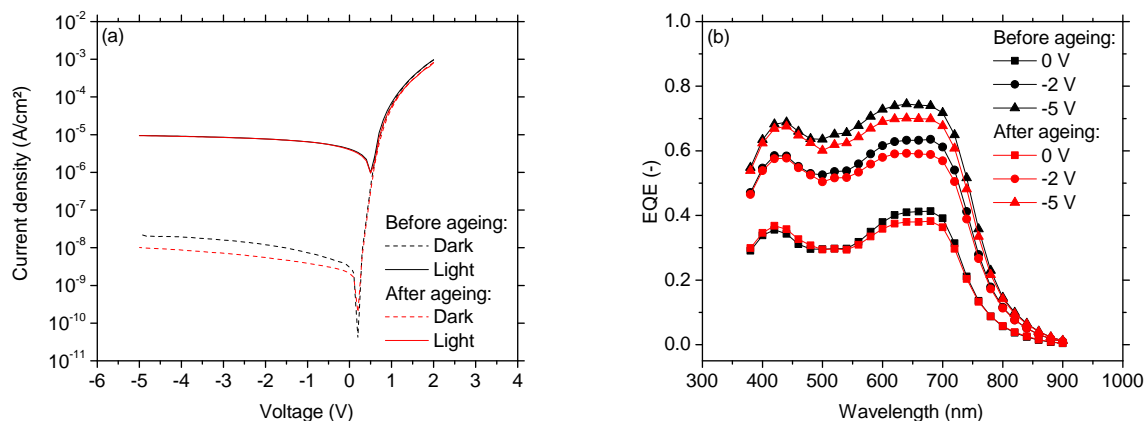


Figure 4.17: Current density in the dark and under illumination (530 nm, 650 mW/m²) (a) and EQE at 0, -2 and -5 V (b) for the diode with p-doped PBDTTT-c as HTL before and after one week at 50°C in the dark.

From this short preliminary ageing study, we show that the OPD with p-doped PBDTTT-c does not suffer from dopant diffusion in the active layer within one week at 50°C. To confirm that Mo(tfd-COCF₃)₃ is less prone to diffusion than the usual p-dopant F₄TCNQ, longer studies need to be carried out at 50°C and higher temperatures. Parallel experiments can be made with F₄TCNQ as comparison. With its planar structure, we expect the diffusivity of F₄TCNQ to be higher than Mo(tfd-COCF₃)₃.

4.4. Preliminary ageing studies on OPDs with p-doped PBDTTT-c as HTL

4.4.3 Establishment of a detailed experimental design for future works

In this thesis we propose an alternative HTL for PEDOT:PSS with the aim of improving the OPD stability with regard to humidity, oxygen and UV. However, introducing small molecules in a complex structure can lead to diffusion issues accelerated with temperature. The preliminary tests previously presented might indicate a good thermal stability of the OPD composed of Mo(tfd-COCF₃)₃ doped PBDTTT-c as HTL. To validate this result and deepen the study on the impact of dopant diffusion on OPD characteristics, we suggest an experimental design for thermal ageing.

During the last part of the thesis, an ageing bench developed by P. Lienhard [200] has been adapted to carry out thermal ageing. I(V) measurements can be made in the dark and under white light illumination over time with a permanent stress applied to the device (bias or illumination). The experimental setup is placed in a glovebox to control the environment in nitrogen or dry air [200]. A heating resistance has been added to the set-up. A PID controller is used to tune the temperature and a thermocouple is placed between the top electrode and the encapsulation of a similar structure to the one studied to reach the desired temperature. The thermocouple can also be used to follow the temperature variations in the diode over time during the ageing experiment.

This experimental set-up can be used to continue the thermal ageing study on OPDs containing a doped layer. The goal of this study is to determine the diffusivity of Mo(tfd-COCF₃)₃ in the active layer and its impact on the device characteristics. I(V) characterization over time at 50°C, 75°C and 100°C can be carried out in order to evaluate the ability of Mo(tfd-COCF₃)₃ to diffuse. A complete electrical characterization (capacitance, linearity, ideality factor) can be made before and after ageing to understand the impact of the evolved doping profile on the OPD figures of merit. A similar study can be carried out on OPD with F₄TCNQ doped PBDTTT-c as HTL in order to confirm the improved thermal stability of Mo(tfd-COCF₃)₃ over F₄TCNQ.

At a given temperature, chosen to induce diffusion for both dopants, the impact of bias stress can also be studied. If the dopants form negative ions by accepting an electron from the polymer HOMO level, they should be influenced by the electric field in the device causing their diffusion toward the positive electrode. When the OPD is used for imaging or sensing applications, a constant voltage is applied to the device (typically -2 or -5 V). The stability of the dopant under constant electric field is then required.

In the reverse bias regime, the bottom electrode in ITO/PEIE is connected to the ground while a negative bias is applied to the top electrode in aluminum. As shown in Figure 4.18, we expect the potential anions formed by activated dopants to be attracted toward the bottom electrode. This phenomenon would accelerate the dopant diffusion in the active layer.

I(V) characterization over time can be reproduced with the addition of a constant bias stress at -2 and -5 V. The ageing kinetic can be compared to the one without bias stress. If anions are formed with doping we expect an accelerated diffusion in the device. However, if a charge transfer complex is formed between the polymer and the dopant creating a strong coupling between both components as suggested in Chapter 3, it is unlikely that

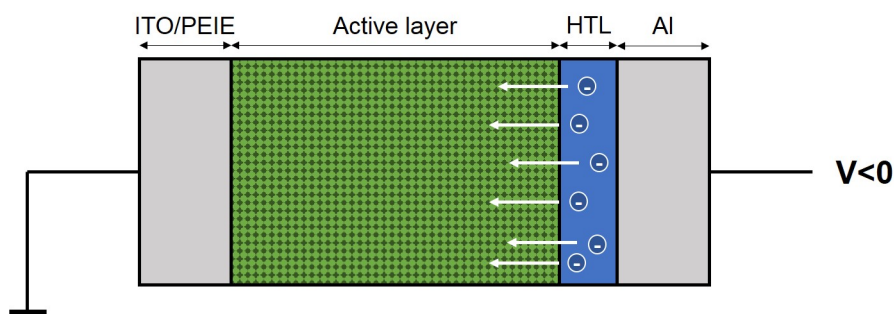


Figure 4.18: Schematic of the OPD cross-section showing the potential diffusion of dopant anions in the active layer under reverse bias condition.

diffusion happens and its kinetic should not be electric field dependent.

Afer having introduced results indicating a better stability of the OPD stored in humidity when PEDOT:PSS is replaced by p-doped PBDTTT-c, we carried out a first experiment to study the influence of thermal ageing on dopant diffusion. Preliminary results are encouraging with no diffusion at 50°C for one week. To complete this thermal ageing study, a detailed experimental design is proposed. It will help assessing the ability of Mo(tfd-COCF₃)₃ to diffuse in the active layer as compared with F₄TCNQ. The use of bias stress might also strengthen the hypothesis of charge transfer complex formation highlighting one of its advantages: a reduced dopant diffusion.

4.5 Summary and outlook

In this chapter the Mo(tfd-COCF₃)₃ doped PBDTTT-c has been integrated in an OPD to replace PEDOT:PSS. It has been demonstrated in the literature that the widely used HTL material PEDOT:PSS plays a role in the relatively poor stability of the devices in the presence of humidity. The goal of this study is to propose an alternative to PEDOT:PSS leading to similar or better performances of the OPD.

OPDs with PEDOT:PSS and p-doped PBDTTT-c are fabricated using Soft Contact Transfer Lamination for the HTL deposition. The J(V) and EQE figures of merit are presented showing similar performances for both diodes with EQEs reaching 70% at -2 V. The use of p-doped PBDTTT-c leads to improved detectivity due to a slight decrease of the dark current density in the reverse bias regime. The detectivity calculated at $1.9 \times 10^{13} \text{ cmHz}^{1/2}\text{W}^{-1}$ for the OPD containing the p-doped polymer layer is among the best values reported in the literature and competes with silicon-made counterpart showing typical detectivities around $10^{13} \text{ cmHz}^{1/2}\text{W}^{-1}$ for imaging applications.

To deepen our understanding of the impact of PEDOT:PSS replacement by a p-doped polymer layer on the OPD behavior, further analyses have been carried out. We have

4.5. Summary and outlook

highlighted the nonlinear evolution of the photocurrent at high light intensities. This issue has been attributed to the significant series resistance of the p-doped polymer compared to PEDOT:PSS leading to Langevin recombination. This study emphasizes the need to improve the doping efficiency in organic semiconductors in order to reach higher conductivities.

The use of a characterization technique enabling a sensitivity mapping on the diode has highlighted an advantage of p-doped PBDTTT-c over PEDOT:PSS as HTL when a top electrode is used. With the use of p-doped polymer, no localization step is required for the HTL as the active area of the diode is determined by the bottom and top electrodes. This difference with PEDOT:PSS has been attributed to the 5 orders of magnitude lower conductivity. The HTL property is enabled by the effective barrier lowering at the interface with the top electrode. However, as the nonlinear behavior of the diode requires the improvement of the doped layer conductivity, HTL patterning might become necessary.

Finally, preliminary ageing studies have been carried out on the OPDs. The first results indicate the improvement of the OPD stability in humid atmosphere. As diffusion is expected to be the main limiting factor for devices containing dopants, a short thermal ageing study has been done. The OPD figures of merit show no degradation after a storage of one week at 50°C. This limited diffusion is attributed to the 3D structure of $\text{Mo}(\text{tfd-COCF}_3)_3$ and we expect a stronger diffusion for F_4TCNQ in a similar structure and ageing condition. To complete this preliminary test a detailed experimental design is proposed. A comparison between both types of dopants can be carried out in temperature completed with bias stress to determine the electric field impact on diffusion.

To conclude, we present a proof of concept for the replacement of PEDOT:PSS in OPDs by a p-doped polymer layer. We deepen this work by studying the limitations and improvements of this alternative and present encouraging results regarding the stability of this new device.

5

Impact of unintentional oxygen doping on organic photodetectors

Chapter contents

5.1	Experiment	145
5.2	Impact of oxygen plasma treatment on OPD performances	146
5.2.1	IV characteristics	146
5.2.2	External Quantum Efficiency (EQE)	147
5.2.3	Capacitance measurements	149
5.2.4	Summary and Hypothesis	153
5.3	p-doping impact on electronic structure of OPD active layer	154
5.3.1	Hole conductivity increase	154
5.3.2	Trap levels determination by admittance spectroscopy	156
5.3.3	Summary	160
5.4	Assumption verification with TCAD simulations	161
5.4.1	Simulation principles and parameters	161
5.4.2	Electrical characterization fitting	162
5.4.3	Band bending explanation	167
5.5	Summary and outlook	173

The first organic photodetectors and solar cells developed were processed with a standard structure [65] where the holes were collected by the bottom electrode and the electrons by the top electrode. However, this architecture shows several issues. In standard structures, a top electrode with a low work-function is required (e.g. aluminum or calcium) which is very sensitive to oxygen and moisture [253, 254]. For example, aluminum is transmuted into Al_2O_3 , which is insulating and lowers the photodetector efficiency. Besides, low work-function electrodes are usually evaporated non-transparent materials, which can be an advantage if we want reflection on the back electrode but also a drawback when illumination from both sides and full solution processing are desired. Moreover, the hole transport layer PEDOT:PSS used as bottom electrode is known to degrade ITO [227]. To overcome those issues, the structure has been inverted and PEDOT:PSS is deposited on top of the active layer [228].

The main challenge of this inverted structure is the HTL processing. Water-based PEDOT:PSS presents the advantage to allow solution processing but is incompatible with the hydrophobic properties of most organic active layers. When processed in solution, we indeed observe a dewetting of the PEDOT:PSS on the previous layer. To allow PEDOT:PSS deposition by solution processing on organic layers, additives need to be used with PEDOT:PSS (e.g. Surfynol [225]) or surface treatments need to be carried out on the active layer to change its surface tension and enable good HTL deposition. Among those surface treatments, O_2 plasma is the most used technique [234, 232]. O_2 plasma treatment at low pressure improves the active layer wettability by creating functional groups at the interface [255, 256].

However, it is widely reported that oxygen is detrimental to organic devices performances [20, 257, 219, 258]. Oxygen is known to p-dope organic semiconductors increasing their conductivity [215] but also to introduce gap states [259, 260, 261, 262]. Oxygen related degradations are nowadays one of the major issues in aging studies of organic photodetectors and solar cells [20]. It is then crucial to understand the impact of oxygen when used as surface treatment on the device initial performances.

The group of Baierl *et al.* [255] compared inverted structure processed with O_2 plasma treatment with standard structures with and without O_2 plasma treatment. In this study they show that O_2 plasma does not lead to performance deterioration of organic solar cells for usual operating voltages. However, the EQE spectra were not fully analyzed and the current density in the direct regime could not be directly compared due to different injection barriers. In the present work, we process the same structure (inverted) with and without O_2 plasma treatment, enabling direct evaluation of plasma impact. Moreover, Wang *et al.* [35] showed that an unintentional n-doping of the solar cell active layer due to polyethylenimine (PEI) coated ITO degrades its performances with a change of the EQE spectra. It is then highly probable that oxygen diffusion in the active layer induced by O_2 plasma treatment would alter OPD performances through unintentional p-doping

5.1. Experiment

of the active layer.

In this chapter we propose a complete study of the O_2 plasma treatment impact on OPD performances with a full electrical characterization of the devices and further analyses are carried out to deepen our understanding on oxygen doping.

5.1 Experiment

The structure of the OPD studied in this chapter is shown in Figure 5.1 and in Appendix A as Structure 5. In this inverted structure, 110 nm thick ITO coated with a mono-layer of PEIE is used as Electron Transport Layer (ETL) and 100 nm thick PEDOT:PSS is used as Hole Transport Layer (HTL). Since PEDOT:PSS is not localized but deposited as full layer, a top electrode in aluminum is evaporated to define the active surface area of the diode. The blend of PBDTTT-c:C₆₀-PCBM is similar to the study carried out in Chapter 4 with a thickness of 500 nm (Structure 4).

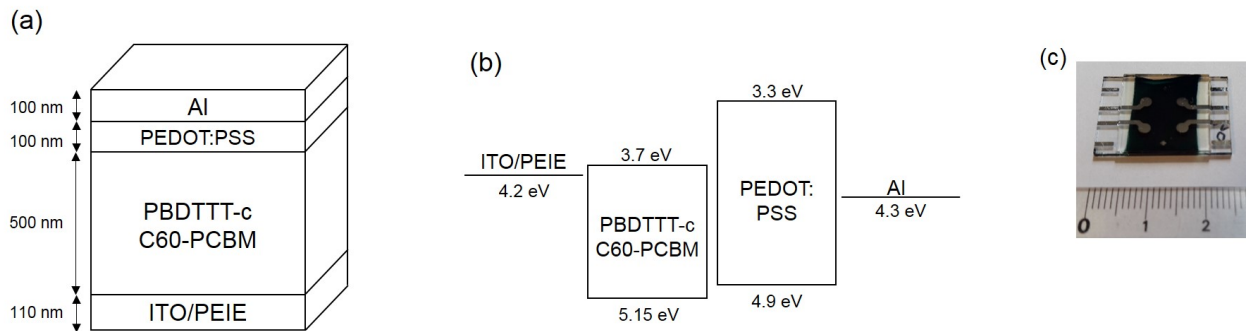


Figure 5.1: Schematic of the OPD stack processed in this study (a) and band diagram (b) showing the energy levels of the different layers. Picture of the final OPD device (c). (Structure 5)

To study the impact of O_2 plasma treatment on the OPD performances we use Soft Contact Transfer Lamination (SCTL) to deposit PEDOT:PSS on the active layer. This deposition technique makes the surface treatment optional and enables the study of its impact using similar structures. The processing steps for PEDOT:PSS lamination are described in Chapter 4 (Figure 4.4).

Two different devices are studied in this chapter. One device has been processed without plasma treatment while the active layer of the second device is treated with O_2 plasma before PEDOT:PSS lamination. The plasma treatment is carried out for 60s with a power of 500 W, a pressure of 1100 mTorr and a flow of 200 sccm. We cover the samples during the plasma treatment with metallic grid, which stops UV-radiations while maintaining the access of ionic species to the layer surface.

Two substrates containing four diodes each are processed for both processing conditions to verify the reproducibility. All electrical characteristics shown in this chapter have been measured on a representative device for each condition.

5.2 Impact of oxygen plasma treatment on OPD performances

5.2.1 IV characteristics

Figures 5.2 (a) and (b) show $J(V)$ characteristics of devices processed with and without O_2 plasma treatment in the dark and under light in semi-logarithmic and linear scales. The current density has been calculated using the active area measured by mapping the sensitivity on the diode. The areas obtained are 3.53 mm^2 for the device without plasma treatment and 4.54 mm^2 for the device with plasma treatment. This difference is due to the manual wiping of PEDOT:PSS. To avoid influence from the surface variations we plot the current density with respect to the applied voltage.

We can observe on Figure 5.2 (a) an injection current increase of one order of magnitude at +2 V after O_2 plasma treatment. This behavior can be explained either by a carrier mobility increase in the active layer or a collection energy barrier decrease at one interface. Figure 5.2 (a) also shows a light current density decrease in the reverse regime after O_2 plasma treatment which could be explained by the formation of deep traps leading to Shockley Read Hall (SRH) recombinations. Using light and dark current densities measured at -2 V we obtain sensitivities of 0.3 A/W for the device without plasma treatment and 0.14 A/W after O_2 plasma exposure.

The linear scale used on Figure 5.2 (b) highlights the V_{OC} decrease from 0.55 V to 0.4 V when an O_2 plasma is used while the built-in voltage V_{bi} remains similar for both devices (0.59 V without and 0.54 V with O_2 plasma treatment). The built-in voltage V_{bi} is determined by the difference between the electrodes work-functions, while the open-circuit voltage V_{OC} is highly influenced by the blend quasi-Fermi levels. As V_{bi} remains similar after O_2 plasma treatment, the V_{OC} decrease is more likely due to the blend layer than the electrodes. This evolution will be further developed in Section 5.4.

The linear scale also highlights the J_{SC} decrease, consistent with the light current density decrease in the reverse bias regime. Finally, the fill factor (FF) increases from 38 % to 59 % after O_2 plasma exposure. This increase is probably due to the injection improvement after O_2 plasma treatment and might be related to the increase in mobility [263]. All extracted parameters are summarized in table 5.1.

Table 5.1: Parameters extracted from I-V characteristics for the devices with and without O_2 plasma treatment.

Diode	V_{OC} (V)	V_{bi} (V)	J_{SC} (A/cm ²)	FF (%)	Sensitivity @ -2 V (A/W)
No plasma treatment	0.55	0.59	-5.75×10^{-6}	38	0.3
O_2 plasma treatment	0.4	0.54	-1.64×10^{-6}	59	0.14

$J(V)$ characteristics measured for similar devices processed with and without O_2 plasma treatment on the active layer show a decline of the photodetection performances after plasma treatment with a significant sensitivity decrease. Further analyses are required to understand the phenomena driving this degradation and the parameters evolution.

5.2. Impact of oxygen plasma treatment on OPD performances

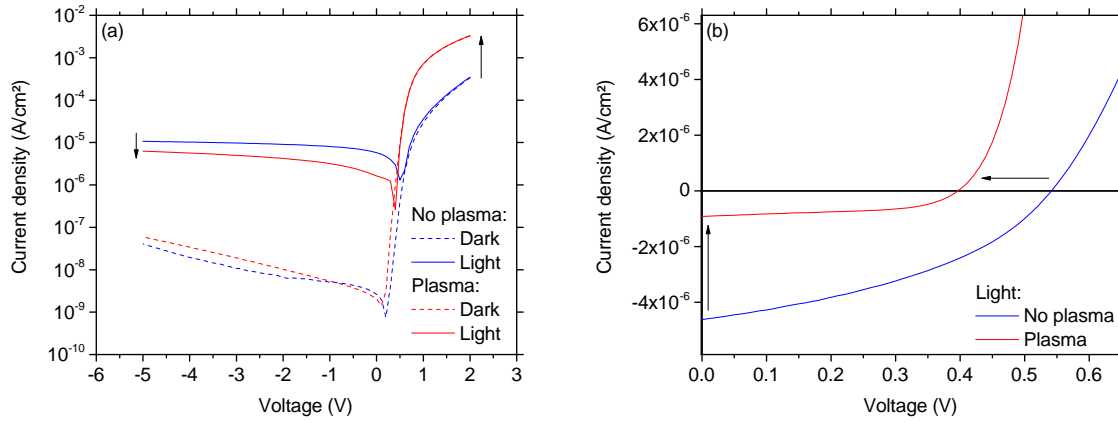


Figure 5.2: Current density in the dark and under illumination (530 nm, 0.3 W/m²) for the device without plasma treatment in blue and the device exposed to O₂ plasma in red in a semi-logarithmic scale (a) and in linear scale (b).

5.2.2 External Quantum Efficiency (EQE)

As explained in Chapter 4, the External Quantum Efficiency (EQE) determines the ratio between incident photons and extracted charges with respect to the incident photon wavelength. This figure of merit can also give clues on field dependent behaviors of photodetectors.

Figure 5.3 highlights the EQE decrease at -2 V due to O₂ plasma treatment, consistent with the sensitivity decrease. The EQE spectra exhibit two peaks, one around 440 nm and the other around 660 nm. The first peak is attributed to the fullerene absorption, while the second one is mainly due to the polymer absorption. When no O₂ plasma is used, the EQE reaches values of 62 % at 440 nm and 65 % at 660 nm while after O₂ plasma treatment the EQE is reduced to 30 % at 440 nm and 46 % at 660 nm. The change in the EQE shape after plasma treatment leads to a wavelength dependent decrease of the EQE (i.e. the peak at 660 nm being less affected than the one at 440 nm).

The EQE spectra evolution suggests a decreasing absorption in the fullerene after O₂ plasma treatment. To identify potential chemical modifications in the blend changing the absorption properties, we carried out UV-visible absorption spectroscopy on a blend before and after O₂ plasma treatment. Figure 5.4 shows that this treatment induces no significant changes on the absorption spectrum in the visible area. Therefore, the changes of the EQE with plasma treatment are not due to modifications in the absorption performances but in the carrier extraction efficiency.

EQE measurements are carried out at different biases (0, -2 and -5 V) for both devices and represented in Figure 5.5 (a) and (b). An increase of the EQE with the applied bias is observed for the device without O₂ plasma and its shape remains independent of the applied bias, and therefore of the electric field in the layer. The device exposed to O₂ plasma exhibits an EQE increase with the applied bias as well, but the electric field has

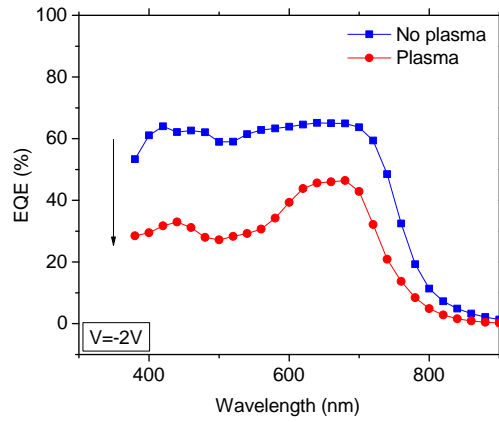


Figure 5.3: External Quantum Efficiency (EQE) at -2 V for the device without plasma treatment in blue and the device exposed to O₂ plasma in red.

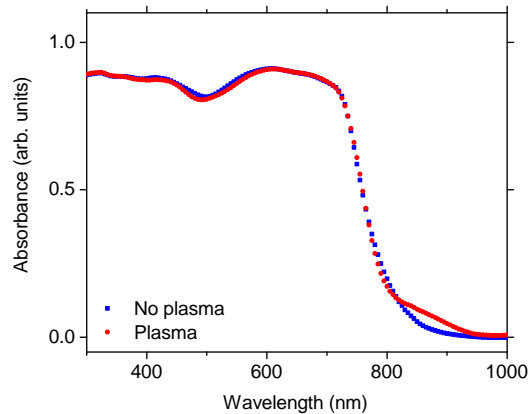


Figure 5.4: Absorption spectra for PBDTTT-c:C60-PCBM blend before (blue) and after (red) an O₂ plasma treatment of 60s.

an impact on the shape of the EQE. Indeed, the peak around 660 nm undergoes a more pronounced increase with bias than the peak around 440 nm. Therefore, the shape of the EQE is similar for both devices when no bias is applied while it is modified by the electric field for the device processed with O₂ plasma treatment.

The electric field dependency of the EQE can be explained by charged traps in the gap leading to band bending at one interface. This hypothesis has already been developed by J. Wang *et al.* [35] with the active layer n-type doping induced by PEI used to tune the work-function of the cathode.

5.2. Impact of oxygen plasma treatment on OPD performances

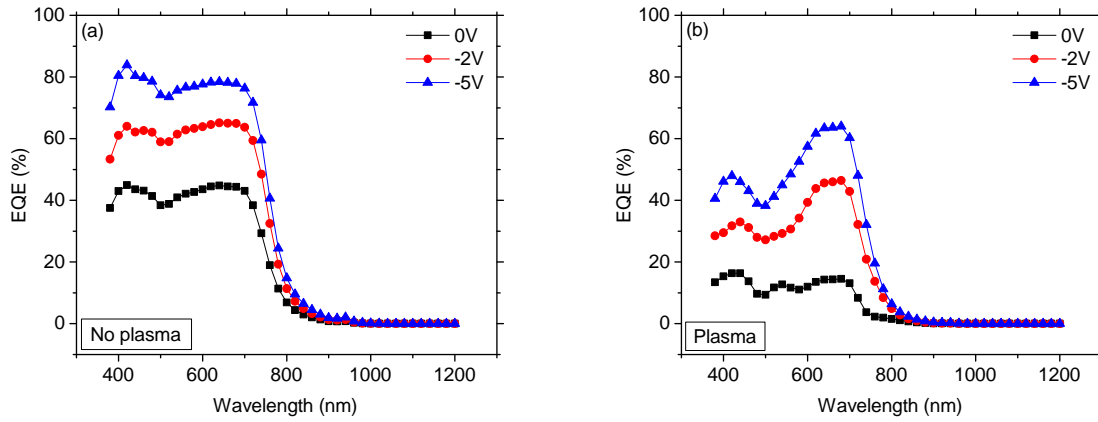


Figure 5.5: External Quantum Efficiency (EQE) at different biases for the device without plasma treatment (a) and the device exposed to O_2 plasma (b).

5.2.3 Capacitance measurements

The capacitance of the diodes with respect to the applied bias has been measured at 300 K with and without O_2 plasma treatment (Figure 5.6). The increase of the capacitance peak at low bias with plasma treatment indicates that more carriers are available in the device. Also, after O_2 plasma treatment the geometric capacitance is not reached at -2 V suggesting that the depletion width is smaller than the active layer thickness. Thus, $C(V)$ measurements suggest the decrease of the depletion width caused by an increased doping concentration when O_2 plasma is used.

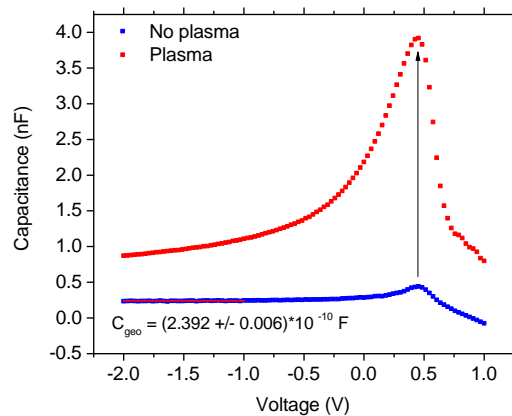


Figure 5.6: Capacitance-Voltage plot for the device without plasma treatment in blue and the device exposed to O_2 plasma in red.

In order to extract the hole density p in the active layer for both devices we use the Mott-Schottky analysis as explained in section 2.3.2. For an homogeneous doping density

in the layer, the hole density p can be calculated using the following relation:

$$p = -\frac{2}{q\epsilon_0\epsilon_r A^2 \frac{d\left(\frac{1}{C^2}\right)}{dV}} \quad [cm^{-3}] \quad (5.1)$$

where q is the elementary charge, ϵ_0 the vacuum permittivity, ϵ_r the relative permittivity of the blend and A the active layer area of the diode. Knowing the area of the diode from sensitivity mapping and the layer thickness, the relative permittivity of the active layer can be extracted from $C(V)$ measurements when the whole layer is depleted. This condition is reached for $V < -1$ V with the saturation at the geometric capacitance C_{geo} for the device without plasma treatment. The geometric capacitance C_{geo} is defined as follows:

$$C_{geo} = \frac{\epsilon_0\epsilon_r A}{t} \quad [F] \quad (5.2)$$

with t the active layer thickness. Using this relation we obtain a relative permittivity of 3.6 ± 0.1 for the active layer. This value is consistent with the relative permittivities usually obtained for organic materials [59].

The hole density for the device without plasma treatment is extracted in the linear region of the Mott-Schottky plot and is around 10^{15} cm^{-3} (Figure 5.7 (a)). However, as it has been developed in Section 2.3.2, Kirchartz *et al.* have determined that, for a diode with a Schottky contact and a layer thickness around 300 nm, the Mott-Schottky technique is not appropriate for hole densities below $4 \times 10^{15} \text{ cm}^{-3}$ [184]. For an active layer thickness of 500 nm, the density limit would be slightly lower but still around 10^{15} cm^{-3} . Therefore, it is difficult to conclude whether the extracted value at $(1.7 \pm 0.1) \times 10^{15} \text{ cm}^{-3}$ is reliable.

The Mott-Schottky plot for the device exposed to O_2 plasma in figure 5.7 (b) does not exhibit a linear regime suggesting that the doping concentration is not homogeneous in the layer. The hole density has been extracted at different bias ranges of the Mott-Schottky plot leading to values around $(3 - 4) \times 10^{16} \text{ cm}^{-3}$. Therefore we can conclude that using an O_2 plasma treatment on the active layer before PEDOT:PSS deposition increases the hole density by at least one order of magnitude. This observation is consistent with the formation of charged traps in the band-gap leading to electric field dependent EQE.

For a non-homogeneous doping, the doping profile in the layer can be determined using the generalized Mott-Schottky law [182]:

$$\frac{d\left(\frac{1}{C_j^2}\right)}{dV} = -\frac{2}{qA^2\epsilon_0\epsilon_r p(w)} \quad (5.3)$$

with

$$C_j = \frac{A\epsilon_0\epsilon_r}{w} \quad (5.4)$$

and w the depth of the depletion zone.

Figure 5.8 shows the hole density profile in the active layer of the device exposed to O_2 plasma, which has been calculated using relations 5.3 and 5.4. We observe an

5.2. Impact of oxygen plasma treatment on OPD performances

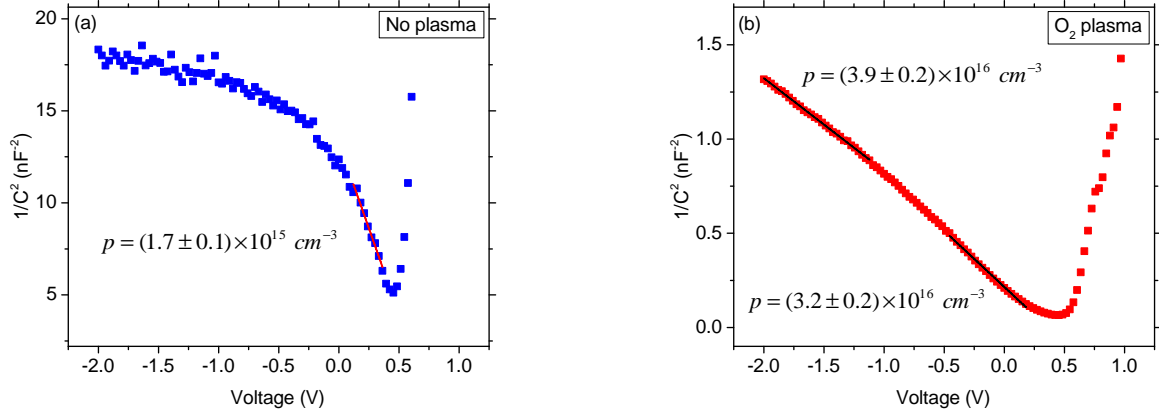


Figure 5.7: Mott-Schottky plots for the device without plasma treatment (a) and the device exposed to O₂ plasma (b).

increase of the hole density p from $2.9 \times 10^{16} \text{ cm}^{-3}$ 75 nm above the ITO/PEIE electrode to $5.4 \times 10^{16} \text{ cm}^{-3}$ 225 nm above the ITO/PEIE electrode. This analysis highlights a doping profile with higher values on the top of the active layer close to the PEDOT:PSS electrode. Since the O₂ plasma treatment is performed on the top of the active layer before the deposition of PEDOT:PSS, this observation would be consistent with oxygen diffusion in the active layer from the top to the bottom leading to a doping density gradient. Therefore, we can notice that the effect of O₂ plasma treatment is not limited to the surface of the active layer.

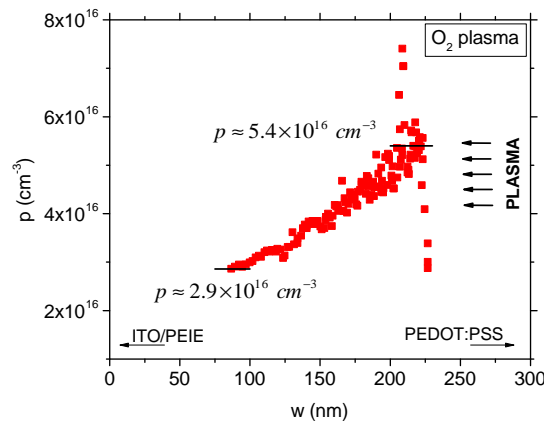


Figure 5.8: Doping density profile in the active layer for the diode exposed to O₂ plasma.

In order to analyze the temperature dependency of hole density p , $C(V)$ measurements are carried out at temperatures ranging from 200 to 300 K. When no plasma treatment is used the $C(V)$ curve remains constant at the geometric capacitance for the voltage range analyzed up to 280 K (Figure 5.9 (a)). At higher temperatures the free carrier density increase leads to the formation of a small peak around V_{bi} . In figure Figures 5.9 (b) we

can observe the strong temperature impact on the free carrier generation process leading to the increase of the peak intensity for the device treated with O₂ plasma.

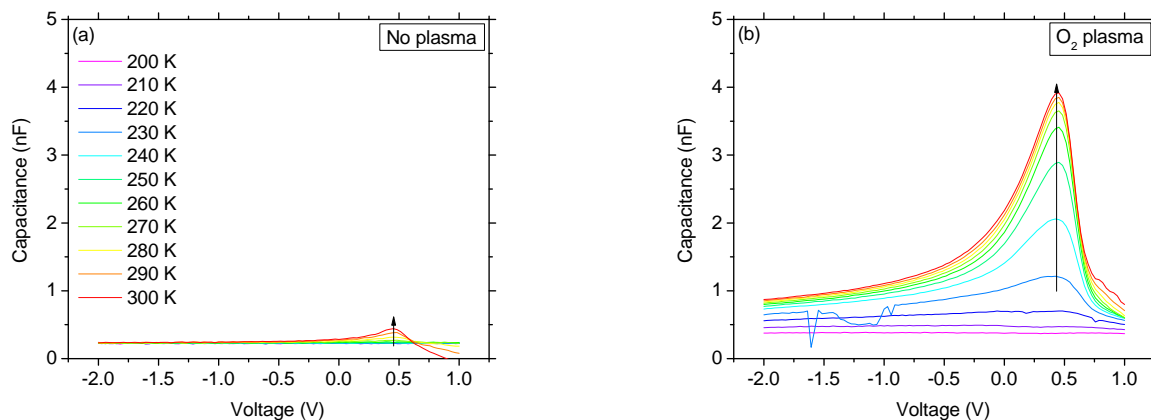


Figure 5.9: Capacitance-Voltage plot for the device without plasma treatment (a) and the device exposed to O₂ plasma (b) for temperatures ranging from 200 to 300 K.

We can extract the hole density p using the Mott-Schottky analysis at different temperatures and follow its evolution. When no plasma treatment is used (Figure 5.10 (a)), the hole density decreases while the temperature increases. However, the opposite evolution can be observed with plasma treatment. Figures 5.10 (b) shows that p is activated by temperature and follows an Arrhenius law:

$$p \propto \exp\left(-\frac{\Delta E_A}{k_B T}\right) \quad (5.5)$$

where ΔE_A represents the activation energy of the doping mechanism [181]. An activation energy of 60 meV is obtained after O₂ plasma treatment. The two different behaviors observed indicate that the origin of the free carriers activation are different for both devices. Although it is not understood why p decreases with temperature without plasma, its temperature dependence after O₂ plasma treatment is characteristic of doping with the formation of acceptor traps above the blend HOMO.

5.2. Impact of oxygen plasma treatment on OPD performances

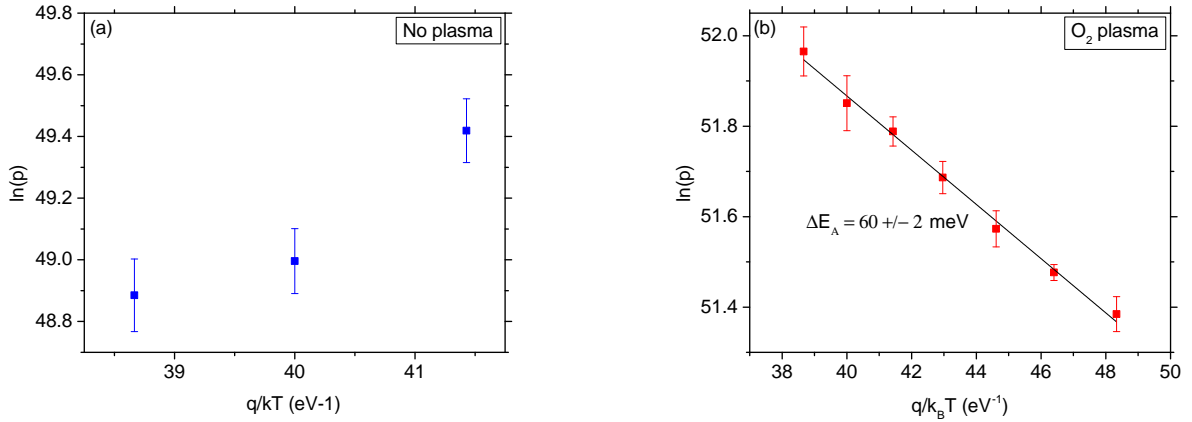


Figure 5.10: Evolution of $\ln(p)$ with $q/k_B T$ for the device without plasma treatment (a) and the device exposed to O₂ plasma (b).

5.2.4 Summary and Hypothesis

Electrical characterizations on photodetectors processed with and without O₂ plasma treatment on the active layer highlight the impact of O₂ plasma on the OPD performances. The sensitivity and the External Quantum Efficiency (EQE) of the photodetectors are reduced after plasma treatment. This degradation can be explained by the formation of deep traps leading to exciton recombination. O₂ plasma also changes the shape of the EQE probably due to band bending in the active layer caused by charged traps in the gap. As charged traps are due to doping this hypothesis is strengthened by the Mott-Schottky analysis revealing an increase in the hole density by approximately one order of magnitude. Finally, the improvement of the injection current after O₂ plasma treatment can be explained either by an injection barrier lowering or a carrier mobility increase. The hole density increase can lead to the hole mobility improvement by trap filling. These analyses are summarized in figure 5.11 (a).

All these observations can be explained by the formation of an acceptor state situated below the Fermi level in the band-gap. If the state is deep enough, it can lead to recombination. If the acceptor state is filled, it induces doping and charged states leading to band bending and electric field dependent EQE. Finally doping can explain the injection current increase if it leads to an increase in mobility. A schematic of this hypothesis is shown in figure 5.11 (b).

O₂ plasma treatment degrades significantly our photodetector performances. It is therefore crucial to understand the origin of the degradation in order to prevent such phenomena and find alternative solutions. Also, the p-doping character of oxygen has been widely reported in the literature [219, 216, 264]. Hence, we need to determine whether this p-doping ability of oxygen is responsible for the OPD degradation and what

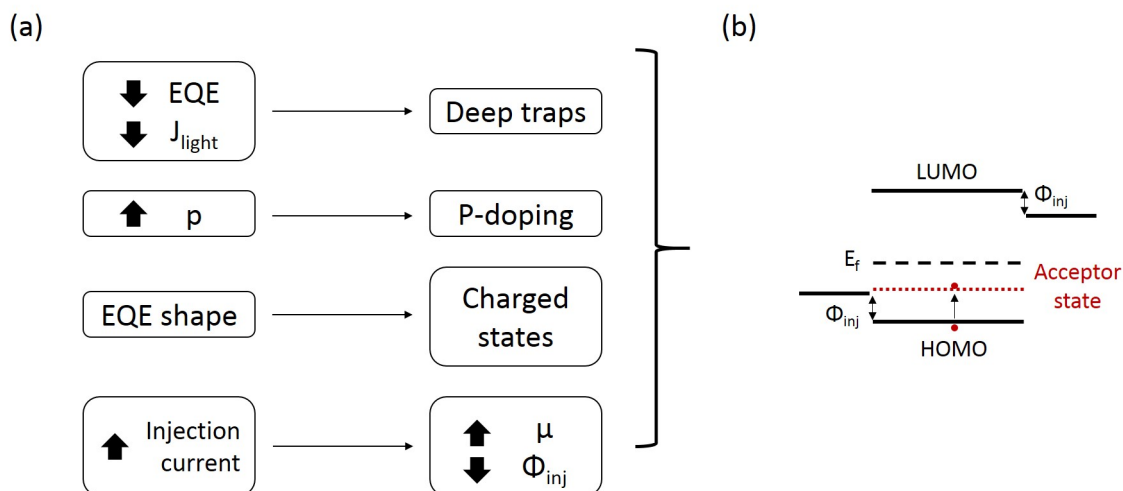


Figure 5.11: Summary of the observations made from electrical characterization and their potential causes (a). Band diagram of the blend with the acceptor level suggested to explain the observations (b).

deterioration processes are involved. Understanding the effect of oxygen is also essential regarding the challenge of organic electronics stability in ambient atmosphere usually leading to oxidation of the active layer. The following sections will be devoted to the verification of this hypothesis.

5.3 p-doping impact on electronic structure of OPD active layer

In order to validate our hypothesis of acceptor state formation above the HOMO and deepen our understanding of the impact of oxygen, complementary analyses have been carried out and will be presented in this section. Conductivity measurements using Transmission Line Method (TLM) will strengthen the p-doping hypothesis and make sure that the O₂ plasma treatment impact is not limited to the surface. Admittance spectroscopy performed at temperatures ranging from 200 to 300 K will probe potential trap states in the band gap and determine their energy level and density.

5.3.1 Hole conductivity increase

In the previous section it has been shown that the OPD processed with O₂ plasma treatment exhibits a hole density increase by approximately one order of magnitude reaching $(3-4) \times 10^{16} \text{ cm}^{-3}$. A doping concentration increase should induce a conductivity increase as both quantities are linked by the following relation:

$$\sigma_p = qp\mu_p \quad [S.cm^{-1}]. \quad (5.6)$$

In this relation σ_p is the hole density and p the hole concentration. The increase in conductivity due to oxygen has been widely observed in the literature [217, 265, 215].

5.3. p-doping impact on electronic structure of OPD active layer

To confirm the p-doping ability of our O₂ plasma treatment on the active layer we used Transmission Line Method (TLM) to follow the evolution of the hole conductivity with plasma exposure time. A cross-section of the TLM device is shown in Figure 5.12 and in Appendix A as Structure 6. Gold is chosen as the electrode material with its work-function around 5 eV close to the blend ionization energy of 5.15 eV. The chosen structure leads to a hole only device with a low contact resistance. We choose to use the same active layer thickness as in the OPD. This enables us to determine whether the O₂ plasma treatment impact is limited to the active layer surface or if the oxygen diffuses in the full layer. In the TLM device shown in Figure 5.12, the channel height is mostly limited by the electrodes thickness d . Therefore, a conductivity evolution measured on a device exposed to O₂ plasma will prove that this treatment has an impact on the bulk.

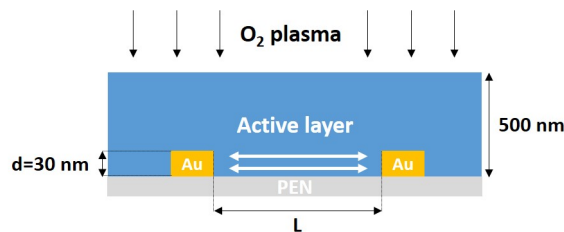


Figure 5.12: Cross-section of the TLM structure showing the active layer and gold electrodes thicknesses (Structure 6). The variable channel length L and the surface exposed to the O₂ plasma treatment are also indicated.

The resistance extracted through $I(V)$ measurements for different L/W ratios with W the channel width and L the channel length are shown in Figure 5.13. Three different treatment conditions have been analyzed: without O₂ plasma treatment, with a 60s treatment and with a 300s treatment. The 60s second treatment is similar to the one used for the OPD process. A longer plasma exposure time of 300s has been carried out to illustrate the time dependency of the plasma treatment.

A blend exposed for 60s to the O₂ plasma exhibits a series resistance decrease by one order of magnitude. Increasing the exposure time to 300s decreases the series resistance by one more order of magnitude reaching $7 \times 10^9 \Omega$. The contact resistance follows the same evolution with a decrease by two orders of magnitude after 300s of O₂ plasma exposure time. Both behaviors are explained by blend p-doping leading to a conductivity increase and the effective injection and extraction barrier lowering at the electrode/blend interface.

The conductivity σ_p has been calculated from the series resistance R_S as follows:

$$\sigma_p = \frac{1}{R_S d}. \quad (5.7)$$

The extracted conductivities, series and contact resistances are summarized in Table 5.2. Since the conductivity is inversely proportional to the series resistance we obtain a one order of magnitude increase of the conductivity after 60s of exposure. This evolution is consistent with the increase by approximately one order of magnitude in p after plasma treatment. When the TLM device is exposed to O₂ plasma for 300s the conductivity increases by two orders of magnitude reaching a conductivity around $5 \times 10^{-5} S/cm$ at

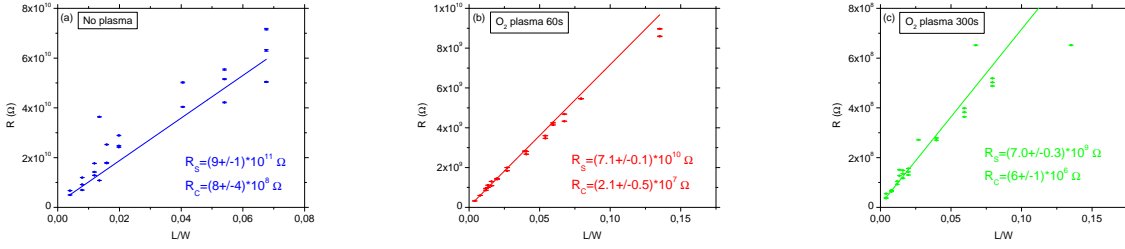


Figure 5.13: Extraction of the resistance with respect to L/W ratio without O₂ plasma treatment (a), with a 60s (b) and with a 300s O₂ plasma exposure time (c).

the bottom part of the layer. Moreover, since the oxygen needs to diffuse over 470 nm to reach the channel area, this analysis provides an additional proof that O₂ plasma has not only a surface effect but a bulk effect.

Table 5.2: Contact resistance, series resistance and conductivity extracted from TLM measurements for three different plasma treatment exposure times.

O ₂ plasma exposure time (s)	R_C (Ω)	R_S (Ω)	σ (S/cm)
0	$(8 \pm 4) \times 10^8$	$(9 \pm 1) \times 10^{11}$	$(3.9 \pm 0.4) \times 10^{-7}$
60s	$(2.1 \pm 0.5) \times 10^7$	$(7.1 \pm 0.1) \times 10^{10}$	$(4.69 \pm 0.07) \times 10^{-6}$
300s	$(6 \pm 1) \times 10^6$	$(7.0 \pm 0.3) \times 10^9$	$(4.76 \pm 0.02) \times 10^{-5}$

This experiment highlights the hole conductivity increase due to oxygen and strengthens the hypothesis of blend p-doping after O₂ plasma treatment. The observation carried out on the electrical characteristics suggests the formation of trap states with plasma treatment. Therefore, the following section will be devoted to the determination of trap states formation induced by the O₂ plasma.

5.3.2 Trap levels determination by admittance spectroscopy

The evolution of EQE and light current density suggests the formation of trap states in the bandgap after O₂ plasma treatment. This assumption is strengthened by the work of D. Knipp and J. Northrup [259] which suggests the creation of an acceptor trap state 290 meV above the pentacene HOMO when exposed to oxygen leading to p-doping when the Fermi level lies above the acceptor state. To probe the potential trap states in the blend with and without O₂ plasma treatment we use admittance spectroscopy performed on the OPDs at temperatures ranging from 200 to 300 K in steps of 10 K. The principles of admittance spectroscopy are explained in Chapter 3 and the experimental set-up is equivalent for both studies.

Frequency dependent capacitance spectra $C(\omega)$ are shown in Figure 5.14 for both devices. When no O₂ plasma treatment is used the $C(\omega)$ spectra remain flat from 10^2 to

5.3. p-doping impact on electronic structure of OPD active layer

10^6 Hz up to 260 K with a capacitance value driven by the geometric capacitance of the active layer. For temperatures above 260 K a step starts to be visible at low frequencies indicating the presence of an energy level in the band gap. When the active layer is exposed to O_2 plasma before PEDOT:PSS deposition, capacitance spectra exhibit a sharp step with a transition frequency increasing with temperature. This first observation suggests the formation of a trap level after O_2 plasma exposure.

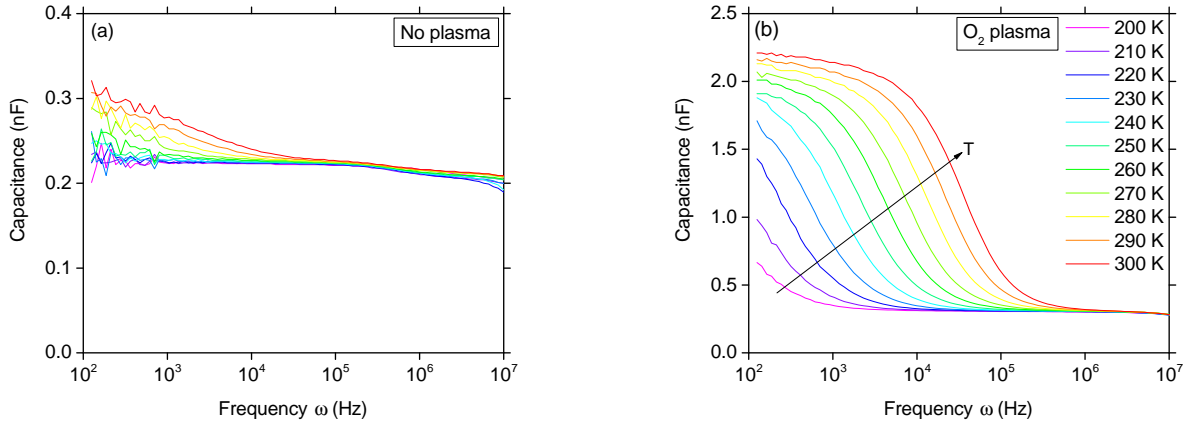


Figure 5.14: Frequency dependent capacitance spectra $C(\omega)$ performed at temperatures ranging from 200 to 300 K at 0 V for the device processed without plasma treatment (a) and the device exposed to O_2 plasma (b).

As it has been explained in Chapter 3, the extraction of the transition frequency ω_T (frequency at which the capacitance drops from C_T to C_{geo}) for each temperature is necessary to determine the activation energy of the trap. To facilitate the transition frequency extraction we plot $(G - G_0)/\omega$ with respect to ω with G_0 the conductance in the static regime. In this analysis G_0 is the conductance value G at the lowest measured frequency. Frequency dependent conductance spectra are shown in Figure 5.15 with and without O_2 plasma treatment. Conductance spectra highlight the formation of a strong peak after O_2 plasma treatment and its position shifts toward higher frequency with increasing temperature. When no plasma is used, some peaks can be analyzed at high temperature but with a lower intensity.

The activation energy E_T and attempt-to-escape frequency ν_0 of the energy level are extracted using the following relation.

$$\ln(\omega_T) = \ln(\nu_0) + E_T \frac{1}{k_B T} \quad (5.8)$$

By plotting the logarithm of the transition frequency ω_T given by the position of the peak with respect to the inverse thermal energy $1/k_B T$ and fitting the data with equation 5.8 we can extract the activation energy and attempt-to-escape frequency.

Figure 5.16 (a) shows the Arrhenius plot of the OPD which was not exposed to O_2 plasma. Due to its low intensity, the peak becomes visible only for temperatures higher than 280 K. The limited amount of data points makes it difficult to extract properly the

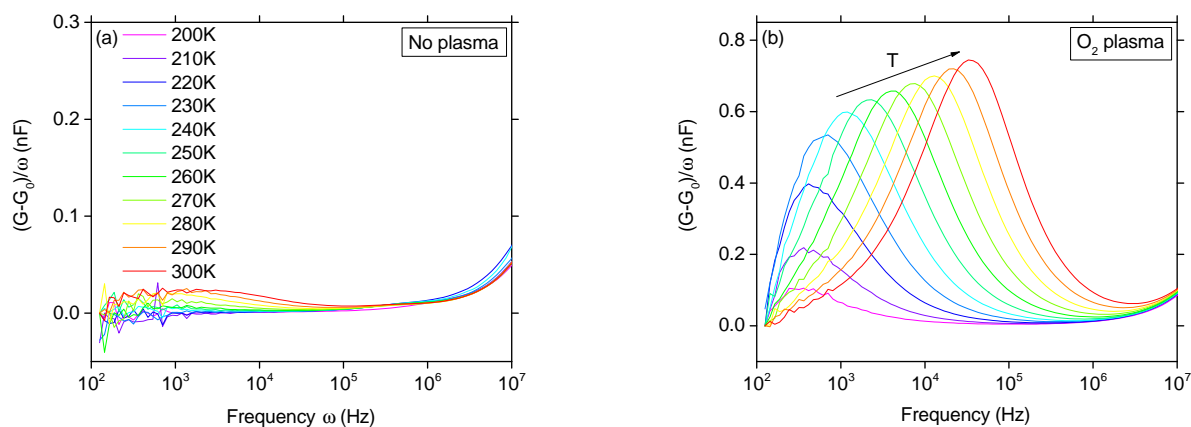


Figure 5.15: Frequency dependent conductance spectra $(G - G_0)/\omega(\omega)$ performed at temperatures ranging from 200 to 300 K at 0 V for the device processed without plasma treatment (a) and the device exposed to O_2 plasma (b).

parameters associated with the energy level. We obtain an activation energy of 287 ± 7 meV and an attempt-to-escape frequency around 10^8 Hz. When exposed to O_2 plasma the OPD exhibits sharp peaks and transition frequencies ω_T can be extracted from 240 to 300 K. The fitting of the Arrhenius plot (Figure 5.16 (b)) leads to an activation energy of 348 ± 5 meV and an attempt-to-escape frequency around 10^{10} Hz. The peak corresponding to the energy level of 290 meV is no longer observed. It is probably hidden below the high peak corresponding to the 350 meV energy level.

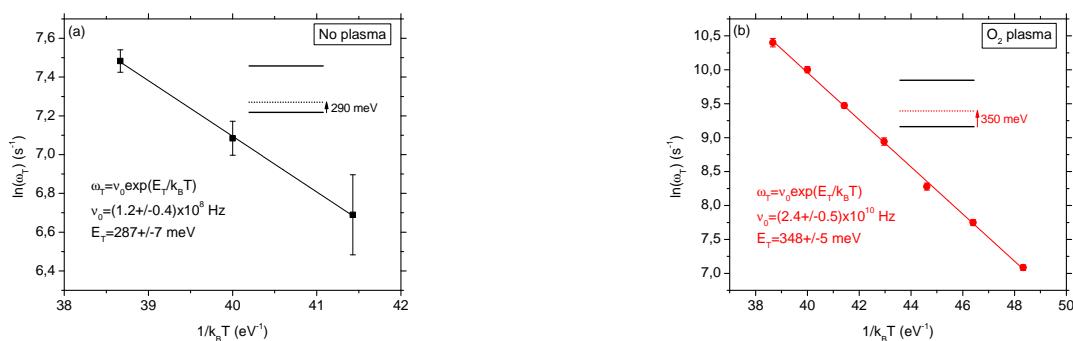


Figure 5.16: Arrhenius plot of transition frequency ω_T extracted at 0 V for the device processed without plasma treatment (a) and the device exposed to O_2 plasma (b). The corresponding band diagram with the energy level of the trap is given as inset.

We were able to extract the activation energies of the trap levels lying in the bandgap. However, at this stage of the study we are unable to say whether the activation energy is given with respect to the blend HOMO or LUMO level. As explained in Chapter 3,

5.3. p-doping impact on electronic structure of OPD active layer

the admittance spectroscopy technique probes states located between the cathode and anode electrode work functions. The schematic in Figure 5.17 illustrates the areas of the blend band gap that are not probed by admittance spectroscopy (hatched area). Since the activation energies measured are both lower than the difference between the cathode work function and the electron affinity of the blend, we can conclude that those energies are necessarily given with respect to the blend HOMO. As a result, we added a band diagram schematic with the energy level measured as inset in Figure 5.16.

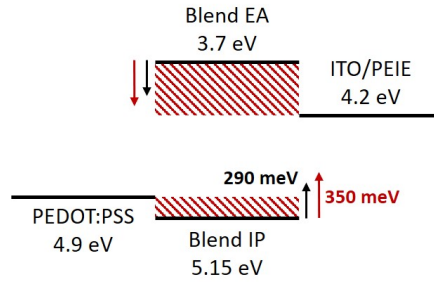


Figure 5.17: Band diagram of the OPD showing the bandgap areas that cannot be probed by admittance spectroscopy (hatched area). The activation energies of 290 and 350 meV are illustrated with black and red arrows respectively from the blend HOMO and from the blend LUMO.

Without O₂ plasma treatment an energy level is observed approximately 290 meV above the blend HOMO. This energy level has also been observed in the pure polymer and it has been shown that its density increases with Mo(tfd-COCF₃)₃ doping concentration. However, in the case of O₂ plasma treated blend this energy level is no longer observed but a new trap level is formed approximately 350 meV above the blend HOMO. This energy level is different from the one obtained with Mo(tfd-COCF₃)₃ doping indicating that it might be due to the O₂-polymer interaction. At this stage of the study we are unable to determine the donor or acceptor character of the energy levels measured.

An acceptor state situated 350 meV above the blend HOMO would induce p-doping if the Fermi level lies above this level. Moreover, acceptor traps 300 meV above the polymer HOMO due to oxygen have already been suggested in the literature for pentacene exposed to oxygen [259], and traps close to the blend HOMO have been measured for poly(3-hexylthiophene) (P3HT) (6,6)-phenyl C61-butyric acid methyl ester (C₆₀-PCBM) exposed to oxygen [182]. It is then possible that the energy level probed approximately 350 meV above the O₂ plasma treated blend is the acceptor state leading to the blend p-doping.

As it has been introduced in Chapter 3, the concentration of traps N_T can be calculated from the capacitance at the transition frequency C_T extracted in the conductance spectra:

$$N_T = \frac{4k_B T C_T}{q^2 A \Delta w} \quad [cm^{-3}] \quad (5.9)$$

with Δw the depletion thickness variation with the oscillating signal. We extract the depletion width w from $C(V)$ measurements for a given applied bias and temperature using the following relation:

$$C = \frac{\epsilon_0 \epsilon_r A}{w}. \quad (5.10)$$

The depletion width variation Δw is obtained by subtracting the depletion width w at $V - AC_{ampl}$ from the depletion width at $V + AC_{ampl}$ where AC_{ampl} is the amplitude of the AC signal. When no plasma is used to deposit PEDOT:PSS, a density of $(6 \pm 1) \times 10^{15} \text{ cm}^{-3}$ is calculated for the trap level approximately 290 meV above the blend HOMO. This value is approximately three times higher than the hole density p . As explained in Chapter 3, in admittance spectroscopy we are limited by the amount of free carriers available to be trapped and detrapped. Therefore, the value of N_T extracted might underestimate the effective density of states. However, a trap concentration of 10^{15} cm^{-3} is sufficient to degrade the device performances regarding the intrinsic carrier densities in organic materials [182].

For the device exposed to O_2 plasma, a trap concentration of $(6.7 \pm 0.1) \times 10^{16} \text{ cm}^{-3}$ is obtained for the level situated approximately 350 meV above the blend HOMO. As mentioned previously, the value of N_T extracted for this trap state might be underestimated due to the hole density of $(2.9 \pm 0.2) \times 10^{16} \text{ cm}^{-3}$. However, the similarity between both concentrations could also indicate that the trap state situated 350 meV above the blend HOMO is the acceptor level leading to p-doping. All N_T and p values extracted at 0 V and 300 K are summarized in Table 5.3.

Table 5.3: Hole density p and trap concentration N_T for both types of devices at 0 V and 300 K.

O_2 plasma	$p \text{ (cm}^{-3}\text{)}$	$N_T \text{ (cm}^{-3}\text{) @ 290 meV}$	$N_T \text{ (cm}^{-3}\text{) @ 350 meV}$
No	$(1.7 \pm 0.1) \times 10^{15}$	$(6 \pm 1) \times 10^{15}$	-
60s	$(2.9 \pm 0.2) \times 10^{16}$	-	$(6.7 \pm 0.1) \times 10^{16}$

5.3.3 Summary

Electrical characterizations ($I(V)$, EQE and $C(V)$) were carried out on devices processed with and without O_2 plasma treatment. These analyses led to the hypothesis that O_2 plasma results in the active layer p-doping through oxygen diffusion in the bulk with the formation of acceptor states situated below the Fermi level. In this section we checked that the impact of O_2 plasma is not limited to the active layer surface. Moreover, the increase in hole conductivity after O_2 plasma is consistent with p-doping. Admittance spectroscopy was carried out on both OPDs and highlighted the formation of trap states centered approximately 350 meV above the blend HOMO. Supported by several studies presented in the literature [182, 259, 266], we suggest that the states observed by admittance spectroscopy are acceptor traps responsible for p-doping. This assumption will be further developed using TCAD simulations in the following section.

5.4. Assumption verification with TCAD simulations

We summarize all the parameters of the trap states extracted by admittance spectroscopy in the bandgap for both types of devices in Figure 5.18.

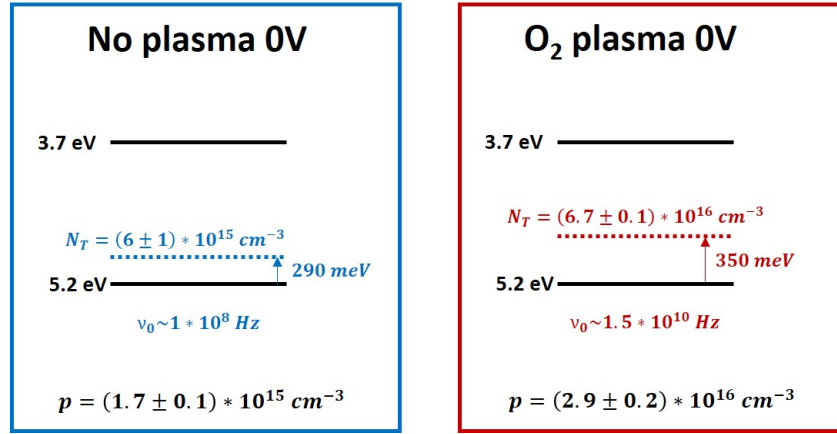


Figure 5.18: Schematic of the trap levels measured by admittance spectroscopy in the device without plasma treatment and in the device exposed to O₂ plasma. The energy level E_T with respect of the blend HOMO, the concentration of traps N_T , the attempt-to-escape frequency of the traps and the hole density p are summarized.

5.4 Assumption verification with TCAD simulations

We have shown that the active layer is p-doped when exposed to O₂ plasma and a new trap distribution is observed approximately 350 meV above the blend HOMO. We believe that the trap state measured is the acceptor state leading to p-doping with the transfer of an electron from the HOMO level to the acceptor level. However, at this stage of the study we cannot be sure whether the trap is an acceptor or donor type. Using numerical simulations we will try to discriminate between both types of trap states and we will check if the formation of an acceptor level 350 meV above the blend HOMO can explain all the evolutions observed in the electrical characterization of the OPD. Finally, the visualization of band diagrams obtained by simulation for different applied biases will illustrate the mechanisms involved in the change of the EQE shape and the decrease in V_{OC} after O₂ plasma treatment.

5.4.1 Simulation principles and parameters

Numerical simulations were carried out with the help of Stéphanie Jacob using the commercial tools available in Silvaco environment. We performed finite element simulations using TCAD (Technology Computer Aided Design) in the software ATLAS enabling electro-optical simulations of our devices.

The 2D structure of the simulated device is presented in Figure 5.19. In this structure ITO/PEIE and PEDOT:PSS electrodes are considered as metals with work-functions of 4.9 and 4.2 eV respectively. Both work-functions have been measured by Kelvin probe.

The Aluminum electrode is not taken into account in this simulation since it has no influence on the electrical characteristics. The optical reflection of the incident beam light on the aluminum surface is neglected. This assumption, which will be verified in Section 5.4.3, does not lead to significant modifications in electrical characteristics since the active layer is thick enough to absorb most of the incident light intensity. The blend is considered as a metamaterial with the ionization potential given by the polymer PBDTTT-c ionization potential at 5.15 eV and the electron affinity given by the fullerene C60-PCBM electron affinity at 3.7 eV. All parameters used in the simulation are summarized in Table 5.4. For each parameter we specify whether the value has been measured experimentally in the lab, if it has been taken from the literature or if it is a fitting parameter.

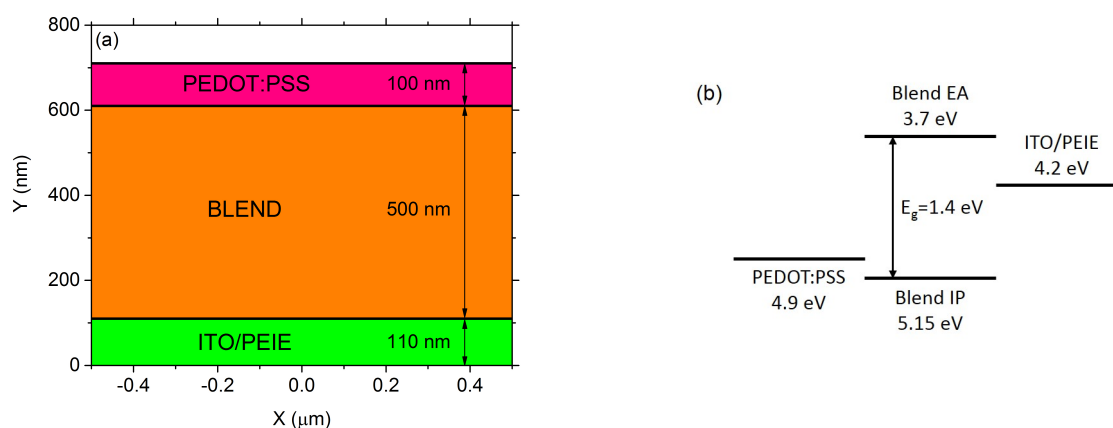


Figure 5.19: 2D structure (a) and band diagram (b) of the OPD structure simulated in Silvaco environment.

The optical constants n (refractive index) and k (extinction coefficient) of the three layers are measured by UV-visible absorption spectroscopy and calculated using OptiChar module of OptiLayer Thin Film Software. This module determines optical constants from spectro-photometric analyses using the method of transfer matrices. Optical constants are required to simulate the photo-generated current in the diode. The photogeneration rate is obtained from the absorption coefficient taking into account an exciton dissociation rate of 100%. The transport properties are simulated using drift diffusion model and recombinations are introduced with Shockley Read Hall theory.

5.4.2 Electrical characterization fitting

As a first step, the $I(V)$ and EQE characteristics of the device processed without plasma treatment are used to optimize the fitting parameters. The density of states N_C and N_V have a strong influence on the injected current density at low bias. Considering equivalent density of states in the HOMO and LUMO, a value of $8 \times 10^{19} \text{ cm}^{-3}$ has been chosen. This value is close to the usual density of states around $10^{20-21} \text{ cm}^{-3}$ determined for organic semiconductors [185].

Using admittance spectroscopy measurements we have identified a trap state situated

5.4. Assumption verification with TCAD simulations

Table 5.4: Parameters used in the OPD simulation in Silvaco environment for both structures. The parameters related to the traps added to the structures are described in Section 5.4.2.

Parameter	No plasma	With O ₂ plasma	Source
ITO/PEIE thickness	110 nm	110 nm	Value from supplier (VisionTek Products)
Blend thickness	500 nm	500 nm	Contact profilometer
PEDOT:PSS thickness	100 nm	100 nm	Contact profilometer
ITO/PEIE work-function	4.2 eV	4.2 eV	Kelvin probe
Blend electron affinity	3.7 eV	3.7 eV	Value from supplier (Sigma Aldrich)
Electrical band gap	1.45 eV	1.45 eV	Calculated from HOMO measured by UPS
PEDOT:PSS work-function	4.9 eV	4.9 eV	Kelvin probe
Relative permittivity	3.6	3.6	C(V) measurements
Electron mobility	$6 \times 10^{-4} \text{ cm}^2/Vs$	$6 \times 10^{-4} \text{ cm}^2/Vs$	From literature [200]
Hole mobility	$1 \times 10^{-3} \text{ cm}^2/Vs$	$1 \times 10^{-3} \text{ cm}^2/Vs$	From literature [200]
Density of states N_C and N_V	$8 \times 10^{19} \text{ cm}^{-3}$	$8 \times 10^{19} \text{ cm}^{-3}$	Fitting parameter
Density of mid-gap states	$2 \times 10^{14} \text{ cm}^{-3}$	$2 \times 10^{14} \text{ cm}^{-3}$	Fitting parameter
Capture cross-section of mid-gap states ($\sigma_p = \sigma_n$)	10^{-15} cm^2	10^{-15} cm^2	Fitting parameter

approximately 290 meV above the polymer HOMO, which has also been observed in the pure polymer in Chapter 3. A density of $(6 \pm 1) \times 10^{15} \text{ cm}^{-3}$ has been calculated at 300 K for this level but the extraction of the trap density might be limited by the amount of free carriers available in the HOMO level. As a results, we can consider that the density of trap states situated above the blend HOMO is equal to or greater than $6 \times 10^{15} \text{ cm}^{-3}$. As we did not extract the electron and hole capture cross-section of the trap state, it must be estimated with respect to the trap density by fitting the data. However, we still need to determine whether this energy level is a donor or acceptor trap state.

The fit of the EQE characteristics with only donor states situated 290 meV above the blend HOMO requires a large density of traps to decrease the EQE level through recombinations. However, large densities lead to non-linearity of the photocurrent with respect to the light intensity. To avoid this issue, which was not observed experimentally, we chose to add mid-gap states. The probability of recombination is high for the states close to the middle of the gap leading to a strong decrease of the EQE. These effective traps account for all recombination centers that cannot be probed by admittance spectroscopy.

In order to set the density and capture cross-section of mid-gap and donor states we need to determine their respective impact on the EQE and J(V) characteristics. Donor states situated 290 meV above the blend HOMO have a strong impact on the injection current density, while the density of mid-gap state has no influence on this parameter (Figure 5.20 (a)). Therefore, the concentration of donor states has been set by fitting the injection current density as shown in Figure 5.20 (b). Once the density of donor states is defined, the fitting of EQE and light current density in the reverse bias regime is used to set the concentration of mid-gap states.

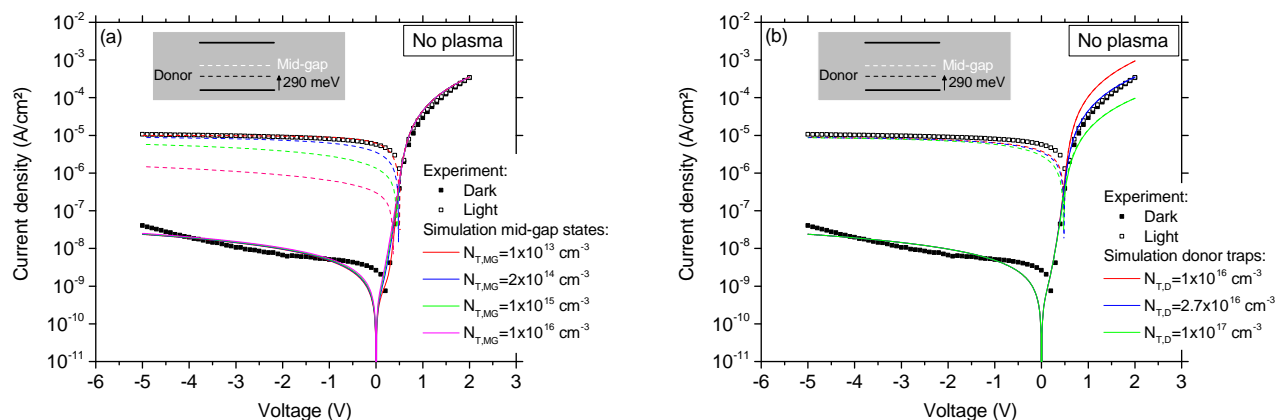


Figure 5.20: Current density in the dark and under illumination (530 nm, 0.3 W/m²) for the device without plasma treatment with the simulations obtained with a donor trap level situated 290 meV above the blend HOMO and mid-gap states with varying concentration (a). The density of mid-gap states is then kept constant while the density of donor traps is varied (b).

Figures 5.21 (a) and (b) exhibit the J(V) and EQE characteristics of the device processed without plasma treatment with the fit obtained for donor states situated 290 meV above the blend HOMO. To optimize the fit of both characteristics, a density of $2.7 \times 10^{16} \text{ cm}^{-3}$ and capture cross-sections for electrons and holes of $5 \times 10^{-16} \text{ cm}^2$ have been chosen. A good fit of the J(V) characteristic under light is obtained except around 0 V. This difference is also visible in the EQE spectra with simulated values slightly lower at 0 V. However, the EQE at -2 V and -5 V are well reproduced by the simulations taking into account a donor-type trap state 290 meV above the blend HOMO.

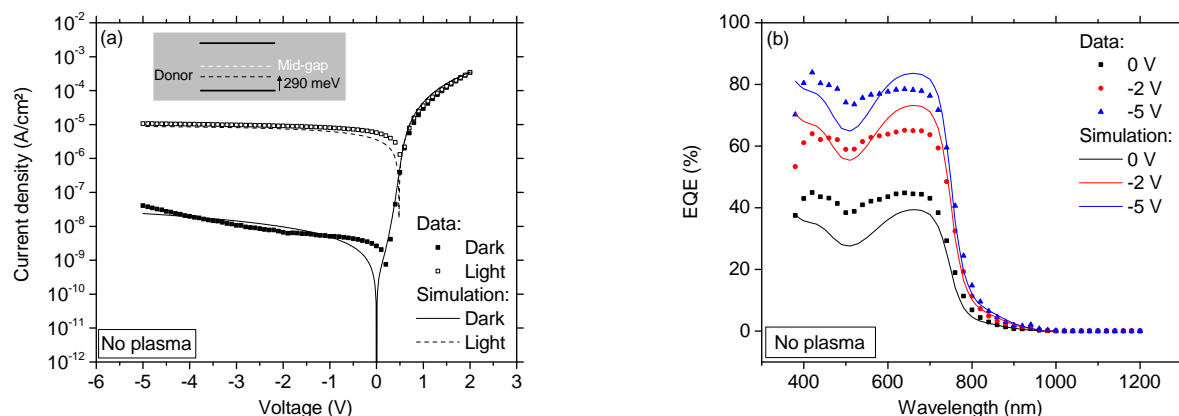


Figure 5.21: Current density in the dark and under illumination (530 nm, 0.3 W/m²) (a) and External Quantum Efficiency (EQE) at 0 V, -2 V and -5 V (b) for the device without plasma treatment. The simulations obtained with a donor trap level situated 290 meV above the blend HOMO are added to the graphs.

5.4. Assumption verification with TCAD simulations

As admittance spectroscopy does not provide information about the type (donor or acceptor) of the states probed, we need to verify whether acceptor states could also be used to fit the electrical characteristics of the OPD without plasma treatment. In Figure 5.22, we compare the $J(V)$ characteristics simulated with an acceptor-type trap state situated 290 meV above the HOMO with the data obtained for the same device. With a trap density similar to the one defined for donor states ($2.7 \times 10^{16} \text{ cm}^{-3}$), the current density (in red) is too high in the injection regime compared to the experimental data. According to admittance spectroscopy measurements, the density of this trap state is greater or equal to $(6 \pm 1) \times 10^{15} \text{ cm}^{-3}$. Therefore, we simulate $J(V)$ characteristics taking a density of $6 \times 10^{15} \text{ cm}^{-3}$ into account for the acceptor levels situated 290 meV above the blend HOMO (in blue). However, the current density remains too high in the injection regime. As a result, we believe that the trap levels measured by admittance spectroscopy 290 meV above the blend HOMO for the device processed without plasma treatment are necessarily donor states.

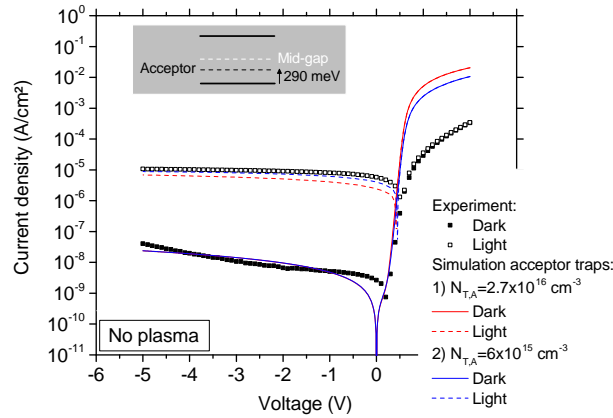


Figure 5.22: Current density in the dark and under illumination (530 nm, 0.3 W/m²) for the device without plasma treatment. The simulations obtained with an acceptor trap level situated 290 meV above the blend HOMO with two different densities are added to the graphs.

The electrical characteristics of the photodetector processed without O₂ plasma treatment can be properly reproduced by TCAD simulations considering a donor energy level situated 290 meV above the blend HOMO. Through the fitting optimization, a trap density of $2.7 \times 10^{16} \text{ cm}^{-3}$ has been extracted. This value is consistent with admittance spectroscopy results indicating a trap density above $6 \times 10^{15} \text{ cm}^{-3}$. These trap states are probably due to defects in the polymer and have already been discussed in Chapter 3.

All the parameters defined above remain unchanged for the simulation of the device processed with O₂ plasma treatment as the trap states situated 290 meV above the blend HOMO are considered intrinsic to the polymer. To fit the $J(V)$ and EQE characteristics

of the second device, we add an additional energy level situated 350 meV above the blend HOMO, as indicated by admittance spectroscopy measurements. Two possibilities must be considered: the trap states can be acceptor levels leading to the p-doping of the blend if they are situated below the Fermi level or they can correspond to defects induced donor levels accompanied by additional acceptor states situated closer to the HOMO level, which have not been measured by admittance spectroscopy. To take these potential acceptor levels into account, we can define a hole density p in the structure, which corresponds to the hole density measured in Section 5.3.

Figures 5.23 (a) and (b) exhibit the $J(V)$ and EQE characteristics of the device processed with O_2 plasma treatment and the simulation obtained with an additional acceptor-type energy level situated 350 meV above the blend HOMO. A good fit is obtained for both characteristics considering a trap density of $8 \times 10^{16} \text{ cm}^{-3}$ and a capture cross-section of $5 \times 10^{-16} \text{ cm}^2$ for electrons and holes. As a result we can observe that the introduction of acceptor states in the bandgap can explain all the modifications observed in the $J(V)$ and EQE characteristics after O_2 plasma treatment. The change in the EQE shape and V_{OC} due to oxygen will be further developed in the following section.

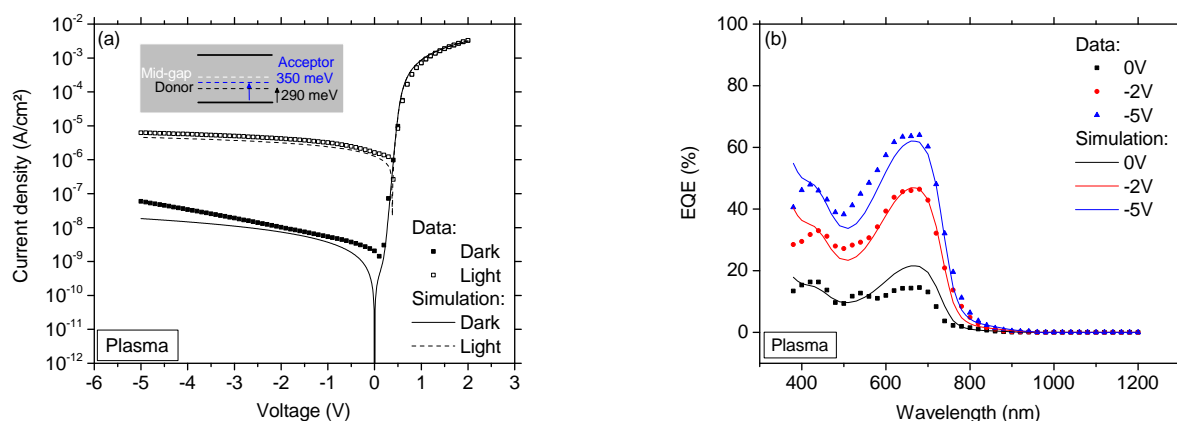


Figure 5.23: Current density in the dark and under illumination (530 nm, 0.3 W/m^2) (a) and External Quantum Efficiency (EQE) at 0 V, -2 V and -5 V (b) for the device processed with O_2 plasma treatment. The simulations obtained with a donor trap level and an acceptor trap level situated 290 meV and 350 meV above the blend HOMO respectively are added to the graphs.

If we consider a donor-type trap state situated 350 meV above the blend HOMO and an additional hole density set at $8 \times 10^{16} \text{ cm}^{-3}$ by the Mott-Schottky analysis on capacitance measurements, similar results are obtained for the $J(V)$ and EQE characteristics as shown in Figures 5.24 (a) and (b). Therefore, TCAD simulations confirm that a p-doping is responsible for the modifications in the $J(V)$ and EQE characteristics but are not sufficient to determine whether the traps introduced 350 meV above the blend HOMO correspond to the acceptor level.

5.4. Assumption verification with TCAD simulations

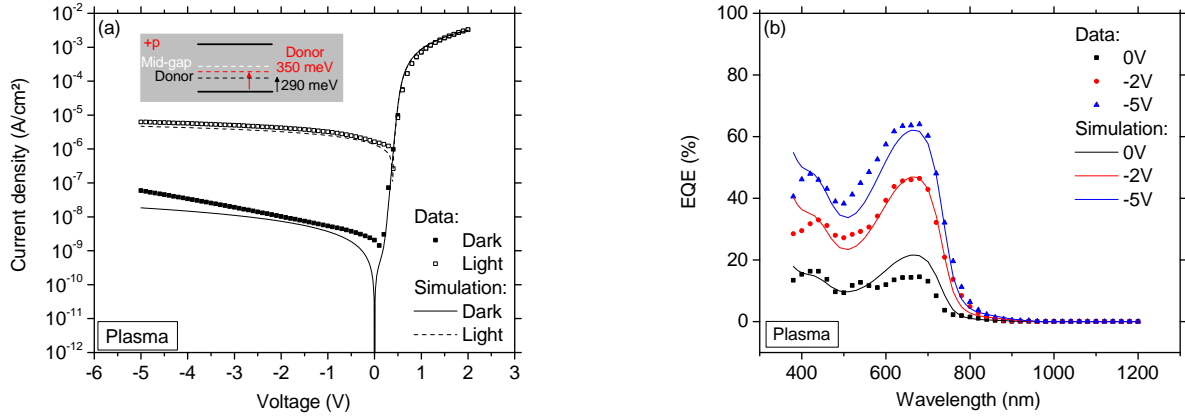


Figure 5.24: Current density in the dark and under illumination (530 nm, 0.3 W/m²) (a) and External Quantum Efficiency (EQE) at 0 V, -2 V and -5 V (b) for the device processed with O₂ plasma treatment. The simulations obtained with donor trap levels situated 290 meV and 350 meV above the blend HOMO and an additional hole density are added to the graphs.

Using TCAD simulations, we were able to confirm that p-doping induced by the O₂ plasma treatment can effectively lead to modifications in the EQE shape, field dependent EQE spectra, a reduction of the EQE level, an increase in the injection current and a V_{OC} decrease. However, two distinct scenarios can explain this p-doping. We can consider that the trap level induced by the O₂ plasma 350 meV above the blend HOMO is the acceptor level responsible for the doping process. Another possibility consists in the formation of donor traps 350 meV above the blend HOMO and acceptor levels closer to the blend HOMO. The trap states too close to the transport level cannot be probed by admittance spectroscopy. Both scenarios successfully reproduced the electrical characteristics of the diode processed with O₂ plasma treatment.

5.4.3 Band bending explanation

In order to better understand the impact of this unintentional p-doping on the electrical characteristics of the photodetectors, we have simulated the band diagram for the different scenarios described previously. Moreover, we need to consider the absorption length in the active layer at different incident wavelengths. The absorption length L_{abs} corresponds to the depth of the layer required to absorb 63% of the incident flux and is defined by the following equation:

$$L_{abs} = \frac{\lambda}{4\pi k(\lambda)} \quad (5.11)$$

where λ is the wavelength of the incident photons and $k(\lambda)$ the wavelength dependent extinction coefficient of the thin film. The refractive index n and extinction coefficient k of the active layer have been calculated from absorption measurements using OptiChar

module of OptiLayer Thin Film Software. The corresponding absorption length of the active layer is given in Figure 5.25 with respect to the wavelength of the incident photons. The values obtained do not exceed 350 nm for incident wavelengths below 700 nm. At the largest absorption length obtained around 500 nm, 75% of the incident light intensity is absorbed in the 500 nm thick active layer. For absorption lengths around 150 nm, 97% of the incident light is absorbed by the active layer. As a result, we chose to neglect the reflection on the Aluminum electrode.

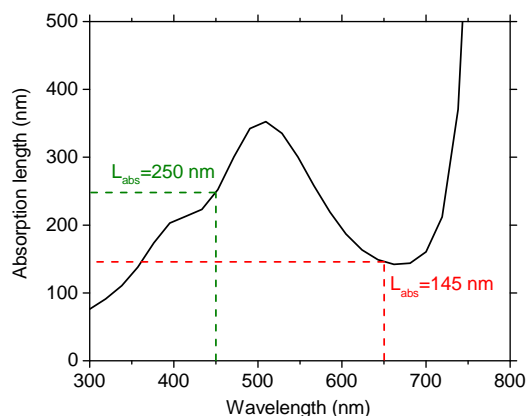


Figure 5.25: Absorption length of PBDTTT-c:C₆₀-PCBM thin film with respect to the wavelength of the incident photons.

The EQE spectra exhibit two peaks around 450 and 660 nm. The absorption lengths corresponding to these wavelengths are 250 nm and 145 nm respectively. This result indicates that the incident flux at a wavelength of 450 nm is absorbed deeper in the active layer than the incident flux at a wavelength of 650 nm. In order to understand how the absorption coefficients play a role in the resulting EQE, the band diagrams of the photodetectors processed with and without O₂ plasma treatment have been simulated.

The distribution of the electron and hole density in the active layer simulated at -2 V for the devices processed without and with O₂ plasma are given in Figure 5.26 (a) and (b) respectively. When no acceptor traps or ionized dopant density is added to the structure, corresponding to the diode without plasma treatment, we observe a charge density of the same order of magnitude for electrons and holes in the center of the active layer. However, the addition of acceptor levels p-doping the active layer or a hole density leads to the accumulation of holes over 350 nm below the PEDOT:PSS layer. The evolution of the charge density distribution in the active layer induces strong modifications in the OPD band diagram.

The band diagram simulated at -2 V for the structure with the donor trap level at 290 meV above the blend HOMO is given in Figure 5.27 (a). This structure corresponds to the photodetector without plasma treatment and exhibits a constant electric field in the whole active layer. The band diagram corresponding to the photodetector processed with plasma treatment and simulated at -2 V is shown in Figure 5.27 (b). As both scenarios described previously lead to similar band diagrams, we have chosen to show the

5.4. Assumption verification with TCAD simulations

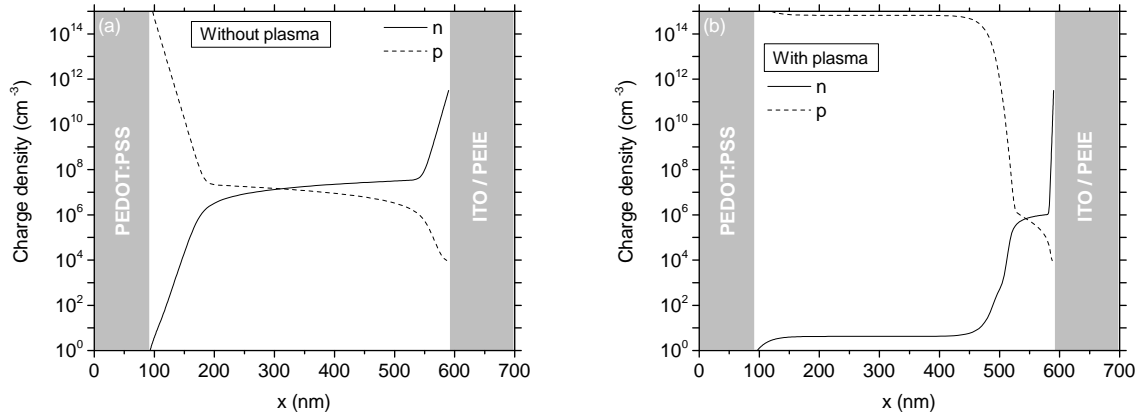


Figure 5.26: Distribution of the charge density in the photodetectors without (a) and with (b) O_2 plasma treatment simulated at -2 V.

structure with an acceptor state added 350 meV above the blend HOMO. The same band diagrams would have been obtained with donor states situated 350 meV above the HOMO accompanied by an additional hole density p . Oxygen induced p-doping results in a strong band bending at the interface with the ITO/PEIE cathode. Therefore, the electric field is high at the cathode interface and close to 0 elsewhere. The absorption lengths associated with the two peaks observed in the EQE spectra for an incident wavelength of 450 and 660 nm are illustrated with green and red arrows respectively. This schematic highlights the influence of the absorption length in a non-uniform electric field.

The band bending at -2 V for the photodetector processed with plasma treatment extends over approximately 140 nm below the ITO/PEIE electrode. With an absorption length of 145 nm at an incident wavelength of 650 nm, most of the light intensity is absorbed in the region of high electric field. The resulting collection of charges is efficient, although the introduction of deep trap states leads to a higher recombination rate. However, for an incident wavelength of 450 nm, the absorption length of 250 nm is larger than the space charge region. The excitons generated by the photons reaching the flat band area have a higher probability to recombine leading to a low collection efficiency. The formation of a space charge region with high electric field and a flat band region with an electric field close to 0 can therefore explain the modification of the EQE shape after plasma treatment with a collection efficiency higher for an incident wavelength of 650 nm than 450 nm.

The evolution of the EQE shape with the applied bias for the photodetector processed with O_2 plasma treatment can be understood by looking at the simulated band diagrams for each applied bias in Figure 5.28. At 0 V (Figure 5.28 (a)) the space charge region is only 70 nm deep leading to comparable collection efficiency for each incident wavelength. As a result, the shape of the EQE is not strongly modified at this bias. However, the strong band bending at the interface leads to a low electric field in almost the entire active layer. As a low electric field increases the probability of recombination, the EQE is lowered compared to the photodetector processed without plasma. By further increasing

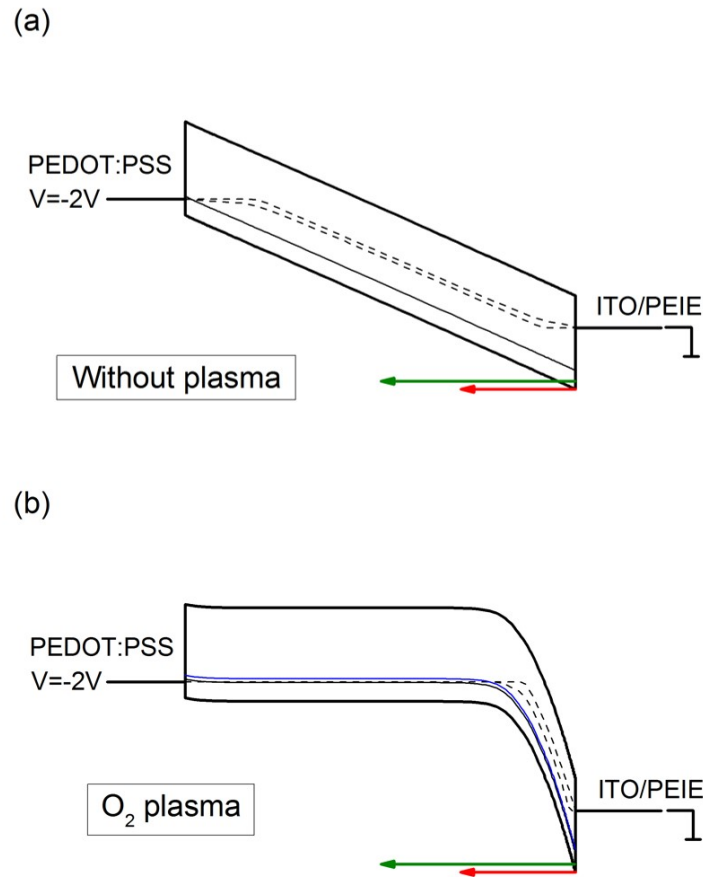


Figure 5.27: Band diagrams of the photodetectors without (a) and with (b) O_2 plasma treatment simulated at -2 V. The diagrams show the electrode work-functions, the active layer HOMO and LUMO, the electrons and holes quasi-Fermi levels and the trap states. The trap level in black corresponds to the donor trap situated 290 meV above the blend HOMO and the trap level in blue corresponds to the acceptor trap situated 350 meV above the blend HOMO. The absorption lengths of 250 nm and 145 nm are illustrated with green and red arrows respectively.

the voltage in the reverse bias regime at -2 V and -5 V (Figure 5.28 (a) and (b)), the space charge region progressively extends in the active layer resulting in an absorption wavelength dependent collection efficiency. A modification of the EQE is therefore observed with increasing bias. It would have been useful to compare EQE spectra for diodes illuminated from the anode side and from the cathode side. B. Bouthinon [267] showed that the EQE ratio between both illumination sides can give information about the band bending in the active layer. However, to carry out this study we would need to replace the aluminum by a transparent electrode.

5.4. Assumption verification with TCAD simulations

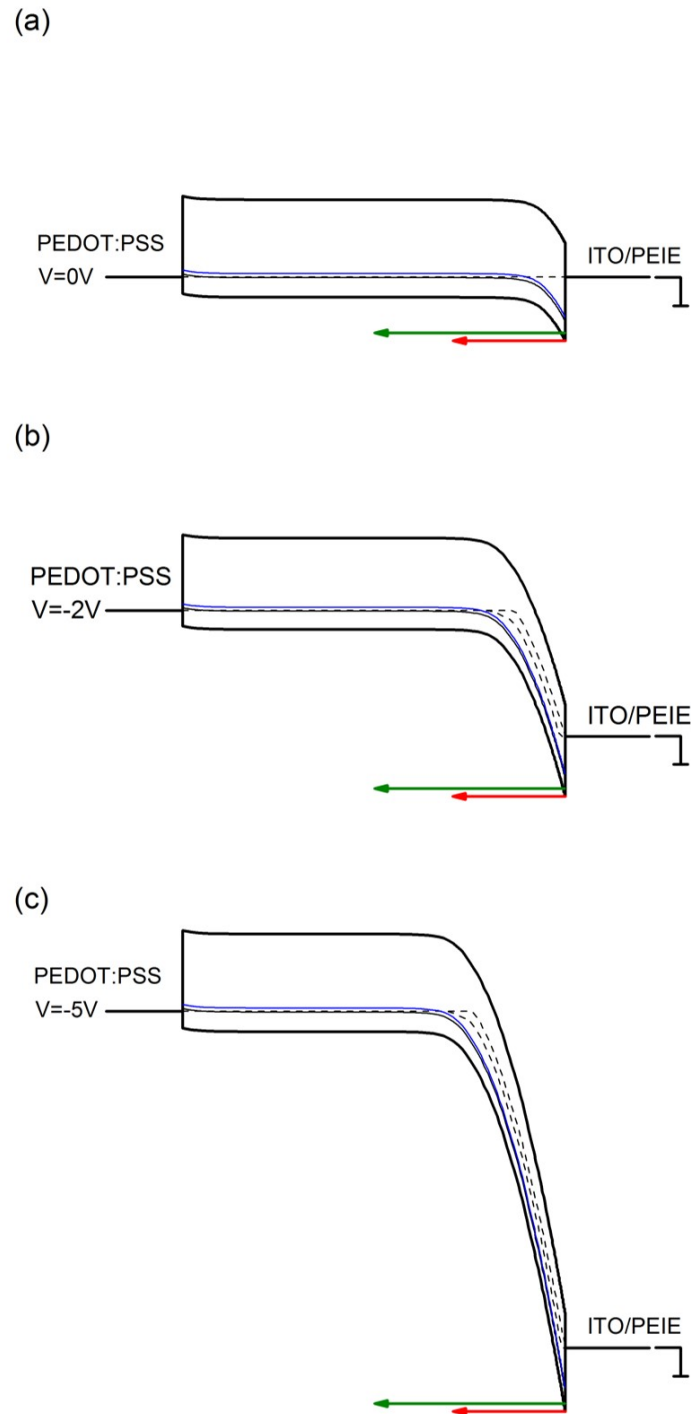


Figure 5.28: Band diagrams of the photodetectors with O_2 plasma treatment simulated at 0 V (a), -2 V (b) and -5 V (c). The diagrams show the electrode work-functions, the active layer HOMO and LUMO, the electrons and holes quasi-Fermi levels and the trap states. The trap level in black corresponds to the donor trap situated 290 meV above the blend HOMO and the trap level in blue corresponds to the acceptor trap situated 350 meV above the blend HOMO. The absorption lengths of 250 nm and 145 nm are illustrated with green and red arrows respectively.

Band diagrams are also useful to understand the origin or the V_{OC} decrease after plasma treatment. Figure 5.29 (a) and (b) exhibits the band diagrams simulated for the OPD without and with plasma respectively. We can notice a reduction of the quasi-Fermi levels splitting after O_2 plasma treatment from 0.54 eV to 0.51 eV. The open-circuit voltage V_{OC} is related to the quasi-Fermi levels splitting as follows [268]:

$$V_{OC} = \frac{1}{q}(E_{FN} - E_{FP}) \quad (5.12)$$

with E_{FN} and E_{FP} the electrons and holes quasi-Fermi levels. Therefore, a reduction of the quasi-Fermi level splitting can directly explain a V_{OC} decrease. However, the quasi-Fermi level splitting obtained by simulation decreases by 0.03 V while V_{OC} decreases by 0.1 V in both simulation and measurements. Moreover, Equation 5.12 does not lead to the obtained V_{OC} . A lower value of V_{OC} can be due to carrier recombination [269]. We observe that the electric field is close to 0 in almost the entire active layer at V_{OC} for the device processed with plasma treatment. Flat bands can contribute to a high recombination rate, leading to a more important decrease of the V_{OC} .

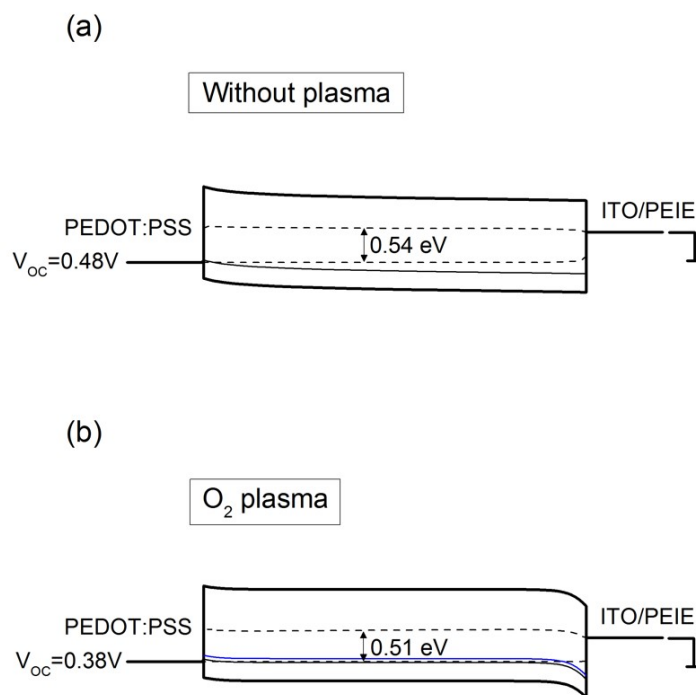


Figure 5.29: Band diagrams of the photodetectors without (a) and with (b) O_2 plasma treatment simulated at V_{OC} . The diagrams show the electrode work-functions, the active layer HOMO and LUMO, the electrons and holes quasi-Fermi levels and the trap states. The trap level in black corresponds to the donor trap situated 290 meV above the blend HOMO and the trap level in blue corresponds to the acceptor trap situated 350 meV above the blend HOMO.

5.5. Summary and outlook

The simulation of the band diagrams at different applied biases for both types of photodetectors (with and without plasma) help understanding the evolution of the V_{OC} and EQE shape. The p-doping induced by the O_2 plasma exposure results in the formation of a space charge region at the cathode ITO/PEIE interface with a strong band bending and high electric field. As a result, the electric field is close to 0 elsewhere in the active layer. This inhomogeneity in the electric field leads to different collection probabilities depending on the absorption length, which depends on the wavelength of the incident photons. Therefore, the EQE peak at 650 nm with a short absorption length benefits from a high collection efficiency driven by the electric field. On the other hand, the peak at 450 nm suffers from a larger absorption length resulting in a significant absorption in the flat band region where the probability of recombination is higher. Moreover, the evolution of the space charge region with the applied bias further amplifies the EQE dependency on the incident photons absorption length.

5.5 Summary and outlook

Oxygen plasma is a widely used surface treatment in solution printed solar cells and photodetectors processing to enable PEDOT:PSS deposition. However, O_2 is known to be detrimental for organic devices. Therefore, it is crucial to determine the impact of this treatment on device performances. To address this issue, we compared the exact similar structure processed with and without O_2 plasma treatment. This experiment requires the ability to deposit PEDOT:PSS without surface treatment on the active layer. This requirement is made possible by the development of lamination techniques, which has been used in the OPD processing in this chapter.

Electrical characterizations on photodetectors processed with and without O_2 plasma treatment highlighted the impact of this surface treatment on the OPD performances. O_2 plasma leads to a sensitivity and EQE decrease while it increases the current density in the injection regime. Moreover, we can observe a change in the shape of the EQE spectra after O_2 plasma treatment. Regarding these results, an hypothesis has been formulated. The formation of acceptor levels between the HOMO and Fermi levels could explain all the evolutions observed in the electrical characteristics. If acceptor levels are situated below the Fermi level they can be charged and p-dope the active layer. Such charged states can explain the increase in current density but also the changes in EQE shape due to strong band bending. Moreover, deep trap states have a high recombination probability, which reduces EQE and sensitivity.

In order to test this hypothesis, further characterizations have been carried out. The increase in conductivity and hole density confirmed the p-doping effect of the O_2 plasma treatment. Conductivity measurements also confirmed the impact of the treatment on the bulk of the active layer through oxygen diffusion. Admittance spectroscopy was used to probe potential trap states in the gap of the active layer. We identified one trap state situated 290 meV above the blend HOMO without plasma treatment and one trap

state situated 350 meV above the blend HOMO after plasma treatment. We can make the hypothesis that the trap state created in the bandgap of the blend by O₂ plasma treatment might be the acceptor state leading to p-doping.

TCAD simulations have been carried with the help of Stéphanie Jacob to further develop this hypothesis. For the OPD processed without O₂ plasma treatment, we obtained a good fit by taking donor trap states situated 290 meV above the blend HOMO into account and we were able to invalidate the possibility of acceptor states at this level. However, the OPD processed with O₂ plasma treatment can be successfully simulated with two different hypotheses. We can consider the trap states situated 350 meV above the blend HOMO as acceptors but we also obtain a good fit with donor states and an additional hole density p . The hole density would stand for acceptor levels that would be situated closer to the HOMO level. Such trap states cannot be probed by admittance spectroscopy with this structure. Therefore, further work needs to be carried out to discriminate between both assumptions. As an example we could carry out Density Functional Theory (DFT) simulations to determine the interaction between the oxygen molecule and the polymer and the potential formation of acceptor levels in the bandgap, as it has been carried out by Knipp and Northrup for pentacene [259].

Using TCAD simulations we were also able to understand the evolution of the EQE shape using band diagrams. The p-doping induced by the O₂ plasma causes a strong band bending at the interface with ITO/PEIE and a very low electric field closer to the PEDOT:PSS electrode. This band bending leads to an absorption length dependent photocurrent explaining a change in the shape of the EQE spectra.

By carrying out electrical characterizations on organic photodetectors processed with and without O₂ plasma treatment we showed that this surface treatment is detrimental for OPD performances. Therefore, we could improve solar cells and photodetectors characteristics by removing the O₂ plasma treatment with the use of PEDOT:PSS lamination. Alternative surface treatments have been developed like Self-Assembled Monolayers (SAM) but their impact on the device characteristics remains to be understood. Moreover, we need to study the impact of O₂ plasma on the device stability in order to determine whether the initial presence of oxygen molecules in the active layer accelerates the aging process.

Finally, this study highlights the need to localize doped layers at the interface to avoid band bending in the active layer. Therefore, unintentional oxygen doping must be avoided and intentional molecular doping needs to offer a limited tendency to diffuse.

General conclusions

This study on organic semiconductor p-doping was motivated by two main goals: deepen our understanding of the doping mechanisms involved and integrate the doped layer in a device to replace the PEDOT:PSS hole transport layer. The knowledge acquired on organic semiconductor doping was beneficial to study the consequences of unintentional oxygen doping in organic photodetectors.

Throughout this work, we have chosen PBDTTT-c as polymer for its promising performances in organic solar cells and photodetectors. To avoid diffusion issues reported for the dopant F_4TCNQ and obtain improved doping efficiencies we have chosen a soluble derivative of $Mo(tfd)$, the p-dopant $Mo(tfd-COCF_3)_3$.

As a first step of this thesis, we verified the effectiveness of p-doping for the mixture $Mo(tfd-COCF_3)_3$:PBDTTT-c. Using electrical characterizations on the PBDTTT-c thin film doped with varying concentrations, we demonstrated the effect of p-doping on the electrical properties of the polymer. The use of $Mo(tfd-COCF_3)_3$ as p-dopant in PBDTTT-c led to a conductivity increase among the best reported in the literature for a doping concentration of 2.5% MR. The evolution of the electrical characteristics with varying doping concentrations highlighted the presence of two regimes. Below 2.5% MR, the addition of molecular dopants leads to the filling of trap states improving the transport properties while increasing the amount of free carriers. However, above 2.5% MR we identified a saturation or decline in the electrical performances. This behavior indicates a reduced impact of the dopant and two possibilities have been suggested to explain this evolution. Polymer dopant aggregates have been observed by SEM and TEM images above 2% MR and can be responsible for a decline in the transport properties. However, polymer-dopant aggregates do not explain a reduced doping efficiency as all molecules of dopant have reacted with the polymer according to NMR analysis. The second hypothesis formulated involves the entry in the dopant reserve regime with the saturation of Fermi level below the acceptor state of doping.

Understanding the limits of the doping efficiency in organic semiconductors is crucial to find clues in order to obtain improved doping efficiencies at lower doping concentrations. This study consisted in determining the doping mechanism involved in the polymer-dopant mixture. In the literature, two doping mechanisms have been suggested: Integer Charge Transfer (ICT) and Charge Transfer Complex (CTC) formation. If CTC is responsible for

the p-doping of PBDTTT-c with $\text{Mo}(\text{tfd-COCF}_3)_3$, it would strengthen the hypothesis of dopant reserve regime at high doping concentration with the saturation of the Fermi level below the anti-bonding state of the complex. To distinguish between ICT and CTC we carried out complementary optical and electrical analyses. One sub-bandgap absorption peak has been identified with doping and can be attributed to polarons, and therefore ICT, or to the absorption in the complex resulting from CTC. The addition of dynamic and static quenching have been identified in the doped polymer through fluorescence and lifetime of the excited state measurements. A dynamic component in the quenching of the polymer fluorescence upon addition of molecular dopants were expected for both ICT and CTC mechanisms. However, the static component implies the absorption of the incident photons in a complex formed between the two molecules. Therefore, the photoluminescence analysis suggests that CTC might be involved in the doping process and is consistent with the second sub-bandgap absorption peak observed with doping. Taking into account the hypothesis of CTC formation, the energy level of the anti-bonding state of the complex, and therefore the acceptor level of doping, has been extracted using absorption measurements. To further verify this hypothesis, admittance spectroscopy measurements have been carried out to probe the potential energy levels created in the polymer bandgap. A trap state is effectively probed for the doped polymer and the energy level is consistent with the absorption spectroscopy study. Therefore, it is very likely that the formation of a CTC is involved in the doping of PBDTTT-c with $\text{Mo}(\text{tfd-COCF}_3)_3$.

Although the doping efficiency in organic semiconductor remains to be improved, doped layers lead to effective injection barrier lowering. Therefore, they can be used in organic devices to obtain a good ohmic contact at the organic semiconductor-metal electrode interface. In this study we chose to use the layer of $\text{Mo}(\text{tfd-COCF}_3)_3$ doped PBDTTT-c as hole transport layer to replace the widely used PEDOT:PSS, known to be responsible for stability issues. Soft Contact Transfer Lamination (SCTL) was used to stack organic layers processed in solution without the use of orthogonal solvents. The p-doped layer was successfully integrated in an organic photodetector (OPD) leading to similar performances than OPDs processed with PEDOT:PSS. The major drawback of the use of p-doped polymer as HTL highlighted in this study is the loss of photocurrent linearity at high light intensities. This degradation has been attributed to the significant series resistance of the HTL associated with the limited conductivity. However, the use of $\text{Mo}(\text{tfd-COCF}_3)_3$ doped PBDTTT-c improves the OPD detectivity, which can compete with its silicon-made counterpart. Moreover, no localization step of the HTL is required for the p-doped layer. Finally, preliminary ageing studies have been carried out suggesting an improved stability in humid atmosphere compared to PEDOT:PSS and a limited impact of the temperature.

Oxygen is known to p-dope organic polymers and degrade organic devices performances. Nevertheless, oxygen plasma treatment is widely used in organic solar cells and photodetector processing to enable the deposition of PEDOT:PSS on the active layer. To our knowledge, the impact of this treatment on the device performances has not been clearly established. In this study, we took advantage of the lamination technique to deposit the PEDOT:PSS layer without the need for surface treatment. Therefore, we were able to compare two identical OPD structures processed with and without O_2 plasma treatment. We highlighted the degradation induced by the surface treatment on the OPD

Summary and future work

external quantum efficiency (EQE) and sensitivity. Moreover, we observed a change in the EQE shape with a strong decrease at lower wavelengths (around 400 nm). Although it is known that oxygen potentially p-dopes organic semiconductors, the origin of the OPD performances degradation remained to be understood in this case. As a first step we checked the effectiveness of p-doping through conductivity and ionized dopant density measurements and showed that the impact of the O₂ plasma treatment is not limited to the surface of the active layer but extends throughout the bulk. In Chapter 3 we have shown that molecular p-doping induces trap states above the polymer HOMO, which could be associated with the acceptor level of p-doping. We repeated this experiment on the active layer and demonstrated the creation of trap states approximately 350 meV above the polymer HOMO upon O₂ plasma exposure. It is still unclear whether this trap state corresponds to the acceptor levels or is a donor-type trap state induced by disorder. Finally, we used TCAD simulations to improve our understanding of the O₂ plasma treatment induced degradations. We were able to reproduce the J(V) and EQE characteristics for untreated and treated OPDs with the formation of an acceptor level 350 meV above the HOMO but also with a donor level at the same position accompanied by a hole density. With the help of simulated band diagram we were able to understand the origin of the sensitivity degradation as well as the wavelength dependent EQE decrease.

Critical Discussion

The work carried out throughout this thesis raised several points, which would require further studies to be solved.

In Chapter 2 we have shown that the formation of polymer dopant aggregates might be responsible for the degradation of transport properties at high doping concentration. However, to reach appropriate conductivities and sufficient energy barrier lowering, the doping concentration must be pushed above the limit of aggregates formation. Therefore, we should work on the origin of these aggregates and study potential solutions to avoid them. As an example, we can study the influence of the solvent or the temperature of the annealing step on the size and density of the aggregates in the polymer layer, but also on the transport properties.

As the formation of polymer-dopant aggregates are not sufficient to explain the limitations observed at high doping concentration, the mechanisms involved in the doping process has been studied. Optical and electrical characterizations converged to the formation of a charge transfer complex (CTC). However, this hypothesis can raise doubts about the probability for the electron to be transferred from the polymer HOMO to the anti-bonding state of the complex. Two preliminary assumptions have been formulated in this manuscript to explain this phenomenon. The first hypothesis considers the broadening of the density of states reaching the deep acceptor level for doping. Although a few studies [127, 173, 214] have demonstrated a density of states broadening induced by doping, it is still unclear whether this phenomenon is responsible for the effectiveness of doping. Further studies are required such as UPS and IPES measurements to follow the evolution of the HOMO level with doping and probe the potential anti-bonding state of

the complex using a strong doping concentration, as it has been done for F₄TCNQ doped 4T by Méndez *et al.* [29]. The second hypothesis deals with the influence of light on the doping process. A short preliminary study suggests that light is involved in the doping effectiveness, recalling the light-assisted doping process identified for oxygen [183, 218]. However, this study needs to be pursued to obtain concrete and reliable results. Longer ageing studies with different illumination conditions are required.

An interesting work to be carried out to continue this study on the mechanisms involved in the doping of PBDTTT-c with Mo(tfd-COCF₃)₃ would be Density Functional Theory (DFT) analysis. This technique could provide important information about the interaction between the two components. In particular, we should be able to determine whether a complex is formed between the polymer HOMO and dopant LUMO and quantify the energy levels associated with this complex, as it has been carried out for several polymer-dopant mixtures [90, 92, 93].

Chapters 2 and 3 could be enriched by similar studies using different types of molecular dopants. A similar sub-bandgap absorption peak observed for several dopants would put into question the CTC hypothesis, recalling the formation of polarons in the polymer. On the other hand, if a CTC is effectively involved in the doping process of Mo(tfd-COCF₃)₃ doped PBDTTT-c, changing the dopant should lead to a different anti-bonding state or a different doping mechanism. Therefore we should observe a correlation between all electrical and optical characterization techniques. As an example, if the use of a different dopant leads to an anti-bonding state situated deeper in the bandgap, the Fermi level should cross the acceptor state at a lower doping concentration, and therefore the conductivity and doping efficiency should decrease at a lower doping concentration threshold.

The Mo(tfd-COCF₃)₃ doped PBDTTT-c layer has been successfully introduced in organic photodetectors, as a replacement for the PEDOT:PSS HTL. However, we have highlighted one drawback of this replacement with the formation of a series resistance by the HTL leading to photocurrent non-linearity at high light intensities. To overcome this issue, the conductivity of the doped layer needs to be improved by several orders of magnitude. This limitation motivates the study about the mechanism responsible for the doping process, which needs to be determined in order to find clues to improve the doping efficiency. However, if the series resistance of the HTL is decreased, the laminated p-doped layer will require a patterning step before the deposition of the electrode top contact. Some work needs to be done to enable lamination of a patterned layer as it has been introduced by Chen *et al.* [270].

The Soft Contact Transfer Lamination (SCTL) technique used in this study to enable the deposition of subsequent organic layers without the need of orthogonal solvents is limited to small areas and highly dependent on the material. Moreover, the yield of this lamination step is low. Therefore, this technique requires further improvements to be transferred to large scale production, with a good reproducibility and compatibility with various polymer layers.

In this work we have shown only preliminary ageing studies on the OPD processed with the p-doped layer as HTL. As molecular dopants are prone to diffusion, a complete

Summary and future work

study is required on the effect of temperature and bias on the evolution of the OPD performances. Further work can also be carried out to compare the degradation of OPDs with PEDOT:PSS and p-doped layer as HTL when exposed to humidity, oxygen and illumination. Although we expect the p-doped layer to lead to improved performances in humidity conditions, oxygen and illumination, induced degradations might not be reduced by the doped layer.

Oxygen, inducing p-doping and chemical degradations in the organic semiconductors, is indeed a major issue for organic devices. An active research is conducted to develop efficient encapsulation solutions in order to delay as much as possible the diffusion of oxygen in the organic layers [271, 272, 273]. For some technologies as light emitting diodes processed with polymers (PLED) and small molecules (OLED), the complete process is carried out in glovebox to avoid detrimental degradations induced by oxygen [254, 274]. However, O₂ plasma treatment remains a widely used technique to enable the deposition of PEDOT:PSS. As we have shown in Chapter 5, this treatment reduces significantly the performances of organic photodetectors due to the oxygen p-doping of the active layer. This study emphasizes the need to control the doping profile in organic devices and restrain high doping concentrations to the interfaces. Moreover, this study highlighted the need to replace the surface treatment or find alternative ways to deposit the PEDOT:PSS layer. Self-assembled monolayers (SAMs) are also used to change the surface tension of the active layer [275], but its impact on the device performances remains to be demonstrated. For future technologies, we can imagine using lamination techniques to deposit the PEDOT:PSS layer without any surface treatment on the active layer. Another solution consists in the replacement of PEDOT:PSS by a laminated p-doped polymer layer, as presented in Chapter 4.

However, the study of the impact of O₂ doping on the active layer properties requires further experiments. Indeed, it is still unclear whether the trap states probed approximately 350 meV above the polymer HOMO correspond to the acceptor level of doping. Further analyses need to be carried out to answer to this question, as DFT analysis to determine the interaction between the polymer and the dioxygen molecule. Such analysis has already been carried out for pentacene and can provide interesting information about the position of potential donor or acceptor levels in the polymer bandgap [259]. We can also push the simulation analysis by scanning the active layer bandgap with acceptor states. This study could help determine whether acceptor levels closer to the polymer HOMO can be responsible for the evolution of the electrical characteristics.

Finally, we need to study the impact of initial unintentional oxygen doping on the stability of the organic photodetector. Comparative ageing studies can be carried out on devices processed with and without O₂ plasma treatment to determine the effect of temperature or bias on the device performances.

Outlook

Complementary studies on organic semiconductor doping are necessary to build a global picture of the doping processes between various types of organic semiconductors

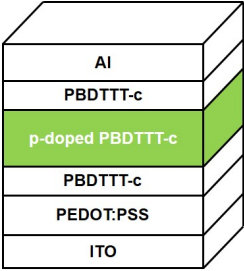
and dopants. We need to understand the limitations of the organic semiconductor doping to unlock the doping efficiencies obtained to this day. If CTC is effectively involved in some polymer dopant mixtures, we need to find a way to reduce the intermolecular electronic coupling between both components. Therefore, we should be able to shift the acceptor level closer to the organic semiconductor HOMO, increasing the doping efficiency.

Although the introduction of doped organic semiconductor layers has been successfully carried out in evaporated devices, the development of this technology in solution printed devices is in its early stages. Dai *et al.* [26] have replaced PEDOT:PSS by a laminated p-doped layer in organic solar cells. Further studies are necessary to repeat this replacement for various doped layers in solar cells and OPDs, improve the lamination technique and study the impact of the doped layer on the device performances and stability. Moreover, tandem solar cells could be processed by solution processing of doped organic layers using lamination techniques. Doped layers are also of great interest for organic field effect transistors (OFETs). Localized doped layers at the interface with the electrodes are beneficial for the contact properties [149, 150] and channel doping can be used to control the threshold voltage [153] and to produce inversion OFETs [144]. However, to our knowledge, no solution processed transistors have been realized with doped organic layers. The development of SCTL with patterning is necessary to use doped layers in organic transistors, especially for interface doping. It has been shown that the introduction of the conducting polymer PEDOT:PSS as interface layer in PLEDs enhances significantly the device performances by reducing the hole injection barrier [276]. This work highlights the need to develop printing-compatible solutions to use doped layers in PLEDs as it is used for evaporated OLEDs. To our knowledge, no solution printed doped layer has been used in PLEDs so far. Overall, doped polymer layers are interesting for all solution printed devices requiring an efficient polymer-electrode contact.

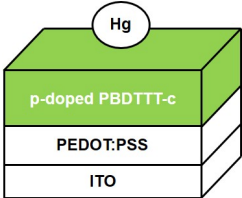
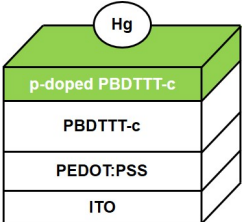
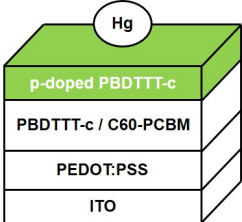
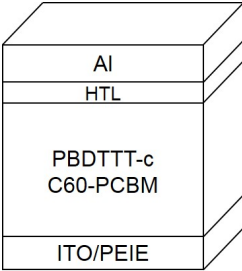
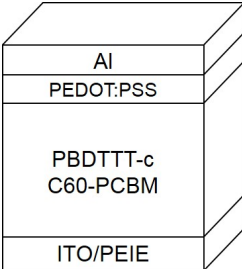
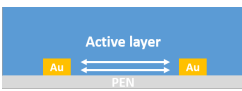
To enable the introduction of doped layers in organic devices and the replacement of unstable interface layers, p and n-doping needs to be developed. Although a lot of work is carried out on p-type doping, the strong instability of n-type doping regarding oxygen makes its study more challenging. Recently, air-stable dimers have been developed, which possess the ability to provide additional electrons to the organic semiconductor when the thin film is formed using thermal activation [121]. Further work is required to optimize this doping process, guarantee its stability and introduce such layers in organic devices.

Device stability is one of the major challenges of organic electronics. In this study we have highlighted that unintentional and uncontrolled oxygen doping is detrimental for organic devices. Therefore, the development of organic semiconductor doping needs to guarantee a good localization and limit diffusion issues. Moreover, we need to find clues to limit stability issues induced by oxygen.

Appendix A-Summary of the structures studied

Structure	Schematic	Experiment	Section
STRUCTURE 1		<ol style="list-style-type: none"> 1. Conductivity 2. Activation energy of hopping transport 	2.2
STRUCTURE 2		<ol style="list-style-type: none"> 1. Mott-Schottky Analysis 2. Admittance spectroscopy 	2.3 3.3

Appendix . Appendix A-Summary of the structures studied

Structure	Schematic	Experiment	Section
STRUCTURE 3A		Injection barrier	2.5
STRUCTURE 3B			
STRUCTURE 3C			
STRUCTURE 4		OPD with different HTLs (PEDOT:PSS and p-doped PBDTTT-c)	Chapter 4
STRUCTURE 5		OPD with and without O ₂ plasma treatment	Chapter 5
STRUCTURE 6		Hole conductivity with and without O ₂ plasma treatment	5.3.1

Appendix B-TLM on pure PBDTTT-c

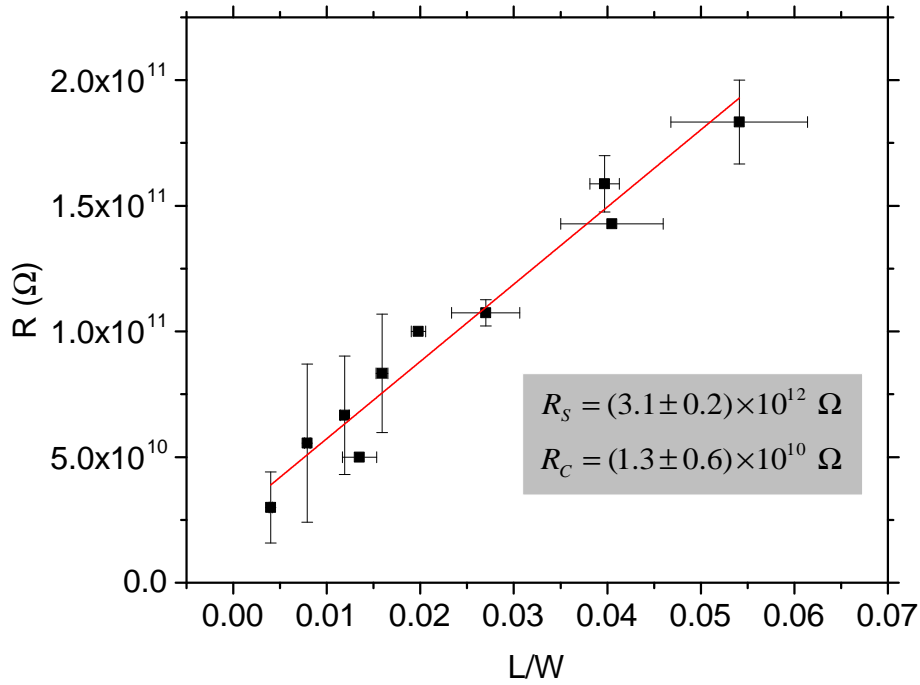


Figure B.1: Resistance with respect to L/W extracted from TLM analysis with a linear fit to extract the series resistance R_s of the layer and the contact resistance R_c with the gold electrode.

Appendix C-Supplier and reference information

Material	Supplier	Reference
ITO coated glass	VisionTek	
PEIE	Sigma Aldrich	$C_w = 35 - 40\%$
PBDTTT-c	Solarmer Materials	SMI-P9001
C ₆₀ PCBM	Merck	PV-A600 lisicon
PEDOT:PSS	Agfa	Orgacon HIL 1005
Mo(tfd-COCF ₃) ₃	Group of Prof. Seth Marder Georgia Institute of Technology	
PDMS	Dow Corning	SYLGARD 184
Gold coated PEN	OIKE	Q65HA
o-xylene	Sigma Aldrich	≥ 99%
Chlorobenzene	Sigma Aldrich	≥ 99.5%
1,2,4-Trichlorobenzene	Merck	
Epoxy glue	DELO	LP
Glass for encapsulation	Verre Industrie	0.7 mm Borosilicate

Appendix D-Experimental Protocol of solid-state NMR

All solid-state NMR experiments were carried out at room temperature using a BRUKER AVANCE DSX 500 MHz spectrometer, operating at a ^1H frequency of 500.13 MHz and a ^{13}C frequency of 125.7 MHz. 1D ^{13}C spectra were acquired with a 4 mm Bruker CPMAS probe-head, using a combination of cross-polarization (CP), magic-angle spinning (MAS), and high-power proton decoupling methods. The MAS speed was set to 12,000 Hz. ^1H radio-frequency field strengths of 70 and 87 kHz were used for proton pulses (90° pulse duration of 2.8 ms) and proton dipolar decoupling, respectively. The ^{13}C radio-frequency field strength was set to match the Hartman-Hahn condition during CP. For each spectrum, 12,000 transients were accumulated with a CP contact time of 2 ms and a recycle delay of 5 s. Signals of quaternary carbons were assigned using dipolar dephasing sequence. The chemical shift values were calibrated indirectly with the carbonyl signal of glycine set at 176.03 ppm relative to tetramethylsilane (TMS). Non-quaternary suppression (NQS) experiments were performed by intervallating the $40\mu\text{s}$ dephasing delay with zero field strength before the acquisition period in the CP experiment. This sequence combined with MAS is referred to as the NQS/MAS experiment.

Bibliography

- [1] NASA. <https://climate.nasa.gov/>.
- [2] OPVIUS. <http://www.opvius.com/en/home.html>.
- [3] V. Bulovic. *Rethinking Solar Energy* - <https://www.youtube.com/watch?v=WoS7PGFjwDQ>.
- [4] V. Benfenati, S. Toffanin, S. Bonetti, G. Turatti, A. Pistone, M. Chiappalone, A. Sagnella, A. Stefani, G. Generali, G. Ruani, D. Saguatti, R. Zamboni, and M. Muccini. “A transparent organic transistor structure for bidirectional stimulation and recording of primary neurons”. *Nature Materials* 12.7 (2013), pp. 672–680.
- [5] A. J. Williamson, L. Kergoat, D. Khodagholy, M. Berggren, C. Bernard, G. G. Malliaras, D. T. Simon, A. Jonsson, S. Inal, I. Uguz, A. J. Williamson, L. Kergoat, and J. Rivnay. “Bioelectronic neural pixel: Chemical stimulation and electrical sensing at the same site”. *Proceedings of the National Academy of Sciences* 113.44 (2016), E6903–E6903.
- [6] K. C. Larsson, P. Kjäll, and A. Richter-Dahlfors. “Organic bioelectronics for electronic-to-chemical translation in modulation of neuronal signaling and machine-to-brain interfacing”. *Biochimica et Biophysica Acta - General Subjects* 1830.9 (2013), pp. 4334–4344.
- [7] OE-A. *Organic and Printed Electronics, Summary - OE-A Roadmap, 7th Edition*. Tech. rep.
- [8] E. WALTZ. <http://spectrum.ieee.org/biomedical/devices/the-quantified-olympian-wearables-for-elite-athletes>. 2015.
- [9] P. Shyamkumar, P. Rai, S. Oh, M. Ramasamy, R. Harbaugh, and V. Varadan. “Wearable Wireless Cardiovascular Monitoring Using Textile-Based Nanosensor and Nanomaterial Systems”. *Electronics* 3.3 (2014), pp. 504–520.
- [10] Talk2myShirt. <http://www.talk2myshirt.com/blog/archives/390>. 2008.
- [11] Guide The Ultimate Glamping Business. <https://www.inspiredcamping.com/solar-powered-tent/>. 2017.
- [12] H. Shirakawa, E. J. Louis, A. G. Macdiarmid, C. K. Chiang, and A. J. Heeger. “Synthesis of Electrically Conducting Organic Polymers : Halogene Derivatives of Polyacetylene, (CH)_x”. *J. C. S. Chem. Comm* 578 (1977), pp. 578–580.
- [13] G. Nisato, D. Lupo, and S. Ganz, eds. *Organic and Printed Electronics: Fundamentals and Applications*. Pan Stanford, 2016.
- [14] OLEDWorks. <https://www.oledworks.com/>.
- [15] Organic Photovoltaics Research. <https://www.energy.gov/eere/sunshot/organic-photovoltaics-research>.

-
- [16] P. Büchele, M. Richter, S. F. Tedde, G. J. Matt, G. N. Anka, R. Fischer, M. Biele, W. Metzger, S. Lilliu, O. Bikondoa, J. E. Macdonald, C. J. Brabec, T. Kraus, U. Lemmer, and O. Schmidt. “X-ray imaging with scintillator-sensitized hybrid organic photodetectors”. *Nature Photonics* 9.12 (2015), pp. 843–848.
- [17] Isorg. http://www.isorg.fr/default.asp?cat_id=76.
- [18] M. Stoppa and A. Chiolerio. “Wearable electronics and smart textiles: A critical review”. *Sensors (Switzerland)* 14.7 (2014), pp. 11957–11992.
- [19] H. Klauk. “Organic thin-film transistors”. *Chemical Society Reviews* 39.7 (2010), p. 2643.
- [20] W. R. Mateker and M. D. McGehee. “Progress in Understanding Degradation Mechanisms and Improving Stability in Organic Photovoltaics”. *Advanced Materials* 29.10 (2017), p. 1603940.
- [21] P. Cheng and X. Zhan. “Stability of organic solar cells: challenges and strategies”. *Chem. Soc. Rev.* 45 (2016), p. 2544.
- [22] H. Ma, H.-L. Yip, F. Huang, and A. K. Y. Jen. “Interface Engineering for Organic Electronics”. *Advanced Functional Materials* 20.9 (2010), pp. 1371–1388.
- [23] S. M. Sze and K. K. Ng. *Physics of semiconductor devices*. John wiley & sons, 2006.
- [24] K. Walzer, B Maennig, M. Pfeiffer, and K. Leo. “Highly Efficient Organic Devices Based on Electrically Doped Transport Layers”. *Chem. Rev.* 107 (2007), pp. 1233–1271.
- [25] A. Dai. “Creating highly efficient carrier injection or collection contacts via soft contact transfer lamination of p-doped interlayers”. PhD thesis. Princeton University, 2015.
- [26] A. Dai, Y. Zhou, A. L. Shu, S. K. Mohapatra, H. Wang, C. Fuentes-Hernandez, Y. Zhang, S. Barlow, Y. L. Loo, S. R. Marder, B. Kippelen, and A. Kahn. “Enhanced charge-carrier injection and collection via lamination of doped polymer layers p-doped with a solution-processible molybdenum complex”. *Advanced Functional Materials* 24.15 (2014), pp. 2197–2204.
- [27] A. Dai, A. Wan, C. Magee, Y. Zhang, S. Barlow, S. R. Marder, and A. Kahn. “Investigation of p-dopant diffusion in polymer films and bulk heterojunctions: Stable spatially-confined doping for all-solution processed solar cells”. *Organic Electronics* 23 (2015), pp. 151–157.
- [28] G. Heimel, I. Salzmann, and N. Koch. “On the fundamental processes in molecular electrical doping of organic semiconductors”. *AIP Conference Proceedings* 148 (2012), pp. 148–156.
- [29] H. Méndez, G. Heimel, S. Winkler, J. Frisch, A. Opitz, K. Sauer, B. Wegner, M. Oehzelt, C. Röthel, S. Duhm, D. Többens, N. Koch, and I. Salzmann. “Charge-transfer crystallites as molecular electrical dopants”. *Nature Communications* 6 (2015), p. 8560.
- [30] I. Salzmann and G. Heimel. “Toward a comprehensive understanding of molecular doping organic semiconductors (review)”. *Journal of Electron Spectroscopy and Related Phenomena* 204 (2015), pp. 208–222.
- [31] W. Gao and A. Kahn. “Controlled p-doping of zinc phthalocyanine by coevaporation with tetrafluorotetracyanoquinodimethane: A direct and inverse photoemission study”. *Applied Physics Letters* 79.24 (2001), pp. 4040–4042.
- [32] W. Y. Gao and A. Kahn. “Electrical doping: the impact on interfaces of pi-conjugated molecular films”. *Journal of Physics: Condensed Matter* 15.38 (2003), S2757–S2770.

Bibliography

- [33] K. Harada, A. G. Werner, M. Pfeiffer, C. J. Bloom, C. M. Elliott, and K. Leo. “Organic homojunction diodes with a high built-in potential: Interpretation of the current-voltage characteristics by a generalized einstein relation”. *Physical Review Letters* 94.3 (2005), p. 036601.
- [34] M. Prosa, M. Tessarolo, M. Bolognesi, O. Margeat, D. Gedefaw, M. Gaceur, C. Videlot-Ackermann, M. R. Andersson, M. Muccini, M. Seri, and J. Ackermann. “Enhanced Ultraviolet Stability of Air-Processed Polymer Solar Cells by Al Doping of the ZnO Interlayer”. *ACS Applied Materials & Interfaces* 8.3 (2016), pp. 1635–1643.
- [35] J. Wang, L. Xu, B. Zhang, Y.-J. Lee, and J. W. P. Hsu. “n-Type Doping Induced by Electron Transport Layer in Organic Photovoltaic Devices”. *Advanced Electronic Materials* 3.2 (2017), p. 1600458.
- [36] M. Jorgensen, K. Norrman, and F. C. Krebs. “Stability/degradation of polymer solar cells”. *Solar Energy Materials and Solar Cells* 92.7 (2008), pp. 686–714.
- [37] K. Norrman, M. V. Madsen, S. a. Gevorgyan, and F. C. Krebs. “Degradation Patterns in Water and Oxygen of an Inverted Polymer Solar Cell”. *J. Am. Chem. Soc.* 132.17 (2010), pp. 16883–16892.
- [38] E. Voroshazi, B. Verreet, A. Buri, R. Müller, D. Di Nuzzo, and P. Heremans. “Influence of cathode oxidation via the hole extraction layer in polymer:fullerene solar cells”. *Organic Electronics: physics, materials, applications* 12.5 (2011), pp. 736–744.
- [39] S. B. Sapkota, M. Fischer, B. Zimmermann, and U. Würfel. “Analysis of the degradation mechanism of ITO-free organic solar cells under UV radiation”. *Solar Energy Materials and Solar Cells* 121 (2014), pp. 43–48.
- [40] M. Ramuz, L. Bürgi, C. Winnewisser, and P. Seitz. “High sensitivity organic photodiodes with low dark currents and increased lifetimes”. *Organic Electronics: physics, materials, applications* 9.3 (2008), pp. 369–376.
- [41] J.-M. Verilhac. “Transistors organiques à base de dérivés du polythiophène : effets de la structure moléculaire et supramoléculaire”. PhD thesis. INP Grenoble, 2006.
- [42] C. K. Chiang, C. R. Fincher, Y. W. Park, A. J. Heeger, H. Shirakawa, E. J. Louis, S. C. Gau, and A. G. MacDiarmid. “Electrical conductivity in doped polyacetylene”. *Physical Review Letters* 39.17 (1977), pp. 1098–1101.
- [43] G. Hadziioannou and G. G. Malliaras, eds. *Semiconducting polymers*. Wiley VCH, 2000.
- [44] M. T. Dang, L. Hirsch, and G. Wantz. “P3HT:PCBM, best seller in polymer photovoltaic research”. *Advanced Materials* 23.31 (2011), pp. 3597–3602.
- [45] X. Liu, H. Chen, and S. Tan. “Overview of high-efficiency organic photovoltaic materials and devices”. *Renewable and Sustainable Energy Reviews* 52 (2015), pp. 1527–1538.
- [46] Y. Liang, D. Feng, Y. Wu, S.-T. T. Tsai, G. Li, C. Ray, and L. Yu. “Highly efficient solar cell polymers developed via fine-tuning of structural and electronic properties”. *Journal of the American Chemical Society* 131.22 (2009), pp. 7792–9.
- [47] H. Mathieu and H. Fanet. *Physique des semiconducteurs et des composants électroniques*. Vol. 6. Paris: Dunod, 2009.
- [48] N. A. Minder, S. Ono, Z. Chen, A. Facchetti, and A. F. Morpurgo. “Band-like electron transport in organic transistors and implication of the molecular structure for performance optimization”. *Advanced Materials* 24.4 (2012), pp. 503–508.

-
- [49] H. Bässler. “Charge Transport in Disordered Organic Photoconductors a Monte Carlo Simulation Study”. *Physica Status Solidi (B)* 175.1 (1993), pp. 15–56.
- [50] A. Miller and E. Abrahams. “Impurity conduction at low concentrations”. *Physical Review* 120.3 (1960), pp. 745–755.
- [51] M. Kobashi and H. Takeuchi. “Inhomogeneity of Spin-Coated and Cast Non-Regioregular Poly(3-hexylthiophene) Films. Structures and Electrical and Photophysical Properties”. *Macromolecules* 31.21 (1998), pp. 7273–7278.
- [52] W. Warta and N. Karl. “Hot holes in naphthalene: High, electric-field-dependent mobilities”. *Phys. Rev. B* 32.2 (1985), p. 1172.
- [53] S. D. Baranovskii, T. Faber, F. Hensel, and P. Thomas. “The applicability of the transport-energy concept to various disordered materials”. *J. Phys.: Condens. Matter* 9.997 (1997), pp. 2699–2706.
- [54] E. A. Schiff. “Diffusion-controlled bimolecular recombination of electrons and holes in a-Si:H”. *Journal of Non-Crystalline Solids* 190.1-2 (1995), pp. 1–8.
- [55] C. L. Braun. “Electric field assisted dissociation of charge transfer states as a mechanism of photocarrier production”. *The Journal of Chemical Physics* 80.9 (1984), pp. 4157–4161.
- [56] M. Silver and R. Sharma. “Carrier generation and recombination in anthracene”. *J. Chem. Phys.* 46.2 (1967), pp. 692–696.
- [57] W. Shockley and W. T. Read. “Statistics of the Recombination of Holes and Electrons”. *Physical Review* 87.46 (1952), pp. 835–842.
- [58] R. N. Hall. “Electron-hole recombination in germanium”. *Physical Review* 87.2 (1968), p. 387.
- [59] S.-J. Yoo and J.-J. Kim. “Charge Transport in Electrically Doped Amorphous Organic Semiconductors”. *Macromolecular Rapid Communications* 36.11 (2015), pp. 984–1000.
- [60] S. R. Forrest. “Ultrathin Organic Films Grown by Organic Molecular Beam Deposition and Related Techniques”. *Chemical Reviews* 97.6 (1997), pp. 1793–1896.
- [61] C. W. Tang. “Two-layer organic photovoltaic cell”. *Applied Physics Letters* 48.2 (1986), pp. 183–185. arXiv: [arXiv:1011.1669v3](https://arxiv.org/abs/1011.1669v3).
- [62] N. S. Sariciftci, L. Smilowitz, A. J. Heeger, and F. Wudl. “Photoinduced Electron Transfer from a Conducting Polymer to Buckminsterfullerene”. *Science* 258.5087 (1992), pp. 1474–1476.
- [63] P. E. Shaw, A. Ruseckas, and I. D. W. Samuel. “Exciton diffusion measurements in poly(3-hexylthiophene)”. *Advanced Materials* 20.18 (2008), pp. 3516–3520.
- [64] N. S. Sariciftci, L. Smilowitz, A. J. Heeger, and F. Wudl. “Semiconducting polymers (as donors) and buckminsterfullerene (as acceptor): photoinduced electron transfer and heterojunction devices”. *Synthetic Metals* 59.3 (1993), pp. 333–352.
- [65] G. Yu, J. Gao, J. C. Hummelen, F. Wudl, and A. J. Heeger. “Polymer Photovoltaic Cells - Enhanced Efficiencies Via a Network of Internal Donor-Acceptor Heterojunctions”. *Science* 270.5243 (1995), pp. 1789–1791.
- [66] J. J. M. Halls, C. A. Walsh, N. C. Greenham, E. A. Marseglia, R. H. Friend, S. C. Moratti, and A. B. Holmes. “Efficient photodiodes from interpenetrating polymer networks”. *Nature* 376.6540 (1995), pp. 498–500.

Bibliography

- [67] S. H. Park, A. Roy, S. Beaupré, S. Cho, N. Coates, J. S. Moon, D. Moses, M. Leclerc, K. Lee, and A. J. Heeger. “Bulk heterojunction solar cells with internal quantum efficiency approaching 100%”. *Nature Photonics* 3.5 (2009), pp. 297–302.
- [68] M. M. Wienk, J. M. Kroon, W. J. H. Verhees, J. Knol, J. C. Hummelen, P. A. van Hal, and R. A. J. Janssen. “Efficient methano [70] fullerene/MDMO-PPV bulk heterojunction photovoltaic cells”. *Angewandte Chemie* 115 (2003), pp. 3493–3497.
- [69] Y. He, H.-Y. Chen, J. Hou, and Y. Li. “IndeneC 60Bisadduct: A New Acceptor for High-Performance Polymer Solar Cells”. *Journal of the American Chemical Society* 132.4 (2010), pp. 1377–1382.
- [70] Y. Sun, C. Cui, H. Wang, and Y. Li. “Efficiency Enhancement of Polymer Solar Cells Based on Poly(3-hexylthiophene)/Indene-C70 Bisadduct via Methylthiophene Additive”. *Advanced Energy Materials* 1.6 (2011), pp. 1058–1061.
- [71] A. Distler, T. Sauermann, H. J. Egelhaaf, S. Rodman, D. Waller, K. S. Cheon, M. Lee, and D. M. Guldi. “The effect of PCBM dimerization on the performance of bulk heterojunction solar cells”. *Advanced Energy Materials* 4.1 (2014), p. 1300693.
- [72] J. U. Lee, J. W. Jung, J. W. Jo, and W. H. Jo. “Degradation and stability of polymer-based solar cells”. *Journal of Materials Chemistry* 22.46 (2012), p. 24265.
- [73] B. Lüssem, M. Riede, and K. Leo. “Doping of organic semiconductors”. *Physica Status Solidi (A)* 210.1 (2013), pp. 9–43.
- [74] I. Salzmann, G. Heimel, M. Oehzelt, S. Winkler, and N. Koch. “Molecular Electrical Doping of Organic Semiconductors: Fundamental Mechanisms and Emerging Dopant Design Rules”. *Accounts of Chemical Research* 49.3 (2016), pp. 370–378.
- [75] J. H. Lee, H. M. Kim, K. B. Kim, R. Kabe, P. Anzenbacher, and J. J. Kim. “Homogeneous dispersion of organic p -dopants in an organic semiconductor as an origin of high charge generation efficiency”. *Applied Physics Letters* 98.17 (2011), pp. 2009–2012.
- [76] T. Menke, D. Ray, H. Kleemann, M. P. Hein, K. Leo, and M. Riede. “Highly efficient p-dopants in amorphous hosts”. *Organic Electronics: physics, materials, applications* 15.2 (2014), pp. 365–371.
- [77] K. H. Yim, G. L. Whiting, C. E. Murphy, J. J. M. Halls, J. H. Burroughes, R. H. Friend, and J. S. Kim. “Controlling electrical properties of conjugated polymers via a solution-based p-type doping”. *Advanced Materials* 20.17 (2008), pp. 3319–3324.
- [78] B. Lüssem, C.-M. Keum, D. Kasemann, B. Naab, Z. Bao, and K. Leo. “Doped Organic Transistors”. *Chemical Reviews* 116.22 (2016), pp. 13714–13751.
- [79] P. Pingel and D. Neher. “Comprehensive picture of p-type doping of P3HT with the molecular acceptor F4TCNQ”. *Physical Review B - Condensed Matter and Materials Physics* 87.11 (2013), p. 115209.
- [80] S. Yu, J. Frisch, A. Opitz, E. Cohen, M. Bendikov, N. Koch, and I. Salzmann. “Effect of molecular electrical doping on polyfuran based photovoltaic cells”. *Applied Physics Letters* 106.20 (2015), p. 203301.
- [81] M. Lögdlund, R. Lazzaroni, S. Stafström, W. Salaneck, and J.-L. Brédas. “Direct observation of charge-induced π -electronic structural changes in a conjugated polymer”. *Physical Review Letters* 63.17 (1989), pp. 1841–1844.

-
- [82] C. Tengstedt, W. Osikowicz, W. R. Salaneck, I. D. Parker, C. H. Hsu, and M. Fahlman. “Fermi-level pinning at conjugated polymer interfaces”. *Applied Physics Letters* 88.5 (2006), p. 053502.
- [83] J. Hwang, A. Wan, and A. Kahn. “Energetics of metal-organic interfaces: New experiments and assessment of the field”. *Materials Science and Engineering R: Reports* 64.1-2 (2009), pp. 1–31.
- [84] S. Olthof, W. Tress, R. Meerheim, B. Lüssem, and K. Leo. “Photoelectron spectroscopy study of systematically varied doping concentrations in an organic semiconductor layer using a molecular p-dopant”. *Journal of Applied Physics* 106.10 (2009), p. 103711.
- [85] M. L. Tietze, L. Burtone, M. Riede, B. Lüssem, and K. Leo. “Fermi level shift and doping efficiency in p-doped small molecule organic semiconductors: A photoelectron spectroscopy and theoretical study”. *Physical Review B - Condensed Matter and Materials Physics* 86.3 (2012), p. 035320.
- [86] C. K. Chan, W. Zhao, S. Barlow, S. Marder, and A. Kahn. “Decamethylcobaltocene as an efficient n-dopant in organic electronic materials and devices”. *Organic Electronics: physics, materials, applications* 9.5 (2008), pp. 575–581.
- [87] C. Falkenberg, C. Uhrich, S. Olthof, B. Maennig, M. K. Riede, and K. Leo. “Efficient p-i-n type organic solar cells incorporating 1,4,5,8- naphthalenetetracarboxylic dianhydride as transparent electron transport material”. *Journal of Applied Physics* 104.3 (2008), p. 034506.
- [88] G. Parthasarathy, C. Shen, A. Kahn, and S. R. Forrest. “Lithium doping of semiconducting organic charge transport materials”. *Journal of Applied Physics* 89.9 (2001), pp. 4986–4992.
- [89] Y. Karpov et al. “High Conductivity in Molecularly p-Doped Diketopyrrolopyrrole-Based Polymer: The Impact of a High Dopant Strength and Good Structural Order”. *Advanced Materials* 28.28 (2016), pp. 6003–6010.
- [90] I. Salzmann, G. Heimel, S. Duhm, M. Oehzelt, P. Pingel, B. M. George, A. Schnegg, K. Lips, R. P. Blum, A. Vollmer, and N. Koch. “Intermolecular hybridization governs molecular electrical doping”. *Physical Review Letters* 108.3 (2012), p. 035502.
- [91] M. L. Tietze, P. Pahner, K. Schmidt, K. Leo, and B. Lüssem. “Doped Organic Semiconductors: Trap-Filling, Impurity Saturation, and Reserve Regimes”. *Advanced Functional Materials* 25.18 (2015), p. 2701.
- [92] H. Méndez, G. Heimel, A. Opitz, K. Sauer, P. Barkowski, M. Oehzelt, J. Soeda, T. Okamoto, J. Takeya, J. B. Arlin, J. Y. Balandier, Y. Geerts, N. Koch, and I. Salzmann. “Doping of organic semiconductors: Impact of dopant strength and electronic coupling”. *Angewandte Chemie - International Edition* 52.30 (2013), pp. 7751–7755.
- [93] L. Zhu, E.-g. Kim, Y. Yi, and J.-L. Brédas. “Charge Transfer in Molecular Complexes with 2,3,5,6-Tetrafluoro-7,7,8,8-tetracyanoquinodimethane (F4-TCNQ): A Density Functional Theory Study”. *Chemistry of Materials* 23.23 (2011), pp. 5149–5159.
- [94] G. D. Sharma, S. G. Sangodkar, and M. S. Roy. “Influence of iodine on the electrical and photoelectrical properties of zinc phthalocyanine thin film devices”. *Materials Science and Engineering B* 41.2 (1996), pp. 222–227.
- [95] A. Ali Benamar, M. Galtier, and A. Montaner. “N-Doping of Polyacetylene”. *Synthetic Metals* 43 (1991), pp. 45–48.

Bibliography

- [96] Y. Kaneko, T. Suzuki, Y. Matsuo, and S. Ikehata. “Metallic electrical conduction in alkaline metal-doped pentacene”. *Synthetic Metals* 154.1-3 (2005), pp. 177–180.
- [97] T. Minakata, M. Ozaki, and H. Imai. “Conducting thin films of pentacene doped with alkaline metals”. *Journal of Applied Physics* 74.2 (1993), pp. 1079–1082.
- [98] J. Jakabovič, A. Vincze, J. Kováč, R. Srnánek, J. Kováč, E. Dobročka, D. Donoval, U. Heinemeyer, F. Schreiber, V. MacHovič, and F. Uherek. “Surface and interface analysis of iodine-doped pentacene structures for OTFTs”. *Surface and Interface Analysis* 43.1-2 (2011), pp. 518–521.
- [99] J. H. Lee, D. S. Leem, and J. J. Kim. “Effect of host organic semiconductors on electrical doping”. *Organic Electronics: physics, materials, applications* 11.3 (2010), pp. 486–489.
- [100] C. Y. H. Chan, C. M. Chow, and S. K. So. “Using transistor technique to study the effects of transition metal oxide dopants on organic charge transporters”. *Organic Electronics: physics, materials, applications* 12.8 (2011), pp. 1454–1458.
- [101] M. Kröger, S. Hamwi, J. Meyer, T. Riedl, W. Kowalsky, and A. Kahn. “P-type doping of organic wide band gap materials by transition metal oxides: A case-study on Molybdenum trioxide”. *Organic Electronics: physics, materials, applications* 10.5 (2009), pp. 932–938.
- [102] J. H. Wemken, R. Krause, T. Mikolajick, and G. Schmid. “Low-cost caesium phosphate as n-dopant for organic light-emitting diodes”. *Journal of Applied Physics* 111.7 (2012), p. 074502.
- [103] K. S. Yook, S. O. Jeon, C. W. Joo, J. Y. Lee, T. W. Lee, T. Noh, H. J. Yang, and S. K. Kang. “Air stable and low temperature evaporable Li₃N as a n type dopant in organic light-emitting diodes”. *Synthetic Metals* 159.15-16 (2009), pp. 1664–1666.
- [104] J. Blochwitz, T. Fritz, M. Pfeiffer, K. Leo, D. M. Alloway, P. a. Lee, and N. R. Armstrong. “Interface electronic structure of organic semiconductors with controlled doping levels”. *Organic Electronics: physics, materials, applications* 2.2 (2001), pp. 97–104.
- [105] B. Maennig, M. Pfeiffer, A. Nollau, X. Zhou, K. Leo, and P. Simon. “Controlled p-type doping of polycrystalline and amorphous organic layers: Self-consistent description of conductivity and field-effect mobility by a microscopic percolation model”. *Physical Review B* 64.19 (2001), p. 195208.
- [106] K. Kanai, K. Akaike, K. Koyasu, K. Sakai, T. Nishi, Y. Kamizuru, T. Nishi, Y. Ouchi, and K. Seki. “Determination of electron affinity of electron accepting molecules”. *Applied Physics A: Materials Science and Processing* 95.1 (2009), pp. 309–313.
- [107] P. K. Koech, A. B. Padmaperuma, L. Wang, J. S. Swensen, E. Polikarpov, J. T. Darsell, J. E. Rainbolt, and D. J. Gaspar. “Synthesis and application of 1, 3, 4, 5, 7, 8- Hexafluorotetracyanonaphthoquinodimethane (F6-TNAP): a conductivity dopant for organic light-emitting devices”. *Chemistry of Materials* 22 (2010), pp. 3926–3932.
- [108] J. Li, G. Zhang, D. M. Holm, I. E. Jacobs, B. Yin, P. Stroeve, M. Mascal, and A. J. Moule. “Introducing Solubility Control for Improved Organic P-Type Dopants”. *Chemistry of Materials* 27 (2015), pp. 5765–5774.
- [109] J. Li, C. W. Rochester, I. E. Jacobs, S. Friedrich, P. Stroeve, M. Riede, and A. J. Moulé. “Measurement of Small Molecular Dopant F4TCNQ and C60F36 Diffusion in Organic Bilayer Architectures”. *ACS Applied Materials and Interfaces* 7.51 (2015), pp. 28420–28428.

-
- [110] J. Li, C. W. Rochester, I. E. Jacobs, E. W. Aasen, S. Friedrich, P. Stroeve, and A. J. Moulé. “The effect of thermal annealing on dopant site choice in conjugated polymers”. *Organic Electronics* 33 (2016), pp. 23–31.
- [111] R. Meerheim, S. Olthof, M. Hermenau, S. Scholz, A. Petrich, N. Tessler, O. Solomeshch, B. Lssem, M. Riede, and K. Leo. “Investigation of C60F36 as low-volatility p-dopant in organic optoelectronic devices”. *Journal of Applied Physics* 109.10 (2011), p. 103102.
- [112] Y. Smets, C. B. Stark, F. Schmitt, M. T. Edmonds, S. Lach, C. A. Wright, D. P. Langley, K. J. Rietwyk, A. Schenk, A. Tadich, M. Wanke, C. Ziegler, L. Ley, and C. I. Pakes. “Doping efficiency and energy-level scheme in C60F 48-doped zinc-tetraphenylporphyrin films”. *Organic Electronics: physics, materials, applications* 14.1 (2013), pp. 169–174.
- [113] Y. Qi, T. Sajoto, M. Kröger, A. M. Kandabarow, W. Park, S. Barlow, E. G. Kim, L. Wielunski, L. C. Feldman, R. a. Bartynski, J. L. Brédas, S. R. Marder, and A. Kahn. “A molybdenum dithiolene complex as p-dopant for hole-transport materials: A multitechnique experimental and theoretical investigation”. *Chemistry of Materials* 22.2 (2010), pp. 524–531.
- [114] Y. Qi, T. Sajoto, S. Barlow, E. G. Kim, J. L. Brédas, S. R. Marder, and A. Kahn. “Use of a high electron-affinity molybdenum dithiolene complex to p-dope hole-transport layers”. *Journal of the American Chemical Society* 131.35 (2009), pp. 12530–12531.
- [115] S. K. Mohapatra, Y. Zhang, B. Sandhu, M. S. Fonari, T. V. Timofeeva, S. R. Marder, and S. Barlow. “Synthesis, Characterization, and Crystal Structure of Molybdenum Complexes of Unsymmetrical Electron-Poor Dithiolene Ligands”. *Polyhedron* 116 (2016), pp. 88–95.
- [116] A. Nollau, M. Pfeiffer, T. Fritz, and K. Leo. “Controlled n-type doping of a molecular organic semiconductor: Naphthalenetetracarboxylic dianhydride (NTCDA) doped with bis(ethylenedithio)-tetrathiafulvalene (BEDT-TTF)”. *Journal of Applied Physics* 87.9 (2000), p. 4340.
- [117] S. Tanaka, K. Kanai, E. Kawabe, T. Iwahashi, T. Nishi, Y. Ouchi, and K. Seki. “Doping effect of tetrathianaphthacene molecule in organic semiconductors on their interfacial electronic structures studied by UV photoemission spectroscopy”. *Japanese Journal of Applied Physics* 44.6 A (2005), pp. 3760–3763.
- [118] C. K. Chan, F. Amy, Q. Zhang, S. Barlow, S. Marder, and A. Kahn. “N-type doping of an electron-transport material by controlled gas-phase incorporation of cobaltocene”. *Chemical Physics Letters* 431.1-3 (2006), pp. 67–71.
- [119] A. G. Werner, F. Li, K. Harada, M. Pfeiffer, T. Fritz, and K. Leo. “Pyronin B as a donor for n-type doping of organic thin films”. *Applied Physics Letters* 82.25 (2003), pp. 4495–4497.
- [120] P. Wei, T. Menke, B. D. Naab, K. Leo, M. Riede, and Z. Bao. “2-(2-Methoxyphenyl)-1,3-dimethyl-1 H-benzimidazol-3-ium iodide as a new air-stable n-type dopant for vacuum-processed organic semiconductor thin films”. *Journal of the American Chemical Society* 134.9 (2012), pp. 3999–4002.
- [121] S. Guo, S. B. Kim, S. K. Mohapatra, Y. Qi, T. Sajoto, A. Kahn, S. R. Marder, and S. Barlow. “N-doping of organic electronic materials using air-stable organometallics”. *Advanced Materials* 24.5 (2012), pp. 699–703.

Bibliography

- [122] Y. Qi, S. K. Mohapatra, S. Bok Kim, S. Barlow, S. R. Marder, and A. Kahn. “Solution doping of organic semiconductors using air-stable n-dopants”. *Applied Physics Letters* 100.8 (2012), p. 54.
- [123] C. G. Tang, M. C. Y. Ang, K.-K. Choo, V. Keerthi, J.-K. Tan, M. N. Syafiqah, T. Kugler, J. H. Burroughes, R.-Q. Png, L.-L. Chua, and P. K. H. Ho. “Doped polymer semiconductors with ultrahigh and ultralow work functions for ohmic contacts”. *Nature* 539.7630 (2016), pp. 536–540.
- [124] P. Pingel, R. Schwarzl, and D. Neher. “Effect of molecular p-doping on hole density and mobility in poly(3-hexylthiophene)”. *Applied Physics Letters* 100.14 (2012), pp. 2012–2015.
- [125] M. Pfeiffer, K. Leo, X. Zhou, J. S. Huang, M. Hofmann, A. Werner, and J. Blochwitz-Nimoth. “Doped organic semiconductors: Physics and application in light emitting diodes”. *Organic Electronics: physics, materials, applications* 4.2-3 (2003), pp. 89–103.
- [126] S. Olthof, S. Mehraeen, S. K. Mohapatra, S. Barlow, V. Coropceanu, J. L. Brédas, S. R. Marder, and A. Kahn. “Ultralow doping in organic semiconductors: Evidence of trap filling”. *Physical Review Letters* 109.17 (2012), p. 176601.
- [127] X. Lin, G. E. Purdum, Y. Zhang, S. Barlow, S. R. Marder, Y.-L. Loo, and A. Kahn. “Impact of a Low Concentration of Dopants on the Distribution of Gap States in a Molecular Semiconductor”. *Chemistry of Materials* 26.8 (2016), pp. 2677–2684.
- [128] Q. Bao, X. Liu, S. Braun, F. Gao, and M. Fahlman. “Energetics at Doped Conjugated Polymer/Electrode Interfaces”. *Advanced Materials Interfaces* 2.2 (2015), p. 1400403.
- [129] F. Deschler, D. Riedel, A. Deák, B. Ecker, E. V. Hauff, and E. Da. “Imaging of morphological changes and phase segregation in doped polymeric semiconductors”. *Synthetic Metals* 199 (2015), pp. 381–387.
- [130] G. Heimel, L. Romaner, E. Zojer, and J. L. Bredas. “The interface energetics of self-assembled monolayers on metals”. *Accounts of Chemical Research* 41.6 (2008), pp. 721–729.
- [131] M. S. White, D. C. Olson, S. E. Shaheen, N. Kopidakis, and D. S. Ginley. “Inverted bulk-heterojunction organic photovoltaic device using a solution-derived ZnO underlayer”. *Applied Physics Letters* 89.14 (2006), p. 143517.
- [132] M. Kano, T. Minari, and K. Tsukagoshi. “Improvement of subthreshold current transport by contact interface modification in p-type organic field-effect transistors”. *Applied Physics Letters* 94.14 (2009), p. 101.
- [133] S. Cho, J. H. Seo, K. Lee, and A. J. Heeger. “Enhanced performance of fullerene n-channel field-effect transistors with titanium sub-oxide injection layer”. *Advanced Functional Materials* 19.9 (2009), pp. 1459–1464.
- [134] A. C. Arias, M. Granström, D. S. Thomas, K. Petritsch, and R. H. Friend. “Doped conducting-polymer–semiconducting-polymer interfaces: Their use in organic photovoltaic devices”. *Physical Review B* 60.3 (1999), pp. 1854–1860.
- [135] Y. Zhou et al. “A Universal Method to Produce Low-Work Function Electrodes for Organic Electronics”. *Science* 873.April (2012), pp. 327–332.
- [136] W. Gao and A. Kahn. “Electronic structure and current injection in zinc phthalocyanine doped with tetrafluorotetracyanoquinodimethane: Interface versus bulk effects”. *Organic Electronics: physics, materials, applications* 3.2 (2002), pp. 53–63.

-
- [137] J. H. Lee and J. J. Kim. “Interfacial doping for efficient charge injection in organic semiconductors”. *Physica Status Solidi (A) Applications and Materials Science* 209.8 (2012), pp. 1399–1413.
- [138] S. Choi, C. Fuentes-Hernandez, C.-Y. Wang, T. M. Khan, F. A. Larraín, Y. Zhang, S. Barlow, S. R. Marder, and B. Kippelen. “A Study on Reducing Contact Resistance in Solution-Processed Organic Field-Effect Transistors”. *ACS applied materials & interfaces* 8.37 (2016), pp. 24744–24752.
- [139] U. Zschieschang, M. J. Kang, K. Takimiya, T. Sekitani, T. Someya, T. W. Canzler, A. Werner, J. Blochwitz-Nimoth, and H. Klauk. “Flexible low-voltage organic thin-film transistors and circuits based on C10 -DNTT”. *J. Mater. Chem.* 22.10 (2012), pp. 4273–4277.
- [140] A. A. Günther, M. Sawatzki, P. Formanek, D. Kasemann, and K. Leo. “Contact Doping for Vertical Organic Field-Effect Transistors”. *Advanced Functional Materials* 26.5 (2016), pp. 768–775.
- [141] F. Guillain, J. Endres, L. Bourgeois, A. Kahn, L. Vignau, and G. Wantz. “Solution-processed p-dopant as interlayer in polymer solar cells”. *ACS Applied Materials & Interfaces* 8.14 (2016), pp. 9262–9267.
- [142] J. Drechsel, B. Männig, F. Kozlowski, M. Pfeiffer, K. Leo, and H. Hoppe. “Efficient organic solar cells based on a double p-i-n architecture using doped wide-gap transport layers”. *Applied Physics Letters* 86.24 (2005), p. 244102.
- [143] J. Huang, M. Pfeiffer, A. Werner, J. Blochwitz, K. Leo, and S. Liu. “Low-voltage organic electroluminescent devices using pin structures”. *Applied Physics Letters* 80.1 (2002), pp. 139–141.
- [144] B. Lüssem, M. L. Tietze, H. Kleemann, C. H. szlig Bach, J. W. Bartha, A. Zakhidov, and K. Leo. “Doped organic transistors operating in the inversion and depletion regime”. *Nature Communications* 4 (2013), p. 2775.
- [145] D. S. Leem, S. Y. Kim, J. H. Lee, and J. J. Kim. “High efficiency p-i-n top-emitting organic light-emitting diodes with a nearly Lambertian emission pattern”. *Journal of Applied Physics* 106.6 (2009), p. 063114.
- [146] G. He, O. Schneider, D. Qin, X. Zhou, M. Pfeiffer, and K. Leo. “Very high-efficiency and low voltage phosphorescent organic light-emitting diodes based on a p-i-n junction”. *Journal of Applied Physics* 95.10 (2004), pp. 5773–5777.
- [147] R. Meerheim, S. Scholz, S. Olthof, G. Schwartz, S. Reineke, K. Walzer, and K. Leo. “Influence of charge balance and exciton distribution on efficiency and lifetime of phosphorescent organic light-emitting devices”. *Journal of Applied Physics* 104.1 (2008), p. 014510.
- [148] S. Hofmann, M. Thomschke, P. Freitag, M. Furno, B. Lüssem, and K. Leo. “Top-emitting organic light-emitting diodes: Influence of cavity design”. *Applied Physics Letters* 97.25 (2010), pp. 2008–2011.
- [149] S. Singh, S. K. Mohapatra, A. Sharma, C. Fuentes-Hernandez, S. Barlow, S. R. Marder, and B. Kippelen. “Reduction of contact resistance by selective contact doping in fullerene n-channel organic field-effect transistors”. *Applied Physics Letters* 102.15 (2013), p. 63.
- [150] T. Minari, T. Miyadera, K. Tsukagoshi, Y. Aoyagi, and H. Ito. “Charge injection process in organic field-effect transistors”. *Applied Physics Letters* 91.5 (2007), p. 053508.

Bibliography

- [151] S. P. Tiwari, W. J. Potscavage, T. Sajoto, S. Barlow, S. R. Marder, and B. Kippelen. “Pentacene organic field-effect transistors with doped electrode-semiconductor contacts”. *Organic Electronics: physics, materials, applications* 11.5 (2010), pp. 860–863.
- [152] F. Ante, D. Köhlein, T. Zaki, U. Zschieschang, K. Takimiya, M. Ikeda, T. Sekitani, T. Someya, J. N. Burghartz, K. Kern, and H. Klauk. “Contact resistance and megahertz operation of aggressively scaled organic transistors”. *Small* 8.1 (2012), pp. 73–79.
- [153] Y. Abe, T. Hasegawa, Y. Takahashi, T. Yamada, and Y. Tokura. “Control of threshold voltage in pentacene thin-film transistors using carrier doping at the charge-transfer interface with organic acceptors”. *Applied Physics Letters* 87.15 (2005), p. 153506.
- [154] J. H. Oh, P. Wei, and Z. Bao. “Molecular n-type doping for air-stable electron transport in vacuum-processed n-channel organic transistors”. *Applied Physics Letters* 97.24 (2010), p. 269.
- [155] M. P. Hein, A. A. Zakhidov, B. Lüssem, J. Jankowski, M. L. Tietze, M. K. Riede, and K. Leo. “Molecular doping for control of gate bias stress in organic thin film transistors”. *Applied Physics Letters* 104.1 (2014), p. 013507.
- [156] M. Pfeiffer. “Controlled p-doping of pigment layers by cosublimation: Basic mechanisms and implications for their use in organic photovoltaic cells”. *Solar Energy Materials and Solar Cells* 63.1 (2000), pp. 83–99.
- [157] B. Maennig et al. “Organic p-i-n solar cells”. *Applied Physics A: Materials Science and Processing* 79.1 (2004), pp. 1–14.
- [158] C. Falkenberg, K. Leo, and M. K. Riede. “Improved photocurrent by using n-doped 2,3,8,9,14,15-hexachloro-5,6,11,12, 17,18-hexaazatrinaphthylene as optical spacer layer in p-i-n type organic solar cells”. *Journal of Applied Physics* 110.12 (2011), p. 124509.
- [159] L. J. A. Koster, V. D. Mihailetchi, and P. W. M. Blom. “Ultimate efficiency of polymer/fullerene bulk heterojunction solar cells”. *Applied Physics Letters* 88.9 (2006), p. 093511.
- [160] M. C. Scharber, D. Mühlbacher, M. Koppe, P. Denk, C. Waldauf, A. J. Heeger, and C. J. Brabec. “Design Rules for Donors in Bulk-Heterojunction Solar Cells—Towards 10 % Energy-Conversion Efficiency”. *Advanced Materials* 18.6 (2006), pp. 789–794.
- [161] G. Dennler, M. C. Scharber, T. Ameri, P. Denk, K. Forberich, C. Waldauf, and C. J. Brabec. “Design rules for donors in bulk-heterojunction tandem solar cells-towards 15 % energy-conversion efficiency”. *Advanced Materials* 20.3 (2008), pp. 579–583.
- [162] H.-Y. Chen, J. Hou, S. Zhang, Y. Liang, G. Yang, Y. Yang, L. Yu, Y. Wu, and G. Li. “Polymer solar cells with enhanced open-circuit voltage and efficiency”. *Nature Photonics* 3.11 (2009), pp. 649–653.
- [163] J. Belasco, S. K. Mohapatra, Y. Zhang, S. Barlow, S. R. Marder, and A. Kahn. “Molecular doping and tuning threshold voltage in 6,13-bis(triisopropylsilylethynyl)pentacene/polymer blend transistors”. *Applied Physics Letters* 105.6 (2014), pp. 2012–2017.
- [164] C. M. Cardona, W. Li, A. E. Kaifer, D. Stockdale, and G. C. Bazan. “Electrochemical considerations for determining absolute frontier orbital energy levels of conjugated polymers for solar cell applications”. *Advanced Materials* 23.20 (2011), pp. 2367–2371.
- [165] F. C. Krebs. “Fabrication and processing of polymer solar cells: A review of printing and coating techniques”. *Solar Energy Materials and Solar Cells* 93.4 (2009), pp. 394–412.

-
- [166] V. S. Gevaerts, L. J. A. Koster, M. M. Wienk, and R. A. J. Janssen. “Discriminating between Bilayer and Bulk Heterojunction Polymer:Fullerene Solar Cells Using the External Quantum Efficiency”. *ACS Applied Materials & Interfaces* 3.9 (2011), pp. 3252–3255.
- [167] K. H. Lee, P. E. Schwenn, A. R. G. Smith, H. Cavaye, P. E. Shaw, M. James, K. B. Krueger, I. R. Gentle, P. Meredith, and P. L. Burn. “Morphology of all-solution-processed "bilayer" organic solar cells”. *Advanced Materials* 23.6 (2011), pp. 766–770.
- [168] D. H. Kim, J. Mei, A. L. Ayzner, K. Schmidt, G. Giri, A. L. Appleton, M. F. Toney, and Z. Bao. “Sequentially solution-processed, nanostructured polymer photovoltaics using selective solvents”. *Energy & Environmental Science* 7.3 (2014), p. 1103.
- [169] M Granstrom, K Petritsch, a. C. Arias, A Lux, M. R. Andersson, and R. H. Friend. “Laminated fabrication of polymeric photovoltaic diodes”. *Nature* 395.6699 (1998), pp. 257–260.
- [170] H. B. Michaelson. “The work function of the elements and its periodicity”. *Journal of Applied Physics* 48.11 (1977), pp. 4729–4733.
- [171] D. T. Duong, C. Wang, E. Antono, M. F. Toney, and A. Salleo. “The chemical and structural origin of efficient p-type doping in P3HT”. *Organic Electronics: physics, materials, applications* 14.5 (2013), pp. 1330–1336.
- [172] H. Kleemann, C. Schuenemann, A. A. Zakhidov, M. Riede, B. Lüssem, and K. Leo. “Structural phase transition in pentacene caused by molecular doping and its effect on charge carrier mobility”. *Organic Electronics* 13.1 (2012), pp. 58–65.
- [173] V. I. Arkhipov, P. Heremans, E. V. Emelianova, and H. Bässler. “Effect of doping on the density-of-states distribution and carrier hopping in disordered organic semiconductors”. *Physical Review B - Condensed Matter and Materials Physics* 71.4 (2005), p. 045214.
- [174] H. Bässler and A. Köhler. “Charge transport in organic semiconductors”. *Topics in Current Chemistry* 312 (2012), pp. 1–65.
- [175] L. Li, G. Meller, and H. Kosina. “Analytical conductivity model for doped organic semiconductors”. *Journal of Applied Physics* 101.3 (2007), p. 033716.
- [176] A. Higgins, S. K. Mohapatra, S. Barlow, S. R. Marder, and A. Kahn. “Dopant controlled trap-filling and conductivity enhancement in an electron-transport polymer”. *Applied Physics Letters* 106.16 (2015), p. 163301.
- [177] J. Xue and S. R. Forrest. “Bipolar doping between a molecular organic donor-acceptor couple”. *Physical Review B - Condensed Matter and Materials Physics* 69.24 (2004), p. 245322.
- [178] I. E. Jacobs, E. W. Aasen, J. L. Oliveira, T. N. Fonseca, J. D. Roehling, J. Li, G. Zhang, M. P. Augustine, M. Mascal, and A. Moule. “Comparison of solution-mixed and sequentially processed P3HT:F4TCNQ films: effect of doping-induced aggregation on film morphology”. *J. Mater. Chem. C* 4.16 (2016), pp. 3454–3466.
- [179] H. Kleemann, B. Lüssem, and K. Leo. “Controlled formation of charge depletion zones by molecular doping in organic pin-diodes and its description by the Mott-Schottky relation”. *Journal of Applied Physics* 111.12 (2012), p. 123722.
- [180] V. W. Schottky. “Vereinfazhte und erweiterte Theorie der Randschicht-”. *Zeitschrift für Physik* 118 (1941), pp. 539–592.

Bibliography

- [181] P. Pahner, H. Kleemann, L. Burtone, M. L. Tietze, J. Fischer, K. Leo, and B. Lüssem. “Pentacene Schottky diodes studied by impedance spectroscopy: Doping properties and trap response”. *Physical Review B - Condensed Matter and Materials Physics* 88.19 (2013), p. 195205.
- [182] S. Khelifi, K. Decock, J. Lauwaert, H. Vrielinck, D. Spoltore, F. Piersimoni, J. Manca, A. Belghachi, and M. Burgelman. “Investigation of defects by admittance spectroscopy measurements in poly (3-hexylthiophene):(6,6)-phenyl C61-butyric acid methyl ester organic solar cells degraded under air exposure”. *Journal of Applied Physics* 110.9 (2011), p. 094509.
- [183] A. Seemann, T. Sauermann, C. Lungenschmied, O. Armbruster, S. Bauer, H. J. Egelhaaf, and J. Hauch. “Reversible and irreversible degradation of organic solar cell performance by oxygen”. *Solar Energy* 85.6 (2011), pp. 1238–1249.
- [184] T. Kirchartz, W. Gong, S. A. Hawks, T. Agostinelli, R. C. I. MacKenzie, Y. Yang, and J. Nelson. “Sensitivity of the Mott–Schottky Analysis in Organic Solar Cells”. *The Journal of Physical Chemistry C* 116.14 (2012), pp. 7672–7680.
- [185] S. L. M. van Mensfoort and R. Coehoorn. “Determination of Injection Barriers in Organic Semiconductor Devices from Capacitance Measurements”. *Physical Review Letters* 100.8 (2008), p. 086802.
- [186] T. Menke, D. Ray, H. Kleemann, K. Leo, and M. Riede. “Determining doping efficiency and mobility from conductivity and Seebeck data of n-doped C60 layers”. *Physica Status Solidi (B)* 252.8 (2014), pp. 1877–1883.
- [187] J. E. Cochran, M. J. N. Junk, A. M. Glaudell, P. L. Miller, J. S. Cowart, M. F. Toney, C. J. Hawker, B. F. Chmelka, and M. L. Chabinyc. “Molecular interactions and ordering in electrically doped polymers: Blends of PBTTT and F4TCNQ”. *Macromolecules* 47.19 (2014), pp. 6836–6846.
- [188] T. Polenova, R. Gupta, and A. Goldbourt. “Magic angle spinning NMR spectroscopy: A versatile technique for structural and dynamic analysis of solid-phase systems”. *Analytical Chemistry* 87.11 (2015), pp. 5458–5469.
- [189] M. R. Hansen, R. Graf, and H. W. Spiess. “Interplay of Structure and Dynamics in Functional Macromolecular and Supramolecular Systems As Revealed by Magnetic Resonance Spectroscopy”. *Chemical Reviews* 116.3 (2015), pp. 1272–1308.
- [190] W. E. Blumberg. “Nuclear spin-lattice relaxation caused by paramagnetic impurities”. *Physical Review* 119.1 (1960), pp. 79–84.
- [191] E. J. Lous, P. W. M. Blom, L. W. Molenkamp, and D. M. D. Leeuw. “Schottky contacts on a highly doped organic semiconductor”. *Physical Review B* 51.23 (1995), pp. 17251–17254.
- [192] C.-L. Fan, W.-C. Lin, H.-S. Chang, Y.-Z. Lin, and B.-R. Huang. “Effects of the F4TCNQ-Doped Pentacene Interlayers on Performance Improvement of Top-Contact Pentacene-Based Organic Thin-Film Transistors”. *Materials* 9.1 (2016), p. 46.
- [193] A. Carbone, B. K. Kotowska, and D. Kotowski. “Space-charge-limited current fluctuations in organic semiconductors”. *Physical Review Letters* 95.23 (2005), p. 236601.
- [194] G. A. H. Wetzelaer and P. W. M. Blom. “Ohmic current in organic metal-insulator-metal diodes revisited”. *Physical Review B - Condensed Matter and Materials Physics* 89.24 (2014), p. 241201.

-
- [195] Y. Zhang, B. D. Boer, and P. W. M. Blom. “Controllable molecular doping and charge transport in solution-processed polymer semiconducting layers”. *Advanced Functional Materials* 19.12 (2009), pp. 1901–1905.
- [196] Y. Zhang and P. W. M. Blom. “Enhancement of the hole injection into regioregular poly(3-hexylthiophene) by molecular doping”. *Applied Physics Letters* 97.8 (2010), pp. 97–100.
- [197] P. E. Burrows, Z. Shen, V. Bulovic, D. M. McCarty, S. R. Forrest, J. a. Cronin, and M. E. Thompson. “Relationship between electroluminescence and current transport in organic heterojunction light-emitting devices”. *Journal of Applied Physics* 79.10 (1996), pp. 7991–8006.
- [198] J.-P. Yang, W.-Q. Wang, F. Bussolotti, L.-W. Cheng, Y.-Q. Li, S. Kera, J.-X. Tang, X.-H. Zeng, and N. Ueno. “Quantitative Fermi level tuning in amorphous organic semiconductor by molecular doping: Toward full understanding of the doping mechanism”. *Applied Physics Letters* 109.9 (2016), p. 093302.
- [199] S. K. Mohapatra, Y. Zhang, B. Sandhu, M. S. Fonari, T. V. Timofeeva, S. R. Marder, and S. Barlow. “Synthesis, Characterization, and Crystal Structure of Molybdenum Complexes of Unsymmetrical Electron-Poor Dithiolene Ligands”. *Polyhedron* 116 (2016), pp. 88–95.
- [200] P. Lienhard. “Caractérisation et modélisation du vieillissement des photodiodes organiques”. PhD thesis. Université Grenoble Alpes, 2016.
- [201] J. Yu, N. W. Song, J. D. McNeill, and P. F. Barbara. “Efficient Exciton Quenching by Hole Polarons in the Conjugated Polymer MEH-PPV”. *Israel Journal of Chemistry* 44.1-3 (2004), pp. 127–132.
- [202] P. Tyagi, S. Tuli, and R. Srivastava. “Study of fluorescence quenching due to 2, 3, 5, 6-tetrafluoro-7, 7, 8, 8-tetracyano quinodimethane and its solid state diffusion analysis using photoluminescence spectroscopy”. *The Journal of Chemical Physics* 142.5 (2015), p. 054707.
- [203] J Hofkens, J Enderlein, M Sauer, J Hofkens, and J Enderlein. “Basic Principles of Fluorescence Spectroscopy”. *Handbook of Fluorescence Spectroscopy and Imaging: From Single Molecules to Ensembles* (2011), pp. 1–30.
- [204] J. R. Lakowicz. *Principles of fluorescence spectroscopy*. Springer US, 1999.
- [205] C. D. Geddes. “Optical halide sensing using fluorescence quenching: theory, simulations and applications - a review”. *Measurement Science and Technology* 12.9 (2001), R53–R88.
- [206] M. I. N. Zheng, F. Bai, F. Li, Y. Li, and D. Zhu. “The Interaction Between Conjugated Polymer and Fullerenes”. *Journal of applied polymer science* 70.3 (1998), pp. 599–603.
- [207] T. Walter, R. Herberholz, C. Muller, and H. W. Schock. “Determination of defect distributions from admittance measurements and application to Cu(In,Ga)Se₂ based heterojunctions”. *Journal of Applied Physics* 80.8 (1996), p. 4411.
- [208] A. Sharma, P. Kumar, B. Singh, S. R. Chaudhuri, and S. Ghosh. “Capacitance-voltage characteristics of organic Schottky diode with and without deep traps”. *Applied Physics Letters* 99.2 (2011), p. 130.
- [209] J. Fischer, D. Ray, H. Kleemann, P. Pahnner, M. Schwarze, C. Koerner, K. Vandewal, and K. Leo. “Density of states determination in organic donor-acceptor blend layers enabled by molecular doping”. *Journal of Applied Physics* 117.24 (2015), p. 245501.

Bibliography

- [210] D. L. Losee. “Admittance spectroscopy of impurity levels in Schottky barriers”. *Journal of Applied Physics* 46.5 (1975), pp. 2204–2214.
- [211] Y. Zohta. “Frequency dependence of C and $\Delta V/\Delta(C-2)$ of Schottky barriers containing deep impurities”. *Solid State Electronics* 16.9 (1973), pp. 1029–1035.
- [212] D. Vuillaume. “Caractérisation de défauts à l’interface silicium-oxyde de silicium dans les structures M.O.S. par des méthodes spectroscopiques”. PhD thesis. 1984.
- [213] J. A. Carr, M. Elshobaki, and S. Chaudhary. “Deep defects and the attempt to escape frequency in organic photovoltaic materials”. *Applied Physics Letters* 107.20 (2015), p. 203302.
- [214] G. Zuo, H. Abdalla, and M. Kemerink. “Impact of doping on the density of states and the mobility in organic semiconductors”. *Physical Review B* 93.23 (2016), p. 235203.
- [215] M. S. A. Abdou, F. P. Orfino, Y. Son, and S. Holdcroft. “Interaction of oxygen with conjugated polymers: charge transfer complex formation with poly (3-alkylthiophenes)”. *Journal of the American Chemical Society* 119.7 (1997), pp. 4518–4524.
- [216] X. Lei, F. Zhang, T. Song, and B. Sun. “P-type doping effect on the performance of organic-inorganic hybrid solar cells”. *Applied Physics Letters* 99.23 (2011), pp. 2013–2016.
- [217] C. Väterlein, B. Ziegler, W. Gebauer, H. Neureiter, M. Stoldt, M. S. Weaver, P. Bäuerle, M. Sokolowski, D. D. C. Bradley, and E. Umbach. “Electrical conductivity and oxygen doping of vapour-deposited oligothiophene films”. *Synthetic Metals* 76.1-3 (1996), pp. 133–136.
- [218] J. M. Zhuo, L. H. Zhao, R. Q. Png, L. Y. Wong, P. J. Chia, J. C. Tang, S. Sivaramakrishnan, M. Zhou, E. C. W. Ou, S. J. Chua, W. S. Sim, L. L. Chua, and P. K. H. Ho. “Direct spectroscopic evidence for a photodoping mechanism in polythiophene and poly(bithiophene-alt-thienothiophene) organic semiconductor thin films involving oxygen and sorbed moisture”. *Advanced Materials* 21.46 (2009), pp. 4747–4752.
- [219] H. H. Liao, C. M. Yang, C. C. Liu, S. F. Horng, H. F. Meng, and J. T. Shy. “Dynamics and reversibility of oxygen doping and de-doping for conjugated polymer”. *Journal of Applied Physics* 103.10 (2008), p. 104506.
- [220] A. C. Arias, J. D. MacKenzie, I. McCulloch, J. Rivnay, and A. Salleo. “Materials and applications for large area electronics: Solution-based approaches”. *Chemical Reviews* 110.1 (2010), pp. 3–24.
- [221] K. J. Baeg, M. Binda, D. Natali, M. Caironi, and Y. Y. Noh. “Organic light detectors: Photodiodes and phototransistors”. *Advanced Materials* 25.31 (2013), pp. 4267–4295.
- [222] X. Liu, H. Chen, and S. Tan. “Overview of high-efficiency organic photovoltaic materials and devices”. *Renewable and Sustainable Energy Reviews* 52 (2015), pp. 1527–1538.
- [223] H. Kang, G. Kim, J. Kim, S. Kwon, H. Kim, and K. Lee. “Bulk-Heterojunction Organic Solar Cells : Five Core Technologies for Their Commercialization”. *Advanced Materials* 28.36 (2016), pp. 7821–7861.
- [224] A. Savva, E. Georgiou, G. Papazoglou, A. Z. Chrusou, K. Kapnisis, and S. a. Choulis. “Photovoltaic analysis of the effects of PEDOT:PSS-additives hole selective contacts on the efficiency and lifetime performance of inverted organic solar cells”. *Solar Energy Materials and Solar Cells* 132 (2015), pp. 507–514.

-
- [225] P. Wilson, C. Lekakou, and J. F. Watts. “A comparative assessment of surface microstructure and electrical conductivity dependence on co-solvent addition in spin coated and inkjet printed poly(3,4-ethylenedioxythiophene):polystyrene sulphonate (PEDOT:PSS)”. *Organic Electronics: physics, materials, applications* 13.3 (2012), pp. 409–418.
- [226] H. Cao, W. He, Y. Mao, X. Lin, K. Ishikawa, J. H. Dickerson, and W. P. Hess. “Recent progress in degradation and stabilization of organic solar cells”. *Journal of Power Sources* 264 (2014), pp. 168–183.
- [227] M. P. D. Jong, L. J. V. Ijzendoorn, and M. J.a. D. Voigt. “Stability of the interface between indium-tin-oxide in polymer light-emitting diodes”. *App. Phys. Lett.* 77.14 (2000), pp. 2255–2257.
- [228] G. Li, C. W. Chu, V. Shrotriya, J. Huang, and Y. Yang. “Efficient inverted polymer solar cells”. *Applied Physics Letters* 88.25 (2006), p. 253503.
- [229] V. A. Kolesov, C. Fuentes-Hernandez, W.-F. Chou, N. Aizawa, F. A. Larrain, M. Wang, A. Perrotta, S. Choi, S. Graham, G. C. Bazan, T.-Q. Nguyen, S. R. Marder, and B. Kippelen. “Solution-based electrical doping of semiconducting polymer films over a limited depth”. *Nature Materials* 1.December (2016), pp. 1–8.
- [230] Y. Li, Y. Wu, and S Ong. “Facile Synthesis of Silver Nanoparticles Useful for Fabrication of High-Conductivity Elements for Printed Electronics Facile Synthesis of Silver Nanoparticles Useful for Fabrication of High-Conductivity Elements for Printed Electronics”. *Journal of the American Chemical Society* 127.10 (2005), pp. 3266–3267.
- [231] L. Huang, Y. Huang, J. Liang, X. Wan, and Y. Chen. “Graphene-based conducting inks for direct inkjet printing of flexible conductive patterns and their applications in electric circuits and chemical sensors”. *Nano Research* 4.7 (2011), pp. 675–684.
- [232] D. Gupta, M. M. Wienk, and R. a. J. Janssen. “Efficient polymer solar cells on opaque substrates with a laminated PEDOT:PSS top electrode”. *Advanced Energy Materials* 3.6 (2013), pp. 782–787.
- [233] E. L. Ratcliff, J. Meyer, K. X. Steirer, N. R. Armstrong, D. Olson, and A. Kahn. “Energy level alignment in PCDTBT:PC 70BM solar cells: Solution processed NiO x for improved hole collection and efficiency”. *Organic Electronics: physics, materials, applications* 13.5 (2012), pp. 744–749.
- [234] A. Pierre, I. Deckman, P. B. Lechêne, and A. C. Arias. “High Detectivity All-Printed Organic Photodiodes”. *Advanced Materials* 27.41 (2015), pp. 6411–6417.
- [235] I. K. Kim, B. N. Pal, M. Ullah, P. L. Burn, S. C. Lo, P. Meredith, and E. B. Namdas. “High-Performance, Solution-Processed Non-polymeric Organic Photodiodes”. *Advanced Optical Materials* 3.1 (2015), pp. 50–56.
- [236] X. Gong, M. Tong, Y. Xia, W. Cai, J. S. Moon, Y. Cao, G. Yu, C.-L. Shieh, B. Nilsson, and A. J. Heeger. “High-Detectivity Polymer Photodetectors with Spectral Response from 300 nm to 1450 nm”. *Science* 325.5948 (2009), pp. 1665–1667.
- [237] J. R. Manders, T. H. Lai, Y. An, W. Xu, J. Lee, D. Y. Kim, G. Bosman, and F. So. “Low-noise multispectral photodetectors made from all solution-processed inorganic semiconductors”. *Advanced Functional Materials* 24.45 (2014), pp. 7205–7210.
- [238] R. D. Jansen-van Vuuren, A. Armin, A. K. Pandey, P. L. Burn, and P. Meredith. “Organic Photodiodes: The Future of Full Color Detection and Image Sensing”. *Advanced Materials* 28.24 (2016), pp. 4766–4802.

Bibliography

- [239] V. D. Mihailetschi, L. J. A. Koster, J. C. Hummelen, and P. W. M. Blom. “Photocurrent generation in polymer-fullerene bulk heterojunctions”. *Physical Review Letters* 93.21 (2004), pp. 19–22.
- [240] V. D. Mihailetschi, J. Wildeman, and P. W. M. Blom. “Space-charge limited photocurrent”. *Physical Review Letters* 94.12 (2005), p. 126602.
- [241] A. Pivrikas, G. Juška, R. Österbacka, M. Westerling, M. Viliunas, K. Arlauskas, and H. Stubb. “Langevin recombination and space-charge-perturbed current transients in regio-random poly(3-hexylthiophene)”. *Physical Review B - Condensed Matter and Materials Physics* 71.12 (2005), p. 125205.
- [242] A. M. Goodman and A. Rose. “Double extraction of uniformly generated electron-hole pairs from insulators with noninjecting contacts”. *Journal of Applied Physics* 42.7 (1971), pp. 2823–2830.
- [243] R. H. Parmenter and W. Ruppel. “Two-carrier space-charge-limited current in a trap-free insulator”. *Journal of Applied Physics* 30.10 (1959), pp. 1548–1558.
- [244] H. L. Kwok. “Carrier mobility in organic semiconductor thin films”. *Reviews on Advanced Materials Science* 5.1 (2003), pp. 62–66.
- [245] M. Pope and C. E. Swenberg. *Electronic Processes in Organic Crystals*. 1982, p. 455.
- [246] L. J. A. Koster, E. C. P. Smits, V. D. Mihailetschi, and P. W. M. Blom. “Device model for the operation of polymer/fullerene bulk heterojunction solar cells”. *Physical Review B - Condensed Matter and Materials Physics* 72.8 (2005), p. 085205.
- [247] L. J. A. Koster, M. Kemerink, M. M. Wienk, K. Maturová, and R. A. J. Janssen. “Quantifying bimolecular recombination losses in organic bulk heterojunction solar cells”. *Advanced Materials* 23.14 (2011), pp. 1670–1674.
- [248] A. Petersen, T. Kirchartz, and T. Wagner. “Charge extraction and photocurrent in organic bulk heterojunction solar cells”. *Physical Review B* 85.4 (2012), p. 045208.
- [249] R. a. Street, K. W. Song, and S. Cowan. “Influence of series resistance on the photocurrent analysis of organic solar cells”. *Organic Electronics* 12.2 (2011), pp. 244–248.
- [250] W. Tress, S. Corvers, K. Leo, and M. Riede. “Investigation of driving forces for charge extraction in organic solar cells: Transient photocurrent measurements on solar cells showing s-shaped current-voltage characteristics”. *Advanced Energy Materials* 3.7 (2013), pp. 873–880.
- [251] W. Tress, K. Leo, and M. Riede. “Influence of hole-transport layers and donor materials on open-circuit voltage and shape of I-V curves of organic solar cells”. *Advanced Functional Materials* 21.11 (2011), pp. 2140–2149.
- [252] S. Duhm, I. Salzmann, B. Bröker, H. Glowatzki, R. L. Johnson, and N. Koch. “Interdiffusion of molecular acceptors through organic layers to metal substrates mimics doping-related energy level shifts”. *Applied Physics Letters* 95.9 (2009), p. 223.
- [253] M. T. Lloyd, D. C. Olson, P. Lu, E. Fang, D. L. Moore, M. S. White, M. O. Reese, D. S. Ginley, and J. W. P. Hsu. “Impact of contact evolution on the shelf life of organic solar cells”. *Journal of Materials Chemistry* 19.41 (2009), p. 7638.
- [254] M. Schaer, F. Nüesch, D. Berner, W. Leo, L. Zuppiroli, and B. M. Schaer. “Water Vapor and Oxygen Degradation Mechanisms in Organic Light Emitting Diodes”. *Advanced Functional Materials* 11.2 (2001), pp. 116–121.

-
- [255] D. Baierl, B. Fabel, P. Gabos, L. Pancheri, P. Lugli, and G. Scarpa. “Solution-processable inverted organic photodetectors using oxygen plasma treatment”. *Organic Electronics: physics, materials, applications* 11.7 (2010), pp. 1199–1206.
- [256] A Vesel and M Mozetic. “Surface functionalization of organic materials by weakly ionized highly dissociated oxygen plasma”. *Journal of Physics: Conference Series* 162 (2009), p. 012015.
- [257] S. Hoshino, M. Yoshida, S. Uemura, T. Kodzasa, N. Takada, T. Kamata, and K. Yase. “Influence of moisture on device characteristics of polythiophene-based field-effect transistors”. *Journal of Applied Physics* 95.9 (2004), pp. 5088–5093.
- [258] E. J. Meijer, C. Detcheverry, P. J. Baesjou, E. Van Veenendaal, D. M. De Leeuw, and T. M. Klapwijk. “Dopant density determination in disordered organic field-effect transistors”. *Journal of Applied Physics* 93.8 (2003), pp. 4831–4835.
- [259] D Knipp and J. E. Northrup. “Electric-Field-Induced Gap States in Pentacene”. *Advanced Materials* 21.24 (2009), pp. 2511–2515.
- [260] D. Knipp, A. Benor, V. Wagner, and T. Muck. “Influence of impurities and structural properties on the device stability of pentacene thin film transistors”. *Journal of Applied Physics* 101.4 (2007).
- [261] D. V. Lang, X. Chi, T. Siegrist, a. M. Sergent, and a. P. Ramirez. “Bias-dependent generation and quenching of defects in pentacene”. *Physical Review Letters* 93.7 (2004), pp. 5–8.
- [262] J. Schafferhans, A. Baumann, A. Wagenpfahl, C. Deibel, and V. Dyakonov. “Oxygen doping of P3HT:PCBM blends: Influence on trap states, charge carrier mobility and solar cell performance”. *Organic Electronics: physics, materials, applications* 11.10 (2010), pp. 1693–1700.
- [263] R. A. Street, M. Schoendorf, A. Roy, and J. H. Lee. “Interface state recombination in organic solar cells”. *Physical Review B* 81.20 (2010), p. 205307.
- [264] H. Hintz, H. Peisert, H. J. Egelhaaf, and T. Chasse. “Reversible and irreversible light-induced p-doping of p3ht by oxygen studied by photoelectron spectroscopy (XPS/UPS)”. *Journal of Physical Chemistry C* 115.27 (2011), pp. 13373–13376.
- [265] L. Lüer, H.-J. Egelhaaf, and D. Oelkrug. “(Photo)conductivity of conjugated oligomer films: mobile charge carrier formation by oxygen”. *Optical Materials* 9.1-4 (1998), pp. 454–460.
- [266] A. R. Völkel, R. A. Street, and D. Knipp. “Carrier transport and density of state distributions in pentacene transistors”. *Physical Review B - Condensed Matter and Materials Physics* 66.19 (2002), pp. 1953361–1953368.
- [267] B. Bouthinon. “Impact des états de gap sur les performances des photodiodes organiques”. PhD thesis. 2014.
- [268] B. Qi and J. Wang. “Open-circuit voltage in organic solar cells”. *Journal of Materials Chemistry* 22.46 (2012), p. 24315.
- [269] M. Dolores Perez, C. Borek, S. R. Forrest, and M. E. Thompson. “Molecular and morphological influences on the open circuit voltages of organic photovoltaic devices”. *Journal of the American Chemical Society* 131.26 (2009), pp. 9281–9286.

Bibliography

- [270] L. Chen, P. Degenaar, and D. D. C. Bradley. “Polymer transfer printing: Application to layer coating, pattern definition, and diode dark current blocking”. *Advanced Materials* 20.9 (2008), pp. 1679–1683.
- [271] N. Kim, W. J. Potscavage, B. Domercq, B. Kippelen, and S. Graham. “A hybrid encapsulation method for organic electronics”. *Applied Physics Letters* 94.16 (2009), p. 163308.
- [272] S. Sarkar, J. H. Culp, J. T. Whyland, M. Garvan, and V. Misra. “Encapsulation of organic solar cells with ultrathin barrier layers deposited by ozone-based atomic layer deposition”. *Organic Electronics* 11.12 (2010), pp. 1896–1900.
- [273] S. B. Sapkota, A. Spies, B. Zimmermann, I. Dürr, and U. Würfel. “Promising long-term stability of encapsulated ITO-free bulk-heterojunction organic solar cells under different aging conditions”. *Solar Energy Materials and Solar Cells* 130 (2014), pp. 144–150.
- [274] J. C. Scott, J. H. Kaufman, P. J. Brock, R. DiPietro, J. Salem, and J. A. Goitia. “Degradation and failure of MEH-PPV light-emitting diodes”. *Journal of Applied Physics* 79.5 (1996), pp. 2745–2751.
- [275] A. Ulman. “Formation and Structure of Self-Assembled Monolayers”. *Chemical Reviews* 96.4 (1996), pp. 1533–1554.
- [276] T. M. Brown, J. S. Kim, R. H. Friend, F. Cacialli, R. Daik, and W. J. Feast. “Built-in field electroabsorption spectroscopy of polymer light-emitting diodes incorporating a doped poly(3,4-ethylene dioxythiophene) hole injection layer”. *Applied Physics Letters* 75.12 (1999), pp. 1679–1681.

List of Publications and Presentations

Publications

J. Herrbach, A. Revaux, D. Vuillaume, and A. Kahn. "P-doped organic semiconductor: Potential replacement for PEDOT: PSS in organic photodetectors." *Applied Physics Letters* 109.7 (2016), p. 073301.

J. Euvrard, A. Revaux, P.-A. Bayle, M. Bardet, D. Vuillaume and A. Kahn. "The formation of polymer dopant aggregates as a possible origin of limited doping efficiency at high dopant concentration." *Organic Electronics*, submitted.

J. Euvrard, A. Revaux, A. Cantarano, S. Jacob, A. Kahn and D. Vuillaume. "Impact of Unintentional Oxygen Doping on Organic Photodetectors." *Advanced Electronic Materials*, submitted.

Presentations

A study of organic semiconductor doping and its application in a photodetector as hole transport layer.

- Oral presentation at International Conference on Organic Electronics (ICOE) in Bratislava, Slovakia, June 13-15, 2016.

- Oral presentation at 9th International Symposium on Flexible Organic Electronics (ISFOE) in Thessaloniki, Greece, July 4-7, 2016.

Characterization of gap state related to organic semiconductor p-doping.

- Poster presentation at Materials Research Society (MRS) Spring in Phoenix, Arizona, United States, April 17-21, 2017.

- Oral presentation at European Materials Research Society (E-MRS) Spring in Strasbourg, France, May 22-26, 2017.